Abstract

Title of dissertation: dc SQUID Phase Qubit

Tauno Palomaki, Doctor of Philosophy, 2008

Dissertation directed by: Professor Frederick C. Wellstood
Department of Physics

This thesis examines the behavior of dc SQUID phase qubits in terms of their proposed use in a quantum computer. In a phase qubit, the two lowest energy states ($n = 0$ and $n = 1$) of a current-biased Josephson junction form the qubit states, with the gauge invariant phase difference across the junction being relatively well defined. In a dc SQUID phase qubit, the Josephson junction is isolated from the environment using an inductive isolation network and Josephson junction, which are connected across the phase qubit junction to form a dc SQUID.

Five dc SQUID phase qubits were examined at temperatures down to 25 mK. Three of the devices had qubit junctions that were $100\,\mu m^2$ Nb/AlO$_x$/Nb junctions with critical currents of roughly $30\,\mu A$. The other two had $16\,\mu m^2$ Al/AlO$_x$/Al junctions with critical currents of roughly $1.3\,\mu A$. The device that had the best performance was an Al/AlO$_x$/Al device with a relaxation time $T_1 \approx 30\,ns$ and a coherence time $T_2 \approx 24\,ns$.

The devices were characterized using microwave spectroscopy, Rabi oscillations, relaxation and Ramsey fringe measurements. I was also able to see coupling between two Nb/AlO$_x$/Nb dc SQUID phase qubits and perform Rabi oscillations with them. The Nb/AlO$_x$/Nb devices had a relaxation time and coherence time that were half that of the Al/AlO$_x$/Al device.

One of the goals of this work was to understand the nature of parasitic quantum systems (TLSs) that interact with the qubit. Coupling between a TLS and a qubit causes an avoided level crossing in the $n=0 \rightarrow n=1$ transition spectrum of the qubit. In the Al/AlO$_x$/Al devices unintentional avoided level crossings were visible with sizes up to 240 MHz, although most visible splittings were of order ~20 MHz. The measured spectra were compared to a model of the avoided level crossing based on the TLSs coupling to the junction, through either the critical current or the voltage across the junction. From the $n=0 \rightarrow n=1$ spectrum, from about 10-11 GHz, I was able to predict interactions between the qubit and the TLS in the $n=0 \rightarrow n=2$ transition spectrum, about 20-21 GHz.

The state of the qubit was measured using escape rate tunneling and a pulsed readout technique. The pulsed technique involved sending a brief (2 ns) pulse of current that allowed the qubit to be operated over a wide frequency range. The amplitude of the current pulse was adjusted such that the population in $n=1$ would tunnel and $n=0$ would not. Analysis of this single-shot measurement revealed the fidelity was potentially as high as 94% in one of the devices I tested. This technique also allowed me to rigorously quantify population in $n=2$ and to calibrate the current pulses.

dc SQUID Phase Qubit

by

Tauno A. Palomaki

Dissertation submitted to the Faculty of the Graduate School of the
University of Maryland, College Park in partial fulfillment
of the requirements for the degree of
Doctor of Philosophy
2008

Advisory Committee:

Professor Frederick C. Wellstood, Advisor/Chair
Professor Richard L. Greene
Professor Christopher J. Lobb
Professor Johnpierre Paglione
Professor Colin Phillips

© Copyright by

Tauno Palomaki

2008

Acknowledgements

I owe a great deal of gratitude to many people. First of all, I would like to thank my advisor Prof. Wellstood. The term advisor doesn’t seem to capture everything he did for me during the past four years. I can’t recall a single instance of him being not available and willing to discuss my latest results or answer a question, no matter how trivial. I always left his office encouraged and motivated. He is an excellent teacher, researcher and physicist. Prof. Chris Lobb and Prof. Bob Anderson were also fundamental in the successes of my thesis work. The distinct styles and backgrounds of the three professors on the project mixed well. Prof. Lobb and Anderson are also excellent physicists, who never forgot their roles as teachers.

I would like to thank the members of my thesis committee, Profs. Johnpierre Paglione, Richard Greene and Colin Phillips. Other Professors at Maryland were also critical in my work, including Prof. Anlage, who was nice enough to lend me microwave equipment. I also thank Dr. Ben Palmer and Dr. Eite Tiesinga for helpful discussions.

I can’t understate how incredibly fortunate I was to have been taught by and collaborate with Sudeep Dutta. The precession and carefulness with which he worked was phenomenal and I inherited the results of his hard work. I would also like to thank him for listening to all my theories about physics and of course, Maryland basketball. I was fortunate to have a post-doc like Dr. Rupert Lewis. His knowledge of low-temperature techniques is extraordinary. He was also a great outlet for my frustrations and a good roommate on the road. I would like to thank Hanhee Paik for teaching me

what I know about fabrication and keeping the sub-basement fun. When I first joined the group, her and Sudeep were excellent role models. I would like to thank Tony Przybysz for taking the lead on fabricating the Al/AlO$_x$/Al devices I tested. Ben Cooper was a great asset in sorting out my latest question about physics and whatever else was on my mind. I am glad my experiment is being passed on to as passionate a student as Hyeokshin Kwon. Kaushik Mitra's quantum mechanical model of the dc SQUID phase qubit was frequently quoted in my work While I never worked beside Huizhong Xu, at times I feel like I did. His thesis was such a valuable resource to me. I owe a debt of gratitude to all the physicists who worked on the project before me, especially Huizhong Xu, Andrew Berkley, Phil Johnson, Fred Strauch, Prof. Alex Dragt, Prof. Roberto Ramos and Mark Guburd. Gus Vlahacos and John Matthews were great for exchanging ideas and thinking about SQUIDs from a different perspective.

Everyone associated with the Physics department here was wonderful. I can't recall a single instance where someone was not helpful or courteous. I apologize for anyone I may miss here: Doug Bensen, Brian Straughn, Belta Pollard, Brian Barnaby, Grace Sewlall, Cleopatra While, Linda O'Hara, Bob Woodworth, Al Godinez, George Bulter, Prof. Nick Chant and Jane Hessing come to mind.

I would like to thank everyone who made graduate school always bearable and at times even fun. Dan Lenski, Ingmar Broemstrup and Bobby Difabio were good friends who happened to also be physics graduate students at Maryland. Sean McWilliams, Nate Orloff, Laura Adams, Josh Higgins, Michael Barns, David Tobias, and everyone on the championship physics football team made life enjoyable as well.

Finally, I have to thank my family. My parents, Donald and Sonja have always been supportive and selfless. My grandparents have and will always be a huge source of inspiration in whatever I do in life. Having the original Dr. Palomaki so close these past few years has been wonderful as well. Thanking Ashley for everything she has done would be impossible. I dedicate my thesis to her.

Table of Contents

List of Tables

List of Figures

Chapter 1

Introduction

1.1 General Introduction to Quantum Computation

Quantum mechanics does a remarkably accurate job of explaining the bulk properties of large interacting quantum systems, such as superconductors. However, bulk properties do not directly reveal possible subtleties in quantum dynamics. Remarkably since about 1970, many techniques have been developed to isolate and study single quantum systems or interacting systems with only a few quantum degrees of freedom. Current examples range from quantum dots, where the spin of a single electron is controlled [1], to neutral atoms, where the internal atomic quantum state of a neutral atom is manipulated [2], to superconducting devices [3].

Besides allowing the exploration of fundamental questions in quantum mechanics, a system of individually controlled quantum objects allows the possibility of quantum computation and quantum information processing. The field of quantum computation began in 1982, when Richard Feynman pointed out that classical computers were inherently ill-suited to model quantum systems [4]. A computer based on quantum bits or qubits would avoid these inherent difficulties by using one quantum system to simulate another. In 1985, David Deutsch formalized these ideas [5], and in 1992 with R. Jozsa, showed that a quantum computer might in fact have computational powers greater than a classical one [6]. In 1994 and 1995, Peter Shor and Lou Grover demonstrated concrete examples of the potential power of a quantum computer, beyond its use for modeling quantum systems. Grover showed that conducting a search through an unstructured subspace could be sped up using a quantum computer [7]. Shor demonstrated that one could efficiently find the prime factors of an integer on a quantum computer [8]. Shor's algorithm in particular has generated enormous interest in quantum computing, in part because RSA encryption relies on the difficulty of factoring large numbers for its security.

The quantum mechanical phenomena of superposition and entanglement are ultimately what give a quantum computer more computational power than a classical computer, at least for certain types of computations. In a classical computer, information is stored as bits and neither entangled nor superposed states are permissible; a classical bit has two possible states or outcomes, 0 or 1. A quantum computer allows superposed states that are a mixture of 0 and 1 qubit states, for example $|\psi\rangle = \alpha|0\rangle + \beta|1\rangle$. Such a state has two measurement outcomes, 0 or 1, with probabilities $|\alpha|^2$ and $|\beta|^2$ respectively. Naively, one might think this enables an infinite storage of information, since the only requirements on α and β are that they are complex numbers such that $|\alpha|^2 + |\beta|^2 = 1$. However for a digital quantum computer α and β would be restricted to a finite set of values.

As a simple example of the distinction between bits and qubits, consider two classical bits $N = 2$; the four (2^N) allowed possible states of the system are 00, 01, 10, and 11. In contrast, two qubits may exist in these four states as well as several others. An example is the Bell state, $|\psi_2\rangle = (|00\rangle + |11\rangle)/\sqrt{2}$. Such a state does not exist in classical mechanics, and it cannot be written as the product of two individual qubit states, *i.e.* it is a type of correlated state between the two qubits. For example, if one measures the state of the first qubit to be 1, then measurements of the second qubit will always give 1. This peculiar behavior was taken a step further by John Bell in his development of Bell's Inequality [9]. Several different types of quantum systems, including photons and ions have been used to verify this inequality, highlighting one of the most counter-intuitive aspects of quantum mechanics [10-12].

A quantum computer algorithm, like a classical one, is composed of a series of gate operations. The simplest single-bit classical gate to consider is a NOT gate, which changes $1 \to 0$ and $0 \to 1$ in a chosen bit. In contrast, all single qubit gates act on the entire Bloch sphere (see Chapter 3). For example, the phase gate $S = |0\rangle\langle 0| + i|1\rangle\langle 1|$, changes the qubit state $|\psi\rangle = (|0\rangle + |1\rangle)/\sqrt{2}$ to $S|\psi\rangle = (|0\rangle + i|1\rangle)/\sqrt{2}$. As another example, the CNOT gate is a prototypical two-qubit gate, which flips the state of the target qubit based on the state of the control qubit. In a two-qubit system, the CNOT gate can be expressed as $CNOT = |00\rangle\langle 00| + |01\rangle\langle 01| + |11\rangle\langle 10| + |10\rangle\langle 11|$, where the first index is the control qubit and the second is the target. The Hadamard, $\pi/8$ gate, phase gate, and the CNOT gate together constitute a universal set of gates for quantum computation (*i.e.* any unitary operation can be approximated to arbitrary accuracy using only combinations of these gates).

I should note that a major consideration in designing a quantum algorithm is ensuring that it is more efficient than simply using a classical algorithm. Very few such algorithms have been theoretically realized thus far. I have also made no mention of error correction, which is crucial for any realistic quantum computer. For a further discussion of quantum gates and qubits in general, I refer the reader to *Quantum Computation and Quantum Information* by Nielsen and Chuang [13].

1.2 DiVincenzo Criteria

In the late 1990s, David DiVincenzo laid out five requirements that a system must satisfy to be suitable as a qubit [14]:

1) The Hilbert space must be precisely delineated, meaning the precise number of degrees of freedom must be known. It is very desirable for the Hilbert space to be decomposable in a direct product form; *i.e.* a set of individual qubits. This second statement is not mandatory, but the Hilbert space should grow exponentially with the number of qubits.
2) The quantum system can be put in a fiducial starting quantum state. Simply put, the qubits must be initialized before gate operations can occur.
3) The quantum system must be isolated from coupling to the environment to a high degree. The requirement can be summarized in the expression $\langle\psi_n|\rho|\psi_n\rangle \geq 1-\varepsilon$. Here ψ_n is the state of an n qubit system, ρ is the density matrix, which will be discussed in Chapter 3, and ε is an error rate. This equation is subject to work from both ends. The quantum algorithms understood as of 1996 required $\varepsilon = 10^{-6}$, within a few orders of magnitude [14]. The threshold is largely dependent on the algorithm and type of error. For example, in 2005, E. Knill [15] proposed that a tolerable erasure error rate for scalable quantum computing could be well above 0.1.
4) A controlled sequence of unitary transformations must be possible. The transformations must be able to act upon specified small collections of qubits. Since a quantum computer derives much of its power over a classical computer

through entanglement, the transformations must be able to create entangled states between the qubits, such as the Bell state mentioned above.

5) The system must be subject to a “strong” form of measurement that can project the final state of the system to the qubit basis. A strong measurement is one that irreversibly projects the waveform. A weak measurement may be sufficient for studying a quantum system, but will not satisfy the requirements for quantum computation.

1.3 Superconducting Qubits

Current work on quantum computing focuses on finding qubits that could satisfy these criteria and improving the performance of the qubit to better satisfy them; all requirements must eventually be satisfied to achieve an operating quantum computer. A surprisingly wide variety of possible qubits have been investigated experimentally and theoretically. A partial list of broad types of qubits includes trapped ions [16], neutral atoms [2], solid-state spin-based systems [1,17] and superconducting systems [18], with each of these choices representing many different actual types of qubits. Superconducting qubits fall naturally into three classes, flux qubits, charge qubits and phase qubits, although some devices are best thought of as overlapping two categories [3].

In virtually all superconducting qubits, a Josephson junction is combined with circuit elements to produce a system that acts like an effective two-level quantum system. While the two levels do not come from what is commonly thought of as a quantum two-level system, such as the spin of a single electron, with the proper choice of parameters, the device behaves like a two-level system. In this case, we can effectively restrict the

Hilbert space to the qubit subspace. This allows us to borrow much of the terminology from nuclear magnetic resonance [19] and other quantum systems and treat the system as a qubit.

An excellent introductory review of the three main types of superconducting qubits is available in Physics Today, by J. Q. You and Franco Nori [3] and the references therein. Some simple insight in to the three types of superconducting qubits comes directly from their names; the name of the qubit generally indicates the dominant degree of freedom in the circuit or the manner in which information is stored. For charge and phase qubits the ratio of E_J / E_c determines the dominant degree of freedom, where E_J is the Josephson coupling energy of the Josephson junction and E_c is the energy to charge the capacitance of the junction with one electron, found solely from electrostatic considerations. Very roughly, $E_J / E_c \leq 10$ for charge qubits, $10^2 \leq E_J / E_c \leq 10^3$ for flux qubits, and $E_J / E_c \geq 10^7$ for phase qubits. I will discuss these parameters in more detail in Chapter 2.

In general, Josephson junction based qubits are promising in that they are highly scalable with current processing techniques, and easy to control. Ironically, the features that make these qubits so advantageous towards satisfying some elements of the DiVincenzo criteria also serve as disadvantages towards realizing others. For example, superconducting qubits are easy to couple to and this makes it easy to perform a controlled sequence of unitary transformation and couple many qubits together. However, this also leads to stronger coupling to the environment, which in turn causes decoherence and difficulty with criterion three.

1.4 Summary of Thesis

The primary goal of my thesis was to understand and improve the performance of phase qubits so as to satisfy the DiVincenzo criteria. The experimental results can be approached from the perspective of one or more of the criteria. While the devices I tested were a particular type of phase qubit, a dc SQUID phase qubit, most of the results and methods would be applicable to other types of phase qubits.

In Chapter 2, I briefly review the basics of Josephson junctions, and superconducting quantum interference devices (SQUIDs). The Hamiltonians for these devices will be given and shown to be analogous to a quantum two-level system. I also then briefly discuss the coupling of two phase qubits. In Chapter 3, I discuss some basic physics of qubits, with an emphasis on results useful for measurements of phase qubits. Chapter 4 provides some details on the design and fabrication of my qubits, based on the results of Chapters 2 and 3. In Chapter 5, I describe the experimental apparatus, and techniques used to interact with a sample at milli-kelvin temperatures.

In Chapter 6, I show experimental results from four devices I tested. I first discuss how I determined the parameters for the devices using the analysis from Chapter 2. In Chapter 7, I demonstrate how to read out the qubit’s quantum state using the escape rate and then give a detailed discussion of a pulsed-current readout technique I developed. In Chapter 8, I show my measurements of a variety of microwave activation experiments. I used these experiments to map out the transition spectrum of the qubit, determine the coupling to the environment, and examine the feasibly of gate operations. As I will show in the final two chapters, the environment includes coupling to other quantum systems that appear to be located in the insulating layers of our devices. In Chapter 9, I focus on what these other quantum systems are and discuss two possible theories of how they may couple to the qubit. In Chapter 10, I show detailed spectroscopic measurements of the coupling between the microstates and a qubit. Finally, in Chapter 11, I summarize the main results and suggest future experiments.

Chapter 2

Josephson Junctions and SQUIDs

This chapter provides background information necessary to understand superconducting phase qubits. I begin with a basic introduction to Josephson junctions and a classical analysis of a junction using the RCSJ model. After viewing Josephson junctions from a classical perspective, I then discuss their quantum properties and how a junction can act as a phase qubit. I also examine some properties of dc SQUIDs and introduce the Hamiltonians of a single Josephson junction and a dc SQUID. Finally, I conclude with a brief introduction to two capacitively coupled phase qubits.

2.1 Josephson Junctions

When two superconducting electrodes are connected by a “weak link” a supercurrent can flow between the electrodes even with no voltage difference across the link. This weak link could be formed by introducing a very thin insulating layer between the superconducting electrodes to form a SIS junction, or by using a normal metal layer (SNS) or by forming a narrow constriction in the superconducting film (SCS). The zero voltage supercurrent is a result of the two superconductors coupling across the weak link. The strength of the coupling is determined by the characteristic length scale of the superconductor’s wavefunction in the weak-link. Brian Josephson first derived this effect in 1962 for the case of a thin-insulating barrier, [see Fig. 2.1(a)] [20]. His seminal paper correctly led to the prediction that the supercurrent through a weak link is given by

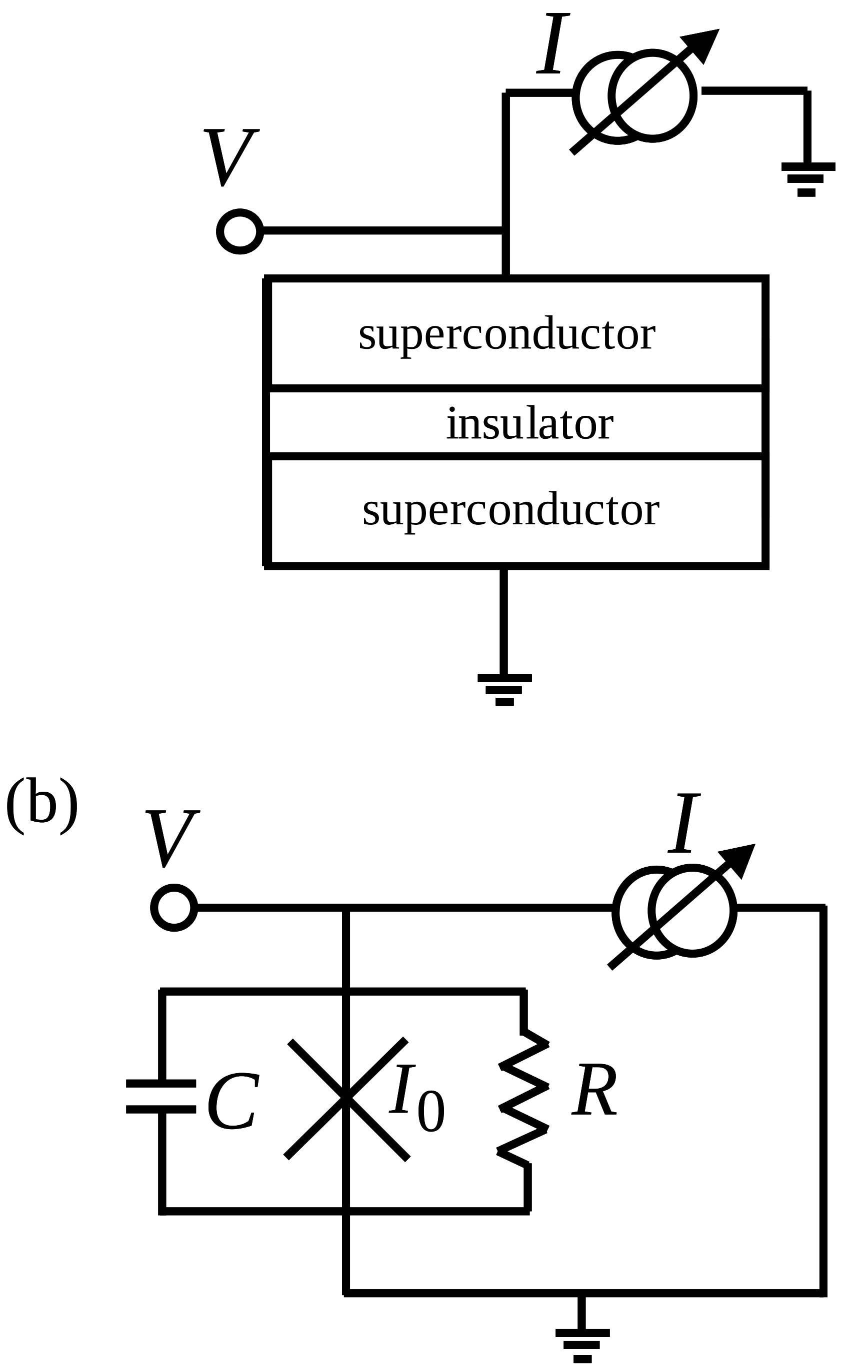

Figure 2.1: (a) Picture of a current biased (S-I-S) Josephson junction. (b) Circuit schematic of RCJS model of a current biased Josephson junction.

$$I = I_0 \sin(\gamma), \tag{2.1}$$

where γ is the gauge-invariant difference in the phase of the Ginzburg-Landau wavefunction Ψ in the two superconducting electrodes and I_0 is the maximum supercurrent possible through the junction. The Ginzburg-Landau wavefunction is a pseudowavefunction where $|\Psi|^2$ represents the local density of superconducting electrons [21]. Therefore γ results from a large number of Cooper pairs in the superconductors contributing coherently to produce a wavefunction Ψ with a well-defined phase. This is one reason why a Josephson junction can be thought of as a macroscopic quantum system. As one would expect, I_0 is determined by the coupling between the superconductors. Josephson also showed that the voltage across the junction is given by

$$V = \frac{\Phi_0}{2\pi}\frac{d\gamma}{dt}, \tag{2.2}$$

where $\Phi_0 = h/2e$ is the flux quantum. Equations (2.1) and (2.2) are known as the dc and ac Josephson relations, respectively.

Another useful relation can be derived from these equations, a non-linear Josephson inductance. The idea is that the junction acts as an effective tunable inductance, based on $V = L_J \frac{dI}{dt}$. From Eq. (2.1) and (2.2), one finds

$$L_J = \frac{\Phi_0}{2\pi I_0 \cos(\gamma)}. \tag{2.3}$$

This inductance is of course different in origin from a geometrical inductance; here the energy is stored in the flow of Cooper pairs.

The dynamics of a Josephson junction are readily understood through the RCSJ model [21-23]. The model treats a real junction as being an ideal Josephson junction that is capacitively and resistively shunted, as shown in Fig. 2.1(b). The capacitance C usually results from the geometric shunting capacitance between the two superconducting electrodes, although it can also account for additional shunting capacitors that have been deliberately added. The shunting resistance turns out to be a more subtle concept, and includes any source of dissipation across the junction, including quasiparticle tunneling, dielectric loss, radiation and any normal shorts. The junctions I used in this thesis have a very large resistance [24] for applied voltages V that are less than the gap voltage $V_g = 2\Delta / e$. For voltages greater than V_g, the resistance of my junctions was roughly $R_n \approx 100\,\Omega$ to $1k\Omega$, the tunneling resistance of the junction in the normal state.

If the Josephson junction is attached to a current bias source I, conservation of current gives

$$I = I_0 \sin\gamma + \frac{V}{R} + C\frac{dV}{dt}. \tag{2.4}$$

Using the Josephson equations this can be rewritten as

$$m\frac{d^2\gamma}{dt^2} = -\frac{dU(\gamma)}{d\gamma} - D\frac{d\gamma}{dt}, \tag{2.5}$$

where $m = C\left(\frac{\Phi_0}{2\pi}\right)^2$, $U = -\frac{\Phi_0}{2\pi}\left(I_0\cos(\gamma) + I\gamma\right)$ and $D = \left(\frac{\Phi_0}{2\pi}\right)^2\frac{1}{R}$. This is the equation of a particle of mass m, in a potential U, with drag force D acting on it. The potential U is commonly referred to as a tilted washboard. I would like to emphasis that there is no actual particle here; the dynamics of a junction are simply analogous to those of a particle moving in a tilted washboard potential.

Figure 2.2(a) shows the potential well with $I_0 = 1.6\,\mu A$ for various currents I, and Fig. 2.2(b) shows a measured current/voltage characteristic. As the bias current I increases, the potential becomes more and more tilted until the potential barrier disappears at current I_0. Once the bias exceeds the critical current, the phase begins to evolve continuously and a voltage develops across the junction. In general, the particle can escape for $I < I_c$ due to quantum mechanical tunneling or thermal activation over the potential well [25]. The voltage across the junction increases very rapidly until it reaches the gap voltage of the superconductor, $V_g = 2\Delta / e$, roughly 360 μV for aluminum and 2.8 mV for niobium. This gap voltage is consistent with the minimum energy 2Δ required to break a Cooper pair. This is not the RCSJ model, which has no gap.

When the bias current is increased above the critical current, the voltage across the junction is given by approximately $V = IR_n$. If the current through the junction is then decreased below the critical current the particle will not retrap in the supercurrent state until it reaches re-trapping current I_r. The fact that the device is highly hysteric (*i.e.* $I_r << I_c$) can be understood from a very small damping acting on the inertia of the moving particle; only when the energy dissipated due to the damping, using the sub-gap resistance, exceeds the potential energy gain from the preceding potential well, will the particle slow down and the system return to the zero-voltage state. The slight back bending in Fig. 2.2(b) near $V = 2\Delta / e$ is indicative of heating.

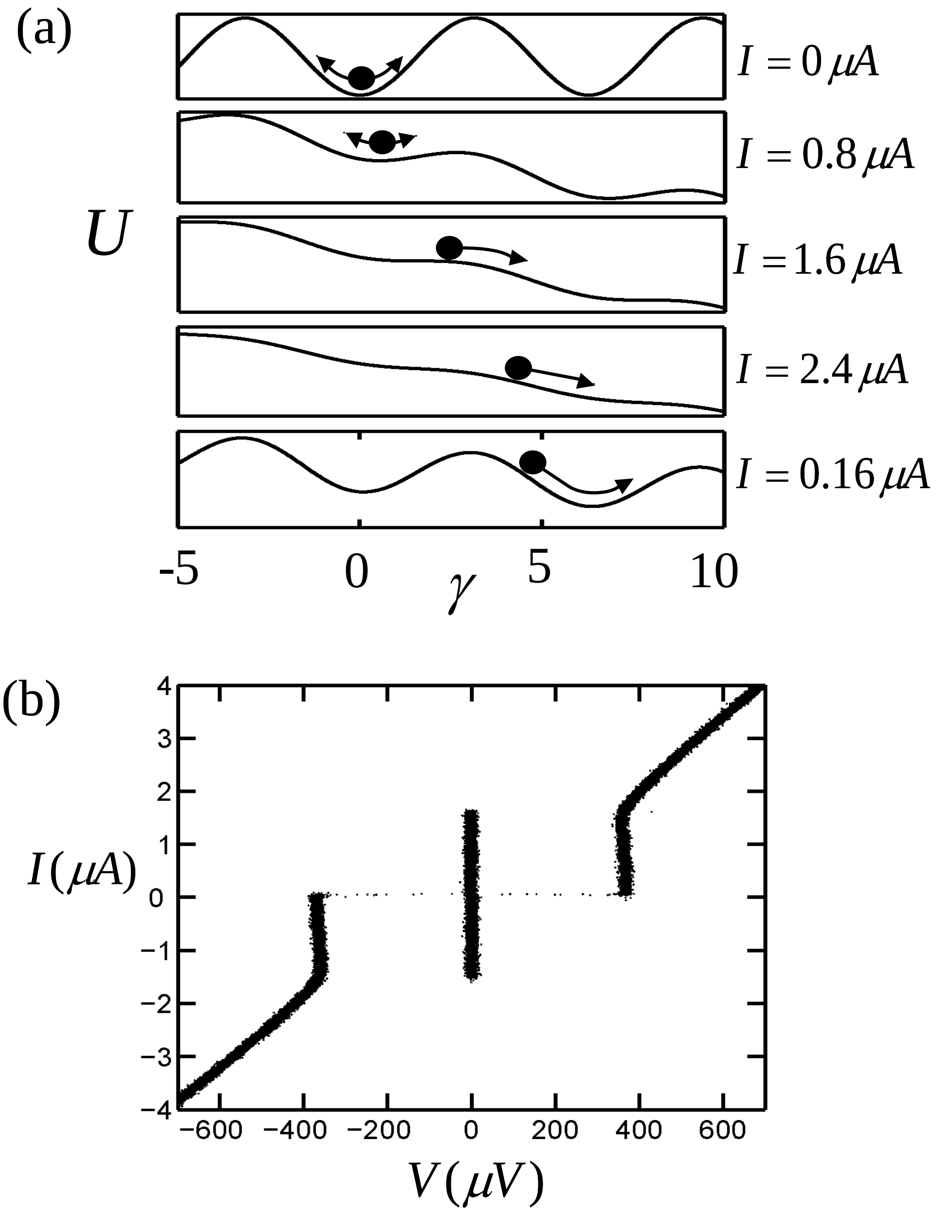

Figure 2.2: (a) Tilted washboard potential at five bias currents I in the RCSJ model for a junction with a critical current of $I_0 = 1.6\,\mu A$. With $I = 0.16\,\mu A$ the phase particle has still not retrapped into the zero voltage state after switching. (b) I-V curve for an Al/AlO$_x$/Al junction (data from a dc SQUID that was never tested further since the critical currents were not as designed) with a critical current of 1.6 μA. The small back bending as the current is decreased below the critical current suggests some heating.

2.2 RCSJ Hamiltonian

The Hamiltonian of a Josephson junction in the RCSJ model can be written in several identical forms. Ignoring damping, I can write

$$\begin{aligned} H &= \frac{p_\gamma{}^2}{2m} + U \\ &= \frac{p_\gamma{}^2}{2m} - \frac{\Phi_0}{2\pi}\left(I_0\cos(\gamma) + I\gamma\right) \\ &= \frac{4E_c}{\hbar^2}p_\gamma{}^2 - E_J\left(\cos(\gamma) + I\gamma / I_0\right) \\ &= 4E_c N^2 - E_J\left(\cos(\gamma) + I\gamma / I_0\right) \end{aligned} \quad , \qquad (2.6)$$

where $p_\gamma = m\dfrac{d\gamma}{dt} = \dfrac{\hbar}{2e}CV = \hbar N$, $E_c = e^2 / 2C$, and $E_J = \Phi_0 I_0 / 2\pi$ [26]. The canonical momentum of the junction p_γ is proportional to the voltage across the junction and the number of cooper pairs N that have been transferred to the junction's capacitor plates. The electrostatic energy necessary to add an additional Cooper pair to the capacitor is given by the charging energy E_c, which appears in an effective kinetic energy term in the Hamiltonian. The maximum potential energy that can be stored in the junction is twice the Josephson energy E_J.

The Hamiltonian in Eq. (2.6) can be expanded about the potential minimum $\gamma_0 = \arcsin\left(I / I_0\right)$ to give

$$H = \frac{p_\gamma{}^2}{2m} - \frac{\Phi_0}{2\pi}\left(\sqrt{I_0{}^2 - I^2} - \frac{1}{2}\sqrt{I_0{}^2 - I^2}\,\gamma'^2 + \frac{1}{6}I\gamma'^3\right), \qquad (2.7)$$

where $\cos(\gamma)$ has been expanded to third order in γ' and $\gamma' = \gamma - \gamma_0$ [27]. It will be useful to separate the bias current I into a dc component, which will be referred to as

$\langle I \rangle$, a microwave component $I_{\mu w}$, which is close to the resonant frequency of the junction, and a mixed frequency noise component I_n. The noise component will include noise close to the resonant frequency of the junction $I_{n\mu w}$ and lower frequency noise I_{nlf}. Adding the microwave component will not affect the minimum γ_0 and will simply add a term $\Delta H_{\mu w} = -I_{\mu w} \frac{\Phi_0}{2\pi} \gamma$ to the Hamiltonian. The low frequency noise component I_{nlf} will vary the minimum location γ_0 and this effect will be considered when noise and decoherence are discussed. The microwave noise component $I_{n\mu w}$ will also add a term to the Hamiltonian $\Delta H_n = -I_{n\mu w} \frac{\Phi_0}{2\pi} \gamma$.

The resonant frequency of small oscillations in the potential $U(I)$ is called the plasma frequency and it can be written as

$$\omega_p = \sqrt{\frac{2\pi I_0}{\Phi_0 C}} \left(1 - \left(\frac{I}{I_0} \right)^2 \right)^{1/4} . \tag{2.8}$$

The potential barrier height is given by [28]

$$\Delta U \approx 2E_J \left(1 - I / I_0\right)^{3/2} . \tag{2.9}$$

From these equations a first order temperature-dependent escape rate can be determined by simply assuming the particle tries to escape at a rate ω_p and succeeds if thermal excitations given by the Boltzmann distribution are greater than ΔU [29]. In my experiments, the temperature T is always such that $k_B T << \Delta U$ and I will in general ignore thermal escape.

2.3 Quantum Properties of Josephson Junctions

The above description of a junction as a particle moving in a tilted washboard potential is entirely classical. At low enough temperatures, quantum effects become important, including the uncertainty principle, discrete energy levels, and quantum mechanical tunneling [26, 30, 31].

As I discuss below a junction has many similarities to a simple harmonic oscillator. In a simple harmonic oscillator, the position and momentum operators x and p obey $[x, p] = i\hbar$ and the ground state has a minimum uncertainty product form, given by $\left\langle(\Delta x)^2\right\rangle\left\langle(\Delta p)^2\right\rangle = \hbar^2/4$ [32]. Similarity, in a Josephson junction the number of Cooper pairs N on one plate of the junction capacitor and the phase difference γ obey the commutation relation $[N, \gamma] = i$. This implies that N and γ also obey the uncertainty relations $\left\langle(\Delta N)^2\right\rangle\left\langle(\Delta \gamma)^2\right\rangle \geq 1/4$. One might guess that $\left\langle(\Delta N)^2\right\rangle$ and $\left\langle(\Delta \gamma)^2\right\rangle$ are of the same order, however this is not generally true. Phase qubits have a very large ratio of E_J / E_c, typically of the order 10^6. This causes $\left\langle(\Delta N)^2\right\rangle >> \left\langle(\Delta \gamma)^2\right\rangle$ and therefore $(\Delta\gamma)^2 << 1$ and thus γ is a good quantum number. A Josephson junction in this regime has a well-defined phase difference, but a relatively imprecise number of pairs participating in the tunneling. It may be relatively precise though, *i.e.* $\left\langle\Delta N\right\rangle / N << 1$.

2.3.1 Harmonic Oscillator

Solving Schrödinger's equation with the potential U produces a series of quantized energy levels in each potential well as shown in Fig. 2.3. Ignoring terms of

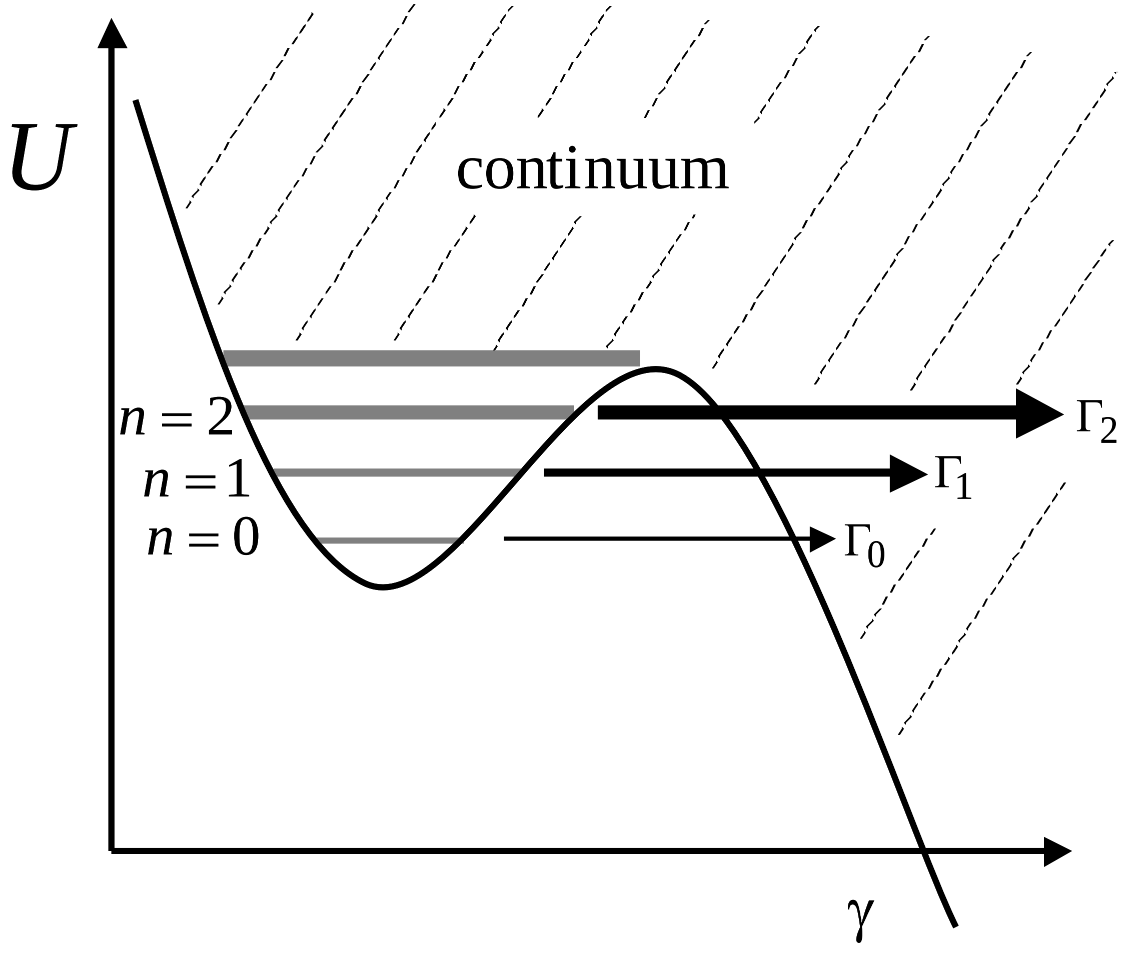

Figure 2.3: Tilted washboard potential in the RCSJ model showing three metastable energy levels, $n=0$, $n=1$ and $n=2$ as well as a continuum of states above the barrier. Higher energy levels have enhanced escape rates Γ_n. The lowest two energy levels $|0\rangle$ and $|1\rangle$ form the qubit basis states.

order γ'^3 and higher in Eq. (2.7) gives the harmonic oscillator approximation to a junction; the truncated Hamiltonian is analogous to the Hamiltonian of a harmonic oscillator $H = \frac{p^2}{2m} + \frac{1}{2} m\omega_p^2 x^2$, implying quantized energy levels $|n\rangle$ separated in energy by $\hbar\omega_p$. The junction operators γ and p_γ are analogous to typical harmonic oscillator operators x and p. From the elementary properties of quantum harmonic oscillators, we thus have that:

$$\langle n|\gamma|n-1\rangle = (\hbar / 2m\omega_p)^{1/2}\sqrt{n}\,, \tag{2.10a}$$

$$\langle n|\gamma|n\rangle = 0\text{, and} \tag{2.10b}$$

$$\langle n|\gamma|n-2\rangle = 0\,. \tag{2.10c}$$

The ground state $|0\rangle$ of the system or $n = 0$ and the first excited state $|1\rangle$ or $n = 1$ will be used as the qubit states [33]. The number of energy levels in the potential well is approximately

$$N_s = \Delta U / \hbar\omega_p \tag{2.11}$$

and is dependent on the bias current through the junction, based on Eqs. (2.8) and (2.9). Figure 2.4(a) shows N_s versus I / I_0 for a Josephson junction with $I_0 = 1.3\,\mu A$ and $C = 0.4\,pF$. Levels with $n \geq 2$ will generally exist in the well and will need to be considered to understand the junction's behavior. There are also resonances above the barrier that form a continuum, which I will ignore.

Just considering the first two levels and ignoring I_{nlf}, the Hamiltonian can be

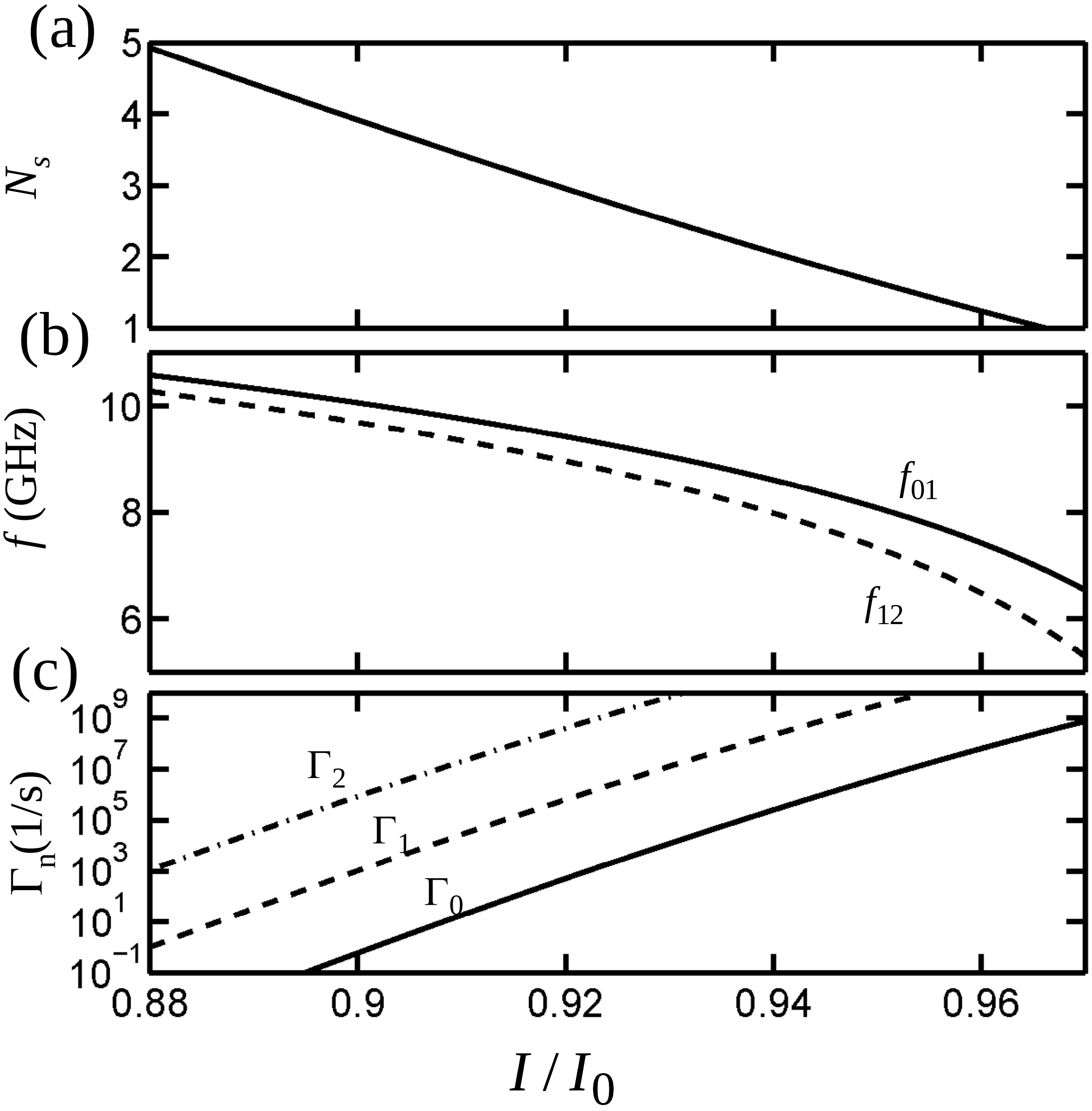

Figure 2.4: Cubic approximation results for a junction with $I_0 = 1.3\,\mu A$ and $C = 0.4\,pF$. (a) Approximate number of levels N_s of the titled washboard potential where $N_s = \Delta U / \hbar\omega_p$. (b) Solid curve is transition frequency f_{01} between $n = 0$ and $n = 1$, dashed line is transition frequency f_{12}. The anharmonicity increases at higher bias currents. (c) Escape rate Γ_n for the metastable energy levels n versus bias current.

written as:

$$H=\begin{bmatrix} E_0+\langle 0|\gamma|0\rangle\frac{\Phi_0}{2\pi}(I_{n\mu w}+I_{\mu w}) & \langle 0|\gamma|1\rangle\frac{\Phi_0}{2\pi}\left(I_{n\mu w}+I_{\mu w}\right) \\ \langle 1|\gamma|0\rangle\frac{\Phi_0}{2\pi}\left(I_{n\mu w}+I_{\mu w}\right) & E_1+\langle 1|\gamma|1\rangle\frac{\Phi_0}{2\pi}\left(I_{n\mu w}+I_{\mu w}\right) \end{bmatrix}. \tag{2.12}$$

In the harmonic oscillator approximation the energy level difference is given by $E_1 - E_0 = \hbar\omega_p = \hbar\omega_{01}$. The matrix elements can be determined from the harmonic oscillator relations given above [see Eqs. (2.10)]. The off-diagonal elements containing $I_{\mu w}$ cause coherent transitions between the energy levels of the qubit (Rabi oscillations) and those containing $I_{n\mu w}$ cause excitation and relaxation between the levels due to current noise. The details of these processes are discussed in Chapter 3, where the effects due to low frequency noise I_{nlf} on the energy level spacing will be included as well.

The qubit states $|0\rangle$ and $|1\rangle$ in the phase qubit are metastable. In particular these states can decay by tunneling through the potential barrier into the finite voltage state [30]. Higher energy levels n will have substantially higher tunneling rate Γ_n based on the smaller barrier heights and widths, as shown in Fig. 2.3. This difference in tunneling rates has been exploited to determine the energy state of the system [34]. I will usually ignore tunneling rates, except in the discussions of state readout, as they are generally much smaller than the other characteristic rates for the bias conditions I used in most of my research.

2.3.2 Cubic Approximation

To obtain more accurate results beyond the harmonic approximation, the γ'^3 term in Eq. (2.7) must be included. Here I will just quote useful results that have been derived elsewhere. Expanding the potential about the minimum phase γ_0 gives

$$U \cong \frac{27}{4}\Delta U\left(\frac{\gamma'}{q_0}\right)^2\left(1-\frac{\gamma'}{q_0}\right)+U_0\,, \tag{2.13}$$

where $\gamma' = \gamma - \gamma_0$ and $q_0 = \frac{1}{2\omega_p}\sqrt{\frac{54\Delta U}{m}}$ [35]. Here the anharmonic energy level spacings are [26]

$$\omega_{01} \cong \omega_p(1-\frac{5}{36N_s}) \text{ and} \tag{2.14}$$

$$\omega_{12} \cong \omega_p(1-\frac{5}{18N_s})\,. \tag{2.15}$$

Using the cubic approximation other matrix elements can be more accurately described, for example,

$$\langle 0|\gamma|1\rangle = \frac{1}{\sqrt{2}}\left(1+\frac{11}{216N_S}\right) \text{ and } \frac{\langle n|\gamma|n-2\rangle}{\langle n|\gamma|n-1\rangle} \approx \frac{1}{\sqrt{54N_s}}\,. \tag{2.16}$$

The escape rates without damping can be approximated as well using the WKB method. Strauch found the tunneling rates out of the energy levels in the cubic approximation to be [26]

$$\Gamma_n = \frac{\sqrt{2\pi}\left[432N_s\right]^{n+1/2}}{n!}\frac{\omega_p}{2\pi}\exp(-7.2N_s)\,. \tag{2.17}$$

Figure 2.4(b) and (c) shows the energy level spacing and escape rates using the cubic approximation with $I_0 = 1.3\,\mu A$ and $C = 0.4\,pF$.

The cubic approximation provides a substantial improvement over the harmonic approximation in describing the dynamics. However for comparison with experiments, it is best to use numerical simulations of Schrödinger’s equation for the full Hamiltonian with appropriate boundary conditions. The complete code I used makes use of complex scaling, where eigenstates are superpositions of harmonic oscillator states [36-37]. A trial energy and wavefunction is numerically relaxed to a solution using inverse iteration (see Appendix A).

2.4 dc SQUID Phase Qubit

The simplest phase qubit is just a Josephson junction attached to a current bias source, as I described above [33]. Unfortunately, in this configuration the junction is strongly coupled to the bias leads. If the junction is prepared in an excited eigenstate it will quickly dissipate energy by emitting photons to the leads, and the system will return to its ground state. By isolating the qubit from the leads this interaction can be minimized. One isolation scheme involves attaching an LC filter between the leads and the junction. When properly configured, current noise at microwave frequencies will be shunted through the capacitor and blocked by the inductor and not reach the qubit junction. The LC filter’s drawback is that it does not block low-frequency noise, which produces decoherence in the phase qubit [38]. This isolation scheme can be improved by replacing the capacitor with another junction and a small inductor [39]. Somewhat inadvertently this produces a highly asymmetric dc superconducting quantum interference device or dc SQUID. This was the isolation scheme I used in my experiments. In this section, I briefly discuss the properties of such SQUIDS.

Figure 2.5(a) shows a schematic of an inductively isolated Josephson junction qubit or “dc SQUID phase qubit”. The qubit junction $J1$ is placed in series with a relatively large inductor L_1, and this combination is placed in parallel with a small inductor L_2 and an isolation junction $J2$. The wavefunction of the Cooper pairs must be single-valued in the SQUID loop and thus leads to the general flux-phase relationship, which I can write [21,40],

$$\gamma_1 - \gamma_2 = 2\pi\Phi / \Phi_0 = 2\pi\Phi_a / \Phi_0 + 2\pi I_1 L_1 / \Phi_0 - 2\pi I_2 L_2 / \Phi_0 , \quad (2.18)$$

where Φ_a is the flux applied to the loop, I_1 is the current through the arm of the SQUID with junction $J1$, and I_2 is the current through the arm of the SQUID with junction $J2$. I can also write

$$I_1 + I_2 = I , \quad (2.19)$$

where $I_1 = C_{J1} \frac{d}{dt}\left(\frac{\Phi_0}{2\pi} \frac{d\gamma_1}{dt} \right) + I_{01} \sin(\gamma_1)$, $I_2 = C_{J2} \frac{d}{dt}\left(\frac{\Phi_0}{2\pi} \frac{d\gamma_2}{dt} \right) + I_{02} \sin(\gamma_2)$ [see Eq. (2.4)] and I_{01} and I_{02} are the critical currents of the two junctions. I will use the variable I for the bias current in the dc SQUID [see Fig. 2.5(a)] as well as the current applied to a single Josephson junction [see Fig. 2.1(a)]

Using the flux-phase relationship Eq. (2.18), the Hamiltonian for the dc SQUID can be written as,

$$H = \frac{p_1^2}{2m_1} + \frac{p_2^2}{2m_2} + U(\gamma_1, \gamma_2, I, \Phi_a) , \quad (2.20)$$

where

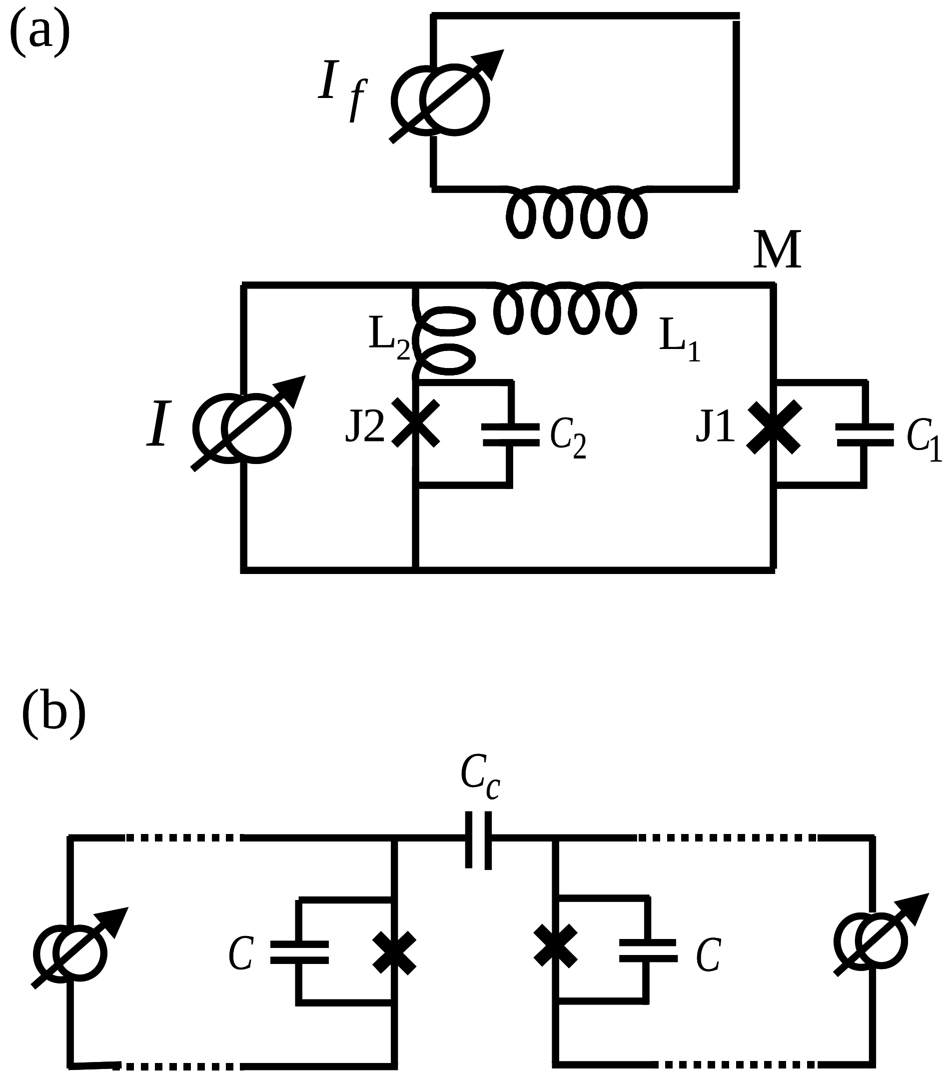

Figure 2.5: Schematics for (a) single dc SQUID phase qubit and (b) capacitively coupled phase qubits. (a) The qubit junction J1 is isolated from the bias line by a large inductance L_1 and a shunting branch with a junction J2 and small inductance L_2. Flux bias current I_f is coupled to the SQUID via a mutual inductance M. Two phase qubits are coupling via a coupling capacitor C_c. The dimensionless coupling constant is $\xi = C_c/(C_c + C)$, where the junction capacitances C are considered to be identical.

$$U(\gamma_1,\gamma_2,I,\Phi_a) = -E_{J1}\cos(\gamma_1) - E_{J2}\cos(\gamma_2)$$
$$-\left(\frac{\Phi_0 I}{2L\pi}\right)\left(L_2\gamma_1 + L_1\gamma_2\right) + \left(\frac{\Phi_0}{2\pi}\right)^2 \frac{1}{2L}\left(\gamma_1 - \gamma_2 - \frac{2\pi\Phi_a}{\Phi_0}\right)^2 . \qquad (2.21)$$

Here $p_1 = C_1\left(\Phi_0/2\pi\right)^2\dot{\gamma}_1 \equiv m_1\dot{\gamma}_1$ and $p_2 = C_2\left(\Phi_0/2\pi\right)^2\dot{\gamma}_2 \equiv m_2\dot{\gamma}_2$ are the canonical momenta, $L = L_1 + L_2$ is the total loop inductance, C_1 and C_2 are the capacitances of the qubit and isolation junctions respectively, $E_{J1} = I_{01}\Phi_0 / 2\pi$ and $E_{J2} = I_{02}\Phi_0 / 2\pi$ are the Josephson coupling energies of the two junctions. The classical behavior of the system is analogous to a particle moving in the 2-D corrugated potential [40] and the qubit states are formed by the lowest two energy levels in a 2-D potential well of Eq. (2.21).

Figure 2.6(a) shows the dc SQUID potential for a symmetric device (*i.e.* $I_{01} = I_{02}$ and $L_1 = L_2$) with $I = 0$ and $\Phi_a = 0$. Figure 2.6(b) shows the calculated potential for a SQUID with parameters chosen to be the same as a device I tested (DS_{2A}). Here I have assumed no applied bias current or applied flux and introduced the energy scale $U_0 = (I_{01} + I_{02})\Phi_0 / 2\pi$. Applying flux to the SQUID tends to “roll” the potential in the $\left(\gamma_1 - \gamma_2\right)$ direction while bias current tilts the potential in the $\left(\gamma_1 + \gamma_2\right)$ direction. By choosing $L\left(I_{01} + I_{02}\right) >> \Phi_0$ and applying flux and bias current the device can be operated such that the potential acts like a 1-D tilted washboard in the γ_2 direction, *i.e.* just like an ideal phase qubit [41,42].

Each potential minimum corresponds to the system being in a specific flux state due to trapped circulating current in the loop. The number of distinct flux states can be determined by taking the 2-D geometry of the potential energy surface into account; a

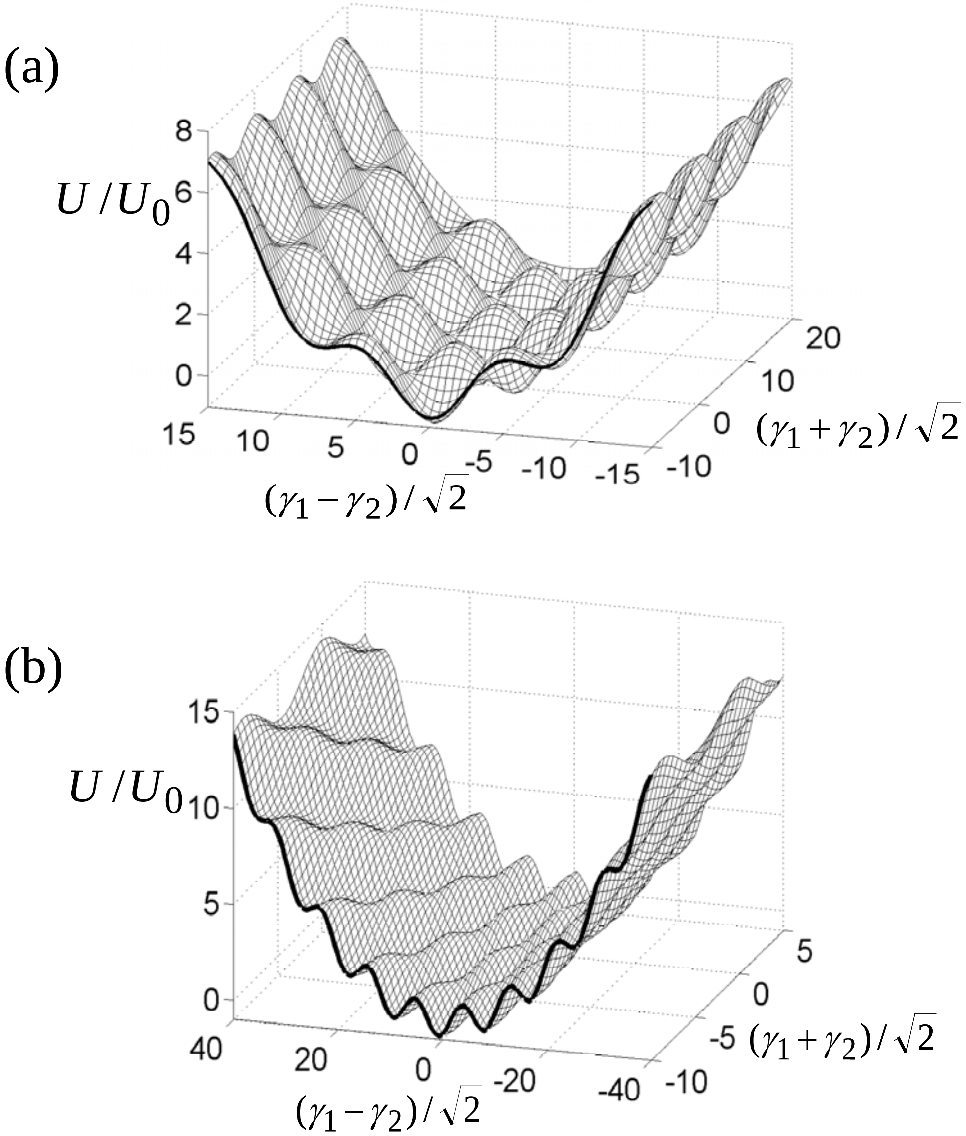

Figure 2.6: Normalized potential energy surface $U(\gamma_1,\gamma_2)/U_0$ for (a) symmetric dc SQUID with current $I=0$, $\Phi_a=0$, $\beta=L(I_{01}+I_{02})/\Phi_0=5.3$, and $I_{01}=I_{02}$ (b) SQUID with $I=0$, $\Phi_a=0$, $\beta=20$, $I_{01}=34\,\mu A$ and $I_{02}=5\,\mu A$. Different potential wells (in $\gamma_1-\gamma_2$ direction) correspond to distinct flux states exist, as well as the indistinguishable repeated wells (in $\gamma_1+\gamma_2$ direction).

slice through $U(\gamma_1, \gamma_2)$ at $\gamma_2 = 0$ will identify each distinct flux state [37]. If the junctions are weakly coupled (*i.e.* $L\left(I_{01} + I_{02}\right) >> \Phi_0$) they will act independently and the maximum current circulating in the loop will be limited by the smaller of the two junction critical currents $I_{0\min}$. In this case, the number of metastable flux states is [41]

$$N_\Phi \cong 1 + 2LI_{0\min} / \Phi_o \approx 1 + \beta(1+\alpha) \tag{2.22}$$

with $\alpha \equiv \left|(I_{02} - I_{01})/(I_{02} + I_{01})\right|$ [43] and $\beta \equiv L(I_{01} + I_{02})/\Phi_0$. The first term in Eq. (2.22) accounts for a state with no trapped flux, and the factor of two accounts for states corresponding to positive and negative circulating current. Thus devices with $\beta >> 1$ will tend to have $N_\Phi >> 1$, provided α is not close to -1.

If flux and bias current are applied such that the potential well ΔU disappears where the phase particle is located, the particle will escape from the well and a voltage will appear across the junction that switches. If the potential is such that both junctions' phase continues to evolve in time, a roughly constant voltage will be measured across the SQUID. If only a small bias current is applied, the SQUID only switches from one flux state to another and no steady voltage will be detected. By ramping the flux and bias current and measuring when the SQUID switches to the voltage state, or switches flux states, the critical currents of the system can be effectively mapped out and used to determine the parameters of the dc SQUID. Experimental results and fits will be shown in Chapter 6 for the SQUIDs I studied.

2.5 Two Capacitively Coupled dc SQUIDs

Two identical dc SQUID phase qubits can be coupled together as shown in Fig. 2.5(b); here the qubits are connected using a capacitor C_c. In this coupled system, the current and flux biases are ramped such that the dc SQUIDs can be thought of as two single Josephson junction phase qubits. Johnson *et al.* found the Hamiltonian for two capacitively coupled phase qubits is [44,45]

$$\begin{aligned} H &= \frac{p_1^2}{2m} - \frac{\Phi_0}{2\pi}\left(I_{01}\cos(\gamma_1) + I_1\gamma_1\right) \\ &+ \frac{p_2^2}{2m} - \frac{\Phi_0}{2\pi}\left(I_{02}\cos(\gamma_2) + I_2\gamma_2\right) + \frac{\xi}{m} p_1 p_2 \end{aligned} , \tag{2.23}$$

where $m = C(1+\xi)(\Phi_0 / 2\pi)^2$. Here, the dimensionless coupling constant is

$$\xi \equiv C_c /(C_c + C), \tag{2.24}$$

$p_1 = (C_c + C)\left(\frac{\Phi_0}{2\pi}\right)^2 (\frac{d\gamma_1}{dt} - \xi \frac{d\gamma_2}{dt})$ and $p_2 = (C_c + C)\left(\frac{\Phi_0}{2\pi}\right)^2 (\frac{d\gamma_2}{dt} - \xi \frac{d\gamma_1}{dt})$.

The dimensionless coupling constant ξ determines the splitting size of the avoided level crossing. In real devices, careful consideration must also be given as to whether an LC mode, with a frequency near the qubit's, is produced by the coupling capacitor and the associated wiring between the qubits [46]. The first coupled device successfully tested in our lab showed resonances consistent with the LC mode forming another coherent quantum system. It is an interesting three-body system, but for my work I shortened the lead length and reduced the capacitance to ensure that the resonance of the coupling network was well above the qubit frequency.

2.6 Summary

In this chapter, I discussed the basic physics of Josephson junctions. In particular, the RCSJ model was used to develop a classical and quantum description of phase qubits. I briefly showed how the quantum nature could be exploited to form a qubit, with the lowest two energy levels forming the basis of the qubit. I described the simple harmonic oscillator approximation for the qubit and then a more exact cubic approximation. To isolate the junction from the environment, a second Josephson junction and an inductor were attached, forming a dc SQUID phase qubit. The basic properties of dc SQUIDs relevant for my experiments were considered and the method for coupling two qubits together was shown.

Chapter 3

Dynamics of a Phase Qubit

In this chapter I discuss the dynamics of two-level systems, with an emphasis on how this applies to superconducting phase qubits. Much of the discussion applies to any two-level system and most of the terminology and techniques were originally developed for nuclear magnetic resonance [19, 47]. Starting from the Hamiltonian of a Josephson junction, I develop a two-level system model of the phase qubit. I then show how the environment affects the dynamics of the qubit and describe experimental techniques to examine this interaction. Finally, I present the density matrix formulism and show how it can be used to simulate the effect of the environment on the qubit.

3.1 The Bloch Sphere and Ensembles

A pure state of a single isolated two-level system with eigenstates $|0\rangle$ and $|1\rangle$ can be expressed as

$$|\Psi\rangle = \alpha|0\rangle + \beta|1\rangle = \cos\frac{\theta}{2}|0\rangle + e^{i\phi}\sin\frac{\theta}{2}|1\rangle \ . \qquad (3.1)$$

A measurement of the energy of the system will project the system to $|0\rangle$ or $|1\rangle$ with probabilities of $|\alpha|^2$ and $|\beta|^2$, respectively. The complex numbers α and β are constrained by the condition

$$\sqrt{|\alpha|^2 + |\beta|^2} = 1 \ . \qquad (3.2)$$

These relations lead nicely to a representation of the state of the system as a point on the surface of the unit sphere. The coefficients θ and ϕ become angles in a spherical coordinate system, with $0 \le \theta \le \pi$ and $0 \le \phi \le 2\pi$. This representation is known as the Bloch sphere. For a pure state the eigenstate can be described by a location on the sphere with radius 1, as shown in Fig. 3.1. For example, the eigenstate $|\Psi\rangle = (|0\rangle + i|1\rangle)/\sqrt{2}$ has $\theta = \pi/2$ and $\phi = \pi/2$ and is represented by a vector pointing from the origin to (0,1,0) on the y-axis. Similarly $|\Psi\rangle = (|0\rangle + |1\rangle)/\sqrt{2}$ has $\theta = \pi/2$ and $\phi = 0$ and is the vector (1,0,0) on the x-axis.

For a pure state, the Bloch sphere provides a convenient graphical representation. It is particularly useful for understanding the dynamics of a two-level system, especially in the rotating wave approximation, as I discuss in the next section. For example, rotations about the z-axis change the phase of the system ϕ. Similarly, a rotation of the state from $|0\rangle$ to $|1\rangle$ can be produced by a torque about the x-axis or y-axis. The driving force needed to produce the rotations will be described in the next section.

The Bloch sphere is also useful for visualizing dissipation and decoherence. Equation 3.1 describes the pure state of a system, but I will also need to consider mixed states, or statistical ensembles of pure states. Here the ensemble accounts for many repeated experimental trials and is assumed to be ergodic [48]. The quantum dynamics of mixed states are most easily understood using the density matrix, which I discuss in section 3.5.

In the ensemble picture, uncertainty or fluctuations in the coefficients ϕ and θ from randomly fluctuating drive terms will smear out the state on the Bloch sphere. For

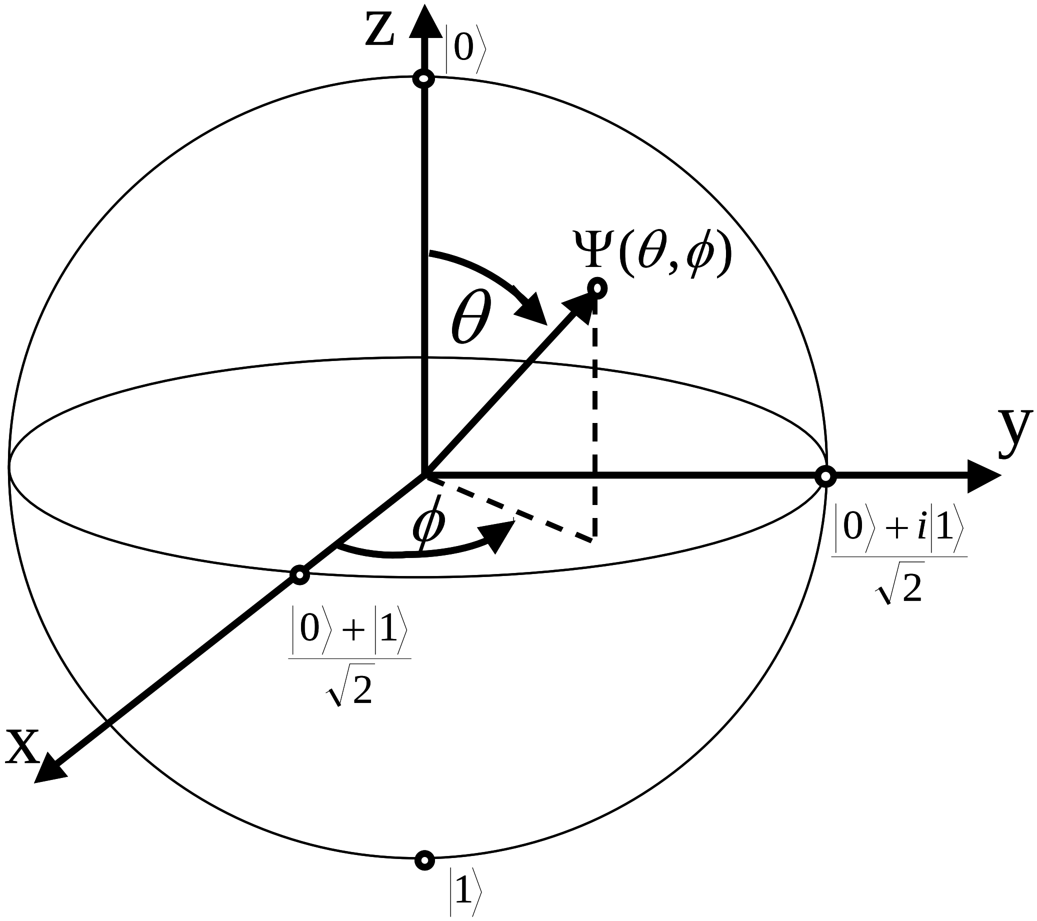

Figure 3.1: Bloch sphere representation of the pure state of a two-level system. A vector of length 1 describes the quantum state $\Psi(\theta,\phi)$. Open circles have been added at locations corresponding to various quantum states. For example, a unit length vector pointing down the x-axis corresponds to the pure state $\Psi = (|0\rangle + |1\rangle)/\sqrt{2}$.

example, if the system is initialized at $\phi = 0$ and $\theta = \pi / 2$, a randomly fluctuating torque around the z-axis will cause $\left\langle \phi^2(t) \right\rangle$ to increase with time until all knowledge of the phase is lost. In a graphical sense the Bloch vector has spread out over the equator of the sphere. This effect is called dephasing, and is distinct from dissipation, which causes changes in the angle θ, as I will discuss below.

3.2 Rotating Frame

Consider a qubit with states $\left|0\right\rangle$ and $\left|1\right\rangle$, with energies E_0 and E_1, respectively. If the qubit is placed into the initial state $\left|\Psi(t=0)\right\rangle = \left(\left|0\right\rangle + \left|1\right\rangle\right)/\sqrt{2}$ at $t = 0$, then at later time t it will have evolved to $\left|\Psi(t)\right\rangle = \left(\left|0\right\rangle + e^{i\omega_{01}t}\left|1\right\rangle\right)/\sqrt{2}$, where $\omega_{01} = \left(E_1 - E_0\right)/\hbar$. Thus $\phi = \omega_{01}t$ and a Bloch vector that is not along the z-axis will continually precess about the z-axis with a frequency ω_{01}. This behavior is completely analogous to the picture of a spin precessing at frequency $\omega_{01} = \gamma H$ about a constant magnetic field $\overline{H} = H\hat{z}$ [19]. If the coordinates are transformed to a rotating frame (non-inertial frame) a “fictitious” torque is created. If the rotating frame is set to co-rotate at frequency ω_{01} the fictitious torque will affectively “cancel” the rotation and the vector will remain fixed in time, unless additional torques act on it. In practice, the rotating frame is usually taken to be at the frequency of a main driving term ω, which may not necessarily be identical with ω_{01}.

In chapter 2, I wrote the two-level Hamiltonian for the phase qubit as [see Eq. (2.12)]

$$H = \begin{bmatrix} \langle 0|\gamma|0\rangle \frac{\Phi_0}{2\pi}(I_{n\mu w} + I_{\mu w}) & \langle 0|\gamma|1\rangle \frac{\Phi_0}{2\pi}\left(I_{n\mu w} + I_{\mu w}\right) \\ \langle 1|\gamma|0\rangle \frac{\Phi_0}{2\pi}\left(I_{n\mu w} + I_{\mu w}\right) & \hbar\omega_{01} + \langle 1|\gamma|1\rangle \frac{\Phi_0}{2\pi}\left(I_{n\mu w} + I_{\mu w}\right) \end{bmatrix}.$$

The Hamiltonian in the rotating frame $\overline{H}$ can be found from [26]

$$\overline{H}(t) = \exp(iH_0 t)H(t)\exp(-iH_0 t) - H_0, \tag{3.3}$$

where

$$H_0 = \begin{pmatrix} 0 & 0 \\ 0 & \hbar\omega \end{pmatrix}. \tag{3.4}$$

If Eq. (2.12) and the harmonic oscillator approximation are used the Hamiltonian in the rotating frame can then be written as

$$\overline{H} = \begin{bmatrix} 0 & \langle 0|\gamma|1\rangle \frac{\Phi_0}{2\pi}\left(I_{n\mu w} + I_{\mu w}\right)\exp(-i\omega t)) \\ \langle 1|\gamma|0\rangle \frac{\Phi_0}{2\pi}\left(I_{n\mu w} + I_{\mu w}\right)\exp(i\omega t) & \hbar(\omega_{01} - \omega) \end{bmatrix}. \tag{3.5}$$

If the driving term is written as $I_{\mu w} = I_x \cos(\omega t) + I_y \sin(\omega t)$, the Hamiltonian can be simplified even further using the Pauli matrices and the identity matrix. Disregarding terms that contain $\exp(\pm i2\omega t)$ (this is equivalent to making the rotating wave approximation [26]) gives [49]

$$\overline{H} = \left(\frac{\langle 0|\gamma|1\rangle}{2}\frac{\Phi_0}{2\pi}\right)\left(I_x\hat{\sigma}_x + I_y\hat{\sigma}_y\right) + \frac{\hbar(\omega_{01} - \omega)}{2}\hat{\sigma}_z + \frac{\hbar(\omega_{01} - \omega)}{2}\hat{I} + H_{n\mu w}, \tag{3.6}$$

where $H_{n\mu w} = \begin{bmatrix} 0 & \langle 0|\gamma|1\rangle \frac{\Phi_0}{2\pi}\left(I_{n\mu w}\right)\exp(-i\omega t)) \\ \langle 1|\gamma|0\rangle \frac{\Phi_0}{2\pi}\left(I_{n\mu w}\right)\exp(i\omega t) & 0 \end{bmatrix}$. I note that both the low frequency current noise I_{nlf} and the dc current $\langle I\rangle$ determine γ_0 and ω_{01}.

With Eq. (3.6) the Bloch sphere in the rotating frame can be used to view how the state of the system or Bloch vector varies when driving currents are applied to the phase qubit. For example, if $\omega_{01} = \omega$, $I_y \neq 0$ and $I_x = 0$, then from Eq. (3.6) we can see how this produces an effective constant torque about the y-axis in the rotating frame. If the state starts at $|0\rangle$, the result is a Rabi oscillation in which θ increases in time. Ignoring decoherence the measured state will rotate back and forth between $|0\rangle$ and $|1\rangle$ at a flopping frequency

$$\Omega_{01} = \left(\langle 0|\gamma|1\rangle I_y \Phi_0 / 2\pi\hbar\right) . \tag{3.7}$$

Interestingly, an off-resonant driving term also effectively acts like a torque about the z-axis. I note that the x and y axis of rotation for a microwave drive depends on the phase of the drive once the axis orientation is set by choosing the phase of the applied microwaves at $t = 0$. Noise at microwave frequencies $I_{n\mu w}$ will act much like the microwave drive term and cause transitions, while low frequency noise I_{nlf} will cause fluctuations in ω_{01} and act like a z-axis drive [49].

3.3 Dissipation and T_1

The fluctuation-dissipation theorem reveals that small fluctuations acting on a system will result in the dissipation of energy in the system and vise-versa [50]. For the phase qubit, fluctuations in the current bias at frequency ω_{01} cause transitions between energy eigenstate (torques about the x or y-axis). The current fluctuations could be due to Johnson-Nyquist noise [51,52], or noise from an external current source, or noise produced by other quantum systems coupled to the qubit, or any other noise source that couples to the qubit. If the qubit is prepared in the first excited state $n=1$ it will decay to $n=0$ with mean lifetime T_1. T_1 is commonly referred to as the relaxation time or dissipation time.

At elevated temperatures the population in the different energy levels is expected to follow a Boltzmann distribution. Johnson-Nyquist current noise $I_{n\mu w}$ at ω_{01} will cause transitions in the qubit from $n=0 \rightarrow 1$ at a rate W_{01}, as well as transitions from $n=1 \rightarrow 0$ at a rate W_{10}. Using first-order perturbation theory the rates W_{01} and W_{10} can be calculated based on the thermal noise spectrum, as shown by Xu [36]. Since the matrix elements for these processes are identical, the rates will be equal. Together with the spontaneous emission rate $1/T_1$ they must produce an occupation in $|0\rangle$ and $|1\rangle$ that obeys the Boltzmann distribution. From these relations $1/T_1$ can then be determined [36].

At the temperatures where I make my measurements, W_{10} and W_{01} were negligible and can be ignored. Since relaxation occurs even at zero temperatures, the zero-point noise spectrum can be used to determine $1/T_1$ directly using first order perturbation theory. Starting from Fermi's Golden rule and using the zero-point current noise power spectrum $S_{I_{zp}}(\omega_{01}/2\pi)$, the relaxation rate can be written as [53]

$$\begin{aligned} 1/T_1 &= \left(\frac{1}{\hbar^2}\right)\left(\frac{\partial\langle 0|H|1\rangle}{\partial I_n}\right)^2 S_{I_{zp}}\left(\frac{\omega_{01}}{2\pi}\right) \\ &= \left(\frac{1}{\hbar^2}\right)\left(\frac{\Phi_0}{2\pi}\langle 0|\gamma|1\rangle\right)^2 S_{I_{zp}}\left(\frac{\omega_{01}}{2\pi}\right) \end{aligned} . \qquad (3.8)$$

To model relaxation using Eq. (3.8) one need to find the noise spectrum that the qubit sees. In general, the qubit is connected across of an admittance $Y(\omega)$ that includes contributions from dissipative and non-dissipative elements. In general, it can be viewed as being formed from an infinite set of LC oscillators in parallel [54] with the qubit, such that $Y(\omega) = \sum_{m=0}^{\infty} Y_m(\omega)$. With an infinite number of oscillators one ensures irreversible behavior. Each oscillator can be viewed as a quantum system that will produce charge and current fluctuations in the qubit [55]. The Fourier transform of the current correlation function $\langle I(0)I(\tau)\rangle$ gives the noise power spectral density [49, 55]

$$S_I(\omega/2\pi) = \frac{2\hbar\omega}{1-\exp(-\hbar\omega/k_BT)}\mathrm{Re}[Y(\omega)], \qquad (3.9)$$

where $f = \omega/2\pi$. Here I use the somewhat unconventional definition in which the power spectral density extends over positive (the qubit releases a photon to the impedance) and negative frequencies (where the qubit absorbs a photon) [55].

At zero temperature the spectral density is [56]

$$S_{Izp}(\omega/2\pi) = 2\hbar\omega\,\mathrm{Re}[Y(\omega)] \qquad (3.10)$$

for $\omega > 0$ and $S_{zp} = 0$ for $\omega < 0$. Thus at $T = 0$, the qubit can only lose energy to the bath of oscillators. Using the zero-point noise and the harmonic oscillator approximation [Eq. 2.10(a)] in Eq. (3.8) gives

$$\begin{aligned} 1/T_1 &= \left(1/\hbar^2\right)\left(\frac{\Phi_0}{2\pi}\right)^2\left(\frac{2e^2}{C\hbar\omega_{01}}\right)2\hbar\omega_{01}\,\mathrm{Re}\left[Y\left(\omega_{01}\right)\right] \\ &= \mathrm{Re}\left[Y\left(\omega_{01}\right)\right]/C \end{aligned} \quad . \qquad (3.11)$$

If the admittance is simply due to a resistor R, then $Y\left(\omega_{01}\right) = 1/R$ and $T_1 = RC$ as expected. In general, the capacitance C includes any effective reactance from the admittance as well as the capacitance of the junction, as I will discuss in Chapter 4.

3.4 Decoherence and T_2

A torque about the z-axis will cause the phase ϕ of the Bloch vector to vary (unless it is in state $|0\rangle$ or $|1\rangle$). A randomly fluctuating torque about the z-axis will therefore give $\left\langle \phi^2(t) \right\rangle \neq 0$ and lead to dephasing. To calculate a characteristic time T_ϕ for dephasing, I assume the noise amplitude probability density can be described with a Gaussian

$$\frac{dp(\phi)}{d\phi} = \frac{\exp(-\phi^2/2\left\langle \phi^2 \right\rangle)}{\sqrt{2\pi\left\langle \phi^2 \right\rangle}} \quad . \qquad (3.12)$$

If I consider an initial state with $\theta = \pi/2$, $\phi = 0$ and only low frequency fluctuations (z-axis torque), the probability $p(t)$ of measuring a projection to this initial state at some later time t is roughly given by [49]

$$p(t)=\int_{-\infty}^{\infty} d\phi \frac{dp(\phi)}{d\phi}\cos^2(\phi/2)\approx 0.5+0.5\exp\left[-\left\langle \phi^2(t)\right\rangle/2\right]. \tag{3.13}$$

Since $\left\langle \phi^2(t)\right\rangle$ increases with time, as $t\to\infty$ all phase information will be lost and the qubit will be in a mixed state. If $\left\langle \phi^2(t)\right\rangle$ is linear in time, one can define an exponential decay time constant $1/T_\phi$ called the dephasing time or phase diffusion time.

A state at $\theta=\pi/2$ is also subject to high frequency noise that will not affect ϕ, but will change the Bloch vector by rotating it about the x or y-axis. If the state is $(|0\rangle+|1\rangle)/\sqrt{2}$, torque fluctuations about y and z (but not x) will affect the state. One can then define an exponential decoherence rate or characteristic time constant T_2, which describes how a state will evolve stochastically in any direction. The coherence time T_2 can be expressed in terms of T_ϕ and T_1 as [19]

$$1/T_2 = 1/T_\phi + 1/2T_1 \,. \tag{3.14}$$

The factor of 2 in front of the T_1 term makes sense in that an x-axis torque does not affect the state $(|0\rangle+|1\rangle)/\sqrt{2}$, where as both x and y torques would affect the state $|1\rangle$ [49].

The fluctuations in the phase ϕ result from current noise fluctuations I_{nlf} that are slow compared to ω_{01}. As is evident from Eq. (3.6), I_{nlf} causes the energy level spacing ω_{01} to vary and not match the rotating wave frequency ω, producing an effective torque about the z-axis. Assuming no other forces act on the Bloch vector and $\phi(0)=0$, then I can write

$$\phi(t) \cong \frac{\partial\omega_{01}}{\partial\langle I\rangle}\int_0^t dt' I_{nlf}(t') + \phi(0), \tag{3.15}$$

where I have assumed ω_{01} varies linearly with I. The mean-squared phase noise is therefore [49]

$$\left\langle\phi^2(t)\right\rangle = \left(\left(\frac{\partial\omega_{01}}{\partial\langle I\rangle}\right)^2\right)\int_0^{\omega_{01}/2\pi} S_{I_n}(f)\frac{\sin^2(\pi f t)}{(\pi f)^2}df \ . \tag{3.16}$$

The cut off at $\omega_{01}/2\pi$ is somewhat *ad hoc* and occurs because at this frequency the noise would cause transitions. For a resistor, $S_{I_n}(f)$ is given by Eq. (3.9) with $\mathrm{Re}[Y(\omega)] = 1/R$, and looks relatively white (flat spectrum) for $\hbar\omega << k_B T$. In this case,

$$\left\langle\phi^2(t)\right\rangle \cong \left(\frac{\partial\omega_{01}}{\partial\langle I\rangle}\right)^2 S_{I_n}(f=0)\frac{t}{2} \ . \tag{3.17}$$

Thus $\left\langle\phi^2\right\rangle$ grows linearly with time and knowledge of the phase will decay exponentially. For a spectrum that is not white, the decay will not be exponential. From Eq. (3.17) and Eq. (3.13), it can be shown that the dephasing time T_ϕ for a white spectrum is [49]

$$T_\phi = \frac{4}{\left(\frac{\partial\omega_{01}}{\partial\langle I\rangle}\right)^2 S_{I_n}(f=0)} \ . \tag{3.18}$$

This also matches the result found using a density matrix approach [57].

3.5 Other Time Constants

From the discussion up to this point, it is clear that there are several time constants that govern the dynamics of phase qubits. The n$^{\text{th}}$ level has a tunneling rate Γ_n to the voltage state that is bias current dependent. A qubit in the first excited state will decay to the ground state at a rate $1/T_1$. Thermal excitation with rate W_{01}, and relaxation with rate W_{10}, are possible at elevated temperatures. The phase ϕ of the qubit decays at a rate $1/T_\phi$. The decoherence rate $1/T_2$ includes dephasing and dissipation [58].

In addition, as was described above, a resonant microwave drive can produce Rabi oscillations in the qubit. The oscillations will precess with a rate Ω_{01}[see Eq. (3.7)] and the amplitude of oscillations will decay with a time constant, which I will define as T'. A new time constant is needed here, since the state of the qubit is affected differently by current noise at different times during the oscillation. For example, for $|\Psi\rangle = |1\rangle$ or $|\Psi\rangle = |0\rangle$ dephasing will not affect the state of the qubit. A long pulse at ω_{01} can also be seen as a concatenation of many π-pulses, which can cause a refocusing effect [59]. As $t \to \infty$ the expectation value should saturate at approximately 50%, and the system will be in a mixed state.

When decoherence is present and low power microwaves are applied, the probability of occupying the excited state will be less than 50% even as $t \to \infty$. The limiting probability will be dependent on the microwave power, how far off resonance the microwaves are with the energy level spacing (detuning), and the coherence time of the qubit. For a sufficiently low power microwave drive the occupation in $|1\rangle$ as a function of the detuning provides a measure of the spectroscopic coherence time [19,58]

$$T_2^* = 1/\pi(\Delta f), \tag{3.19}$$

where Δf is the full width at half max of the resonant peak (see Fig. 8.1). In the absence of dephasing the spectroscopic coherence time can be easily understood from the Fourier decomposition of the decay T_1 and/or an imaginary energy associated with the energy level. This measurement is sensitive to low frequency noise and drift, so that $T_2^* < T_2$.

Another common experiment is a Ramsey fringe measurement (see Fig. 8.13). In a Ramsey experiment, a detuned π/2 pulse first prepares the system in the state $|\Psi\rangle = (|0\rangle + |1\rangle)/\sqrt{2}$. Since the microwave drive term at ω does not match the resonant frequency ω_{01}, after the π/2 pulse the Bloch vector in the rotating frame will precess in ϕ at a rate that matches the detuning $\omega_{01} - \omega$. If another π/2-pulse is then applied at a later time Δt the probability of finding the system in $|1\rangle$ will oscillate as a function of $(\omega_{01} - \omega)\Delta t$. As was mentioned above, for $\theta = \pi/2$ (after the π/2 pulse), T_2 describes the decay of this state. From this it may appear that the amplitude of the oscillation will decay with time constant T_2. However, this ignores the need to average multiple measurements together, and low frequency noise has a significant impact (inhomogeneous broadening). This time is actually better described using a time constant $T_{2Ramsey}$; it is also sometimes written as T_2^*, although I will reserve this for the spectroscopic coherence time.

I have so far avoided a subtlety of low-frequency noise versus high frequency noise. In particular, the state of a qubit can be “refocused” using a π-pulse in the middle of the delay Δt to remove the effects of fluctuations that occur on a time scale longer than Δt. This is commonly referred to as spin echo. Faster fluctuations can still be removed if the fluctuations are slow compared to $\Delta t / n$ and a train of *n* refocusing pulses is applied, each preceded and followed by a time interval $t / 2n$ of free evolution [59]. This is the so-called Carr-Purcell sequence and gives the coherence time T_2 [60]. The distinction between the loss of phase coherence, which can be removed with echo techniques and that which cannot is somewhat artificial in that any time evolution can in principle be reversed by a sufficiently rapid sequence of echo pulses [61].

3.6 Density Matrix

The density matrix formalism provides a powerful tool to model the dynamics of a qubit that is subject to dissipation and decoherence. Specifically one can model an ensemble that takes into account pure and mixed states. The density matrix is defined based on the density operator $\hat{\rho}$ [32], where

$$\hat{\rho} = \left(\sum_i w_i \left| \alpha^{(i)} \right\rangle \left\langle \alpha^{(i)} \right| \right). \tag{3.20}$$

Here w_i is the probability of the ensemble being in the pure quantum state $\left| \alpha^{(i)} \right\rangle$, and $\sum_i w_i = 1$.

The density matrix is Hermitian, with $tr(\hat{\rho}) = 1$. The ensemble average of an operator $\hat{A}$ is given by $\langle A \rangle = tr(\hat{\rho}\hat{A})$. For a pure state $\hat{\rho}^2 = \hat{\rho}$ and thus $tr(\hat{\rho}^2) = 1$; for a mixed state or statistical ensemble $tr(\hat{\rho}^2) < 1$. The time evolution of the density operator is governed by [32]

$$\frac{\partial \rho}{\partial t} = -\frac{i}{\hbar}\left[H, \rho\right] . \tag{3.21}$$

As mentioned above, dissipation in the qubit can be modeled as the qubit being coupled to an infinite number of LC oscillators. The density matrix would need to include all these oscillators, which would be very challenging. Instead, one can trace over the "rest of the universe" and construct a reduced density matrix [62]. By tracing over the rest of the universe a pure state can evolve into a mixed state, as we expect when decoherence is included.

If the harmonic oscillator approximation is used for the phase qubit and $I_{\mu w} = I_x \cos(\omega t)$, the time evolution of the density matrix can be written as

$$\begin{pmatrix} \dot{\rho}_{00} & \dot{\rho}_{01} \\ \dot{\rho}_{10} & \dot{\rho}_{11} \end{pmatrix} = \frac{-i}{\hbar}\left[\begin{pmatrix} 0 & \hbar\Omega_{01}\cos(\omega t) \\ \hbar\Omega_{01}\cos(\omega t) & \hbar\omega_{01} \end{pmatrix}, \begin{pmatrix} \rho_{00} & \rho_{01} \\ \rho_{10} & \rho_{11} \end{pmatrix}\right] . \tag{3.22}$$

Expanding this out leads to four differential equations [63,64],

$$\begin{aligned} \dot{\rho}_{00} &= -i\Omega_{01}(\rho_{10} - \rho_{01})\cos(\omega t) + \rho_{11}/T_1 \\ \dot{\rho}_{01} &= -i\Omega_{01}(\rho_{11} - \rho_{00})\cos(\omega t) + i\omega_{01}\rho_{01} - \rho_{01}/T_2 \\ \dot{\rho}_{10} &= +i\Omega_{01}(\rho_{11} - \rho_{00})\cos(\omega t) - i\omega_{01}\rho_{10} - \rho_{10}/T_2 \\ \dot{\rho}_{11} &= +i\Omega_{01}(\rho_{10} - \rho_{01})\cos(\omega t) - \rho_{11}/T_1 \end{aligned} . \tag{3.23}$$

Here I have added the relaxation and decoherence rates in an *ad hoc* manner. The relaxation rate is fairly intuitive to add since it simply corresponds to the expectation value decaying exponentially. The addition of T_2 is a little more subtle, but a few comments can be made. Since dephasing will not affect the state $\Psi = |0\rangle$ or $\Psi = |1\rangle$ it would make no sense to include it in $\dot{\rho}_{00}$ or $\dot{\rho}_{11}$. If the qubit were dominated by dephasing, I would expect an x-axis Bloch vector $\rho(t=0) = \begin{pmatrix} 1/2 & 1/2 \\ 1/2 & 1/2 \end{pmatrix}$ to decay to

$\rho(t) = \begin{pmatrix} 1/2 & 0 \\ 0 & 1/2 \end{pmatrix}$, as Eq. (3.23) predicts. A decoherence rate T_2 is required, instead of simply a dephasing term T_ϕ to keep the equations consistent, as can be easily seen by considering a system without dephasing; dissipation alone will force $\rho_{01} \to 0$ as the qubit relaxes to the ground state. I note that the addition of T_2 also somewhat mimics the addition of an imaginary term to the energy of the qubit. This will be exploited later to model the coupling of two quantum systems.

By going to the rotating frame the density matrix becomes [37]

$$\rho = \begin{pmatrix} \tilde{\rho}_{00} & \tilde{\rho}_{01} e^{i\omega t} \\ \tilde{\rho}_{10} e^{-i\omega t} & \tilde{\rho}_{11} \end{pmatrix} . \tag{3.24}$$

If I make the rotating wave approximation, $\langle \exp(\pm i 2\omega t) \rangle = 0$, the density matrix equations can be simplified somewhat to get [63]

$$\begin{aligned} \dot{\tilde{\rho}}_{00} &= +i\Omega_{01}(\tilde{\rho}_{01} - \tilde{\rho}_{10})/2 + \tilde{\rho}_{11}/T_1 \\ \dot{\tilde{\rho}}_{01} &= -i\Omega_{01}(\tilde{\rho}_{11} - \tilde{\rho}_{00})/2 - i(\omega - \omega_{01})\tilde{\rho}_{01} - \tilde{\rho}_{01}/T_2 \\ \dot{\tilde{\rho}}_{10} &= +i\Omega_{01}(\tilde{\rho}_{11} - \tilde{\rho}_{00})/2 + i(\omega - \omega_{01})\tilde{\rho}_{10} - \tilde{\rho}_{10}/T_2 \\ \dot{\tilde{\rho}}_{11} &= -i\Omega_{01}(\tilde{\rho}_{01} - \tilde{\rho}_{10}) - \tilde{\rho}_{11}/T_1 \end{aligned} . \tag{3.25}$$

In future discussions I refer solely to the rotating frame and drop the tilde, for example $\tilde{\rho}_{11} \to \rho_{11}$.

3.7 Some Simple Solutions to the Evolution of the Density Matrix

From the density matrix equations (Eq. 3.25), the other time constants defined earlier can be determined. For example, suppose a steady microwave drive at freq ω near ω_{01} is applied. In this case one find that the excited state population settles down to [63]

$$\rho_{11}^{eq} = \frac{\Omega_{01}^2 T_1 T_2 / 2}{1 + (\omega_d - \omega_{01})^2 T_2^2 + \Omega_{01}^2 T_1 T_2} . \tag{3.26}$$

This is a lorentzian with a peak height of

$$\rho_{11}^{eq} = \frac{\Omega_{01}^2 T_1 T_2 / 2}{1 + \Omega_{01}^2 T_1 T_2} \tag{3.27}$$

and a full width at half maximum of

$$\Delta\omega = \frac{2}{T_2}\sqrt{1 + \Omega_{01}^2 T_1 T_2} . \tag{3.28}$$

The fact that an off-resonant term saturates at a lower population can be understood by considering the Bloch vector, which will now include some torque about the z-axis due to detuning [see Eq. (3.6)]. As expected for a high power microwave drive, (*i.e*. such that $\Omega_{01}^2 >> 1/T_1T_2$) the population will approach 50% on resonance. For low power (i.e. such that $\Omega_{01}^2 << 1/T_1T_2$), Eq. (3.28) simplifies to give $T_2 = 2/\Delta\omega$, and thus $T_2 = T_2^*$. However this simple analysis doest include effects of low frequency fluctuations in ω_{01} As I noted earlier, low frequency noise or inhomogeneous broadening causes T_2^* to be less that T_2, and in general

$$\frac{1}{T_2^*} = \frac{1}{T_2} + \frac{1}{T_2^+} , \tag{3.29}$$

where T_2^+ is the inhomogeneous broadening time constant [19].

At larger microwave drives Eqs. (3.25) can be used to describe Rabi oscillations. With the system starting at $|0\rangle$ and a resonant microwave drive applied at $t = 0$ the population in the excited state is given by [63]

$$\rho_{11}(t) = \rho_{11}^{eq} - \rho_{11}^{eq} \exp\left(-t/T'\right)\left[\cos(\overline{\Omega}_{01}t) + \sin(\overline{\Omega}_{01}t)/T'\overline{\Omega}_{01}\right] , \qquad (3.30)$$

where $1/T' = 1/2T_1 + 1/2T_2$ and $\overline{\Omega}_{01} = \sqrt{\Omega_{01}^2 - \left(1/2T_1 - 1/2T_2\right)^2}$. As mentioned previously the Rabi decay time T' can be longer than T_2 due to refocusing and the fact that dephasing and relaxation act differently on the state of the system at different times.

The density matrix can also be used to model a Ramsey Fringe experiment. Ideally, with each pulse causing a rotation about the y-axis by exactly $\Delta\theta = \pi/2$, the population in $n = 1$ evolves as

$$\rho_{11}(t) = 0.5 - 0.5\exp(-\Delta t/T_2)\cos((\omega - \omega_{01})\Delta t) . \qquad (3.31)$$

In real experiments, the π/2-pulses are some fraction of the relaxation and decoherence times. In this case it is much better to time evolve Eq. (3.25) for the actual shape of the pulses. In addition, inhomogeneous broadening from low frequency noise must be accounted for. The time evolution is best done by expressing Eqs. (3.25) in the form $\frac{d\hat{\rho}}{dt} = \overline{\overline{P}}\hat{\rho}$. The density matrix can then be numerically time evolved in small steps Δt by $\rho(t + \Delta t) \approx \exp(\underline{P}\Delta t)\rho$.

Tunneling can also be included in the density matrix framework by adding rates of $-\left(\Gamma_i + \Gamma_j\right)/2$ to the right side of $\dot{\rho}_{ij}$ in Eq. (3.25) [36]. A large tunneling rate will need to be included in the low power spectroscopic widths and acts somewhat like a relaxation process. In the limit of no dephasing, $\Delta\omega \cong 1/T_1 + \Gamma_0 + \Gamma_1$. Generally the qubit is operated where the tunneling rates are negligible and they can often be ignored until used for readout.

3.8 Summary

A current biased Josephson junction can be approximated as a two-level system. Dissipation and decoherence can be understood in terms of microwave and low frequency current noise coming from an admittance across the junction. The admittance must include contributions from any intrinsic resistance across the junction, as well as contributions from any bias leads. The density matrix provides a powerful tool to model a qubit subjected to dissipation and decoherence as it evolves and can no longer be described as a pure state.

Another important point, which I ignored here, is that higher levels exist in real phase qubits. The large microwave powers often used in Rabi oscillation lead to a large spectral broadening, which will allow for transition from $n=1$ to $n=2$. This leakage to higher energy levels, which can reach a few percent, must be considered to fully model the qubits [65].

Chapter 4

Qubit Design and Fabrications

In Chapter 2, I briefly discussed the dc SQUID phase qubit and that we chose this design to isolate the qubit from the environment. In Chapter 3, I discussed why the qubit must be well isolated from noise at the resonant frequency of the junction as well as at lower frequencies; a broadband isolation isolated scheme is needed. In this chapter, I discuss the design considerations for the dc SQUID phase qubit. I then give an overview of the devices I tested and how they were fabricated.

4.1 dc SQUID Design Considerations

4.1.1 Admittances

In Chapter 3, I showed that the relaxation time of a phase qubit was proportional to the capacitance of the junction and the effecting shunting resistance [see Eq. (3.11)]. It is expected that the gate fidelity necessary for a quantum computer will require the coherence time to be orders of magnitude larger than the time to complete gate operations. Superconducting qubit gates have been operated as fast as a few nanoseconds [37]. Although considerable progress has occurred, a coherence time of tens of microseconds in a phase qubit is still a daunting task. However, coherent dynamics can be seen with a coherence time of only a few nanoseconds.

If an unfiltered bias line with an impedance of $Z_0 = 50\,\Omega$ was connected directly to a phase qubit with a capacitance of $C = 4\,pF$, Eq. (3.11) predicts a relaxation time T_1

of only 0.2 nsec. This can be improved significantly by placing an on-chip LC filter on the bias line before the qubit junction [38]. The LC filter acts like a current divider and shunts noise at the junction plasma frequency if $\omega_p > 1/\sqrt{L_f C_f}$, where L_f is the filter inductance and C_f is the filter capacitor. However this approach fails to isolate the qubit from low frequency noise, which would lead to dephasing (for a complete discussion of an LC isolated phase qubit see refs. [27, 36, 37]). By replacing the capacitor with a small inductor L_2 the isolation can be improved significantly, because this provides broadband isolation over all frequencies. This configuration is now an rf SQUID with a bias line attached.

State readout in phase qubits has so far only been done by switching to the voltage state or to a different flux state. Since an rf SQUID can never switch to the continuously running voltage state, it can’t be measured by a switch to the voltage state. Martinis *et. al*. realized by adding another Josephson junction J2 to the small inductor the device would be able to switch to the voltage state; by measuring the voltage across the bias line the switch can be detected directly. With the additional readout junction or “isolation junction” the device is a dc SQUID phase qubit [39], [see Fig. 4.1(a)].

Depending on the parameters of the qubit and isolation junctions, and the bias point, when the qubit junction switches it will either cause the SQUID to switch flux states or switch to the constant voltage state. If the dc SQUID contains only a few flux states, a change in flux state can be detected easily by using a modified switching technique, as I will show in Chapter 6. I note that a change of flux state in an rf SQUID could be detected with an auxiliary SQUID, and this technique has been used by Martinis and others [66, 67].

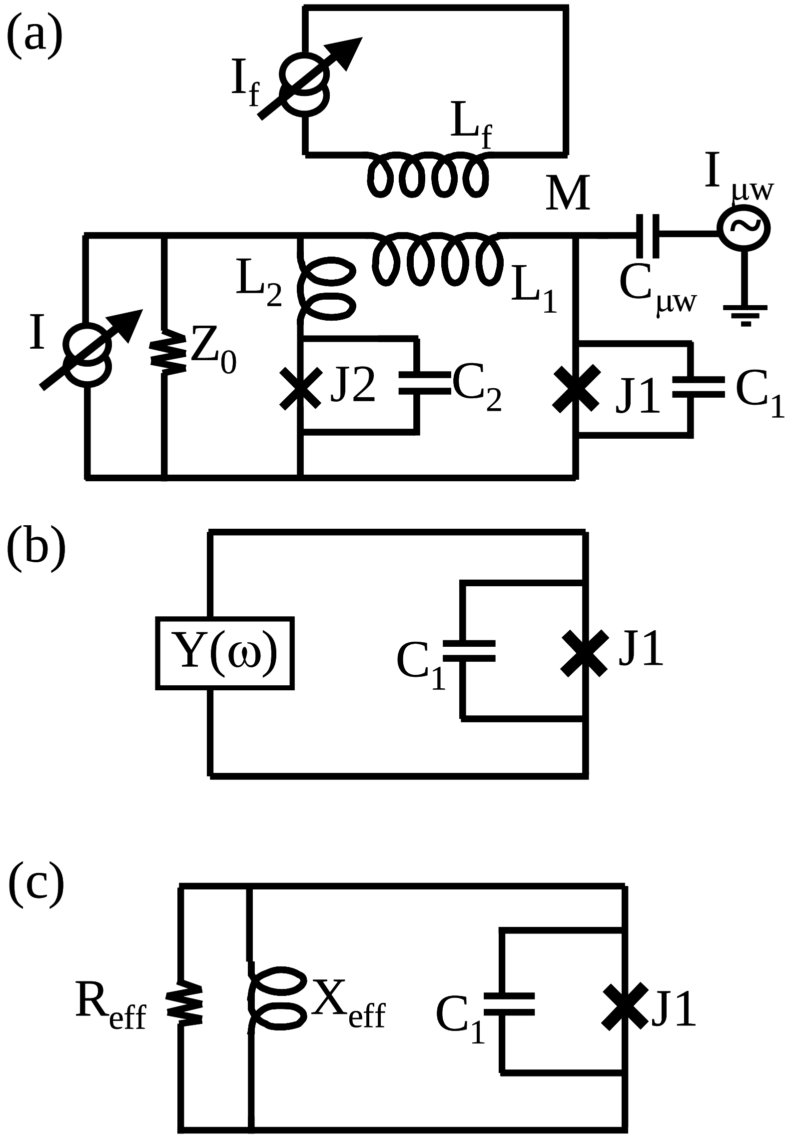

Figure 4.1: (a) dc SQUID phase qubit. The qubit junction J1 is isolated from the bias line by a large inductance L_1 and a smaller inductance L_2 and isolation junction J2. The flux line and current bias line enable independent control of the current through each junction. (b) Relaxation in the qubit is modeled as an effective admittance $Y(\omega)$ across the junction. (c) The admittance is more easily thought of as an effective resistance $R_{eff}(\omega)$ and reactance $X_{eff}(\omega)$ across the junction.

The basic idea behind the design of the dc SQUID phase qubit is that the bias current I will be shunted through the isolation branch, consisting of the isolation junction $J2$ and small inductor L_2, and not reach the qubit junction. Since the qubit junction still needs to be biased, a current bias I_f is attached to a coil with mutual inductance M to the SQUID loop. With both current sources the current through each junction can be controlled independently. The qubit analysis in the previous chapters, which was based on the RCSJ model, must be modified to include current noise from both bias sources; fortunately this is easily incorporated and doesn't change the analysis significantly.

To understand how well the isolation branch filters out current noise, consider bias current noise I_{nbi} present on the current bias line. I can define the current noise power isolation factor $r_I \equiv (I_{nbi}/I_n)^2$, where I_n is the noise current through the qubit junction $J1$. If the frequency f of the current fluctuations is much less than the resonance frequency of either junction, then one finds

$$r_I = \left(\frac{L_{J1} + L_1 + L_2 + L_{J2}}{L_2 + L_{J2}}\right)^2 \approx \left(\frac{L_1}{L_2 + L_{J2}}\right)^2, \tag{4.1}$$

where $L_1 >> L_{J1}$, as appropriate for our devices [68,69]. The Josephson inductance of the junctions, L_{J1} and L_{J2}, is given by Eq. (1.3). The current noise spectral density that reaches the qubit is given by $\mathrm{S}_{\mathrm{I_n}}(f) = \frac{\mathrm{S}_{\mathrm{I_{nbi}}}(f)}{\mathrm{r_I}}$. This provides a simple classical picture of how the isolation scheme performs. Choosing $L_1 >> L_2$ thus provides a large r_I and good broadband current noise rejection.

As discussed in Chapter 3, to calculate $T_1 = C / \mathrm{Re}\left[Y(\omega_{01)}\right]$, the admittance $Y(\omega)$ across the junction must be determined [see Fig. 4.1(b)]. The admittance is more easily visualized in term of an effective resistance $R_{eff}(\omega) = 1/\mathrm{Re}[Y(\omega)]$ and an effective reactance $X_{eff}(\omega) = -1/\mathrm{Im}[Y(\omega)]$, [see Fig. 4.1(c)] [37]. In actuality, if $X_{eff}(\omega_{01}) < 0$ the effective capacitance of the isolation circuit should be included along with that of the qubit junction C_1 [37], to give

$$T_1 = \left(C_1 - 1/\omega_{01} X_{eff}(\omega_{01})\right) R_{eff}(\omega_{01}) \ . \tag{4.2}$$

Just considering the bias line and the isolation, the admittance can be written as

$$Y(\omega) = \left[i\omega L_1 + 1/\left(\frac{1}{Z_0} + 1/i\omega\left(L_2 + \frac{L_{J2}}{1 - \omega^2 L_{J2} C_2} \right)\right)\right]^{-1} , \tag{4.3}$$

where Z_0 is the impedance of the current bias line connected to the SQUID.

If the plasma frequency of the isolation junction is somewhat larger than that of the qubit, which it will be during normal operation, the equation can be simplified further. I find $Y(\omega) \approx \left[i\omega L_1 + 1/\left(1/Z_0 + 1/i\omega\left(L_2 + L_{J2}\right)\right)\right]^{-1}$, and this gives

$$R_{eff} = \frac{\omega^2 L_1^2}{Z_0} + Z_0 \left(\frac{L_1 + L_2 + L_{J2}}{L_2 + L_{J2}} \right)^2 \text{ and} \tag{4.4}$$

$$X_{eff} = \frac{\omega^3 L_1^2 L_2^2 + Z_0^2 \omega (L_1 + L_2 + L_{J2})^2}{Z_0^2 (L_1 + L_2) + \omega^2 L_1 L_2^2} , \tag{4.5}$$

where I have assumed Z_0 is real.

This more rigorous modeling also shows that L_1 / L_2 should be made as large as possible to achieve a maximum relaxation time. As I showed in Chapter 2, a large L_1 has the effect of creating multiple stable flux states. Since only one potential well forms the basis for the qubit, the SQUID will need to be initialized to the same well every time [41]. From Eq. (4.5), one also sees that $X_{eff} > 0$. Since $X_{eff} > 0$ for the dc SQUID isolation scheme, the reactance is more accurately thought of as an inductor in parallel with the qubit junction and it has only a very small effect on T_1.

The contribution to the admittance from a flux line with impedance R_{fL} must also be considered. Using the model in Fig. 4.1, the admittance from the flux line using the model in Fig. 4.1 is

$$Y(\omega) = \left[i\omega\left(L_1 + L_2 + \frac{L_{J2}}{1-\omega^2 L_{J2} C_2} \right) + \frac{\omega^2 M^2}{R_{fL} + i\omega L_f} \right]^{-1} . \tag{4.6}$$

Separating out the real and imaginary parts of the admittance again gives an effective shunting resistance and reactance of

$$R_{eff}^{M} \approx R_{fL} \left(L_1 + L_2 + L_{J2} \right)^2 / M^2 \tag{4.7}$$

and

$$X_{eff}^{M} \approx \omega\left(L_1 + L_2 + L_{J2} \right) . \tag{4.8}$$

From Eq. (4.7) we see that choosing L_1 / M as large as possible ensures good isolation. Of course, if M is made too small, then I would need to provide a very large current to flux bias the SQUID. For this reason, in practice making M smaller than a few pH is undesirable. A microwave line is also attached to the qubit junction through a coupling capacitor; the coupling capacitor should be small enough, $C_{\mu w} < 2\ fF$, that the microwave line should not add significant dissipation to the qubit.

Flux noise [53, 70-74] (not related to the flux leads) also leads to decoherence in phase qubits. SQUIDs with vastly different sizes and materials, and measured differently all produce a flux noise spectrum of roughly

$$S_\Phi(f) \approx S_\Phi(1Hz)/f^{\alpha}, \tag{4.9}$$

where $0.66 < \alpha < 1$ and $2\,\mu\Phi_0/\sqrt{Hz} < S_\Phi^{1/2}(1Hz) < 20\,\mu\Phi_0/\sqrt{Hz}$ for temperatures under ~100 mK [53, 70-74]. The current noise power spectral density that flux noise would produce in the qubit is given by

$$\mathrm{S}_{\mathrm{I_n}}(f) \sim \frac{\mathrm{S}_\Phi(f)}{\left(\mathrm{L}_1 + L_2 + L_{1J} + L_{2J}\right)^2}\ . \tag{4.10}$$

A large loop inductance is therefore once again desirable. Flux noise should have little affect on relaxation, since if falls as approximately $1/f$, but it could contribute appreciable decoherence in phase qubits. If it dominates other sources of decoherence, the coherence time would no longer be well described with an exponential time constant, since the spectrum isn’t white [53]. Finally dielectric loss in the junction will also be present. Such intrinsic losses are unaffected by the isolation circuit.

The effective resistance from each admittance source, including the junction dielectric, need to be combined in parallel to find the total effective resistance shunting the junction. In practice one source will often dominate. I note that this analysis assumes the line impedances Z_0 and R_{fL} can be determined and that the lump element model is valid. For very high microwave frequencies the second assumption fails and more careful modeling of the distributed physical circuit is necessary.

4.1.2 Junction Coupling

In the dc SQUID phase qubit, the isolation junction ensures that the SQUID can switch to the voltage state for readout. If a current biased junction can act like a quantum 2-level system, a question can be raised, “Why is the isolation junction not considered a second qubit, coupled to the first through the inductor L_1?” In actuality, the isolation junction can be considered as another qubit. However, several different factors suggest that such a treatment is unnecessary. First, the coupling between the isolation junction and qubit junction is weak in the dc SQUID phase qubit, as I will show below. Also, the resonant frequency ω_{p2} of the isolation junction will usually be much larger than ω_{p1} of the qubit junction, which will reduce the dynamical coupling between the two junctions. Finally the isolation junction experiences a large amount of noise and dissipation since it is connected directly to the bias leads. This tends to hide quantum effects.

To determine the coupling to lowest order, we can approximate the SQUID as two coupled harmonic oscillators (one for each junction). In this case, the isolation junction will produce a fractional shift in the resonant frequency ω_1 of the qubit junction given by [41]

$$\frac{\Delta\omega}{\omega_{p1}} = \left|\frac{\omega_1 - \omega_{p1}}{\omega_{p1}}\right| \approx \frac{{\omega_0}^4}{2(\omega_{p2}^2 - \omega_{p1}^2)\omega_{p1}^2} \; , \qquad (4.11)$$

where $\omega_0^4 \equiv 1/({L_1}^2 C_1 C_2)$, $\omega_{p2} > \omega_{p1}$ (as is typical for operation of the dc SQUID phase qubit) and the shift is small compared to ω_{p1}. Here the resonant plasma frequencies of the uncoupled junctions are ω_{p1} and ω_{p2}. The frequency shift is a measure of the dynamical coupling κ between the junctions and I can define this coupling as just

$\kappa = \Delta\omega / \omega_{p1}$. For the two junctions to act independently, one requires $\kappa << 1$.

For the SQUID phase qubit, Eq. (4.11) can be written in the form [41]

$$\kappa \cong \frac{2}{(2\pi\beta)^2 (1-\alpha^2)\sqrt{1-(I_1/I_{01})^2}}\,, \tag{4.12}$$

where I_1 is the current through the qubit junction, $\alpha = (I_{02} - I_{01})/(I_{02} + I_{01})$ is the current asymmetry parameter and $\beta = L(I_{01} + I_{02})/\Phi_0$ is the SQUID modulation parameter [43]. Thus $\kappa << 1$ implies that we choose

$$\beta >> \frac{1}{2\pi}\sqrt{\frac{2}{1-\alpha^2}}\,\frac{1}{[1-(I_1/I_{01})^2]^{1/4}}\ . \tag{4.13}$$

I note that Eq. (4.11) is not what one would find by simply examining the dc SQUID Hamiltonian, as given in Eq. (2.20). Expanding the last term in the Hamiltonian reveals a term that couples the two junction’s phase, given by,

$$H_{\text{int}} = -(\Phi_0/2\pi)^2\, \gamma_1\gamma_2/L_1 \tag{4.14}$$

between the two junctions. With the overall energy scale set by $E_{J1} + E_{J2}$ this suggests a naïve dimensionless coupling strength of

$$\kappa_0 = 1/(2\pi\beta)\ . \tag{4.15}$$

Equation (4.15) suggests that $\kappa_0 << 1$ and thus $\beta >> 1/2\pi$ is required in order for the two junctions to be weakly coupled, while Eq. (4.13) gives a different relationship. Although Eq. (4.13) may appear to be even more restrictive than the naïve condition, it is in fact less restrictive since the coupling is set by $\kappa \propto 1/\beta^2$ rather than $\kappa_0 \propto 1/\beta$. Either way, I can conclude that a large β is desired, which tends to give many stable flux states. Note however that the coupling also depends on the critical current asymmetry α; and by choosing I_{01} sufficiently small, multiple flux state can be eliminated. In Chapter 6, the difficulty of operating a device with many stable flux states will be addressed.

4.2 Fabrication Techniques

4.2.1 Hypres Fabrication

The first dc SQUID phase qubits I tested (DS_1, DS_{2a} and DS_{2b}) were fabricated by Hypres, Inc., in Elmsford New York [75]. These devices were based on a CAD drawing we supplied. The Hypres multi-level process consists of Nb/AlO_x/Nb trilayer junctions, four sputtered Nb metal layers (including two for the junction), a Mo layer, a Ti/Pd/Au layer, four sputtered SiO_2 insulating layers and process steps where vias were formed. Table 4.1 summaries the Hypres layer designations, materials and thicknesses. The

Table 4.1:Hypres layer parameters

	Physical Layer properties: Resistance, Capacitance	Thickness (nm)	Deviation (± nm)
M0	Nb, superconductor. Penetration depth λ=100 nm	100	10
I0	SiO_2 insulator Capacitance 0.277 fF/μm^2	150	15
M1	Trilayer base electrode, superconductor λ=100 nm	135	10
I1A	AlO_x	45	5
SiO_2	SiO_2 insulator Capacitance 0.416 fF/μm^2	100	10
R2	Mo, resistor	100	20
SiO_2	SiO_2 insulator Capacitance 0.277 fF/μm^2	100	10
I1B	Contact hole through the above two SiO_2 ;auers		
M2	Nb, superconductor. Penetration depth λ=90 nm	300	20
SiO_2	SiO_2 insulator Capacitance 0.08 fF/μm^2	500	40
I2	Contact hole through the above insulator		
M3	Nb, superconductor. Penetration depth λ=90 nm	600	50
R3	Ti/PdAu resistor	350	60

critical current density was 100 A/cm^2 for DS$_1$, and 30 A/cm^2 for DS$_{2A}$ and DS$_{2B}$; a magnetic field was used to suppress the critical currents in device DS$_{1.}$ For DS$_{2A}$ and DS$_{2B}$ the molybdenum layer was used for quasiparticle traps.

Figure 4.2 (a) shows a photograph of the single dc SQUID phase qubit DS$_{1.}$ Data were already being taken on this device when I first joined the group. The light region at the top of Fig. 4.2(a) is the ground plane where the currents were returned to the sample box and out through the dilution unit. The design parameters [37] are listed in Table 4.2.

For my measurements, a magnetic field was used to reduce the critical currents of DS$_1$ to approximately $I_{01} = 34\,\mu A$ and $I_{02} = 5\,\mu A$ (see Chapter 6). The mutual inductance from the flux line was expected to be $M = 54\,pH$ and experimentally we found $M = 51\,pH$, the largest contribution to M came from the return path through the ground plane. This was an undesirable consequence of the large ground plane layer next to the SQUID loop [see Fig. 4.2] and we eventually removed this layer in later designs. Based on the design parameters with a line impedance of 50 ohms, the expected relaxation time would be $T_1 \approx 250\,ns$, and the coupling would be $\kappa \approx 0.001$ for typical

Table 4.2: Parameters for dc SQUID phase qubit DS$_1$ [34].

Element	Size (μm x μm)	Layers	Design Value	Measured Value (suppressed value)
Bond Pad	280 x 280	R3, M3		
L_2	40	M1 and M2	< 40 pF	< 30 pF
C_{J2}	7 x 7	M2, I1B, I1A / M1	2.09 pF	
I_{02}	7 x 7	I1A / M1	46 μA	51.7 μA (5 μA)
L_1	84 x 84	M1	3.3 nH	3.5 nH
C_{J1}	10 x 10	M2, I1B, I1 / M1	4.17 pF	4.43 pF
I_{01}	10 x 10	I1A / M1	97 μA	107.9 μA (34 μA)
$C_{\mu w}$	4 x 4	M3 / M1	0.9 fF	

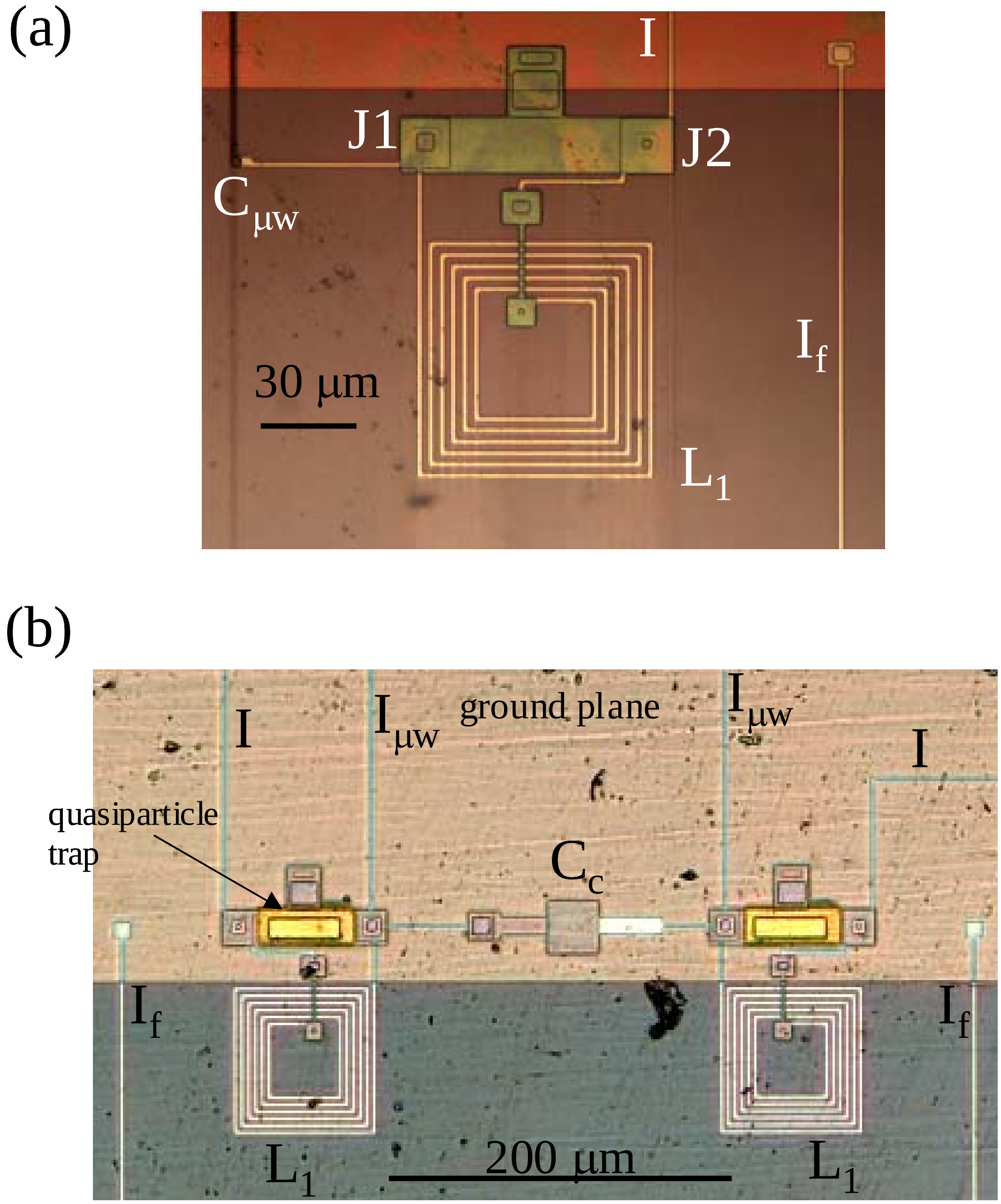

Figure 4.2: (a) Photograph of dc SQUID phase qubit DS_1. The device is a single dc SQUID phase qubit. A magnetic field was applied to reduce the critical currents. (b) Coupled devices DS_{2A} and DS_{2B}. The individual qubits are almost identical to DS_1, except for having a smaller critical current density and making use of quasiparticle traps.

operating conditions. This T_1 is clearly not enough for quantum computing, but would be more than sufficient for studying coherent quantum dynamics and performing the experiments mentioned in Chapter 3.

The second chip I tested had devices DS_{2A} and DS_{2B} [see Fig. 4.2 (b)]. The qubits were designed to be identical to each other and they were similar to DS_1. The parameters as given by S. K. Dutta [37] are listed below in Table 4.3.

In this case it was necessary to find the mutual inductance between the devices and the four current sources. Since the ground current was taken out on one side of the ground plane there was a large difference in the mutual inductances of the current bias and flux lines to the two qubits. The mutual inductance is best described with a matrix equation, $\overline{\Phi} = \underline{\overline{M}}\,\overline{I}$, where

Table 4.3: Parameters for device DS_{2A} and DS_{2B}. When both values are equal one value is listed, otherwise the value for DS_{2A} is listed first.

Element	Size (μm x μm)	Layers	Design Value	Exp. Value (DS_{2A}, DS_{2B})
Bond Pad	280 x 280	R3, M3		
L_2	40 μm	M1 and M2	< 40 pF	< 30 pF
C_{J2}	7 x 7	M2, I1B, I1A / M1	1.92 pF	
I_{02}	7 x 7	I1A / M1	13.8 μA	3, 6 μA
L_1	84 x 84	M1	3.3 nH	3.4 nH
C_{J1}	10 x 10	M2, I1B, I1 / M1	3.82 pF	4.4 pF
I_{01}	10 x 10	I1A / M1	29.1 μA	24, 20 μA
$C_{\mu w}$	4 x 4	M3 / M1	0.9 fF	
L_C	280 μm	M0, M1, and M2	200 pH	
C_C	30 x 30	M2 / M1	190 fF	130 fF
QP Trap	56 x 20	R3, M3, I2, M2		

$$\begin{pmatrix} \Phi_A \\ \Phi_B \end{pmatrix} = \begin{pmatrix} M_f^{AA} & M_b^{AA} & M_f^{BA} & M_b^{BA} \\ M_f^{AB} & M_b^{AB} & M_f^{BB} & M_b^{BB} \end{pmatrix} \begin{pmatrix} I_f^A \\ I^A \\ I_f^B \\ I^B \end{pmatrix} . \tag{4.16}$$

Here, for example, M_f^{BA} is the mutual inductance from the flux line of device B to dc SQUID A. The measured values were [37]

$$M = \begin{pmatrix} +71.92 & --- & 0.44 & -1.10 \\ -52.82 & -54.94 & 17.73 & ---- \end{pmatrix} pH . \tag{4.17}$$

This could be compared with values computed based on the layout of the device,

$$M = \begin{pmatrix} 90.7 & 28.3 & -0.18 & 2.7 \\ -62.5 & -45.7 & 13.4 & -27.5 \end{pmatrix} pH . \tag{4.18}$$

Controlling the current through the four junctions in this chip therefore required careful control of the four current lines. Since the bandwidth of the filters was not necessarily the same on each current line, this created additional complications.

4.2.2 Al/AlO$_x$/Al Fabrication

The final two devices I tested, DS$_{3A}$ and DS$_{4B}$, were built at the University of Maryland. Device DS$_{3A}$ was built by T. A. Palomaki, A. J. Przybysz and H. Kwon. Device DS$_{4B}$ was built by A. J. Przybysz. The devices were made using contact photolithography and double-angle evaporation on a sapphire substrate. Photolithography was used instead of e-beam lithography due to the relatively large features needed and to avoid charging effects on the sapphire substrate (it was also a simpler process). Creating a bridge and evaporating aluminum at two angles was used to create the junctions much as in a standard e-beam double-angle evaporation technique [76]. A negative resist, LOR30B [77], forms the undercut layer used under the bridge for the junction; LOR30B develops faster than the upper layer of S1813 negative resist used to make the bridge. The masks were designed using the 2-D CAD program ICED and sent to U. C. Berkeley Microlab [78] for fabrication. Here I will just summarize the procedure used, since the method was the same as described by H. Paik [68], with only a few small changes. The specific parameters quoted below are those that were used for device DS_{3A}.

Procedure:

1) A clean 2’’ sapphire wafer with orientation [0001], single-sided polished and 430 microns thick [79] was placed in the Trion Flourine RIE-1 etcher in the Kim building with a pressure of 200 mTorr. A power of 100 W was used for 100 s to clean the substrate.
2) The mask was cleaned using acetone, methanol, and isopropanol and then dried off with N_2 gas.
3) LOR30B photoresist [77] was spun on the substrate at 5000 RPM for 45 s and then baked at 150 ºC for 10 minutes.
4) Shipley S1813 [77] was then spun at 4500 for 45 seconds and baked at 110 ºC for one minute.
5) If any resist became caked on the back of the substrate, a cloth with PG remover was use to wipe it off, being careful not to touch the front surface of the wafer.

6) The mask was aligned in the Karl-Suss MJB3 contact mask aligner [80] with the wafer, such that is just made direct contact. It was exposed for 11 sec at 8 mW/cm^2.

7) The wafer was then developed for roughly 30 seconds in MF319 developer [77] and immediately rinsed with DI water. The timing is highly sensitive; the undercut should be developed completely and still leave a bridge. The bridge can be seen in an optical microscope with a red filter. We then diced the wafer by scribing with a diamond point and breaking off individual chips.

8) A chip was then placed in the cryo-pumped evaporator in room 0215 of the Physics building and pumped to roughly 10^{-6} Torr. Approximately 50 nm of Al was deposited at a rate of roughly 1nm/s from the first boat at an angle of ~ 45º. The sample was then exposed to 18 Torr of O_2 for 10 minutes. The system was pumped out again and the chip was rotated to the second angle (~ -45º) and a second boat of Al was evaporated.

9) The resists were removed using PG remover [77] at 60 ºC for 45 minutes. This was repeated with clean PG solution and a final cleaning was done with isopropanol and DI water.

Figure 4.3(a) shows a photograph of device DS_{3A} that was fabricated according to the above procedure. It was originally planned to be a coupled device with two identical qubits. Unfortunately one of the qubits did not work (DS_{3B}) and device DS_{3A} had a flux line that did not work, or possibly an open was created in the wiring upon cooling the

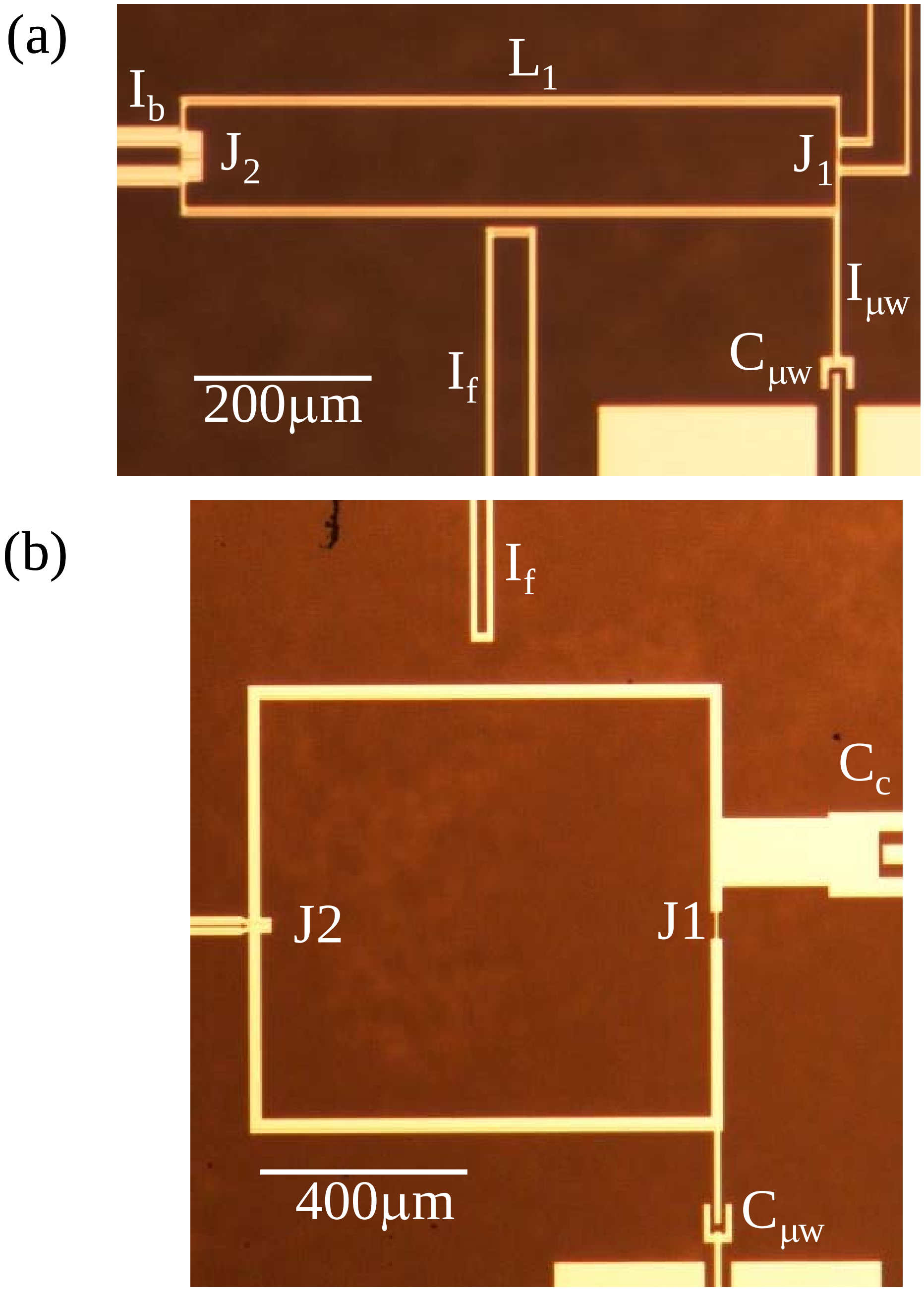

Figure 4.3: Photograph of dc SQUID phase qubits DS_{3A} and DS_{4B}. Both were fabricated at the University of Maryland. These devices had a substantially smaller qubit junction area than our previous devices. (a) Device DS_{3A} was coupled to a second qubit (not shown) that did not work. (b) Device DS_{4B} was almost identical to DS_{3A}, except for a larger inductance L_1. The large coupling capacitor is clearly visible.

device down, so I used the flux line of device DS_{3B} to couple flux into DS_{3A}. The working device DS_{3A} matched the design parameters fairly well, as listed in Table 4.4 with the nominal design values in parenthesis.

Here the mutual inductance used was that from DS_{3B}'s flux line, $M_{AB} = 1.4\,pH$, the mutual inductance of the device's flux line was expected to be $M_{AA} = 14\,pH$, but this line was found to be open when I cooled the device. The SQUID loop pickup area was approximately (600 μm x 100 μm) with a loop line width of roughly 4 μm. The coupling capacitor between the two SQUIDs was expected to be $C_C = 10\,pF$. I note that the expected relaxation time for DS_{3A} based solely on the bias lead impedance should have been $\sim 8\,ns$ if $Z_0 = 50\,\Omega$ and $\sim 50\,ns$ if $Z_0 = 300\,\Omega$, substantially smaller than the expected values for DS_1, DS_{2A} and DS_{2B}. This was because DS_{3A} had a much smaller junction capacitance than the previous device. The coupling constant for DS_{3A} is approximately $\kappa \approx .01$ [see Eq. (4.12)]. I also note that DS_{3A} was generally biased much deeper in the potential well than the previous devices.

The final chip I briefly worked with had two SQUIDs in it, DS_{4A} and DS_{4B}; I tested DS_{4B}. They were both Al/AlO_x/Al devices on a sapphire substrate. Device DS_{4A} and DS_{4B} had inductances $L_1 = 3\,nH$ and microwave coupling capacitance $C_{\mu w} = 2\,fF$. Figure 4.3(b) shows a photograph of the devices DS_{4B}. In the chip, both devices and all

Table 4.4 Parameters for DS_{3A}

I_{01}	C_1	I_{02}	L_1	L_2	$C_{\mu w}$	M_{AB}	M_{AA}
1.26 μA (1 μA)	0.37 pF (0.2 pF)	8.5 μA (10 μA)	1.05 nH (1 nH)	~20 pH	1 fF	1.4 pH	(14 pH)

lines worked as expected with mutual inductances of $M_{AA} = 12\,pH$ in device DS_{4A} and $M_{BB} = 18\,pH$ in DS_{4B}. The idea behind this device was to only change the loop inductance from the previous device and look for the expected effect on the relaxation time. Here the loop area was 400 μm x 400μm, with a linewidth of 2 μm. The relaxation time was expected to be roughly 9 times that of the previous device, *i.e.* about $\sim 90\,ns$ if $Z_0 = 50\,\Omega$ and $\sim 360\,ns$ if $Z_0 = 300\,\Omega$. The coupling constant κ should also be 9 times less. Table 4.5 summarizes the parameters of DS_{4B}, which were only very roughly determined.

4.3 Material and Fabrication Issues

The above predictions for T_1 are based solely on the transformed line impedances. They would be accurate if there were no other sources of dissipation. However, the junction can also have dissipation associated with dielectric loss in the insulation used to create the tunnel barrier. No amount of isolation from the leads will improve the relaxation time if loss is dominated by the junction dielectric. Similarly, a lossy insulator layer could lead to dissipation. The Hypres devices had sputtered trilayer junctions and four sputtered SiO_2 layers. The Maryland fabricated devices had AlO_x in the barrier and grown over all aluminum surfaces, but no other insulators except the substrate itself. The two substrates, Si in the Hypres devices and sapphire for the Al

Table 4.5 Parameters for DS_{4B}

I_{01}	C_1	I_{02}	L_1	L_2	$C_{\mu w}$	M_{BB}
1.1 μA	0.4 pF	7.5 μA	3 nH	~20 pH	2 fF	18 pH

devices were also different, which may have an effect. Other groups have reported that the removal of lossy dielectrics and insulators enhanced the coherence times [81]. These results motivated our design of the Maryland fabricated devices DS_{3A} and DS_{4B}. In addition, the qubit junction areas were much smaller in devices DS_{3A} and DS_{4B} than DS_1, DS_{2A} and DS_{2B}. This was done to remove as much AlO_x as possible in the barrier. Also, a sapphire substrate was used and no insulating SiO_2 layers were used in an attempt to minimize possible sources of dielectric loss.

I should also note that devices DS_{3A} and DS_{4B} were not exactly identical to the model described by Fig. 4.1(a), even ignoring the lumped element approximation. In these devices, parasitic junctions (I_{x1}, I_{x2} and I_{x3}), and loops (L_{p1}, L_{p2} and L_{p3}), were created during the double-angle evaporation, as can be clearly seen from an enlarged photograph of the qubit junction in Fig. 4.4(a). The parasitic loops result from the two Al layers not overlapping. In other parts of the device, the double angle evaporation process creates large area junctions. Figure 4.4(b) shows a schematic with the extra junctions and loops. These parasitic structures may be causing loss or introducing additional quantum systems, especially if the AlO_x is lossy.

In Chapter 10, I will show evidence that loss in these devices is produced by defects in the materials. The junction qubit appears to be coupled to many other quantum systems. If a large number of quantum systems coupled to the junction, they could cause dissipation, just as dissipation was modeled as an infinite number of coupled LC oscillators.

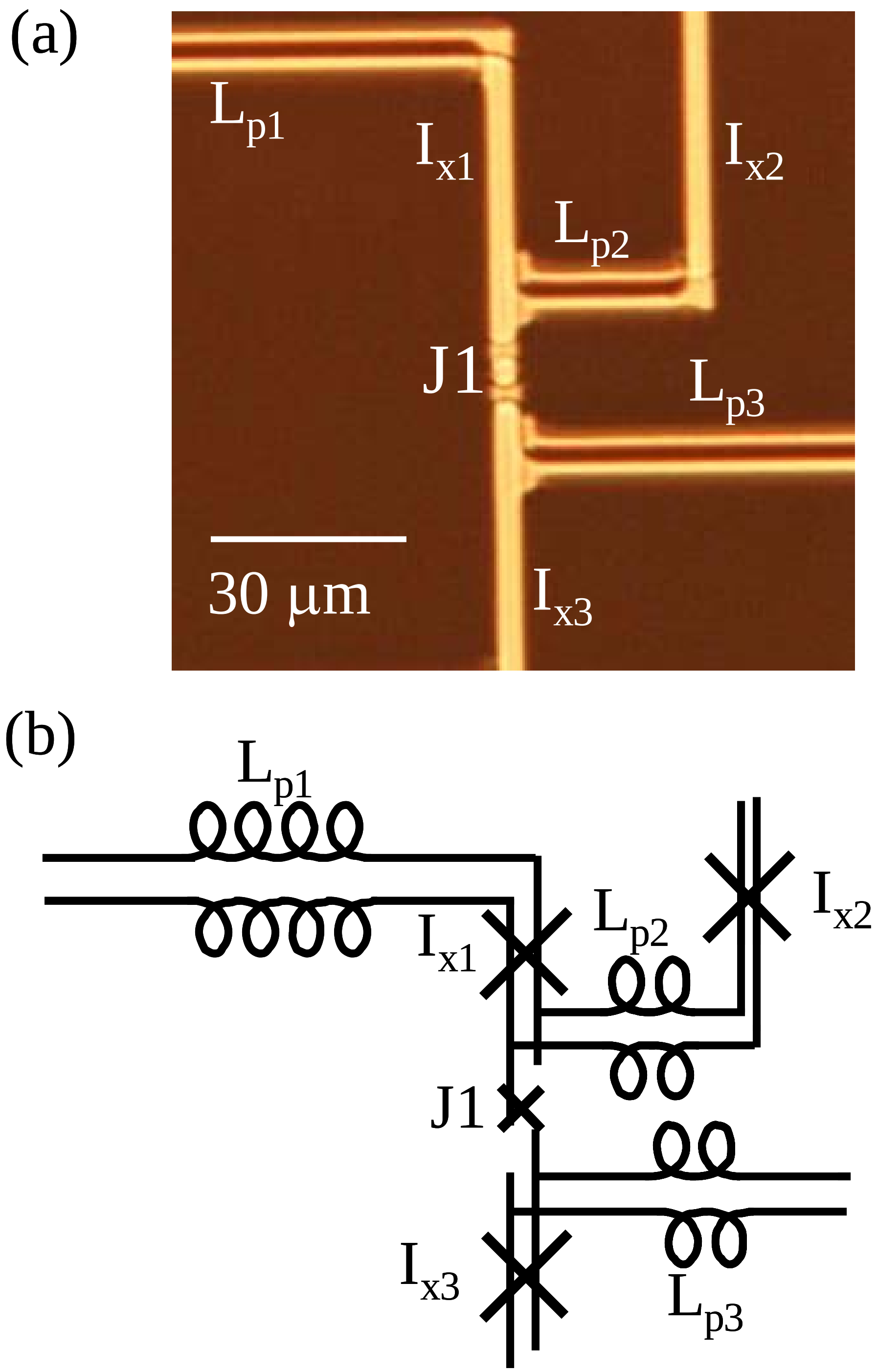

Figure 4.4: (a) Photograph of the region near qubit junction J1 in device DS_{3A} showing small parasitic loops and junctions that have been created during the double-angle evaporation of the Al films. (b) Schematic of circuit in (a), showing parasitic loops L_{p1}, L_{p2} and L_{p3} and parasitic junctions I_{x1}, I_{x2} and I_{x3}.

4.4 Summary

In this chapter, I described the layout and parameters of the SQUID phase qubits I tested. Three qubits were fabricated by Hypres (DS_1, DS_{2A} and DS_{2B}) and two were fabricated at Maryland (DS_{3A} and DS_{4B}). The Hypres devices consisted of Nb/AlO_x/Nb trilayer junctions with four sputtered SiO_2 insulating layers on oxidized silicon wafers. The devices fabricated at Maryland consisted of Al/AlO_x/Al junctions on a sapphire substrate. For a 50 Ω lead impedance, both Hypres devices had predicted $T_1 \sim 250\,ns$, the Maryland device DS_3 had a predicted $T_1 \sim 8\,ns$ and DS_4 was predicted to have $T_1 \sim 90\,ns$, *i.e*. about 9 times longer than DS_3. The coupling between the isolation and the qubit junction should not have affected the qubits, although in DS_3, $\kappa \sim 0.01$, so there could have been some effect [42]. I emphasis that these predictions ignore losses in the materials. In Chapter 10, I show evidence of material defects affecting the performance of the qubit.

Chapter 5

Experimental Setup

This chapter focuses on the experimental apparatus I used to make measurements. From one experiment to the next, I made only minor changes to the dilution unit, wiring and electronics. The main thing that changed between experiments was the qubit and how I used the equipment. When changes were made between experiments, I will specifically mention what they were. The largest change was before run DS_2; the lines and electronics were doubled to allow for two qubit operations and I used a new sample box. Excellent description of the set-up and electronics can be found in references [36] and [37]. The schematics of the electronics [36] and transfer functions of the filters and lines [37] are explained there in detail. Here I discuss the considerations that went into designing the system, particularly the wiring.

5.1 Dilution Refrigerator Operation

A common misconception is that superconducting qubits are operated in dilution refrigerators in order to make them superconducting. The real reason is that our qubits have energy level spacing $\omega_{01}/2\pi \approx 6-10\,GHz$, so we require a device temperature of less than 70 mK to ensure the system initializes to the quantum ground state with over 99% probability. Reaching such temperatures is most easily done using a dilution refrigerator. Roughly speaking, a dilution refrigerator generates cooling power by transporting He^3 atoms across a liquid He^3/He^4 phase boundary [82]. Figure 5.1 shows a schematic of the stages of a typical dilution unit along with a photograph of the dilution refrigerator I used.

All of my experiments were carried out using a Model 200 TLE Dilution Refrigerator by Oxford Instruments [82]. This unit has a cooling power of 200 μW at 100 mK and can reach a base temperature of 20 mK. All experiments were done with a mixing chamber temperature of less than 30 mK, unless otherwise noted. I assumed that the samples were very close to the mixing chamber temperature. During operation the unit requires approximately 100 L of liquid Helium every four days, including transfer losses. If the vacuum space of the super-insulated dewar is not property evacuated, the hold time will decrease quite noticeably. In addition, there is a nitrogen trap for cleaning the circulating He^3 that requires daily filling. Detailed procedures for operating the refrigerator are in Appendix [B], originally recorded by S. K. Dutta.

Each stage of the dilution unit has a calibrated resistance thermometer. These resistances are read using a four-wire measurement, controlled by a Picowatt AVS-47 resistance bridge [83]. (see Table 5.1 for a list of the equipment) A RuO_2 thermometer

Table 5.1: List of the commercial electronics I used in my experiments.

Function	Instrument
I_f, I	Agilent 33120A Arbitrary Waveform Generator (AWG), Opt. 001
Master Clock	Dynatech Nevada Exact 628 Function Generator
Timer	Stanford Research Systems SR620 Universal Time Interval Counter Opt. 01
Pulse Generator	Stanford Research Systems DG 535 Digital Delay Generator, Opt. 01
$I_{\mu w}$	(1)Hewlett-Packard 83731B Synthesized Signal Generator (2)Hewlett-Packard 83732B Opt. 1E1, 1E2, 1E5, 1E8, 1E9, 800
GPIB	National Instruments PCI-GPIB
DAC/ADC	National Instruments PCI-6110 Data Acquisition Card & BNC-2110 BNC Connector Block
Temperature	Picowatt AVS-47 resistance bridge

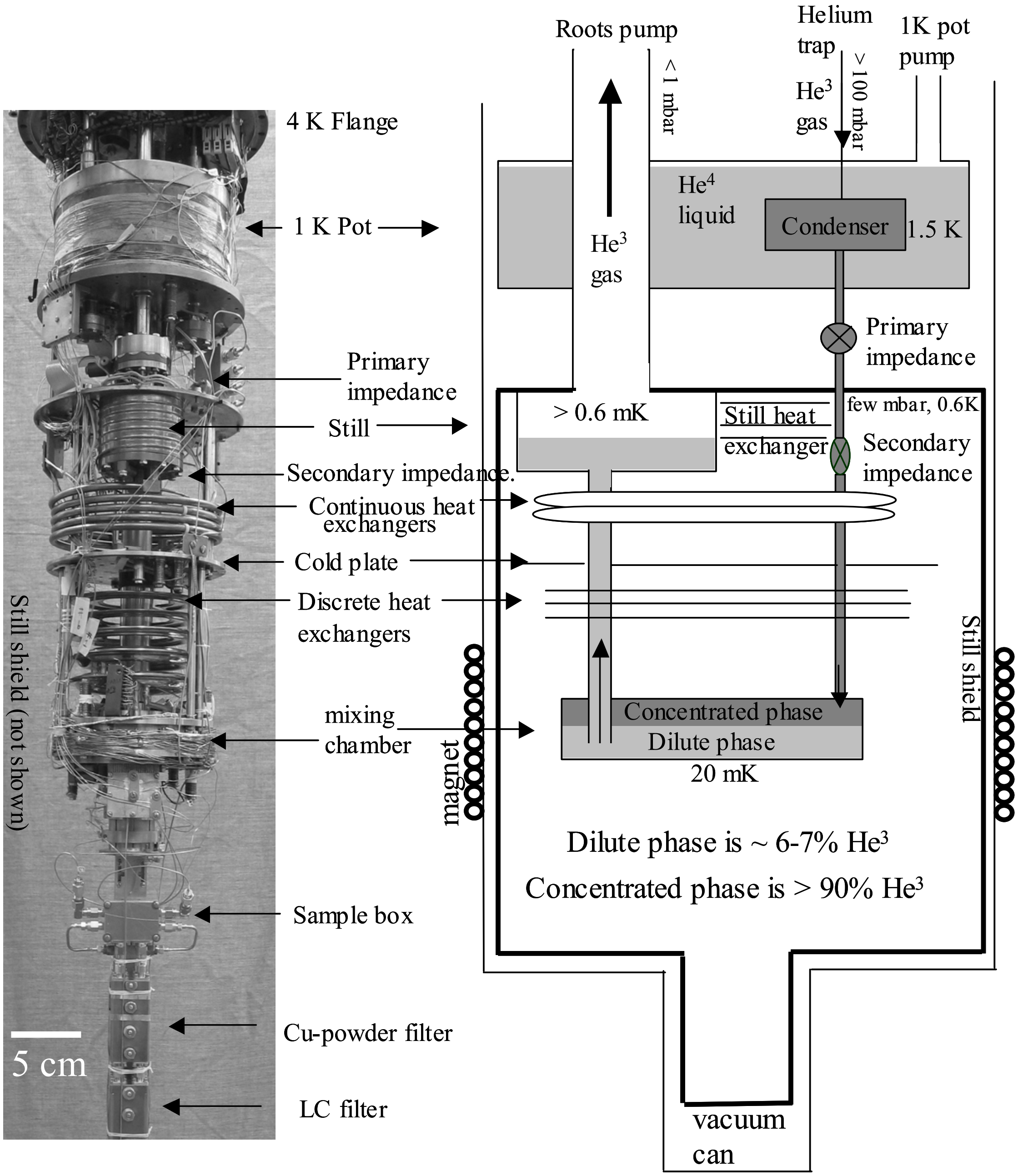

Figure 5.1: Photograph of Model 200 TLE Dilution Refrigerator by Oxford Instruments with LC and copper powder filters. Illustration on the right highlights the main section of the refrigerator and shows the path the helium mixture takes through the various stages.

labeled R7 gives the mixing chamber temperature. The bridge measures the resistance in ohms, which is converted to temperature T in kelvin using [37]

$$\ln(T) = -7.98 + 53.2/\ln(R) + 354\ln(R)/R\,. \tag{5.1}$$

A superconducting magnet surrounds the vacuum can and is used to generate a field parallel to the junction, if needed. The magnet was built by Cryo-magnetics [84] using twisted multifilamentary NbTi in a copper matrix. The field to current ratio is 111.3 gauss/A. Operating instructions for the superconducting magnet are given in Appendix B.

The dewar is surrounded by a room temperature μ-metal shield and the entire set-up is fixed to an xyz vibration isolation table. The μ-metal shield and dewar can be lowered through a hole to the floor below, where the rotary and roots pumps and the power panel are located. The dilution unit, table, shield and some electronics are located in a screened room built by Universal Shielding Corporation [85] in the basement of the Physics building.

5.2 Wiring and Filters

Each SQUID required four lines: for the flux bias, current bias, voltage readout, and for applying microwaves or pulses. In addition, I used a common ground configuration with the ground pad of the device wire-bonded to the sample box, which was anchored to the refrigerator. Each of these lines had its own requirements and considerations for optimal performance. Figure 5.2 shows an overview of the experimental setup and Fig. 5.3 shows the wiring for the lines.

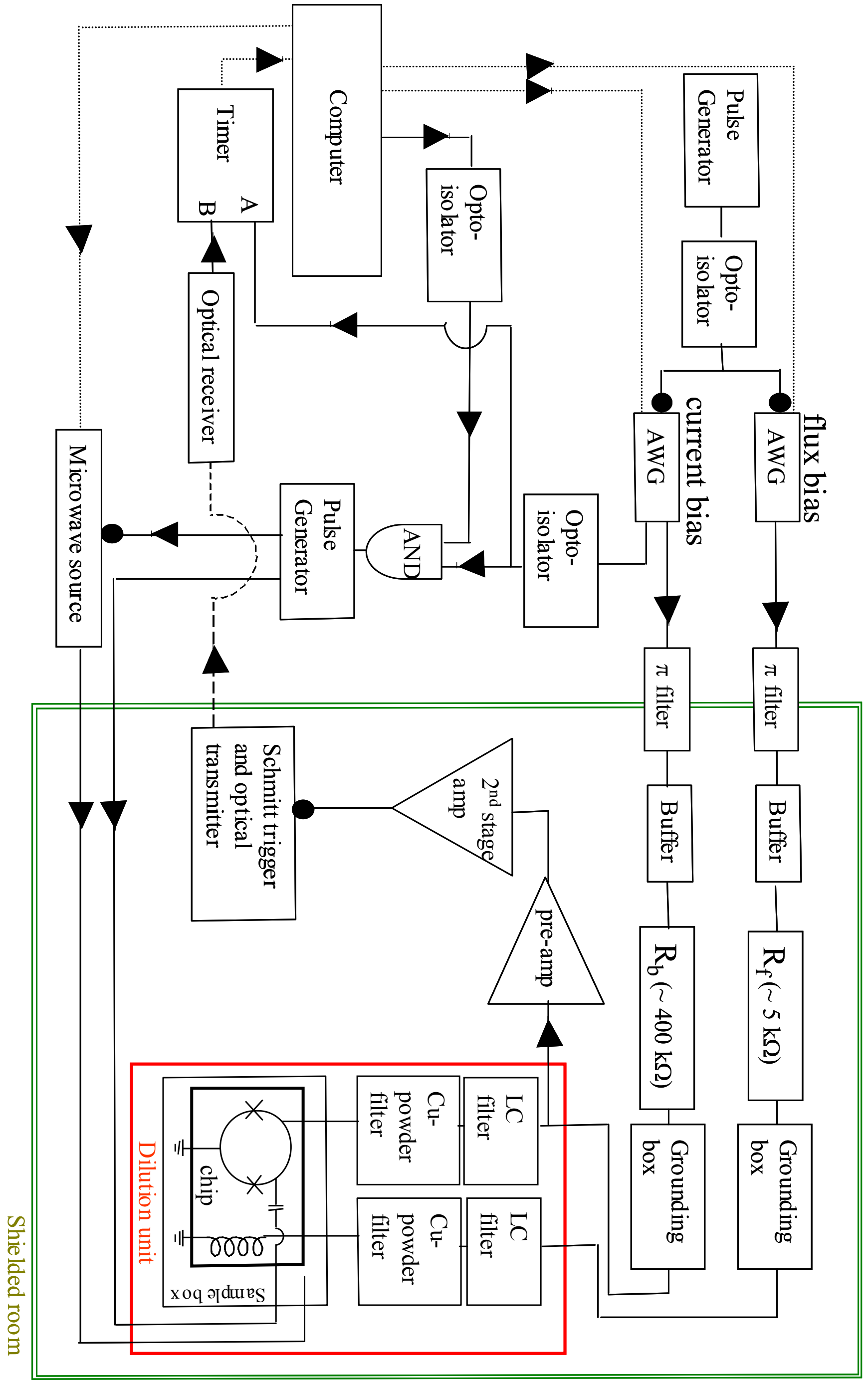

Figure 5.2: Overview of experimental set-up for DS_{3A} and DS_{4B}. The filled circles represent a trigger and the arrows show the direction of current. The opto-isolators and all of the electronics inside the screen room were battery powered.

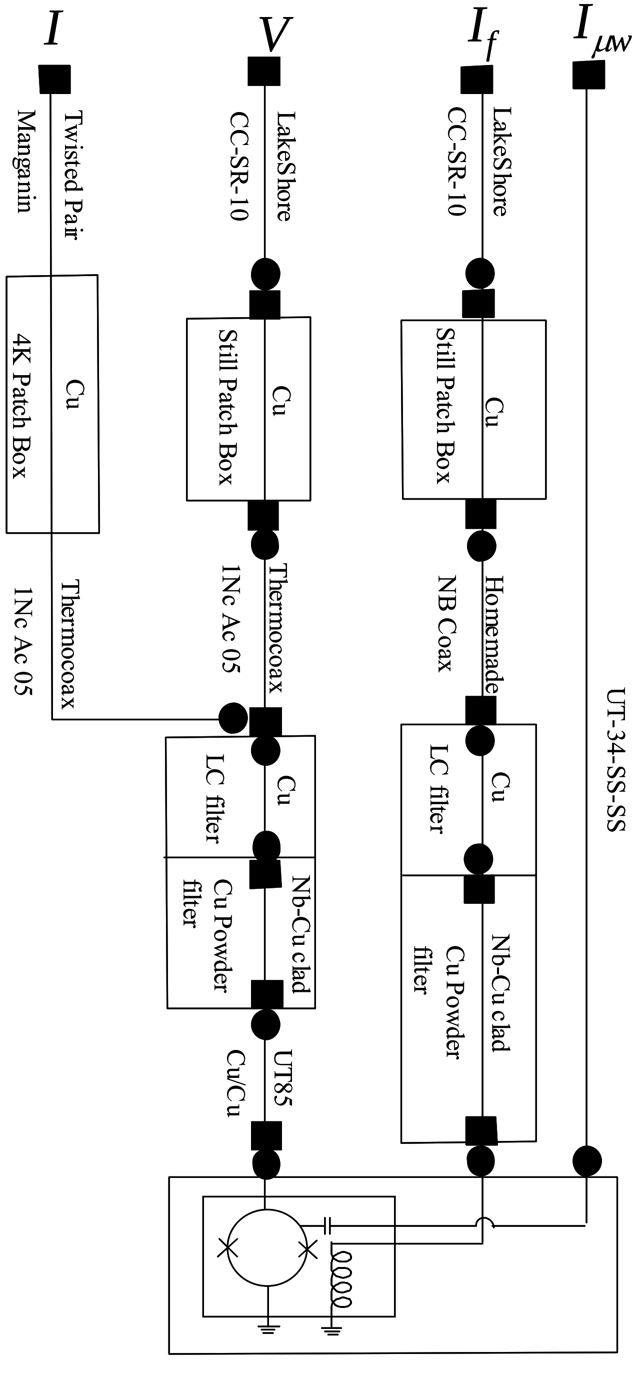

Figure 5.3: Schematic of refrigerator wiring. Circles represent male SMA connectors and the squares represent female connectors. For devices DS$_{2A}$, DS$_{2B}$, DS$_{3A}$ and DS$_{4B}$ these wires were doubled to allow for two dc SQUIDs to be operated simultaneously.

For each line, careful consideration must be given to how noise currents generated at room temperature propagate to the sample at 25 mK. Also, thermal shorts can ruin the performance of the refrigerator; wires with high thermal conductivity cannot be used to connect stages that are at different temperatures.

5.2.1 Current Bias Line

The current bias line is used to apply low frequency μA currents to the SQUID. We require that GHz signals be heavily filtered, since otherwise they could excite transitions in the qubit. In fact, all frequencies must be heavily filtered as mentioned in Chapter 3. To generate the current, an Agilent 33120A Arbitrary Waveform Generator (AWG) was used to generate a voltage ramp that was sent to a π-filter in the screen room wall, with a roll-off frequency of 20 kHz. The signal was then sent to a buffer (AMP03 differential amplifier) inside the screened room [see Fig. 5.2]. The buffer serves to disconnect the ground at the AWG, from the ground inside the refrigerator, which is found through multiple vacuum connections [27]. The buffer removes the pick-up loop that would be created by having two ground connections from the top of the dilution unit to the screen room. After the buffer, the voltage was dropped across a bias resistor of order 100 kΩ (varied often for each device) to generate a current of order 10 μA. The current then passed through a grounding/switch box at the top of the refrigerator. The boxes were designed such that a switch connects the bias resistor to ground when closed. When open the connection to ground is cut and current is applied to the wiring connection at the top of the fridge. In ordinary operation, the current line is always connected; this prevents voltage spikes from occurring when the switch is opened and closed.

From the ground/switch box to the 4K-connection box, the bias line is a 40-inch long manganin wire. A schematic of the wiring for the lines inside the refrigerator is shown in Fig. 5.3. The manganin wires were done in twisted pairs, although only one wire was used, as the refrigerator itself was the current return line. The twisted manganin wires were inserted into Teflon tubing, with a Cu/Ni shield and run through a vacuum tube to the 4K-connector box mounted just above the 1K-pot. Manganin and Cu/Ni were chosen for their low thermal conductivity, since these span a temperature gradient of 296 K across 40 inches. Stainless steel has a lower conductivity, but is harder to bend and solder (it requires acid flux). The manganin wires are somewhat resistive, so that only low currents can be applied without causing significant heating; typically less than 30 μA.

From the 4K-connection box to the mixing chamber, the current was carried on a 40-inch long Thermocoax cable (type 1NcAc) [86,87]. The Thermocoax cable has a stainless steel (type 304L) jacket with an outer diameter of 0.5 mm and an inner diameter of 0.35 mm. The central wire is a NiCr (80/20) alloy with an outer diameter of 0.17 mm and is surrounded by a dielectric of highly compacted MgO. The Thermocoax has a dc resistance of 50 Ω/m and 6.9 Ω/m for the inner conductor and the jacket, respectively, a capacitance of ≈ 490 pF/m and an inductance of ≈ 0.14 μH/m. Besides the low thermal conductivity of the stainless steel jacket, Thermocoax was chosen for its large attenuation at microwave frequencies [87]. The attenuation varies from 99 dB/m at 5 GHz to 140 dB/m at 10 GHz.

The Thermocoax ended at the mixing chamber state at an SMA connecter, where it joined the voltage readout line. Connecting the Thermocoax to the SMA connector requires first fluxing, and tinning an inch of the Thermocoax, then filing down the end of the outer connector (steel shield), and carefully breaking it off. After cleaning the NiCr wire and using "hard-core" flux to tin it (without shorting the conductors together), the SMA connector can be attached. In buying SMA connectors one should be careful to always get close-capture center-pin connectors (CC) [88]. Push-pin connectors were originally bought and later removed from the LC filters because they occasionally opened up during cool down.

The SMA connector was attached to an LC filter box, that was mounted on the mixing chamber [see Fig. 5.4(a)]. In the box, a copper wire (for thermal contact) connected to a 3.3 μH-100 pF-3.3 μH T-filter [36], which gave a 3 dB point of about 10 MHz. An LC filter was used instead of an RC filter to prevent heating associated with resistors. The current then passed through SMA connectors to copper-powder filters. From there, UT85 Cu/Cu wires were used to connect to the sample box. The copper-powder filters [89,90] were built based on the design presented in ref. [89]; a 50-50 mix of Stycast and 200 mesh copper powder was cast into a cylindrical core, and a signal wire of 3 mil Nb with a Cu cladding was wound around the core. For the copper powder filters, Cu clad Nb wire was used since Nb becomes a superconductor below 9 K. This ensured no heating in the wire even though the wire was about a meter long wrapped around the core.

All together, the filtering on the bias line gave an attenuation of over 200 dB at 5 GHz. Unfortunately, at lower frequencies the performance was not nearly as good.

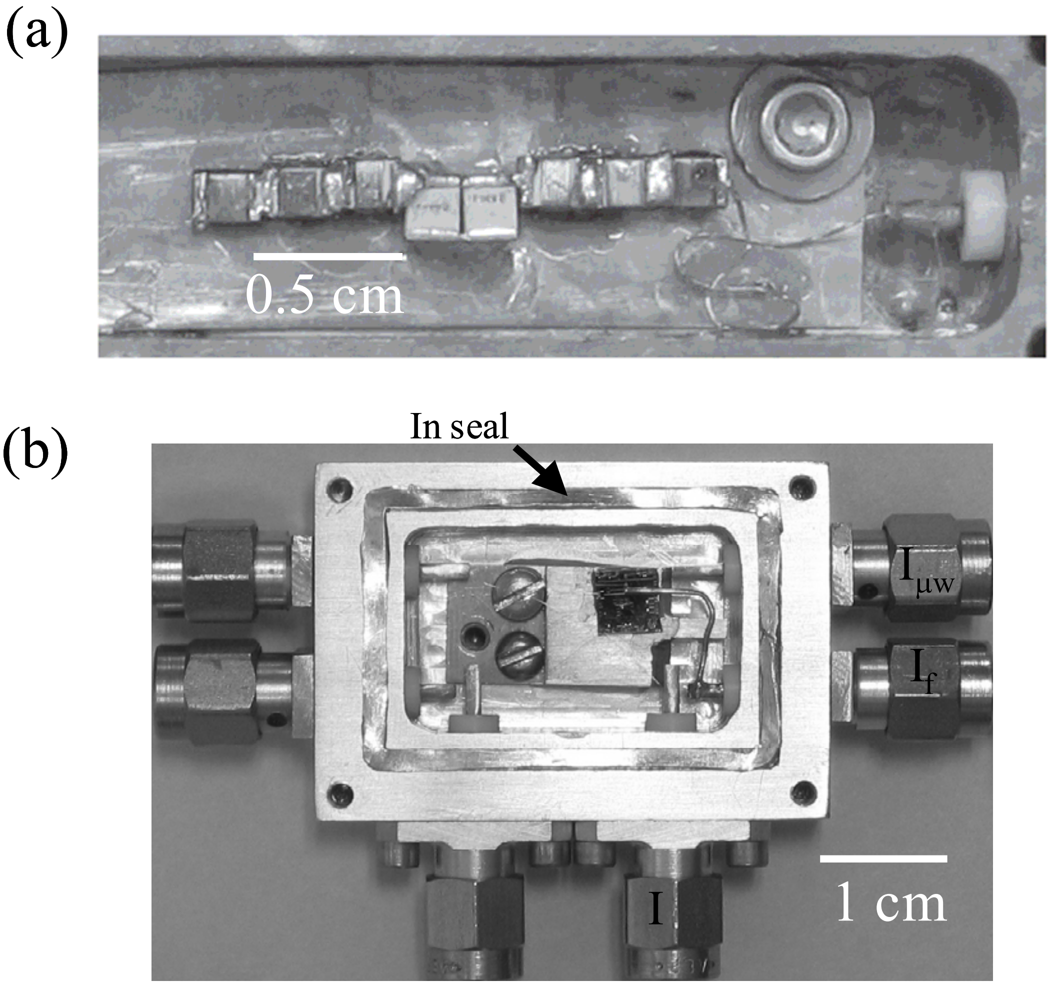

Figure 5.4: LC filter and sample box. (a) The discrete LC filter is mounted in a copper box and has a cut-off frequency of around 10 MHz. (b) The aluminum sample box used for devices DS_{2A}, DS_{2B}, DS_{3A} and DS_{4B}. The copper mounting plate under the chip was replaced with an identical aluminum one for devices DS_{3A} and DS_{4B}.

Several resonances existed in the bias filters at 1-10 MHz and the LC filter and copper powder filter only gave –13 dB of attenuation at 100 kHz when terminated with a 10 Ω resistor [37]; this does not include the attenuation due to the filters at the screen room wall.

5.2.2 Flux Line

The flux line is used to apply low frequency flux to the SQUID. We again require broadband filtering, but here we must be more careful of heating because the currents on the line can be as high as a few mA. For this line, an Agilent 33120A Arbitrary Waveform Generator (AWG) was used to generate voltage that was sent to a π-section filter in the screen room wall (see Fig. 5.2). The voltage was then sent to a battery-powered buffer amplifier and a bias resistor of roughly 5 kΩ. The current was then passed through a grounding/switch box to wires at the top of the refrigerator (see Fig. 5.3).

From the top, the flux line was LakeShore CC-SR-10 coax [91] that connected to a patch box on the still plate. Manganin was not used due to its dc resistance, which would cause significant heating with mA currents. LakeShore CC-SR-10 coax uses a silver-plated copper-weld steel center-conductor with a thermal conductivity of about 0.016 W/(cm • K) at 4.2 K and a low dc resistance. The center conductor is copper-weld steel, which is used for its price and low thermal conductivity. The current will flow on the silver plate surrounding the copper-weld steel. The outer conductor is stainless steel, again chosen for its low thermal conductivity. The line provides 14 dB and 20 dB of attenuation at frequencies of 5 GHz and 10 GHz, respectively. The patch box was used to thermally sink the line to the still, which has a relatively high cooling power. Inside the patch box the line was either niobium-clad copper, or copper with an enamel shield, that was GE varnished to the copper patch box. Formvar shielding on the copper wire has a reputation of degrading over time [92].

From the patch box to the SMA-LC filters, the flux line was a homemade coax, consisting of niobium wire threaded through Teflon tubing that was then inserted into a stainless steel tube. Since this line was for low frequencies, impedance matching was not a concern. From the SMA-LC filters the line was passed through copper-powder filters to the sample box.

5.2.3 Voltage Readout Line

For the voltage readout line, I also used LakeShore CC-SR-10 from a grounding/switch box to the still patch box. Here I needed low resistance on the line to minimize Nyquist noise voltages, thereby ensuring a clean signal when the junction switches [36]. Thus manganin would not work. At the patch box the line was thermally anchored, similar to the flux line. From the patch box to the SMA on the LC filter, I used Thermocoax, as in the current bias line.

From the LC filter to the junction, one line serves as the common voltage readout and current bias line. Ideally, from the LC filters to the device, the wires are superconducting, and so we can obtain a 3-wire measurement, or something very close to it. A 4-wire is not possible without dedicated return lines and all of my ground lines returned through the metal tubes of the refrigerator itself.

5.2.4 Microwave Line

The microwave line I used for driving and pulsing the qubit was connected from the microwave source, an HP 83732B, to SMA connectors in the screen room wall. From the wall, the line connects to a single UT-34-SS-SS semi-rigid coax at the top of the refrigerator, which then carriers the microwaves to the sample box. Since there was a direct connection from 300 K to the sample box, stainless steel coaxial lines were used. The outer stainless steel conductor was directly clamped to the refrigerator at multiple stages for cooling.

5.2.5 Sample Box

The aluminum sample box used for samples DS_{2A}, DS_{2B}, DS_{3A} and DS_{4B} is shown in Fig. 5.4(b) with the cover removed. SMA connectors (coaxicom 3214-1) are attached outside the box and the center pin inside the box was sanded down to provide a flat surface to wire bond to. This was not an ideal set-up. The SMA connectors are stainless steel plated with gold. The stainless steel was magnetic and not a superconductor. Magnetic and non-superconducting materials should remain as far from the SQUIDs as possible. Another experiment in our lab ran into serious problems when magnetic materials were located near the junction; they suppressed the critical currents of the junctions [92].

The chip was attached to a plate in the sample box using GE varnish. During runs DS_1 and DS_2 the sample was silver painted to a copper plate, to help cool the sample. However, having a normal metal, such as gold, silver or copper, under the junction is a bad idea since Johnson noise current can add significant flux noise to the SQUID loop. For devices DS_3 and DS_4, the copper plate was remade in aluminum and silver paint was not used. The SMA pins inside the sample box were connected to the sample pads using aluminum wire bonds. The wire bonds from the pins to the sample pads ranged in size from approximately 0.5 cm to 1.5 cm, depending on the positioning of the sample. The ground pads on the chip were wire-bonded to the aluminum plate. In creating strong wire bonds the main factor is the cleanliness of the SMA pins. I got good results by gently filing and sanding the pins and then cleaning with acetone and isopropanol before wiring bonding. The box was closed by 4 screws, which clamped an aluminum plate to the top. We used an indium gasket to provide a good superconducting joint between the box and cover to improve the magnetic shielding.

5.3 Instrumentation

Figure 5.2 shows a block diagram of the electrical setup used to control and measure the qubits. An experimental trial was initiated by using a Dynatech Exact Model 628 to generate a pulse at a repetition rate of 100-500 Hz. The pulse passed through an opto-isolator to trigger all of the HP 33120A AWGs used in the experiment. Opto-isolators were used to break electrical contacts, preventing ground loops. The AWGs were configured from a PC for burst mode, single trigger, and arbitrary waveform. The command for the desired waveform was generated using a Labview program and sent to the AWG via a GPIB interface. The outputs of each AWG went to the screen room wall, where the wall filters could be used if desired. The SYNC front panel output of the AWG passed through another opto-isolator to input A of an SR620 timer. Input A's trigger, and all others, were set at the maximum slope of the signal. The AWG rear-panel input triggers have a 25 ns jitter time, so the AWG that the qubit is most sensitive to should be used to start the timer.

If microwaves or pulses were desired, input A was also attached to an and gate (see Fig. 5.2). It performed an and operation on input A and an opto-isolated 5V pulse from the computer when a test with microwaves/pulses was required. The and-gate output was sent to a DG535 pulse generator. Pulses from the DG535 were used to trigger the microwaves from the HP83732B, using its external trigger as a control, and to send pulses directly to the qubit. In sending pulses to the microwave source, a TTL pulse with HIGH Z load seemed to work best. Pulses were sent to the qubit with a high Z load with a variable output of 0.10 V to 0.70 V. Attenuators were placed right before the signal reached the screen room wall. This way I could attenuate the output pulse further if I needed to. When both microwaves and pulses were required, I connected the pulse output to the qubit's microwave line and used the auxiliary microwave line (see Fig. 5.2) for the microwaves. A microwave combiner would be needed to simultaneously control two qubits.

5.4 Detection of Switching

When a dc SQUID switches to the finite voltage state a voltage of 2.8 mV will be generated across a niobium junction and 400 μV across an aluminum junction. This voltage must propagate to the top of the fridge before it can be detected and used to determine when the SQUID switched. At the top of the refrigerator, the voltage was amplified using a common-source JFET inverting amplifier, consisting of sixteen

2SK117 transistors wired in parallel [36]. This amplifier has a gain of 40, a bandwidth of about 2 MHz and a voltage noise of less than $0.3\,nV/\sqrt{Hz}$. All electronics in the screen room were powered from ultra-low noise power supplies inside the screen room. This amplifier was followed with an AD829 op-amp inverting amplifier, with a gain of 50 above 10 kHz. This amplifier rolls off above 1 MHz and has a voltage noise of about $4.0\,nV/\sqrt{Hz}$. The 10 kHz low frequency cutoff is set from a high pass filter created with an additional AD829. By filtering out low frequencies, the 5 V offset from the JFET is removed as well as the voltage from the drop along the bias lines. The schematics and properties of these amplifiers are available in ref [36].

The switching signal was converted to an optical pulse using a Schmitt trigger made from a high speed CLC420 op-amp. When the signal from the op-amp reaches a certain threshold it produces a pulse that drives an LED, which is coupled to an optical fiber. The fiber passed through the screen room and the signal was converted to a TTL-compatible pulse using a second CLC420. This TTL pulse was then sent to input B of the timer and the time between receipt of pulses of A (which was triggered at the start) and B (which triggered when a switch was detected) was recorded and sent via GPIB to a PC running a custom LABview program.

The custom amplifiers improved the timing resolution substantially. With the amplifiers, experiments on a 130 μA critical current Nb junction showed a switching slope of 10 mV/μs [37]. Based on 720 μV rms of noise, this gave a resolution of under 100 ps. For a critical current of less than 20 μA the switching slope begins to decrease. For a Nb SQUID, the slope ranged from 5 to 10 mV/μs. An aluminum SQUID with critical currents of 1.5 μA and 10 μA had a maximum slope of approximately 1.1 mV/μs, which would have significantly degraded the timing resolution. Fortunately, for pulse measurements, which I will discuss in Chapter 7, sub-microsecond resolution in the output voltage becomes completely unnecessary. The only important factor is the timing between the applied current measurement pulse and the microwave source, both of which are externally controlled, as discussed in Chapter 7.

The current at which the switch occurred was determined by calibrating the bias current and flux current versus time. The voltage across a room temperature resistor was amplified with a Stanford Research Systems SR560 in differential mode and then recorded versus time using the analog-to-digital converter on the computer's PCI-6110 data acquisition board. A reference pulse to define $t = 0$ was simultaneously recorded from the optoisolated sync from the bias waveform generator.

5.5 Summary

In this chapter, I described the experimental apparatus used for my measurements, including the dilution refrigerator, wiring and instrumentation. The wiring inside the refrigerator must be carefully constructed, taking into account the current and voltage requirements for each of the different lines. Thermal considerations are also crucial to prevent the wiring from carrying heat to the mixing chamber. The sensitivity of the measurements and low noise requirements demand a careful design of the electronics, and detailed consideration of the current sources, timers and triggering.

Chapter 6

Flux Shaking and dc SQUID Control

This chapter describes how I calibrated my measurements, determined the device parameters and operated the SQUIDs as qubits. To determine the device parameters, I measured the flux and bias currents that caused the SQUID to switch to a new flux state or into the voltage state; these plots are referred to as I-Φ curves. The I-Φ curves are essential for finding some of the key experimental parameters of a device. The I-Φ curves also provide a graphical representation of how to optimally operate the dc SQUID as a Josephson junction phase qubit. The plots were also helpful in preparing the SQUID in a specific flux state using flux shaking.

6.1 Device Calibration and I-Φ Curves

As shown in Chapter 2 [see Eq. (2.18)], the flux-phase relation for two Josephson junctions in a superconducting loop is

$$\gamma_1 - \gamma_2 = 2\pi \Phi / \Phi_0 = 2\pi \Phi_a / \Phi_0 + 2\pi I_1 L_1 / \Phi_0 - 2\pi I_2 L_2 / \Phi_0 , \quad (6.1)$$

where Φ is the total flux in the SQUID. For static currents and fluxes, I can also write $I_1 + I_2 = I$, $I_2 = I_{02} \sin(\gamma_2)$ and $I_1 = I_{01} \sin(\gamma_1)$. For a particular I and Φ_a, each different solution to these equations corresponds to the system in a different flux state. The equations determine the bias current I and applied flux Φ_a at which the device will switch for a given initial flux state. A switch to the voltage state or to a different flux state will occur when the current through either of the junctions in the dc SQUID exceeds its critical current. An initial flux state n_f will act something like $n_f \Phi_0$ of applied flux, and induce a circulating current in the loop, *i.e.* if $n_f \Phi_0$ of applied flux does not cause one of the junctions to exceed its critical current, that flux state is stable. In Chapters 2 and 4, I noted that our dc SQUIDs tend to have a large $\beta \approx L(I_{01} + I_{02}) / \Phi_0$ and therefore a tendency to have many stable flux states, [see Eq. (2.22)].

Figure 6.1 shows part of the I-Φ curve calculated for an asymmetric dc SQUID with $I_{01} = 3.5 \mu A$, $I_{02} = 1 \mu A$, $L_1 = 2.3 nH$, $L_2 = 0.4 nH$ and $M = 71.4 pH$. The characteristics are periodic in the applied flux Φ_a, and only a few flux states are shown. Notice that the plot consists of five overlapping regions. Here I have just shown curves for trapped flux of 0, $\pm \Phi_0$ and $\pm 2\Phi_0$. Graphically, a switch will happen if I and Φ_a are changed such that the new values of I and Φ_a are no longer inside the loop corresponding to the initial flux state. At $I = 0$ and $I_f M = \Phi_a = 0$, three flux states are stable; this point is inside the three black curves, while states corresponding to the gray curves are not stable. Whether the device switches to the voltage state or simply switches to a new flux states depends on the bias current at which the switch occurs and the critical currents. For example, at $I = 0$ the device will never switch to the voltage state; Φ_a only rolls the SQUID potential in $(\gamma_1 - \gamma_2)/\sqrt{2}$ (as I discussed in Section 2.4 and later in 6.2). If the device switches to a new flux state it will switch to a stable one, *i.e.* one that encloses the bias current I and applied flux Φ_a values at the time of the switch. By fitting these curves to the experimental data the parameters (L_1, L_2, I_{01}, I_{02}) of a dc SQUID can be determined.

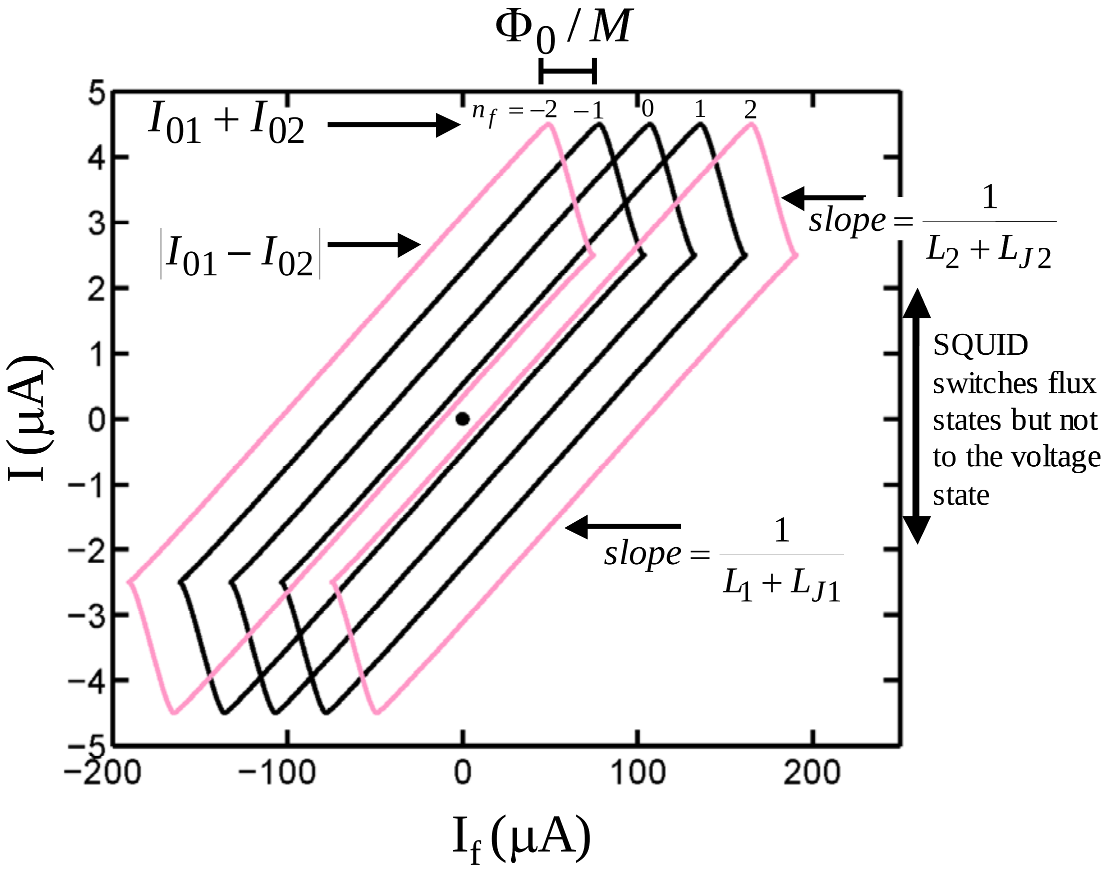

Figure 6.1: Calculated I-Φ curves showing five flux states $n_f = \pm 2, \pm 1, 0$ in an asymmetric dc SQUID. By measuring the I-Φ curves, the inductance and critical current of the SQUID can be determined, as well as the number of stable flux states. In this case at $I = 0\,\mu A$ and $I_f = \Phi_a / M = 0\,\mu A$, just three flux states are stable. This device has $I_{01} = 3.5\,\mu A$, $I_{02} = 1.0\,\mu A$, $L_1 = 2.3\,nH$, $L_2 = 0.4\,nH$ and $M = 71\,pH$.

The different sloped lines in Fig 6.1 correspond to which of the junctions switches first. For example, in Fig. 6.1, if the bias current is ramped at a constant applied flux, it is likely that a relatively shallow positive sloped branch will be crossed. This corresponds to the isolation junction J2 switching first. This makes sense considering the large asymmetry in the inductance of the two branches and the smaller critical current I_{02}; applied bias current mainly goes through J2. Complete control of the two junctions is possible by ramping the flux and bias current simultaneously. Equation (6.1) also implies that the equations are symmetric about negative currents as seen in Fig. 6.1.

Without rigorously fitting the data, a few parameters can be quickly estimated as shown in Fig. 6.1. Since $n_f \Phi_0$ acts like an applied flux, the mutual inductance can be determined by measuring the flux current ΔI_f necessary for the curve to repeat itself. Then I can use $M = \Phi_0 / \Delta I_f$. Also, the maximum possible switching current occurs where both junctions are carrying their critical current, *i.e.* $\max[I] = I_{01} + I_{02}$. This occurs where the two different sloped lines meet at the top. Similarly the other corner where the two slopes meet is given by $|I_{01} - I_{02}|$. In addition, the slopes of the branches of the I-Φ curve where J1 or J2 switches first are given by roughly $1/(L_2 + L_{J2})$ and $1/(L_1 + L_{J1})$, respectively. Unfortunately, the capacitance of the junctions cannot be determined from fitting I-Φ curves. Also, while the curves allow I_{01} and I_{02} to be extracted, the values are somewhat approximate. Fortunately, the capacitance and more accurate values for I_{01} and I_{02} can be obtained from spectroscopy (see Chapter 8).

6.1.1 Sample DS_2

Figure 6.2 shows an experimental I-Φ curve measured for device DS_{2A}. Each gray point corresponds to one switching event (I note that device DS_1 was calibrated before I joined the project and the results can be found in Ref. [36] and Ref. [37]). In the plot, I also show black curves on every other flux state. These curves are from fits with $I_{01} = 21.8\mu A$, $I_{02} = 2.5\mu A$, $L_1 = 3.3nH$, $L_2 = 0.01nH$ and $M = 71.436\,pH$ (these are not that fits used to determine the parameters given in Table 4.3). The fits are somewhat coarse since the lower bend at $I = I_{01} - I_{02}$ is not visible. L_2 is especially difficult to determine from the fits since it is so small, especially if I_{02} is not well known. In fact, for all of the devices I found the value of L_2 could vary by 100% and still produce a reasonable fit to the I-Φ curve.

It is important to understand that the flux states shown in Fig. 6.2(a) are not stable at $I = 0\,\mu A$ and $I_f = \Phi_a / M = 0\,\mu A$. This can be seen by extending the calculation over a larger range of current and flux, [see Fig. 6.2(b)]. Note that if the bias current is ramped at a fixed Φ_a, initial stable flux states become unstable and the SQUID must change to a new flux state, without switching to the voltage state. Six of these I-Φ curves were taken for this device to find the mutual inductance for each of the qubits and each of the flux and bias lines as given in Eq. (4.17). I will ignore the mutual inductance from the qubit's bias line. I also note that the bias current I was generally negatively ramped, but for simplicity I will always plot it positively.

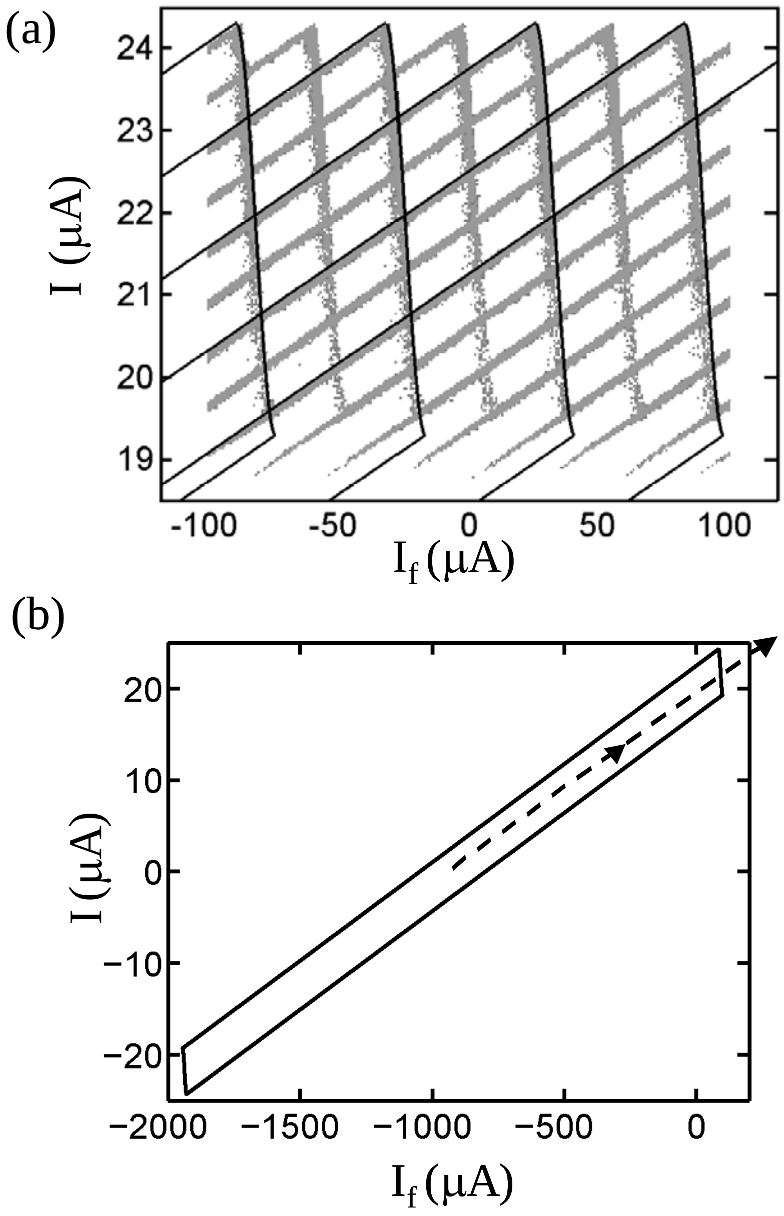

Figure 6.2: (a) Experimental I-Φ curve for device DS_{2A} and a fit. Each gray point corresponds to the location of a switch and the black curves are a fit to the data. Since the system will always switch before the true critical current is reached, a region defined by the closed black curve encloses the corresponding gray points. (b) Schematic of the entire I-Φ curve for a single flux state and a current trajectory such that the device is optimized as a qubit.

6.1.2 Samples DS_3 and DS_4

Figure 6.3 shows experimental I-Φ curves and best-fit curves for device DS_{3A}. In this device the qubit junction had a substantially smaller area than the isolation junction, opposite from the previously tested SQUIDs. Three flux states are fit here with $I_{01} = 1.22\,\mu A$, $I_{02} = 8.625\,\mu A$, $L_1 = 1.05\,nH$, $L_2 = 0.01\,nH$ and $M = 71.436\,pH$. The light gray points represent experimental values where the SQUID switched to the voltage state, while the open circles are points where the system only switched flux states (not to the voltage state). These flux-switch points were found by (a) initializing the system into the initial flux state, (b) ramping the bias to a fixed point, (c) negatively pulsing the applied flux, and then (d-f) increasing the bias current (see Fig. 6.3). The circles represent the flux pulse amplitude (in I_f) and I for which the SQUID switched flux states 50% of the time. To determine whether a flux jump occurred, I ramped the bias current and monitored whether the SQUID switched at $I < 8\mu A$ (the flux state did not change) or $I > 8\mu A$ (the flux pulse made the SQUID switch flux states). This procedure allowed me to obtain a more accurate estimate of the SQUID parameters.

In chip DS_4, I performed rough experimental I-Φ curves for each of the qubits. For device DS_{4B}, I found $I_{01} \approx 1.2\,\mu A$, $I_{02} \approx 7.5\,\mu A$, $L_1 = 3\,nH$, $L_2 \approx 0.01\,nH$ and $M = 18\,pH$. These fit values were very close to those of DS_{3A}, except for the larger inductance L_1.

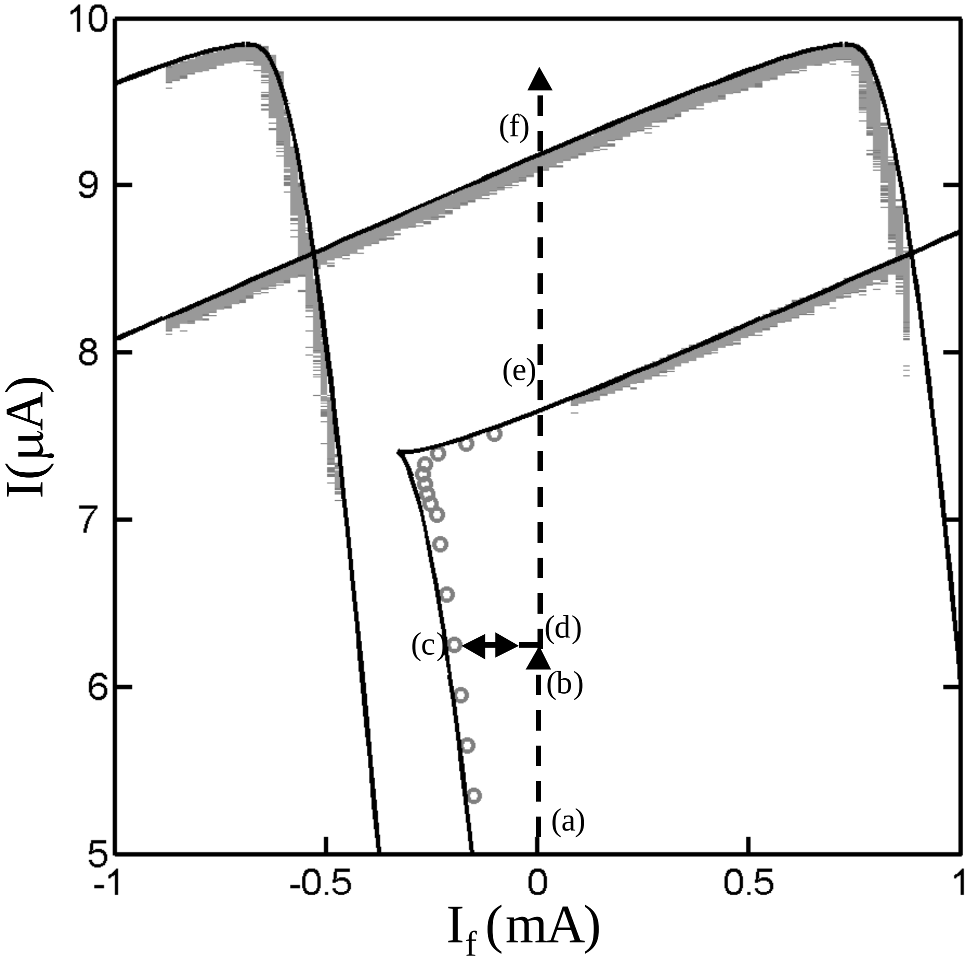

Figure 6.3: I-Φ curve for device DS_{3A}. The gray points correspond to where the system switched to the finite voltage state and the open circles represent the location where the system switched flux states during a flux current pulse. The solid black curves are a fit to the data. By following the switching curve below $|I_{02} - I_{01}|$ the fit parameters are substantially more accurate. The dashed line shows an example of a measurement trajectory to determine the circles. Starting at (a), the current I is increased to (b), a negative flux pulse quickly takes the system to (c), and then back to (d). The current I is then increased to (e). If the flux pulse did not cross the solid curve at (c), then the SQUID will switch at (e); otherwise it will switch at (f).

6.2 Flux Shaking

The dc SQUID phase qubit will generally have more than one stable flux state, and these states are not equivalent. In particular, at the same applied flux, each flux state has a different plasma frequency. For this reason the SQUID must always be initialized to the same flux state before it can be used as a qubit. Our approach to selecting one flux state out of the N_Φ possible states is an extension of Lefevre-Seguin's "forced-retrapping" technique [93]. Their technique involved applying an oscillating bias current I to a hysteretic SQUID with a maximum current that was somewhat less than $I_{01} + I_{02}$, the maximum critical current of the SQUID. If flux is trapped in the loop, a static circulating current will be present that adds current to one junction and subtracts it from the other. If the net current from the bias and trapped flux exceeds the critical current of one of the junctions, the device switches to the finite voltage state and then retraps into another flux state once I decreases below the retrapping current. By choosing the amplitude of I correctly, all of the flux states can be made unstable except for the state corresponding to zero trapped flux. If the SQUID is in an undesired state, than at each cycle it is forced to retrap into another allowed flux state. If the new state is the desired one, than it would be stable during the rest of the cycle and the SQUID would end up in the desired one. If the device did not reach the desired state during the cycle, then it would have another chance at the next cycle. Lefevre-Seguin *et al.* applied many current oscillations to ensure that the probability of reaching the selected state was near unity.

In our technique, instead of applying an oscillating current, I apply an oscillating flux to the SQUID [41]. By also applying a static flux, our "flux-shaking" technique allows me to choose *any* one of the allowed flux states. Moreover, the technique resets the flux state with minimal energy release since switching to the voltage state only occurs for extremely brief intervals. Energy considerations are important because we operate our qubits at $25\,mK$, and significant heating occurs when a junction is in the finite voltage state.

To gain insight into both techniques, I again consider the potential energy $U(\gamma_1, \gamma_2, I, \Phi_a)$. Figure 6.4 shows U for the simple case of a symmetric SQUID with $\beta = 5.3$, when $I = 0$ and $\Phi_a = 0$. There is a degeneracy due to the periodicity of the potential in the $(\gamma_1 + \gamma_2)/\sqrt{2}$-direction, and the physically distinct flux states occur at the minima of the wells with different $(\gamma_1 - \gamma_2)/\sqrt{2}$. In the current shaking technique, increasing the bias current tilts the potential in the $(\gamma_1 + \gamma_2)/\sqrt{2}$ direction. Wells of higher potential have larger $|(\gamma_1 - \gamma_2)/\sqrt{2}|$, and lower barrier heights, and thus become unstable at lower bias current. In the flux shaking technique, increasing the flux effectively tilts or shifts the potential in the $(\gamma_1 - \gamma_2)/\sqrt{2}$ direction, changing which flux state corresponds to the minimum potential energy. Again, wells corresponding to stable states can become unstable while previously unstable states can become stable; the total number of stable states will not change in the large β limit. I note that for $I = 0$, the potential, and thus the flux-shaking process, does not depend on the inductive asymmetry of the SQUID.

As mentioned above, if the SQUID is in a flux state that becomes unstable due to applied current or flux, there are two distinct options: The SQUID can re-trap in another stable well, producing a short-lived voltage (undetectable to us), or it can roll

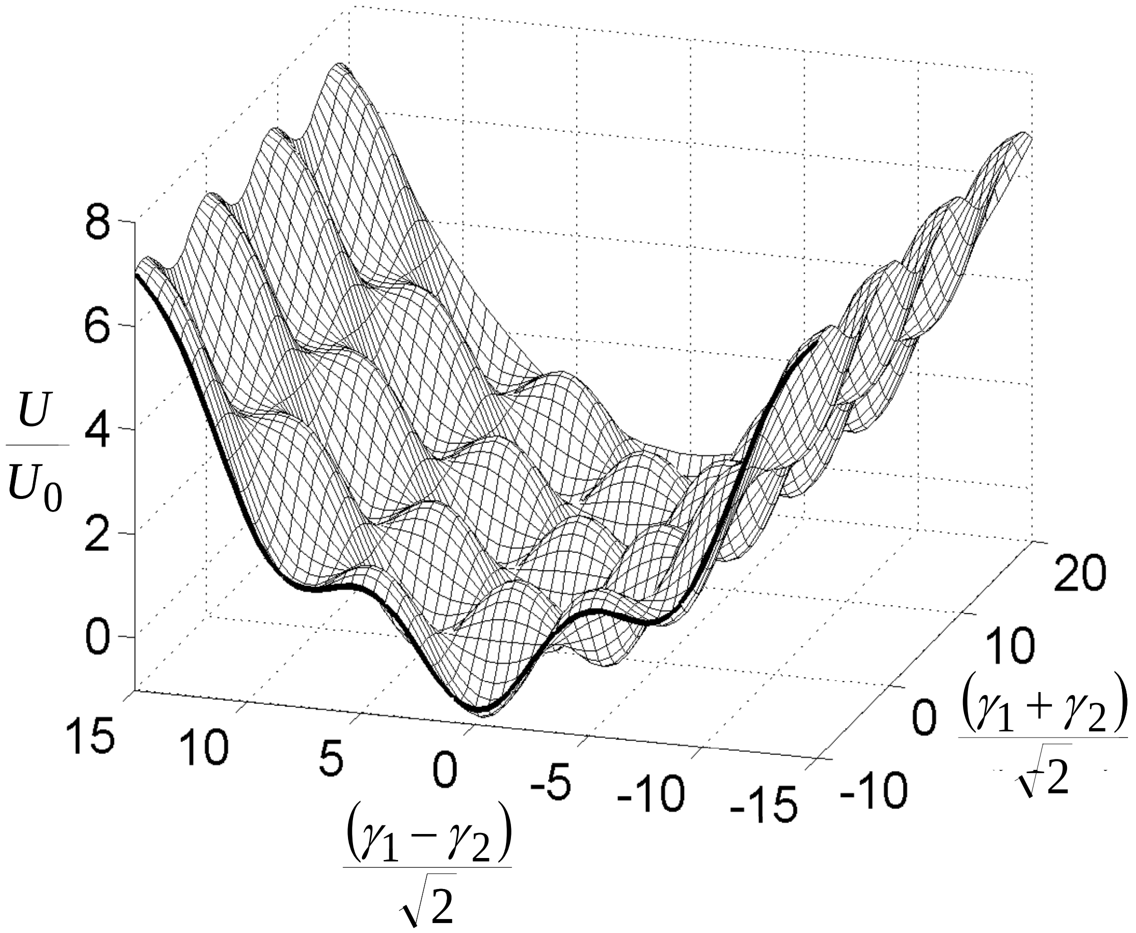

Figure 6.4: Normalized potential energy surface $U(\gamma_1,\gamma_2)/U_0$ for a symmetric dc SQUID with current $I=0$, $\Phi_a=0$, $\beta=5.3$ and $I_{01}=I_{02}$. Applied flux Φ_a will tilt the potential in the $(\gamma_1-\gamma_2)/\sqrt{2}$ direction forcing the system to switch if it is in a well that becomes unstable. If the SQUID switches with $I=0$, it will quickly retrap into a new flux state.

continuously in the $(\gamma_1+\gamma_2)/\sqrt{2}$ direction, producing a steady measurable voltage, until the current through the junction drops below the retrapping current. If the system does switch to the voltage state, it stays there until the current falls below the retrapping current. On the other hand, if the system is in a potential well that becomes unstable due to a change in flux with $I=0$, it escapes and must always re-trap in another well, just releasing the difference in energy between the original and final state.

To choose just one flux state using the flux-shaking technique, I make all but the desired well unstable at some point during each flux oscillation. In this way if the SQUID is trapped in an undesired well, this well becomes unstable at some point in each cycle and the system will be forced to choose a new well. If it happens to retrap in the desired well, then it will be trapped there for the remainder of the oscillations since this one desired flux state is always stable. If the system lands in any other well, then during the next oscillation it will again be forced out and have to find a new flux state. Although the retrapping is random, the probability of being in the wrong well decreases exponentially with the number of oscillations; very low failure rates can be achieved with relatively few oscillations (50 to 100). Different flux states can be selected by applying an appropriate static flux so that the desired well has the lowest energy.

Before performing the initialization procedure, I determined the initial probability of finding the system in each flux state. To do this, I ramped the bias current and flux such that the qubit junction switched first and a minimal amount of bias current passed through the isolation junction, [see Fig. 6.2(b)], as I will describe in more detail below. This simultaneous sweep of current and flux was repeated every $5\,ms$ to build up a histogram of the bias current at which the junction switched to the voltage state. After each ramp, the current I and applied flux Φ_a were set to zero, forcing the system to re-trap randomly in an allowed flux state. By summing the counts in each peak of the histogram, I found the starting probability of being in each well. Figure 6.5(a) shows the initial histogram for device DS_1. There were about 10 states that had a significant occupation probability.

To set the system in a specific well using flux-shaking, I chose a number of oscillations N, flux offset, and flux oscillation amplitude. I then applied the flux at a fixed frequency of $44\,kHz$ until N oscillations were completed. I next ramped the bias current I and measured the current, at which the device switched (see Fig. 6.6 for sample waveforms for this procedure). I repeated this entire process to build up histograms for each set of conditions. Each amplitude, flux offset and number of oscillations produced a different histogram. For a specific range of amplitudes and offsets it is possible to make every well unstable at some point in the oscillation except one chosen desired well. Applying more oscillations in this case produces a steady increase in the probability p_{nf} of finding the SQUID in the desired flux state n_f [see Fig. 6.5(b-d)]. This somewhat awkward notation has been used to distinguish the probability in a flux state p_{nf} from the probability in an energy level p_n; thus p_{2f} is the probability of finding the SQUID in the $n_f = 2$ flux state. Increasing the amplitude too much results in no continuously stable flux state during the initialization process and no single peak develops an increasing probability. The offset value $\Delta\Phi_a$ of the oscillation determines which peak becomes heavily populated. In Fig 6.5(b-d) no flux offset was applied, and the $n_f = 0$ state was selected using flux oscillations with an

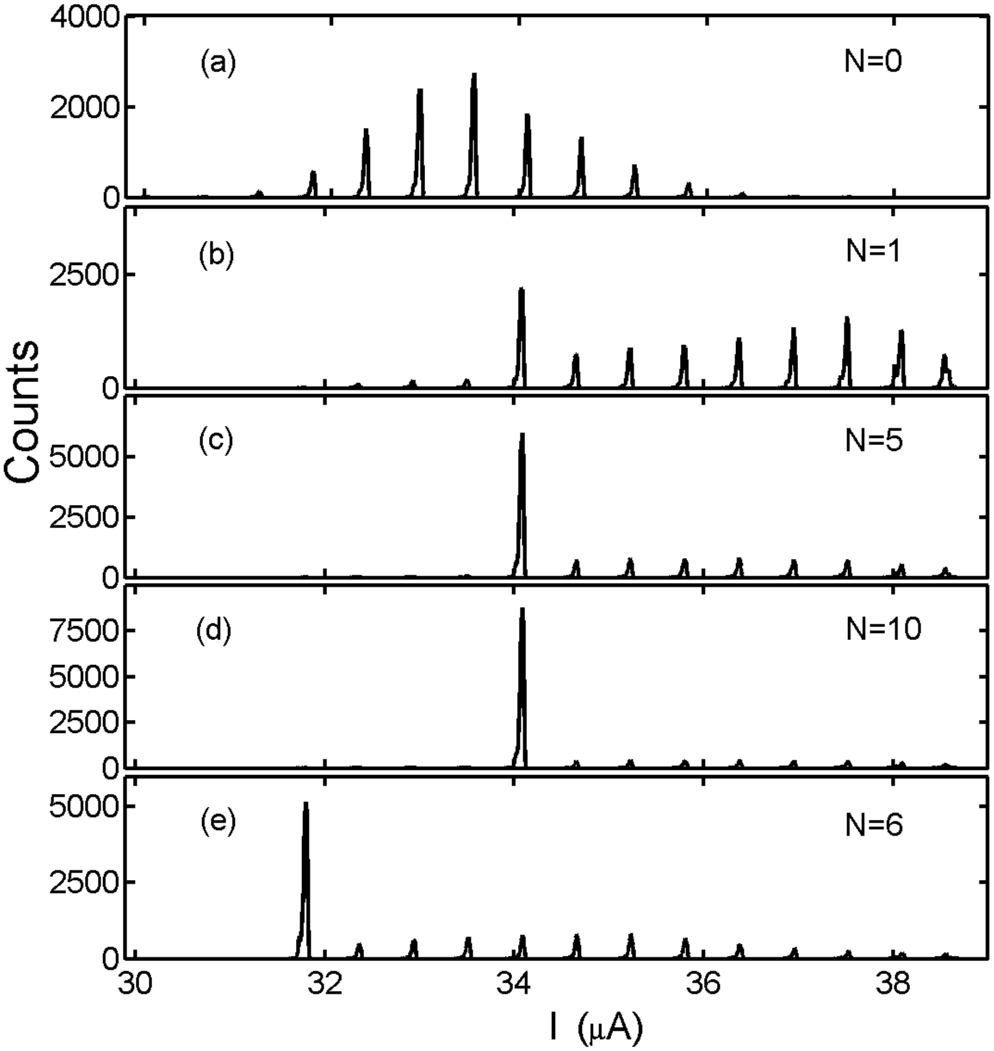

Figure 6.5: (a) Initial switching histogram, for device DS_1. (b) Switching histogram after $N = 1$ oscillations, (c) $N = 5$ oscillations, and (d) $N = 10$ oscillations of amplitude $7.4\Phi_0$ ($I_f = 0.3 mA$) at $44 kHz$. For b-d, no flux offset was applied and the $n_f = 0$ state was selected. (e) Isolating the $n_f = -4$ flux state using $N = 6$ oscillations of amplitude $7.4\Phi_0$, at $44 kHz$ and with a flux offset of $4.4\Phi_0$ ($I_f = 0.177 mA$).

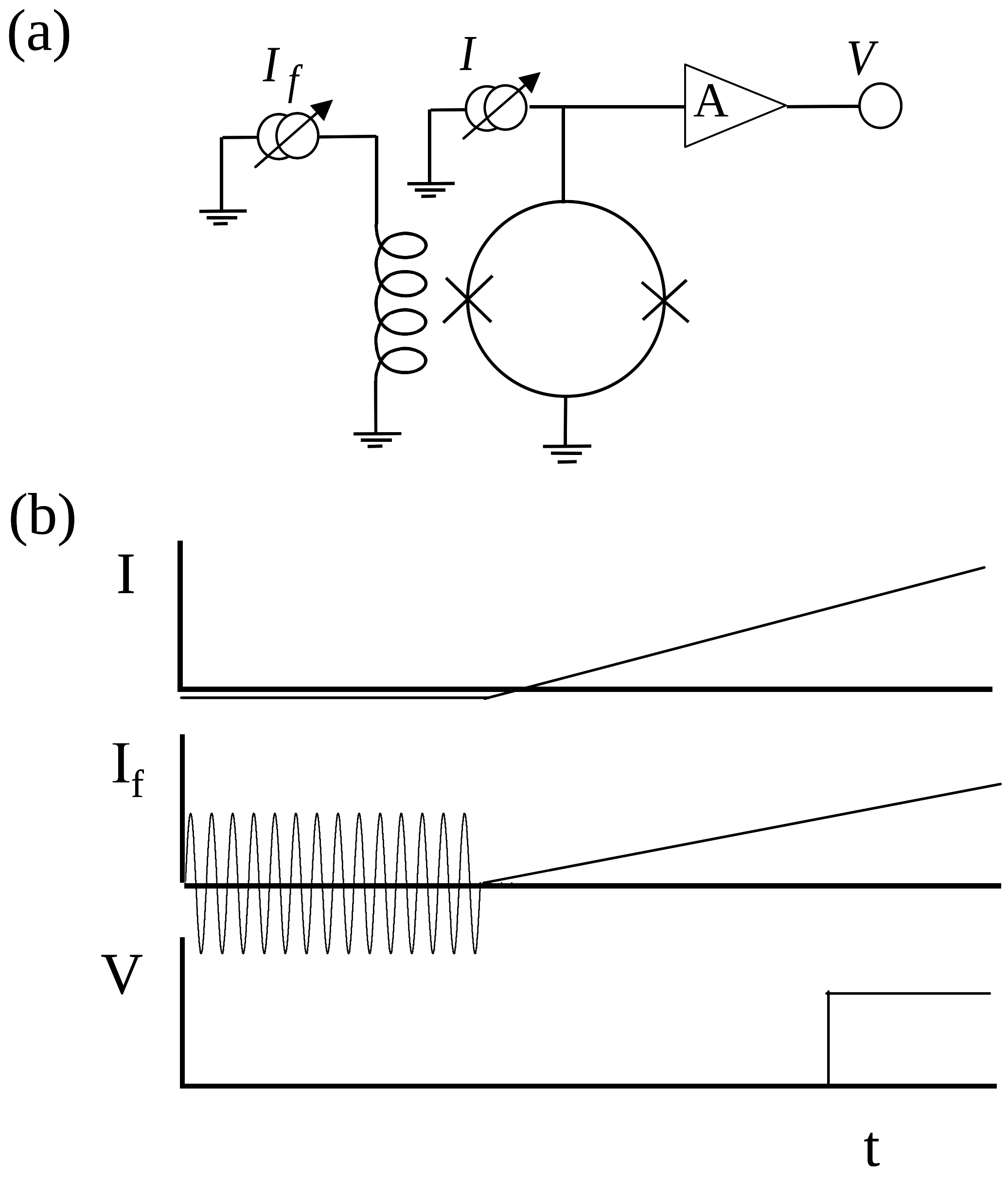

Figure 6.6: Schematic and waveforms used for flux shaking. (a) dc SQUID (b) I vs. t, I_f vs. t, and V vs. t for flux shaking a SQUID about the $n_f = 0$ flux state with $N = 14$. The bias current includes a small offset to ensure the SQUID re-traps after switching to the voltage state.

amplitude of $7.4\Phi_0$. In Fig. 6.5(e) I applied an offset of $4.4\Phi_0$ to select the $n_f = -4$ state.

I note that during flux shaking of DS$_1$, flux states appeared at bias currents of 38 and $38.5\,\mu A$ [see Fig. 6.5(b)], while no such states were evident in the original switching distribution [see Fig. 6.5(a)]. Evidently, these states are stable states of the system, but had a negligible probability of being occupied initially.

I also tested DS$_1$ when its critical current was not suppressed. In this case the critical current was $I_{01} \approx 108\,\mu A$, or about an order of magnitude higher, and I found 167 flux states. I found the initial probability of occupying the $n_f = 0$ well (corresponding to no circulating current) was $p_{0f} = 0.03$. Figure 6.7 shows that after 45 oscillations I could increase this to $p_{0f} = 0.493$.

To use such a device as a qubit, ultimately one will need to initialize the system with near unity probability. Figure 6.8 shows how the failure rate $q_{0f} = 1 - p_{0f}$ for selection of the $n_f = 0$ state falls with the number of oscillations for up to 50 oscillations. These oscillations were performed on device AL1 by H. Paik [68]. By 50 oscillations, the probability of being in the desired state, which is initially $p_{0f} = 0.13$, increases to $p_{0f} = 0.99996$. For this measurement we chose the oscillation frequency so that the entire initialization process always took $2.2\ m\sec$, independent of the number of oscillations; e.g. a frequency of $22.6\ kHz$ was used for 50 oscillations. As expected, the failure probability decreases exponentially with the number of oscillations. More oscillations are clearly possible; extrapolating the trend to 100 oscillations implies

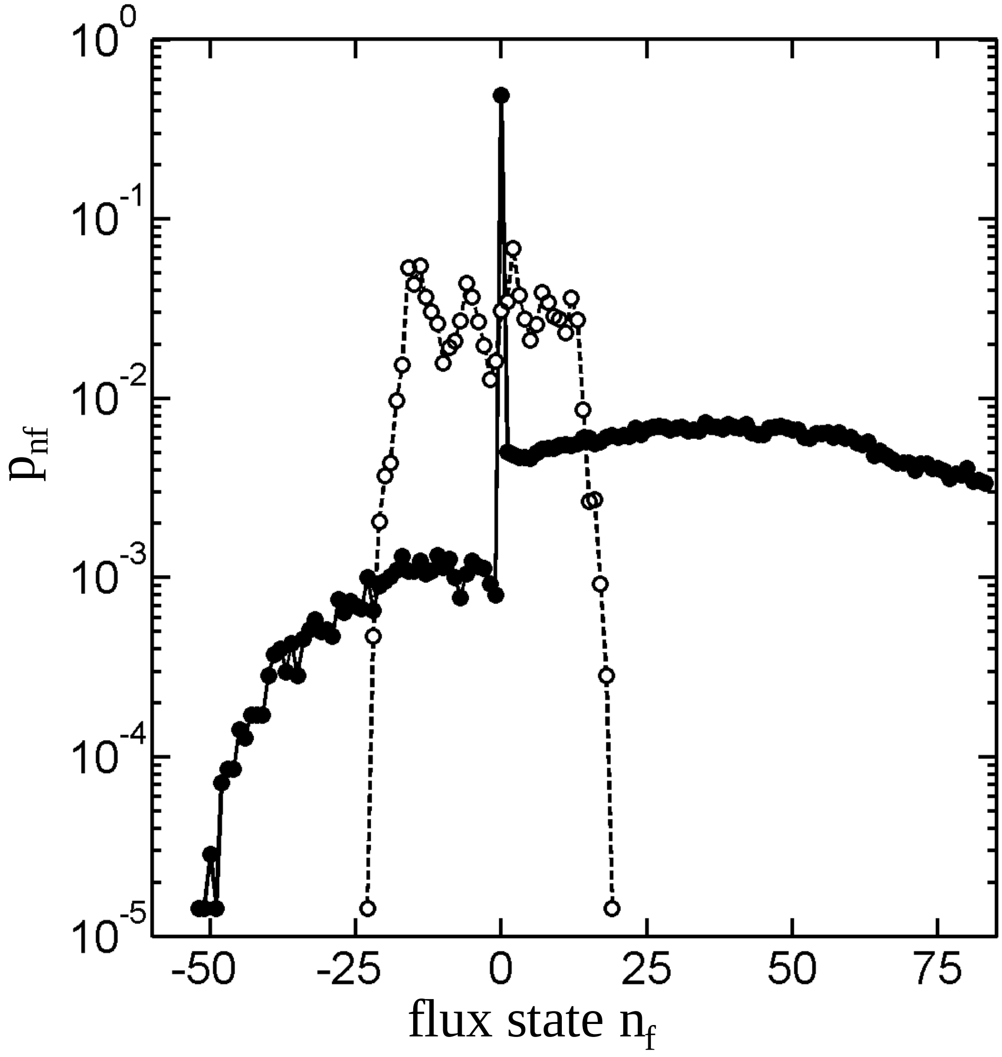

Figure 6.7: Zero flux state selected in DS_1 using $N = 45$ oscillations of amplitude $3.37\,mA$ $(83.4\Phi_0)$ and $f = 20\,kHz$. In this case the critical currents were unsuppressed and the device had 167 states. The filled circles show the probability of each flux state being selected. The dashed line and open circles shows the initial probabilities (p_n).

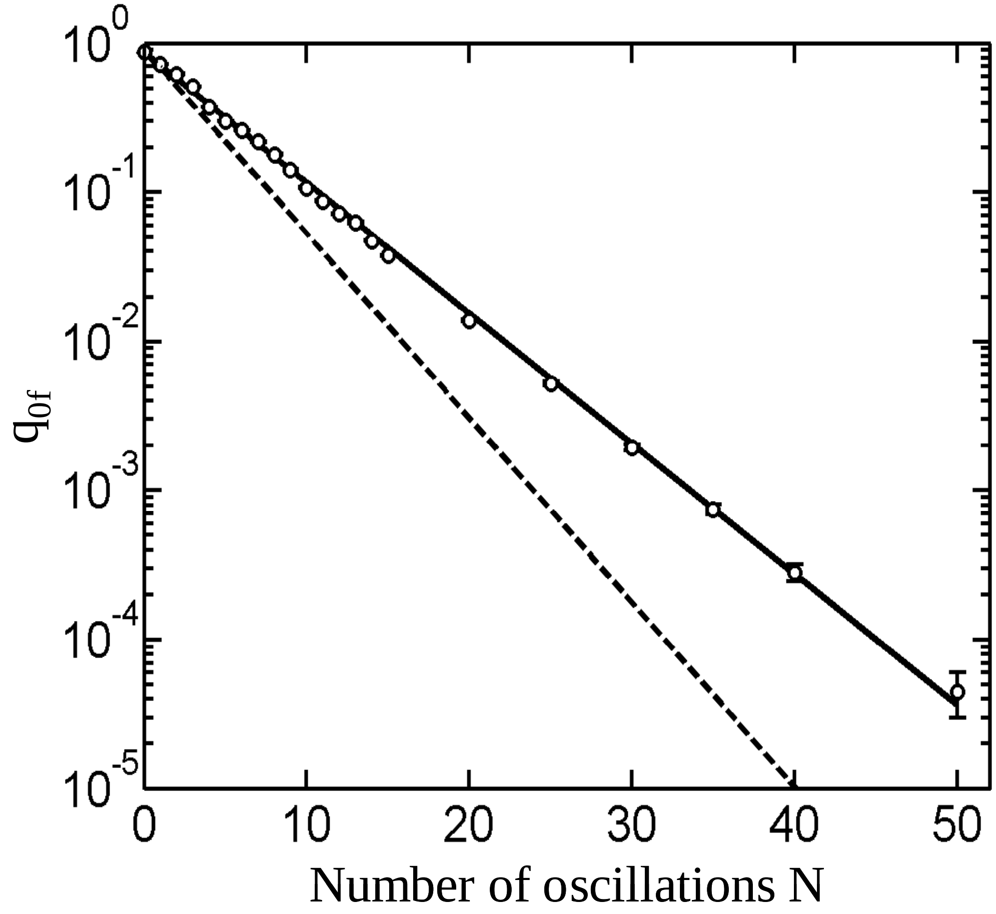

Figure 6.8: Probability $q_{0f} = 1 - p_{0f}$ of <u>not</u> occupying the $n_f = 0$ state versus number of flux oscillations N, showing the exponential decay of $1 - p_{nf}$ with N for another device AL1 [68,41]. For each point, 2×10^5 cycles of initialization and readout were performed. The dashed line shows simulation results based on the initial distribution. The solid line is an exponential fit to the data.

$1 - p_{nf}$ would fall to about 2×10^{-9}.

To understand the switching histograms produced by flux-shaking, we developed a simple model for this process. When a change in the flux makes the SQUID unstable, I assume it will retrap in a stable state with the same probability as the initial distribution $p_{nf}(t = 0)$ [*e.g.* see Fig. 6.5(a)], except shifted by the applied flux. For example, consider a system with five stable flux states with the flux oscillation centered about the $n_f = 0$ state. After the oscillation forces the flux state $n_f = 2$ to become unstable, *i.e.* $p_{2f}(t + \Delta t) = 0$, the probability in the stable flux states $\left(n_f = -3, -2, \pm 1, 0\right)$ are given by

$$p_{nf}(t + \Delta t) = p_{nf}(t) + p_{2f}(t) p_{n+1f}(t = 0). \tag{6.2}$$

This model naturally causes $1 - p_{nf}$ to decrease exponentially with N for the desired well (see dashed line in Fig. 6.8). Figure 6.9 shows a comparison between the measured probability for each well and this simple model for 4 oscillations of device DS$_1$. While I find reasonable qualitative agreement for small N, significant differences arise for large N, most likely because the re-trapping probability is not identical to the initial probability distribution.

To be useful in a quantum computer where N_q qubits are coupled together, the time to initialize the entire system must not grow faster than a polynomial in N_q. The situation for multiple coupled qubits appears favorable. In principle, if the resetting of one qubit does not disturb the flux state of the others, then the same flux oscillation could be supplied to every qubit at the same time. By way of example, suppose that $N = 100$

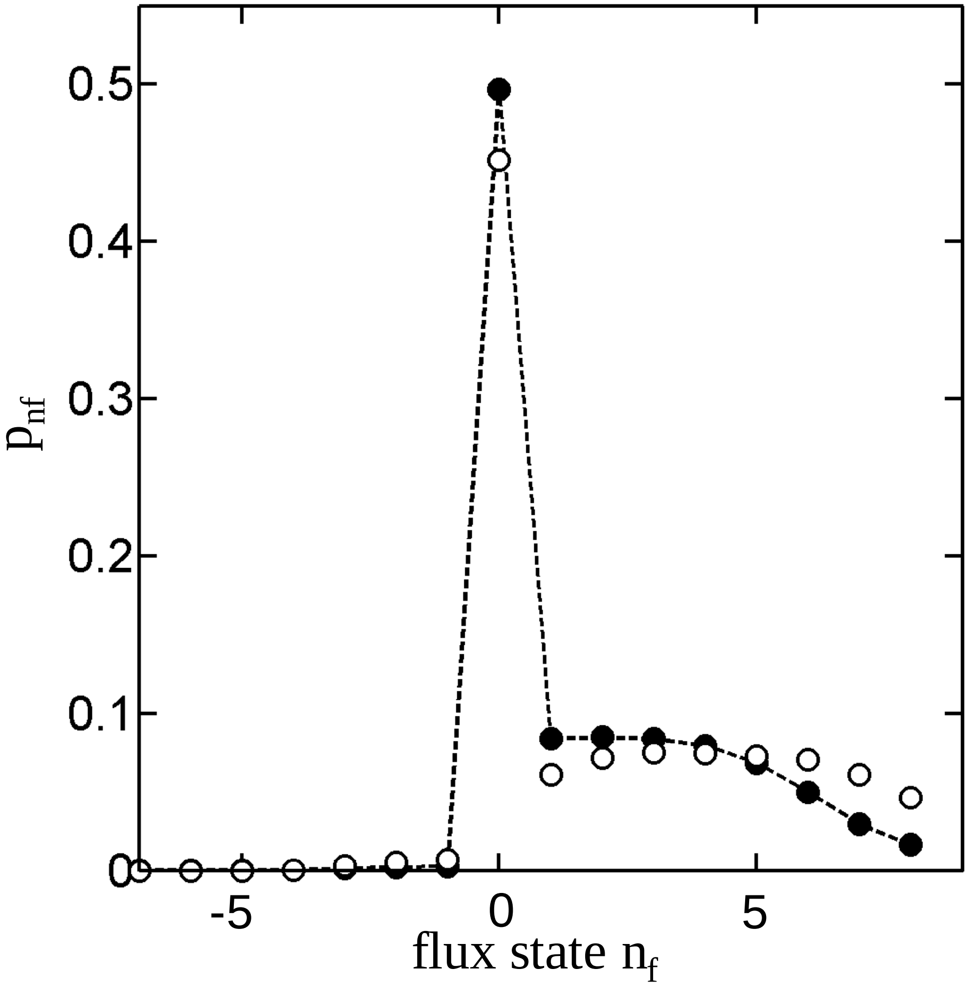

Figure 6.9: Probability of occupying different allowed flux states after four oscillations in device DS_1 for simulations (dashed lines and filled circles) and data (open circles).

oscillations will set the state of one qubit with a probability $p_{nf} = 1 - q_{nf} = 1 - 10^{-6}$. Then the probability that all of $N_q = 1000$ qubits are set to the correct initial state after 100 oscillations will be $p \sim 1 - N_q q_{nf} = 1 - 10^{-3} \sim 1$. Since the one qubit probability of failure q decreases exponentially with the number of oscillations N, reducing the failure rate of N_q to a set level only requires increasing N logarithmically with N_q. Although resetting one qubit may disturb the state of others, particularly nearest neighbors, most qubit schemes involve relatively weak qubit-qubit coupling, suggesting that little disturbance will be created.

More energy would be produced if two neighbors of a qubit reset at the same time. While this would be a relatively rare occurrence, it could be prevented by first applying flux oscillations to every other qubit (each qubit has two neighbors that are not being reset), and then applying oscillations to the remaining devices. This would increase the time to initialize the entire system by a factor of 2, independent of the total number of qubits.

In sample DS_2, both dc SQUIDs required initialization before any measurements could occur, even if just one qubit was being measured. This was necessary because the flux in one qubit coupled to the other, affectively adding a small flux state dependent offset. I found that by carefully considering the mutual inductances, both qubits could be initialized simultaneously or one after the other with no added complexity.

6.3 Qubit Control

After initializing the flux state of the qubit, the dc SQUID needs to be biased such that the:

- (i) qubit's energy levels are sufficiently anharmonic
- (ii) qubit remains well isolated from the environment
- (iii) two junctions are weakly coupled
- (iv) qubit's energy state can be measured.

In devices DS_1, DS_{2A} and DS_{2B} the qubit junction had a substantially larger critical current than the isolation junction; if the qubit junction switched the isolation junction would also switch and the device could be measured in the constant voltage state. Figure 6.1(b) shows a trajectory for $\Delta I = (M / L_1)\Delta I_f$ in device DS_{2B}. This I-Φ trajectory ensures that almost no additional current (other than current from the initial flux state) is applied to the isolation junction during the sweep. In this trajectory the current through the qubit I_1 is approximately equal to the bias current I plus any trapped circulating current. I note that the current in the isolation junction does change somewhat during the sweep. This happens because the inductance L_{J1} of the qubit junction varies as more current is applied, causing some current to be directed through J2. Since $L_1 >> L_{J1}$, this is a small effect. The inductance of the isolation junction J2 is dependent on the current through it [see Eq. (1.3)], $L_{J2} = \Phi_0 / 2\pi I_{02} \cos(\gamma_2)$. By initializing the qubit to a flux state with no circulating current and following the trajectory $\Delta I = (M / L_1)\Delta I_f$, the current noise isolation power isolation factor $r_I \approx \left(\frac{L_1}{L_2 + L_{J2}} \right)^2$ is maximized because L_{J2} is minimal. Since the current through the isolation junction can be controlled, r_I can be varied to test the qubit under various isolation conditions [69]. Finally, I note that by following a trajectory that keeps the current through J2 small, I can also keep the plasma frequency of the isolation junction far from the plasma frequency of the qubit junction.

Devices DS_{3A} and DS_{4B} required a different I-Φ biasing trajectory due to the qubit junction having a smaller critical current than the isolation junction. Here if the qubit junction switched, the SQUID would only switch flux states, unless the isolation junction was heavily biased, in which case it would switch to the voltage state. By following the trajectory shown in Fig. 6.10, the flux state switch for DS_{3A} could still be determined from voltage switching measurements. The trajectory was as follows:

1) Starting from the desired flux offset (point 0), the current I was ramped to the desired bias point (point 1), based on the isolation desired.
2) The SQUID was shuffled to the desired flux state, in Fig. 6.10 the dashed curve shows the I-Φ switching boundary for this state. In this case oscillations were not necessary since only one flux state exists at certain values of I and Φ_a (point 2).
3) The flux current I_f is ramped to the desired qubit bias (point 3'). After stabilizing there, the desired qubit operation can occur until a pulse is used to force population in the $n=1$ to switch flux states (point 3).
4) The flux current I_f is returned to a point where the flux states are very stable (point 4).
5) The bias current I is ramped such that if the SQUID switched flux state during step 3, then it will switch to the constant voltage state at about 8 μA and if not at 9.5 μA (point 5). The actual switch current is measured,

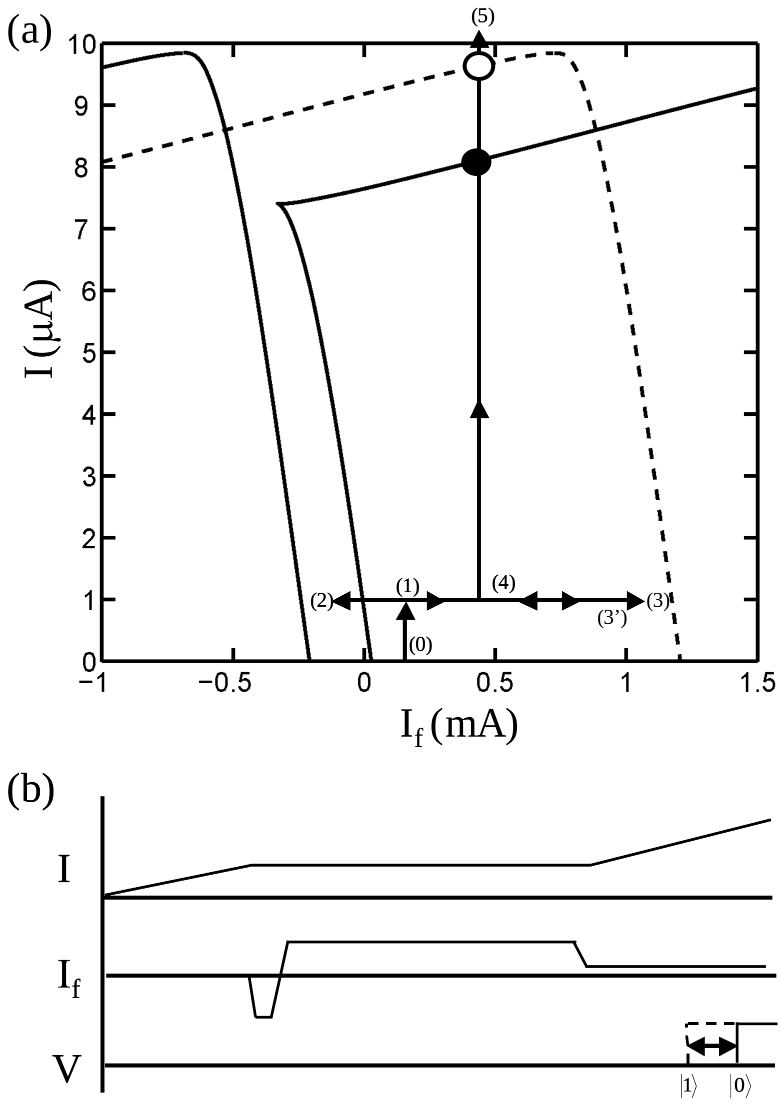

Figure 6.10: (a) I-Φ trajectory used for to operate device DS_{3A} such that it acts like a Josephson junction phase qubit; the trajectory starts at (0) and proceeds through (5). The dashed line corresponds to switching curve for the flux state used for qubit operations. The solid circle shows where the device will switch to the constant voltage state if the qubit switched flux states at point (3). The open circles shows where the device will switch if it did not switch flux states at (3). (b) Current waveforms used in the trajectory described in (a). The device will switch at one of two currents, dependent on the state of the qubit after step 3.

thereby determining whether or not the qubit was in state $|1\rangle$ at step 3.

The same procedure was applied to device DS_{4B}, but with flux shaking at step two since device DS_{4B} had several stable flux states. I note that in the biasing trajectory for devices DS_{3A} and DS_{4B} calibrating the current through the qubit I_1 requires accurate knowledge of n_f, I, Φ_a and any flux offset. This required careful measurements of the I-Φ curves as discussed in section 6.1.

6.4 Summary

In this chapter I discussed the control and calibration of my dc SQUID phase qubits. I-Φ curves provide an essential step in determining the parameters of the device and guiding how to operate it. I also showed how flux shaking enables a system with a many-well potential to be used as a qubit. In Chapter 7, I discuss in detail how escape rate measurements and pulse measurements can be used to read out the energy level of the qubit.

Chapter 7

State Readout Techniques

In this chapter, I discuss how I measured the energy state of the qubit. I investigated two related techniques, both of which relied on the dc SQUID to switch, either to the voltage state or another flux state. The first technique (escape rate readout) relied on performing qubit operations at a bias current such that $n = 1$ had an escape rate that was much larger than $n = 0$. A weakly interacting measurement process, tunneling, acted continuously on the qubit. The second technique (pulsed state measurement) allowed for the qubit to be operated at any bias point; when a measurement was desired a pulse was applied such that with a high probability the population in $n = 1$ would tunnel while the population in $n = 0$ would not.

To quantify undesirable leakage to other energy levels, it is essential for the state measurement technique to be able to also measure small populations in upper levels such as $n = 2$, as well as the qubit levels $n = 0$ and $n = 1$. I found clear evidence for small $n = 2$ populations in the qubits. In fact, $n \geq 2$ effects often dominate the escape rate readout technique. The fidelity of the pulsed measurement technique and other potential difficulties are discussed in this chapter, including the effect of Landau-Zener transitions due to other coupled quantum systems.

7.1 Escape Rate Readout

The average tunneling rate $\langle\Gamma\rangle$ of the qubit junction to the voltage state depends on the tunneling rates Γ_n of each energy level and the probability in each level p_n,

$$\langle\Gamma\rangle = \sum_{n=0}^{N} \Gamma_n p_n \,. \tag{7.1}$$

If the individual tunneling rates Γ_n are well known and levels greater than $n = 1$ are negligible, p_1 at time t can therefore be determined by simply measuring the system escape rate at time t. If the tunneling rates are substantially less than the other characteristic transition rates of the qubit, tunneling will affectively act as a continuous weakly-interacting measurement of the qubit. If the tunneling rates are not small, then they will need to be explicitly considered and included in the density matrix. Relatively large tunneling rates will broaden a spectroscopic measurement [36]. Surprisingly, for a Rabi oscillation found by measuring Γ, the decay of the Rabi oscillation in Γ does not depend on the tunneling rate, although the populations obviously will [63].

The escape rate of a current-biased Josephson junction can be approximated as

$$\Gamma_n = \frac{\sqrt{2\pi}\,[432 N_s]^{n+1/2}}{n!}\frac{\omega_p}{2\pi}\exp(-7.2 N_s)\,, \tag{7.2}$$

where $N_s \approx 2E_J(1 - I/I_0)^{3/2}/\omega_p$ and $\omega_p = \sqrt{\frac{2\pi I_0}{\Phi_0 C}}\left(1-(I/I_0)^2\right)^{1/4}$ [94]. For example, the parameters of DS$_{2B}$ ($I_0 = 20\,\mu A$ and $C = 4.4\,pF$) at $I/I_0 = 0.99$ give rates of $\Gamma_0 = 70/\sec$, $\Gamma_1 = 9.6x10^4/\sec$ and $\Gamma_2 = 6.6x10^7/\sec$. If $1/T_1 >> 10^5/\sec$ and I can ignore population in $n \geq 2$, then these escape rates will only weakly disturb the population in $n = 0$ and $n = 1$.

To determine the escape rate experimentally, I ramped the bias current I and flux Φ_a so that the current I_1 through the qubit junction changed at a rate of approximately $20\mu A/ms$; faster and slower rates enable one to operate and observe higher and lower escape rates, respectively. By recording when the junction switched, a histogram $h(t)$ can be constructed [see Fig. 7.1(a)]. This can then be converted to an escape rate versus time using

$$\Gamma(t) = -\frac{1}{\Delta t}\ln\left(\frac{N_t(t+\Delta t)}{N_t(t)}\right), \tag{7.3}$$

where $N_t(t) = \sum_t^{\infty} h(t)$ denotes the number of times that the system did <u>not</u> tunnel before t [28,36]. By calibrating the current versus time, the escape rate as a function of current can be found and compared to Eq. (7.2) or a simulation of Schrödinger's equation [37]. For example, Figure 7.1(b) shows the calibrated escape rate versus bias current for device DS$_{2B}$, based on the histogram in 7.1(a).

Figure 7.1(c) demonstrates how the escape rate can be used to read out the state of the qubit and map the spectrum. For this plot the qubit bias I_1 was slowly ramped while low power 6.5 GHz microwaves were applied. When the qubit came into resonance with the applied microwaves this produced a noticeable enhancement in p_1 and the total escape rate increased as expected from Eq. (7.1). By repeating this for many frequencies, I could find the spectrum of allowed transition frequencies, as I will show in Chapter 8. For all of my data the ramp rate was always slow enough that the qubit reached equilibrium at each bias point. The escape rates also provide a method to measure relaxation in the qubit without applying microwaves. By measuring the total escape rate

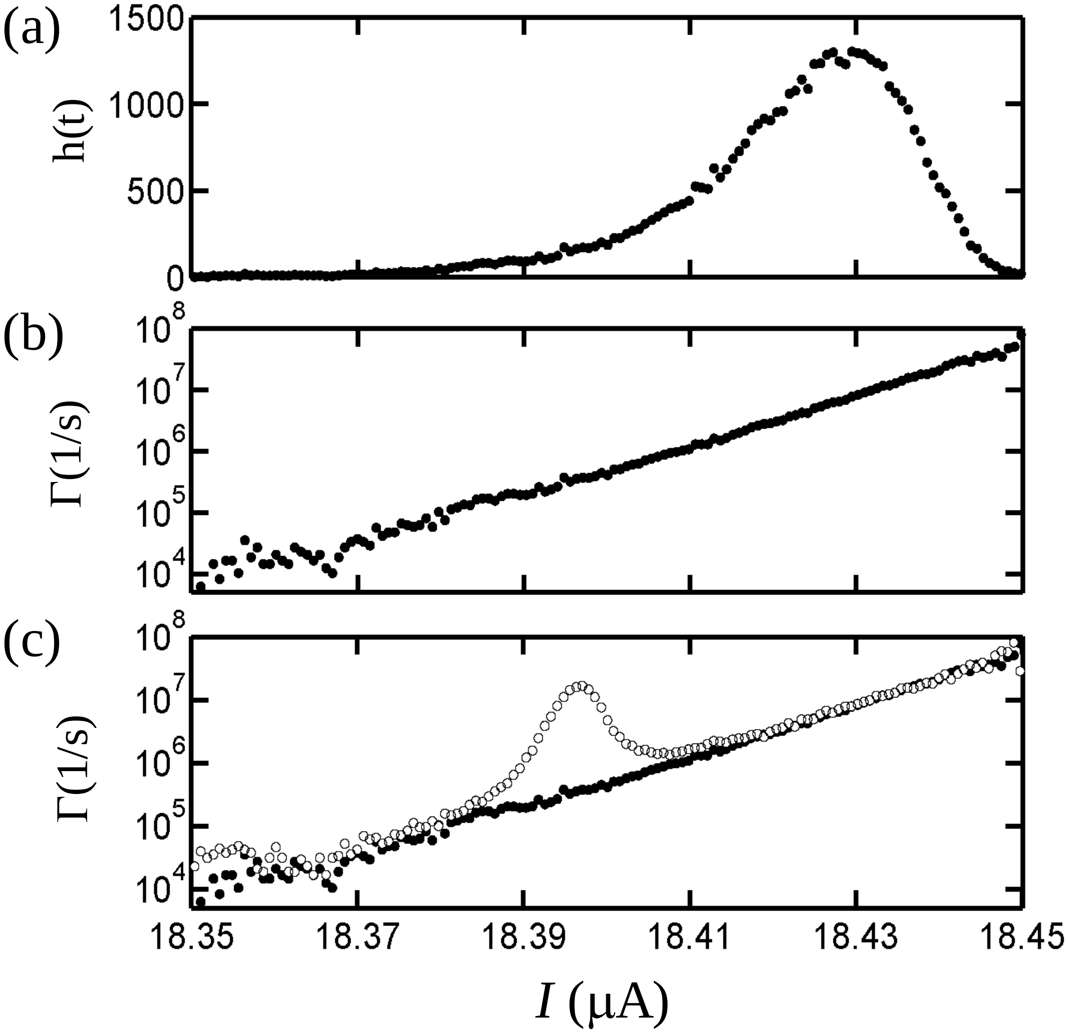

Figure 7.1: Measured histogram and escape rate in dc SQUID DS_{2B}. (a) Calibrated histogram versus current *I*, measured at 20 mK using simultaneous current and flux sweeps and (b) escape rate from the same data. (c) The open circles are escape rates when continuous 6.5 GHz microwaves were applied to the sample. The solid circles are repeated from (b) to highlight the enhancement when the qubit is on resonance with the microwaves at $I_1 = 18.397 \mu A$.

as a function of temperature, Dutta *et. al.* showed that the experimental escape rate can be fit to determine T_1 [95].

High speed operation is desirable in qubits, as there is less chance for the system to decohere, and this generally requires the use of higher microwave power. However, high power causes resonances to broaden, and since the levels are not strongly anharmonic this leads to a potentially significant population in higher levels. Occupancy of $n = 2$ and higher levels is undesirable unless the levels are being used as auxiliary states for gate manipulation or readout [39, 96].

It is also important to realize that even fairly small populations in the upper levels can dominate escape rate based measurements. For example, if we use the escape rate to measure Rabi oscillations, the effects of higher levels are readily seen as a continuous increase in the escape rate with power, up to and beyond the escape rate Γ_1. In the example given above $\Gamma_2 / \Gamma_1 = 690$, therefore even for $p_2 = 0.2\%$ the $n = 2$ level will dominate the total escape rate. Fortunately p_2 often acts to simply enhance p_1, since it can result from an off-resonant transition that remains approximately constant throughout the qubit operation. While this enables us to probe many basic properties of the qubit, leakage is an added complication that limits the measurement of fidelity. Clearly for quantum computation a measurement based on a tunneling is not ideal since the system leaves the qubit basis when the measurement of $|1\rangle$ occurs. The strength of this technique is the simplicity with which data can be taken, and for some situations, being able to detect higher energy levels is advantageous [65].

7.2 Pulsed State Readout

The second readout technique I used involved applying a current pulse to the qubit junction and determining if the pulse forced the device to escape to the voltage state or to another flux state [66, 97, 98]. The main difference between the pulse technique and the escape rate technique is that in the pulse technique the measurement happens at a chosen time and returns a yes or no answer, while in the escape rate technique there is a continuous measurement. For both techniques the switch can be detected by measuring the voltage across the bias leads as discussed in Chapter 6. The pulse technique also exploits the different escape rates of the levels; each successive energy level has a tunneling rate that is two to three orders of magnitude larger than the level below it (see Fig. 7.2). As Silvestrini *et al.* first showed experimentally, different energy levels become unstable, or reach a specified high escape rate, at different currents [99]. Thus by carefully choosing the size of the current pulse, one can ensure with a high probability that levels n and higher will tunnel, while $n-1$ and below will not.

7.2.1 Optimizing the State Detection Process

To analyze the state detection process, I now introduce conditional probabilities P_{ij}, where i corresponds to the initial quantum state of the system, and j indicates whether the system has switched during the current pulse ($j=1$ indicates that the system has switched, $j=0$ indicates that it has not switched). When the system is in state $n=1$, P_{11} is the probability that a correct detection occurs, *i.e.* P_{11} is the probability that the state $n=1$ switches to the voltage state during the current pulse. Similarly, I will define

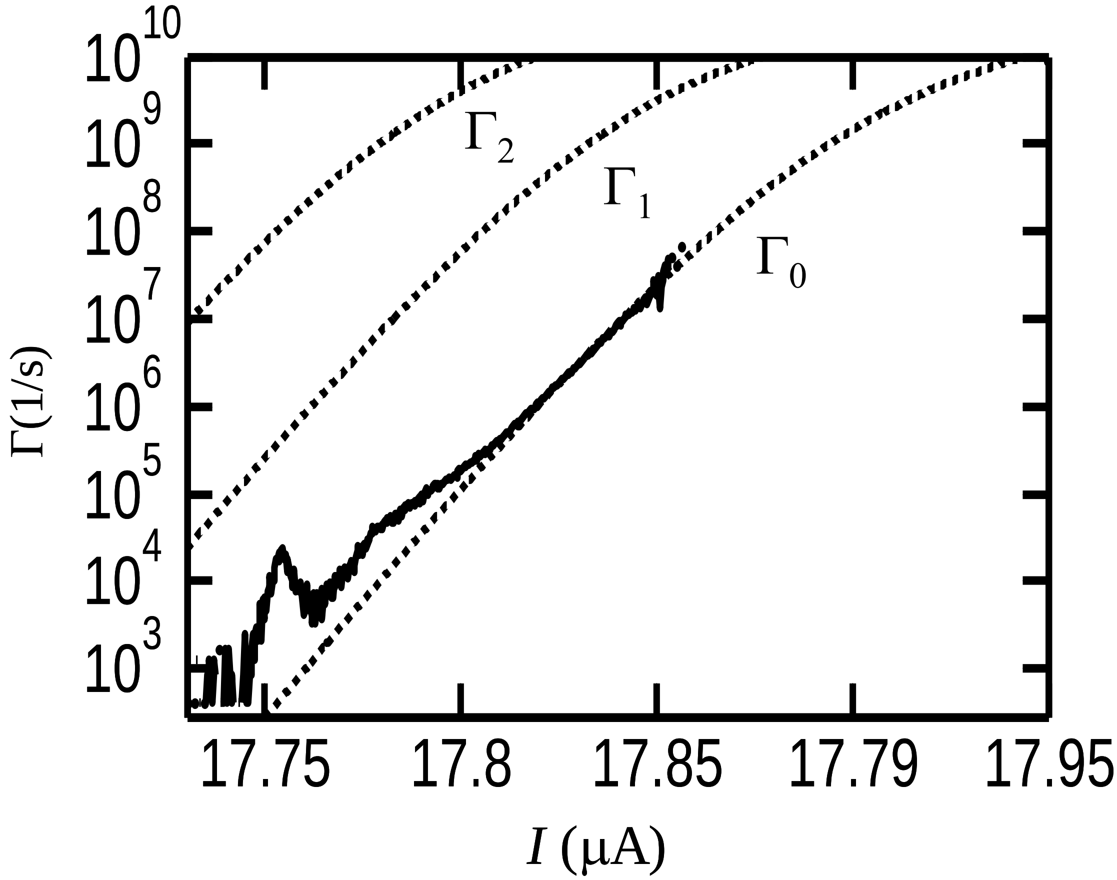

Figure 7.2: Solid curve shows the escape rate of dc SQUID phase qubit DS$_{2B}$ plotted versus current. The flux and bias current are ramped such that the current through the qubit junction is equal to the bias current. The lowest dashed curve is a fit using a single Josephson junction model with $C = 4.3pF$ and $I_0 = 17.957\mu A$, to the escape rate Γ_0 from the ground state. The theoretical escape rates Γ_1 and Γ_2 from the first and second excited levels are plotted as well. The large feature in the escape rate at 17.755 μA appears to be due to a very small population (about 0.01%) in the second excited state.

P_{00} as the probability of correctly reporting a 0 when the system is in the state $n = 0$, *i.e.* the state $n = 0$ does not switch to the voltage state during a current pulse. Four main types of errors will occur:

(i) False detection of the state $n = 1$ when the system was in the state $n = 0$, corresponding to switching when the system was in $n = 0$, occurs with probability P_{01}.

(ii) Missed detection of the state $n = 1$, corresponding to not switching when the system is in the state $n = 1$, occurs with probability P_{10}.

(iii) False detection of the state $n = 1$ when the system was in the state $n = 2$, corresponding to switching from $n = 2$, occurs with probability P_{21}.

(iv) False detection of the state $n = 0$ when the system is in the state $n = 2$, corresponding to not switching when in the state $n = 2$, occurs with probability P_{20}.

Additional errors will occur if there is occupancy in higher levels, *i.e.* $n = 3$ or 4. However, this is a significant effect only at very high microwave drive power, which I ignore here. Conservation of probability forces some constraints, in particular

$$1 = P_{01} + P_{00} = P_{11} + P_{10} = P_{21} + P_{20} \quad . \tag{7.4}$$

It is also important to realize that in general $P_{01} \neq P_{10}$ and that under typical pulse conditions $P_{21} >> P_{20}$.

Optimizing the detection process involves maximizing the probability of detecting the anticipated signal while minimizing the errors. I can optimize the process by varying the duration and height of the current pulse, since this affects the probabilities

P_{ij} differently.

In order to optimize the detection process, one needs to know what the expected signal is. Different signals will typically require a different optimized pulse size. Let p_i be the probability of the system truly being in the i^{th} quantum state. For simplicity, I will assume that the qubit is equally likely to be in $n = 0$ or $n = 1$ and that there is no probability to be in $n = 2$, *i.e.* $P_0 = P_1 = 0.5$ and $P_2 = 0$. This assumption corresponds to a situation where the qubit has been manipulated within its basis states but there is no *a priori* information about the state of the qubit before the measurement. With this choice, the probability of correctly detecting the state of the system (the average signal) is

$$S = P_0 P_{00} + P_1 P_{11} = \left(P_{00} + P_{11}\right)/2 \ . \tag{7.5}$$

The corresponding probability of making an error or the average noise is

$$N_e = P_0 P_{01} + P_1 P_{10} = \left(P_{01} + P_{10}\right)/2 \, . \tag{7.6}$$

Using Eq. (7.5) and (7.6), the single-shot signal-to-noise ratio is then:

$$S / N_e = \frac{P_{00} + P_{11}}{P_{01} + P_{10}} = \frac{\left(2 - P_{01} - P_{10}\right)}{P_{01} + P_{10}} = \frac{2}{P_{01} + P_{10}} - 1 = \frac{1}{N_e} - 1 \ , \tag{7.7}$$

where I have used Eq. (7.4) to eliminate P_{00} and P_{11}. I can now define the measurement fidelity F as

$$F \equiv 1 - P_{01} - P_{10} = 1 - 2N_e \ . \tag{7.8}$$

Notice that if the detection pulse does not make any errors then $F = 1$. While the fidelity mainly has been used in discussions of Rabi oscillations, the closely related concept of the average error N_e is probably more appropriate for error correction.

Examination of Eqs. (7.6-7.8) reveals that minimizing N_e will simultaneously maximize the S/N_e ratio and F. Since P_{01} and P_{10} can be obtained from switching measurements on a device as a function of pulse parameters, Eqs. (7.6-7.8) can be used to find the optimum detection conditions from experimental data. To understand the ultimate limits to the pulse detection technique, I first analyze the system analytically using approximate forms for P_{01} and P_{10} and then compare the results to full numerical simulations and our measurements.

From the escape rates in Eq. (7.2), the probability that the system has tunneled can be determined. To proceed, I adopt a simple model of the pulse: The current pulse starts at I_a where there is negligible probability of escape, and then at $t = 0$ ramps to a value $I_a + I_p$ where it holds steady, and then returns to I_a after a time τ has passed. If the current does not vary too rapidly during the pulse rise and fall, then it will act adiabatically on the system [26, 100]. If I also ignore T_1 and avoided crossings the only changes in the occupancy of the levels will be due to tunneling. The average escape rate at any time during the pulse will then be well represented by Eq. (7.1).

If the system starts with $P_0 = 1$ at $t = 0$, the cumulative probability $P_{01}(\tau)$ that the state $n = 0$ has escaped (detected as a 1) after the time τ has passed is

$$P_{01}(\tau) = 1 - \exp\left(-\int_0^{\tau} \Gamma_0(t')dt' \right) = 1 - \exp\left(-\Gamma_0 \tau\right) = 1 - y\,, \tag{7.9}$$

where $y = \exp\left(-\Gamma_0 \tau\right)$ and Γ_0 is the escape rate from the $n = 0$ state during the pulse. Similarly, if the system starts with $P_1 = 1$ at $t = 0$ the probability $P_{11}(\tau)$ that the state $n = 1$ has escaped (detected as a 1) after the time τ has passed is

$$P_{11}(\tau) = 1 - \exp\left(-\int_0^\tau \Gamma_1(t')dt'\right) = 1 - \exp(-\Gamma_1\tau) = 1 - \exp(-u\Gamma_0\tau) = 1 - y^u, \quad (7.10)$$

where Γ_1 is the escape rate from the first excited state during the pulse, and $u \equiv \Gamma_1 / \Gamma_0$ is the ratio of the escape rates during the pulse. From Eqs. (7.4) and (7.10), I find

$$P_{10}(\tau) = 1 - P_{11}(\tau) = y^u. \quad (7.11)$$

Equations (7.5)-(7.8) can then be written in the form

$$S = \left(1 + y - y^u\right)/2, \quad (7.12)$$

$$N_e = \left(1 - y + y^u\right)/2, \quad (7.13)$$

$$S / N_e = \frac{2}{\left(1 - y + y^u\right)} - 1 \text{ and} \quad (7.14)$$

$$F = y - y^u. \quad (7.15)$$

Equations (7.12-7.15) are shown in Fig. 10.3 for $u = 100$. Minimizing the noise N_e with respect to y, will also maximize F with respect to the size of the current pulse or the pulse time τ. Solving $\partial N_e / \partial y = 0$, I find the minimum error N_e occurs for

$$y^{opt} = \left(\frac{1}{u}\right)^{\frac{1}{u-1}}. \quad (7.16)$$

For $u = 100$, I found $y^{opt} = 0.9545$ as can be seen from Fig. 10.3 as well.

This final expression can be rearranged to show that at the optimum pulse height one has

$$\Gamma_1\tau = u\ln(u)/(u-1) \approx \ln(u), \quad (7.17)$$

where in the last step I have used the fact that $u = \Gamma_1 / \Gamma_0 >> 1$. The optimum values for

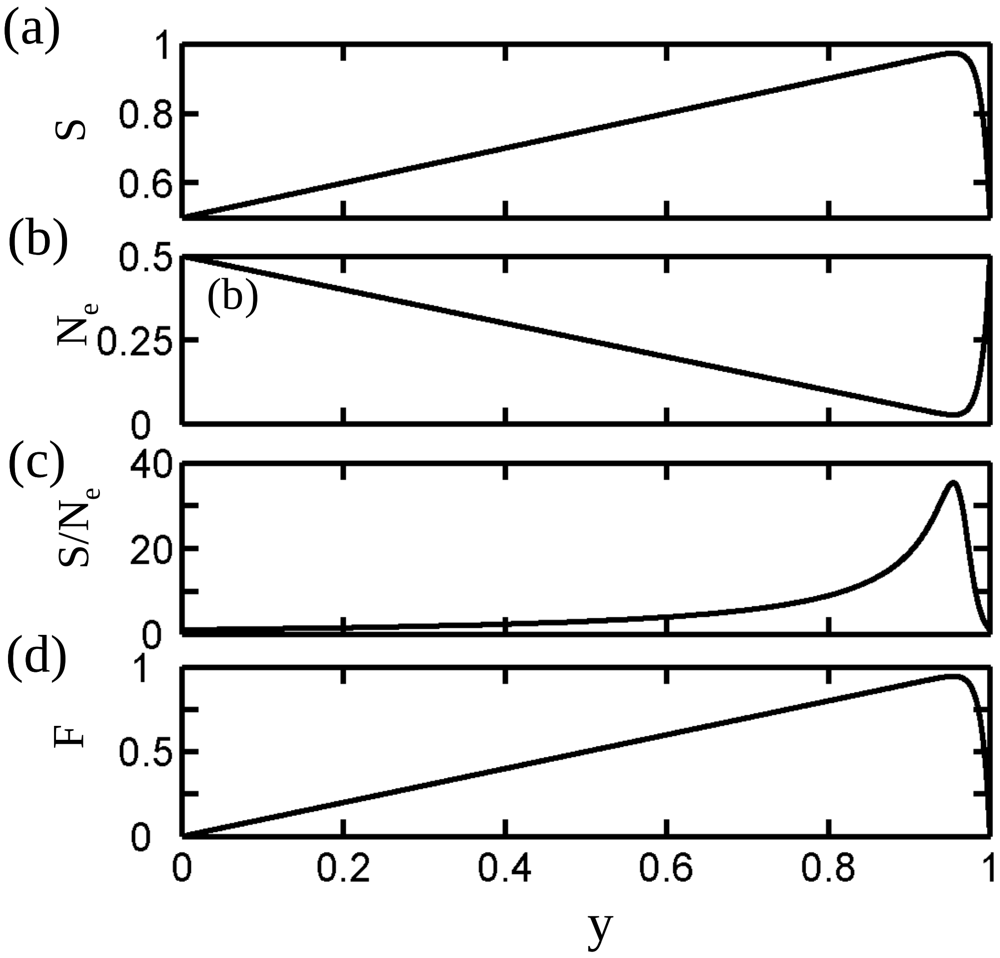

Figure 7.3: (a) Average signal S, (b) average noise N_e, (c) average signal-to-noise S/N_e, and (d) measurement fidelity F using Eq. (7.12-7.15) for $u = 100$. The optimal fidelity $F = 0.945$ and signal-to-noise $S/N_e = 35$ is found at $y = 0.9545$. These results assume the qubit is equally likely to be in $n = 0$ and $n = 1$.

the signal S, error rate N_e, the S/N_e ratio, and fidelity then become

$$S^{opt}=\frac{1}{2}\left(1+\left(\frac{1}{u}\right)^{\frac{1}{u-1}}-\left(\frac{1}{u}\right)^{\frac{u}{u-1}}\right)\ , \tag{7.18}$$

$$N_e{}^{opt}=\frac{1}{2}\left(1-\left(\frac{1}{u}\right)^{\frac{1}{u-1}}+\left(\frac{1}{u}\right)^{\frac{u}{u-1}}\right), \tag{7.19}$$

$$\left(S/N_e\right)^{opt}=\frac{2}{1-\left(\frac{1}{u}\right)^{\frac{1}{u-1}}\left(\frac{u-1}{u}\right)}-1 \text{ and} \tag{7.20}$$

$$F^{opt}=\left(\frac{1}{u}\right)^{\frac{1}{u-1}}-\left(\frac{1}{u}\right)^{\frac{u}{u-1}}. \tag{7.21}$$

Examination of Eqs. (7.18)-(7.21) reveal that the optimal values only depend on $u=\Gamma_1/\Gamma_0$ during the pulse. Figure 7.4 shows plots of the optimal N_e and S/N_e for typical values of u. I find that log $\left(S/N_e\right)^{opt}$ varies nearly linearly with log u while $N_e{}^{opt}$ varies approximately inversely with u. Since the maximum u is about 1000 for typical junction parameters, Fig. 7.4(b) shows that the ultimate minimum probability of making a single-shot detection error is $N_e \cong 0.004$ with this technique. This level of measurement error is probably low enough to be compatible with some error correction schemes [101-103]. However, in practice devices have tended to have considerably lower values of u because the ratio $u=\Gamma_1/\Gamma_0$ decreases at the large current values needed to achieve the high escape rates required for short measurement times (see Fig. 7.2).

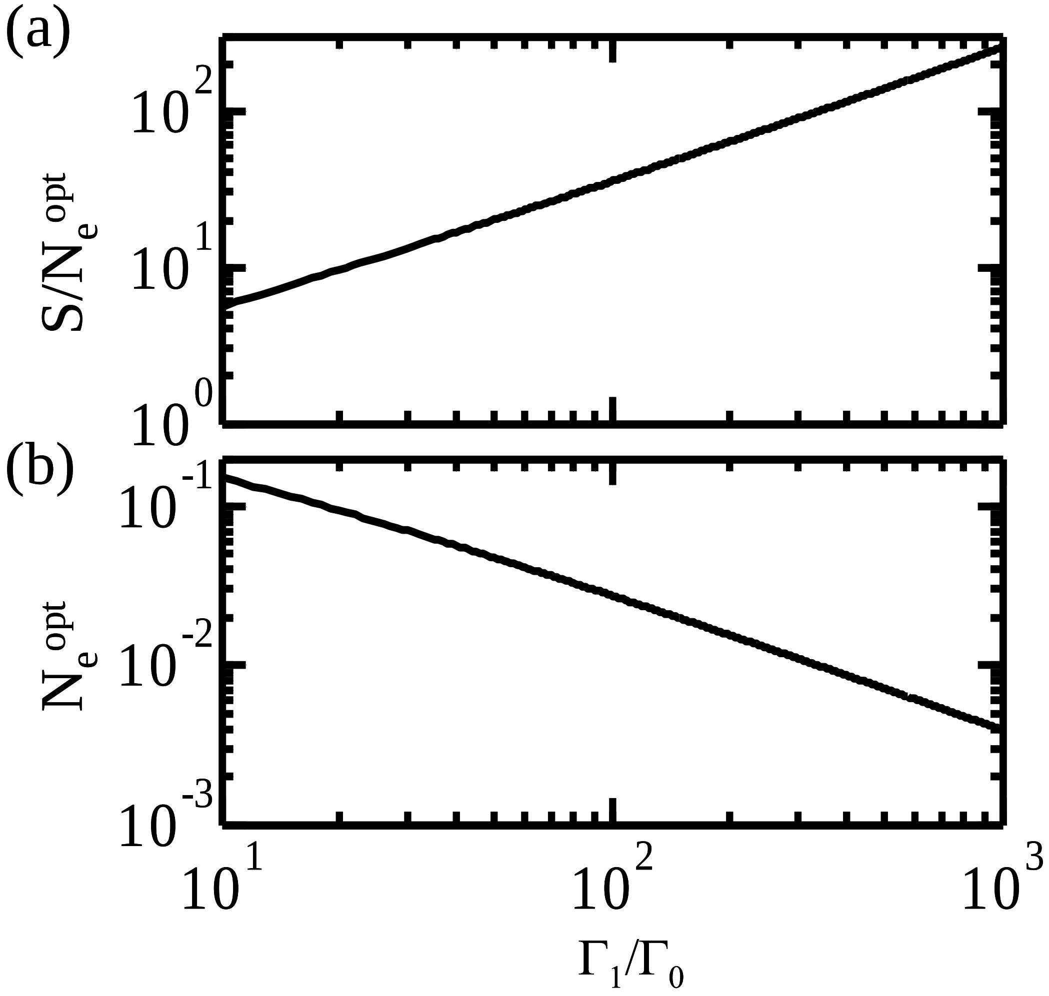

Figure 7.4: (a) Single-shot signal-to-noise ratio S/N_e and (b) average error N_e for optimized square adiabatic pulses, plotted as a function of the ratio of the escape rates $u = \Gamma_1/\Gamma_0$. As expected, the larger the ratio between the escape rates the smaller the detection error.

Table 7.1. Calculated results for optimum pulses for representative values of $u = \Gamma_1 / \Gamma_0$, the ratio of the escape rates during the measurement current pulse. These results correspond to a state that is equally likely to be $n = 0$ or $n = 1$.

$u = \Gamma_1 / \Gamma_0$	$\Gamma_1 \tau$	P_{01}	P_{10}	N	F
100	4.6	0.046	0.0094	0.028	0.945
250	5.5	0.022	0.0035	0.013	0.974
500	6.2	0.013	0.0018	0.007	0.986
750	6.6	0.009	0.0015	0.005	0.990
1000	6.9	0.007	0.0013	0.004	0.992

I also note that at the optimal bias point, the error probabilities P_{10} and P_{01} are not the same (see Table 7.1). For $u = 250$ with the optimum pulse, I find $N_e = 0.013$ and $F = 0.974$. In this case the dominant error is $P_{01} = 0.022$ while $P_{10} = 0.0035$ is about 7 times smaller. For comparison, if $u = 750$, the average error falls to $N_e = 0.005$, the dominant error is $P_{01} = 0.009$ while $P_{10} = 0.0015$ is six times smaller, and $F = 0.99$.

7.2.2 Experimental Results

To test the pulse measurement scheme, I applied current pulses to SQUID DS_{2B} through the on-chip capacitor $C_{\mu w} = 1\,fF$. This was the same capacitor I used for applying microwave power to excite transitions. Some of the pulse current also flows through the isolation junction, but since it is not biased this should produce no significant effects. To form a short pulse ($< 2\,ns$) at the qubit junction, I used the capacitor $C_{\mu w}$ to differentiate the rising edge of a slower current pulse; the overall applied pulse was ~2 μs long with the rising edge of the pulse producing the ~2 ns pulse at the qubit. I monitored the output voltage across the SQUID using a low-noise amplifier, keeping track of whether or not the device switched, and resolved the timing of the individual escape events to better than 100 ps. Repeating this for many switching events, I constructed the average probability of switching for a given pulse size and the escape rate as a function of time during the pulse.

The pulsed method presents one difficulty: The current in the qubit during the pulse differs greatly from the current applied at the top of the refrigerator. What is needed is a way to determine the actual pulse current in the qubit vs. time. To calibrate the pulses, I made use of the escape rate of the system. Figure 7.2 shows the measured escape rate $<\Gamma>$ of the qubit junction as a function of time for device DS_{2B}. Also plotted are fitted results (dotted lines) for Γ_0, Γ_1, and Γ_2 using numerical analysis (see section 2.5) for an effective qubit critical current, $I_{01} = 17.957\,\mu A$ and $C_1 = 4.3\,pF$. I note that this isn't the actual critical current of the qubit, but an effective critical current that depends on the flux state. Based on the device parameters, the single junction cubic approximation model provides a good description of the escape rates [41]. Quantum simulations have also verified this approximation [42]. The disagreement between the measured $<\Gamma>$ and expected Γ_0 is due to high-frequency noise producing a very small population in $n = 2$, as discovered using the pulse measurement technique [104]. Since the escape rate of the second excited state is approximately $\Gamma_2 = 10^8 / s$ in the region of the disagreement, even a small $n = 2$ population leads to an easily observable enhancement in $<\Gamma>$.

Since the escape rate depends on the current through the junction; I could use measurements of the escape rate to infer the current during the pulse. I carefully measured the escape rate versus time during a pulse and then used Fig. 7.2 to map from escape rate versus time to current versus time for the pulse. Figure 7.5(a) shows the actual measured escape rate versus time for three sample pulses with amplitudes of 0.61, 0.79 and 0.85 V at the pulse generator and 10 dB of additional attenuation on the line. Figure 7.5(b) shows nine pulses with successively larger amplitude, from 0.4 V to 0.64 V (the peak voltage of the pulse at the top of the refrigerator was used to characterize the amplitude) after converting the escape rate to current. To improve statistics, the two smallest pulses in Fig. 7.5(b) were calibrated at relatively high bias currents, $I = 17.81 \mu A$, while larger pulses were calibrated at lower bias currents, $I = 17.74 \mu A$. This was done so that the escape rate during the pulse was always easily measured. Figure 7.5 shows that our pulses were quite short, only 1-2 ns in duration, and at the peak of the pulse the current appears to be resolvable to better than 10 nA in 100 ps time intervals.

Figure 7.6 shows examples of switching curves when the qubit was prepared in different initial states. The open diamonds show the probability P_e that the system escaped versus pulse size for the situation where the qubit was predominantly in its ground state (no resonant microwave excitation applied). For small pulses, the data follow a straight line on a semi-log plot, as expected since in this limit the probability of switching is $P_{01} \sim \Gamma_0 \tau$ and Γ_0 depends approximately exponentially on current. The solid squares show the corresponding measured switching probability P_e after a resonant microwave pulse of 6.5 GHz was used to produce some population in the first excited state; the measurement pulse was applied 3 ns after the microwaves were turned off to

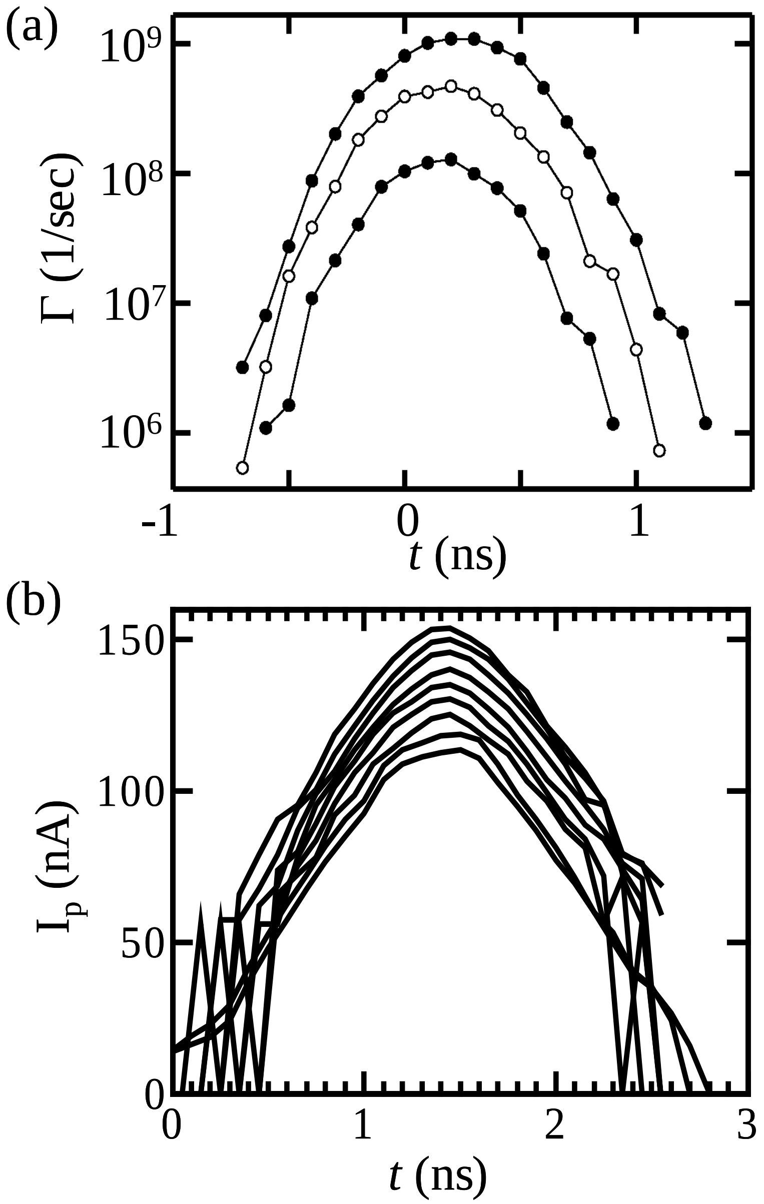

Figure 7.5: (a) Escape rate through device DS_{2B} plotted versus time for three measurement pulses of amplitude 0.61, 0.79 and 0.85 V at the pulse generator and 10 dB of attenuation on the line. (b) The current through the qubit for nine pulses with amplitudes ranging from 110 nA to 150 nA (0.4 to 0.64 V at the pulse generator) as determined from the ground state escape rate of Fig. 7.2. The conversion assumes that the system is entirely in the ground state during the measurement pulse.

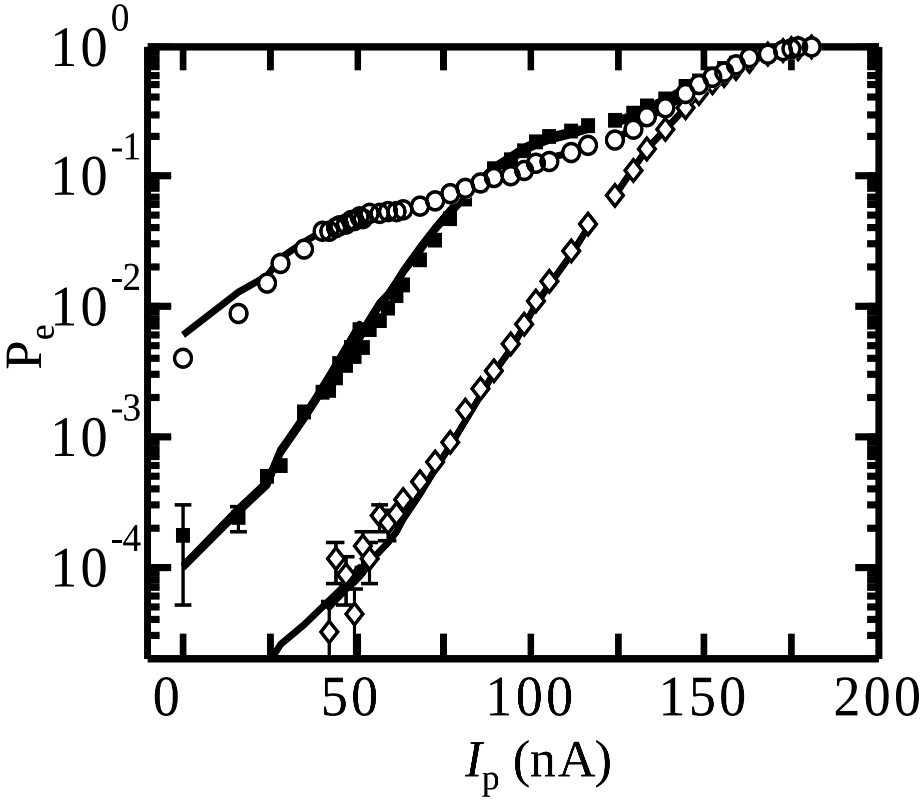

Figure 7.6: Switching probability P_e versus pulse amplitude for three population distributions. The diamonds correspond to the situation when no microwaves were applied and the qubit was predominantly in the ground state. The solid squares show the measured fraction that escaped when 6.5 GHz microwaves were applied to enhance $n = 1$ state population. The open circles show data where $n = 2$ and $n = 1$ excited state populations were produced by pumping with microwaves at 12.5 GHz. The solid lines are fits with the only variable being the populations of $n = 0$, 1, and 2. The three solid curves show fits to the diamonds with $P_0 = 0.99996$, $P_1 = 0$ and $P_2 = 4\times10^{-5}$, the squares with $P_0 = 0.80096$, $P_1 = 0.199$, $P_2 = 4\times10^{-5}$, and then $P_0 = 0.78996$, $P_1 = 0.21$, $P_2 = 4\times10^{-5}$ and the circles with $P_0 = 0.867$, $P_1 = 0.088$, $P_2 = 0.045$. The difference in the two fits to the square data is not distinguishable in this plot.

ensure that any undesired transients had decayed away. Finally, the open circles show the corresponding result after a 12.5 GHz resonant microwave pulse was used to produce some population in the second excited state. In this case, $n=1$ was also occupied due to relaxation from $n=2$.

Examination of Fig. 7.6 reveals clear bending in the switching curves corresponding to the currents at which individual energy levels become highly likely to escape (about 150 nA for $n=0$, 100 nA for $n=1$ and 50 nA for $n=2$). In order to extract the population in each level, I first used the pulse current calibration (Fig. 7.5) to determine the current at time t, and then found the escape rate at time t from Fig. 7.2. Starting from an initial occupancy of the levels, I numerically time evolved the occupancies in 0.1 ns increments ($dt = 0.1ns$), accounting for loss due to tunneling from each of the levels,

$$P_n(t+dt) = P_n(t)\exp\left(-\Gamma_n(t)dt\right). \tag{7.22}$$

The only variables in this procedure are the initial populations of the levels. The diamonds in Fig. 7.6 were fit using $P_0 = .99996$, $P_1 = 0$ and $P_2 = 4\times10^{-5}$; the squares were fit using $P_0 = 0.80096$, $P_1 = 0.199$ and $P_2 = 4\times10^{-5}$; and the circles were fit using $P_0 = 0.867$, $P_1 = 0.088$ and $P_2 = 0.045$. For the 6.5 GHz data (squares), the best λ^2 fit for the entire data set came from $P_1 = 0.199$. However, $P_1 = 0.21$ fits the bend more accurately and is plotted as well. Figure 7.7 shows a linear representation for the case of no microwaves and with microwaves applied at 6.5 GHz, here only $P_1 = 0.21$ is used to fit the 6.5 GHz data. In general, the agreement is quite good between the fit and the data, with the most serious discrepancies being in the $n=2$ data, probably due to uncertainties

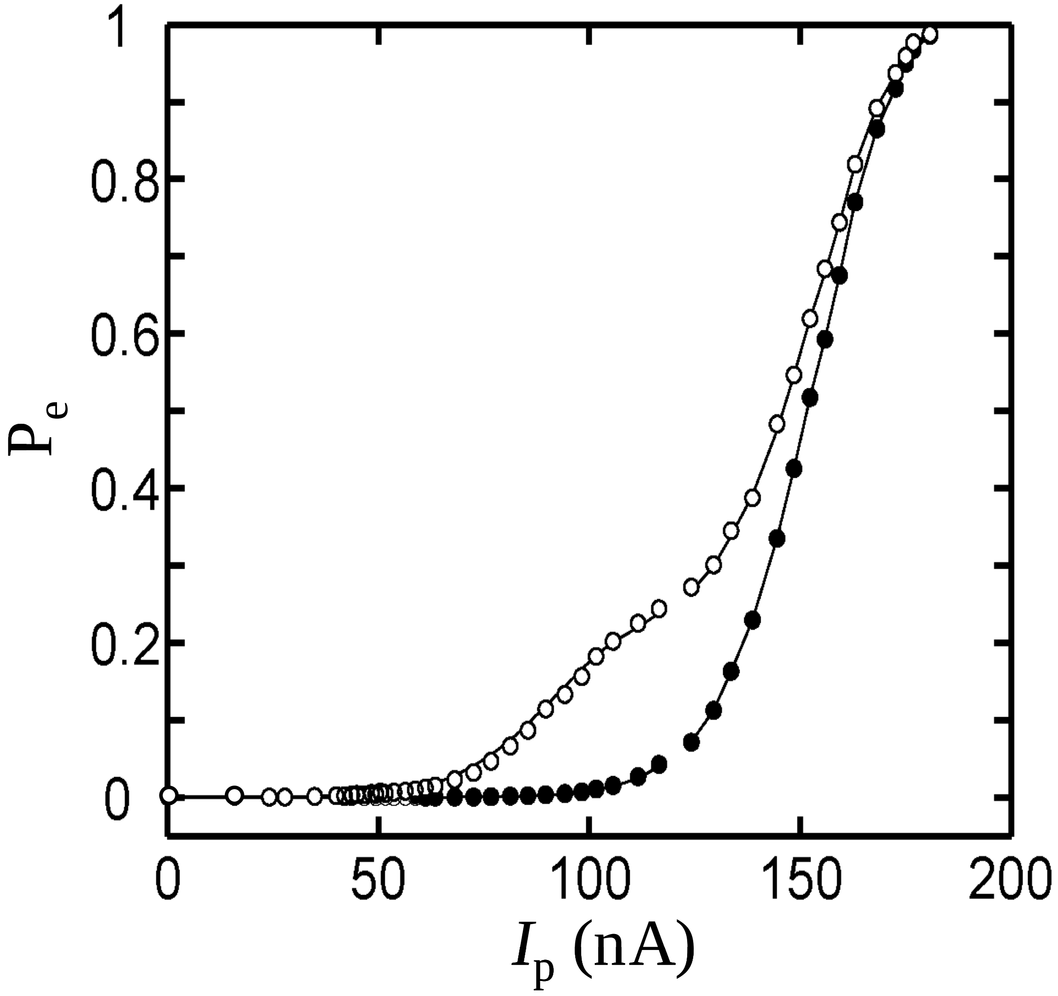

Figure 7.7: Switching probability P_e versus pulse amplitude for two population distributions. The solid circles correspond to the situation when no microwaves were applied and the qubit was predominantly in the ground state. The open circles show the measured fraction that escaped when 6.5 GHz microwaves were applied to enhance the $n=1$ state population. The solid circles are fit with $P_0 = 0.99996$, $P_1 = 0$ and $P_2 = 4\times10^{-5}$ using Eq. (7.22). Here the solid curve through the open circles uses $P_0 = 0.78996$, $P_1 = 0.21$, and $P_2 = 4\times10^{-5}$, since this captures the bend at $I_p \sim 110\,nA$ better on a linear plot.

in Γ_2 and the small population in $n = 2$. Note that since there is no independent way to determine the population during the pulse, we can only check for self-consistency.

To the extent that these fits determine the state populations, P_{10} can be found from the measurements. I emphasize here that P_{10} is the probability that a single shot measurement incorrectly detects $n = 1$, not the error in fitting many pulse amplitudes. Figure 7.8 shows the resulting determination of P_{10} (circles), P_{01} (squares), and N (pluses) from the data and fits shown in Fig. 7.6. The filled circles show P_{10} determined using P_{01} data for parameters $P_0 = 0.80096$, and $P_1 = 0.199$. The open circles and plot of N are based on $P_1 = 0.21$, since the behavior near the bend is critical. This gives a better representation of the data near the optimal point. Examination of Fig. 7.8 reveals that the optimum single-shot pulse occurred for an amplitude of 117 nA, which yielded an optimum error of $N_e \cong 0.03$ and optimal fidelity $F = 94\%$. This error matches the predicted error from Fig. 7.2 for $u = 100$, which is roughly consistent with the expected ratio of Γ_1 / Γ_0 at the peak of the pulse at $I = 17.875 \mu A$.

For comparison, Fig. 7.8 also shows theoretical results (solid and dashed curves) for P_{01}, P_{10} and N_e for the pulses shown in Fig. 7.5. The P_{10} curve came from time evolving Eq. (7.22) from an initial population $P_1 = 1$ for different pulses. The P_{01} curve was found by time evolving Eq. (7.22) from an initial population $P_0 = 1$. As expected for small pulse amplitudes, P_{10} is large, since the pulse isn't large enough to give the first excited state a large escape rate. For large pulse amplitudes, $n = 1$ tunnels rapidly so that P_{10} is small, however the ground state has a very large escape rate so that P_{01} becomes

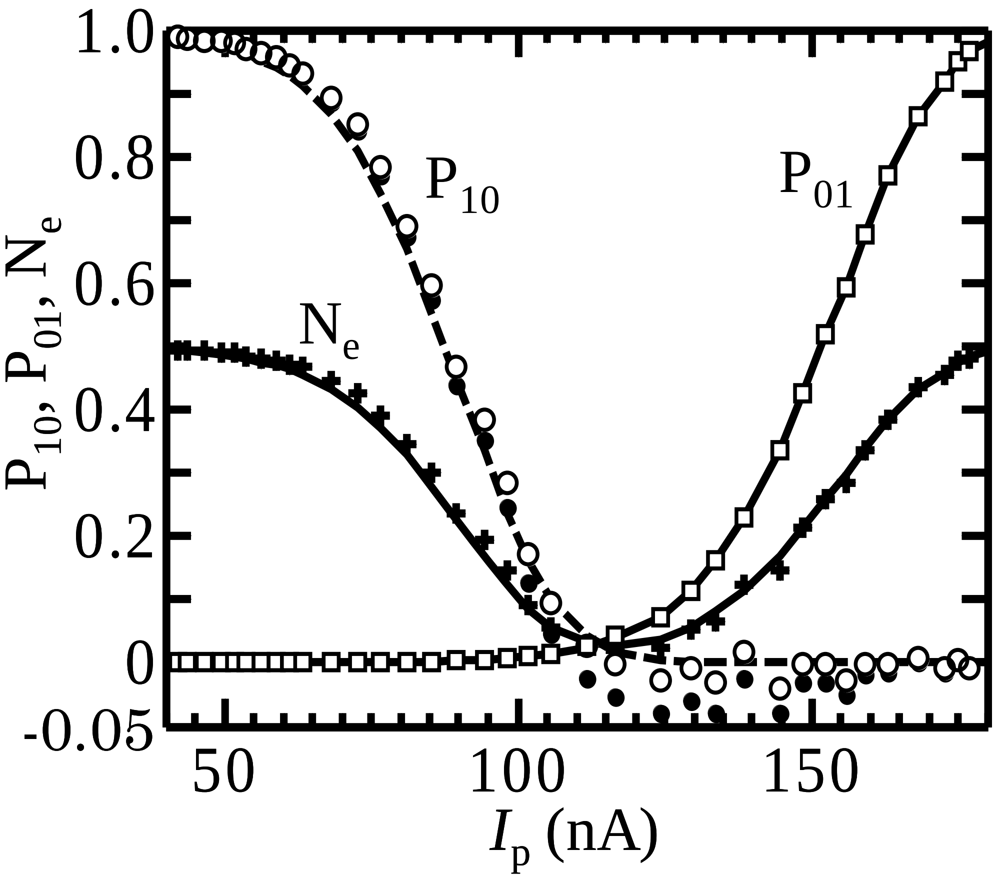

Figure 7.8: Measured error P_{01} (squares) and inferred average error N_e (pluses) and P_{10} (circles) found from data shown in Fig. (7.5) for SQUID DS_{2B}. Solid and dashed curves show theoretical curves based on the pulse current calibration. Open circles show P_{10} if a population of $P_1 = 0.21$ is inferred from Fig. 7.6, closed circles show P_{10} for $P_1 = 0.199$. Note offset zero on y-axis and that $P_1 = 0.199$ produces unphysical (negative) values for P_{10}, while $P_1 = 0.21$ is better behaved.

large. Also shown is a solid curve for the resulting average single-shot error N_e for $P_1 = 0.5$, $P_0 = 0.5$ and $P_2 = 0$. As noted above, the minimum error does not occur when $P_{10} = P_{01}$. P_{01} agrees very well with the data. On the other hand P_{10} shows a small discrepancy, which may come from errors in Γ_1 or the difficulty in determining the relatively small population $P_1 = 0.21$ in the excited state $n = 1$, which I used to get P_{10} (open circles in Fig. 7.8).

7.2.3 T_1 and Landau-Zener Fidelity Loss

In the above analysis I had to make some assumptions that may not be true. Ideally, I could simply prepare the population in a few known states and compare with the measured result to determine the measurement fidelity. Of course, this assumes you can perfectly prepare a state with a known probability in a specific state. Since we do not have an independent way of determining the populations in each level, this was not possible. One possibility would be to use the fixed escape rate measurements to cross-check the pulse measurements. Since the escape rate measurements do not involve sweeping the bias, they are much less susceptible to Lanau-Zener effects [105]. However, they require precise knowledge of Γ_n and do not give independent measurements of each P_n.

The previous discussion also made no reference to relaxation and assumed that the rate of relaxation was negligible compared to the width of the pulse. To demonstrate the potential problems with this assumption, imagine a qubit with $T_1 = 20\,ns$. An initial population with $P_1 = 1$ will appear after 1 ns as $p_1 = 0.95$. This problem is actually less serious than it appears at first. The idea is that one should assume that the measurement happens not when the pulse begins, but when the majority of the events switch, at the peak of the pulse. Thus the drop in p_1 is being honestly reflected in the measurement.

A more serious issue is the loss of measurement fidelity due to Landau-Zener transitions [106]. This seemed to be particularly noticeable in device DS$_3$ and DS$_4$. As I will discuss in detail in Chapters 9 and 10, our qubit is coupled to many parasitic quantum systems, which produce avoided level crossings in the transition spectrum [37, 106]. During the measurement pulse, the transition frequency of the qubit varies, and the qubit has some probability of transferring energy to these other quantum system before the qubit switches. Landau-Zener transitions will only affect the error P_{10}, since if the qubit is in $n = 0$ there is no energy to transfer. Assuming that the system starts with $n = 1$, the probability of transferring the energy to a coupled quantum system with the same transition frequency is: [63, 66, 105]

$$P_i(1 \to 0) = 1 - \exp\left(\frac{-\pi^2 \Delta_{fi}^2}{df_{01}/dt} \right) , \tag{7.23}$$

where Δ_{fi} is the frequency splitting caused by the i$^{\text{th}}$ avoided level crossing and df_{01}/dt is the rate at which the current pulse changes the $0 \to 1$ transition frequency f_{01}. Equation (7.23) implies that large splittings will dominate the measurement error. For example, a splitting size $\Delta_f = 10\,MHz$ and pulse ramp rate $df_{01}/dt = 2\,GHz/ns$, will lead to an additional $P_{10} = 0.0005$, where as $\Delta_f = 60\,MHz$ gives $P_{10} = 0.012$. The distribution of splittings will need to be considered to determine the actual measurement fidelity in a device, with special attention given to any large individual splittings. In fact, the effect of many small uniformly distributed splittings is exactly like T_1; energy is transferred from the qubit to a bath on a time scale that is independent of the sweep rate.

When fine spectroscopic measurements were performed on DS_{2A} and DS_{2B}, only very fine splittings $\Delta_f < 10\,MHz$ were seen [37]. This includes a large section of the spectrum (from 5.5 GHz to 6.25 GHz in DS_{2B}) that the qubit would pass through during a measurement pulse. Unfortunately, we were unable to clearly resolve splittings $\Delta_f < 10\,MHz$. An exact prediction is therefore not possible, but if we take as a worse case estimate that the qubit would transverse through 20 splittings with $\Delta_f = 10\,MHz$, this would lead to $P_{10} < 0.01$. Additionally if large splittings were affecting the measurement fidelity we would expect to see discrete steps in Fig. 7.6, corresponding to a larger measurement pulse crossing a new splitting; we see no evidence of this. Of course, our results do not rule out effects of small splittings, which would cause a loss of measurement fidelity and lead to underestimating the population in $|1\rangle$.

While determining the measurement fidelity by preparing a perfectly known state is not possible, measurements of Rabi oscillations should reveal significant discrepancies. In device DS_{2B}, Rabi oscillations typically had decay times of $T' = 10ns - 15ns$ using either the pulse measurement technique or the escape rate technique (see Chapter 8). With this range of T' and a Rabi flopping frequency of $\omega = 2\pi / 9ns$ one expects a maximum peak $p_1 \approx 0.83 - 0.87$ during the oscillation. As I will show in Chapter 8, an on-resonance Rabi oscillation was viewed using the pulse measurement technique in DS_{2B}. From fitting the entire switching curve, I found peak values of $p_1 \approx 0.75$ and $p_2 \approx 0.05$ at $t = 4ns$, as shown in Fig. 7.9. If I assume a relaxation time $T_1 = 15ns$ and

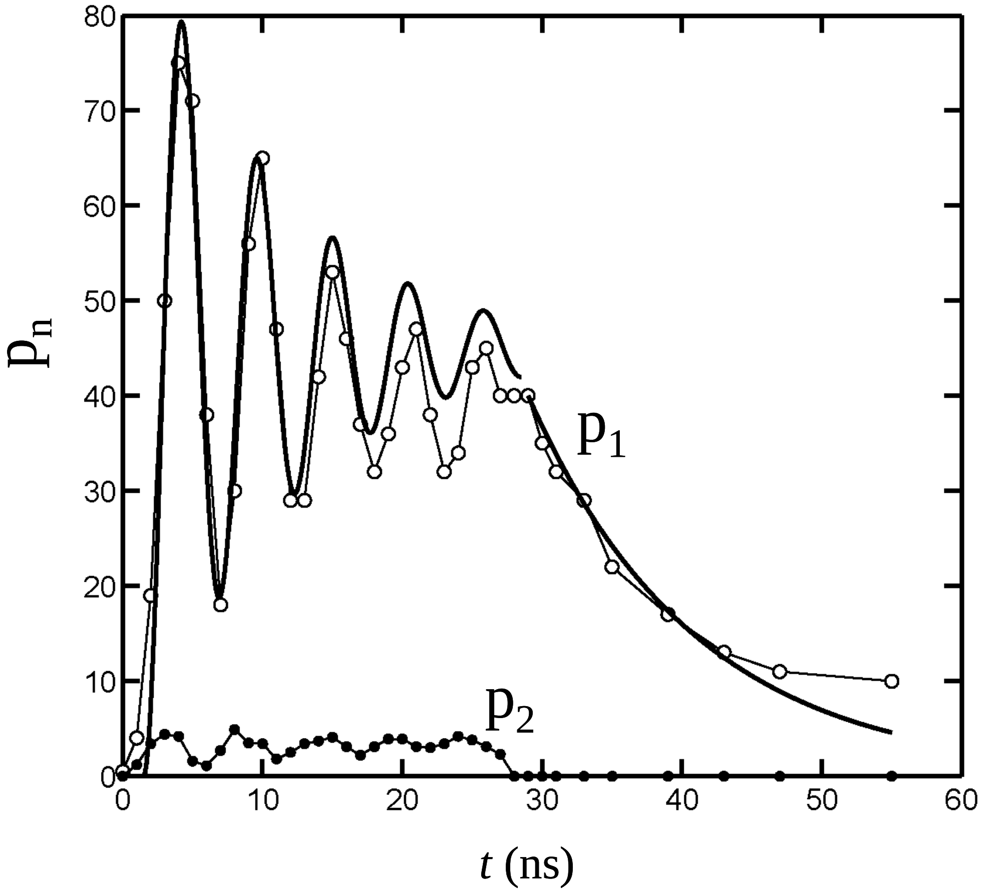

Figure 7.9: Rabi oscillation in the probability p_1 of occupying $n=1$ in device DS_{2B} using the pulsed readout technique. On-resonance 6.2 GHz microwaves were applied for 28 ns to induce Rabi oscillations between $t=0$ and $t=28ns$. By fitting the entire switching curve the population in $n=2$ was also determined. The dark solid curve plotted from $t=0$ to $t=28ns$ is a fit to the Rabi oscillation using $T'=10ns$ (see Section 8.2.2 for details). The maximum excited state populations were $p_1 \approx 0.75$ and $p_2 \approx 0.05$ at $t=4ns$.

1 ns of delay after the microwaves are no longer resonant, p_1 falls from 0.83 to 0.78 before tunneling occurs. This probability is close to what I found. This example demonstrates the difficulty in determining the measurement fidelity within a few percent if the device has relatively short coherence times and leakage to higher levels. However, these rough calculations demonstrate with confidence that any additional measurement error to the single shot estimate is rather small in DS_{2B}. Surprisingly, Rabi oscillations measured in DS_{2B} using the pulse readout technique tended to drift downwards in time (see Fig. 7.9) for some data sets; the cause of this was never determined

As I will show in Chapters 9 and 10 spectroscopic measurements on device DS_{3A} showed prominent large avoided level crossings over the range experimentally tested, with a maximum $\Delta_f > 250\,MHz$. While some of these large splittings were avoided by operating at lower frequencies (so that a pulse would not transverse the crossings), others could not be avoided. Unfortunately the entire spectrum covered during a measurement pulse could not be measured, but only portions of the spectrum within about 500 MHz of the operating point due to the biasing conditions. The problem is that devices with $I_{01} < I_{02}$ could not be operated at high escape rates when optimally biased. As I will discuss in Chapter 8, Rabi oscillation in these devices always had measured peak probabilities $p_1 < 0.70$, consistent with lower measurement fidelity due to Landau-Zener transitions, even though the coherence times were double those of device DS_{2B}.

7.3 Summary

In this chapter, I described my use of two measurement techniques to view the energy level of the qubit, both of which require measuring when the SQUID switches to the voltage state. In the first technique, I measured the total tunneling rate of the qubit junction and used this to detect population in higher levels. This technique requires many repetitions to determine the total tunneling rate at the desired resolution and could only be used at bias points where the tunneling was non-negligible. In the pulse measurement technique the qubit could be operated at any bias point. The time resolution is determined by the jitter (between the qubit operation and measurement pulse) and the width of the pulse (typically 1-2 ns in DS_{2B}). Using the pulse measurement technique also allowed me to selectively measure at any time during the operation. The main drawbacks to the pulse technique are the influence of Landau-Zener transitions, which reduce the measured fidelity of $n = 1$ and the additional complexity in setting up the experiment. In contrast, the escape rate technique is plagued by leakage to higher levels of the qubit, which dominate the measurement, and it does not give individual population levels in each state without resorting to detailed modeling [65].

Chapter 8

Qubit Performance

In this chapter, I describe my results on the control of the quantum state of dc SQUID phase qubits. Using the methods previously described to calibrate, initialize, control and readout the qubit, I performed a series of measurements on three different devices. The goal of these measurements was to test our understanding of the system as well as demonstrate control of the quantum state. I measured the spectrum, Rabi oscillations, Ramsey fringes and relaxation, and used this data to determine quantitatively the relaxation and decoherence times of the qubits. Here, I also discuss the relationships between the different characteristic times of these measurements. Evidence of coupling between two qubits and manipulation of the coupled states will also be shown. The results will be compared to theoretical predictions from Chapters 2 and 3. I finally conclude this chapter with a comparison of the different devices and some potential sources that might be the causes of the short coherence times I find in these qubits.

8.1 SQUID DS_1

8.1.1 SQUID DS_1 Spectrum

The first device I tested was device DS_1, which was an uncoupled dc SQUID phase qubit fabricated by Hypress, Inc. [75], see [Fig. 4.2(a)]. A spectrum for the device at 100 mK is shown in Fig. 8.1(a-b). This specific data set was taken before I joined the

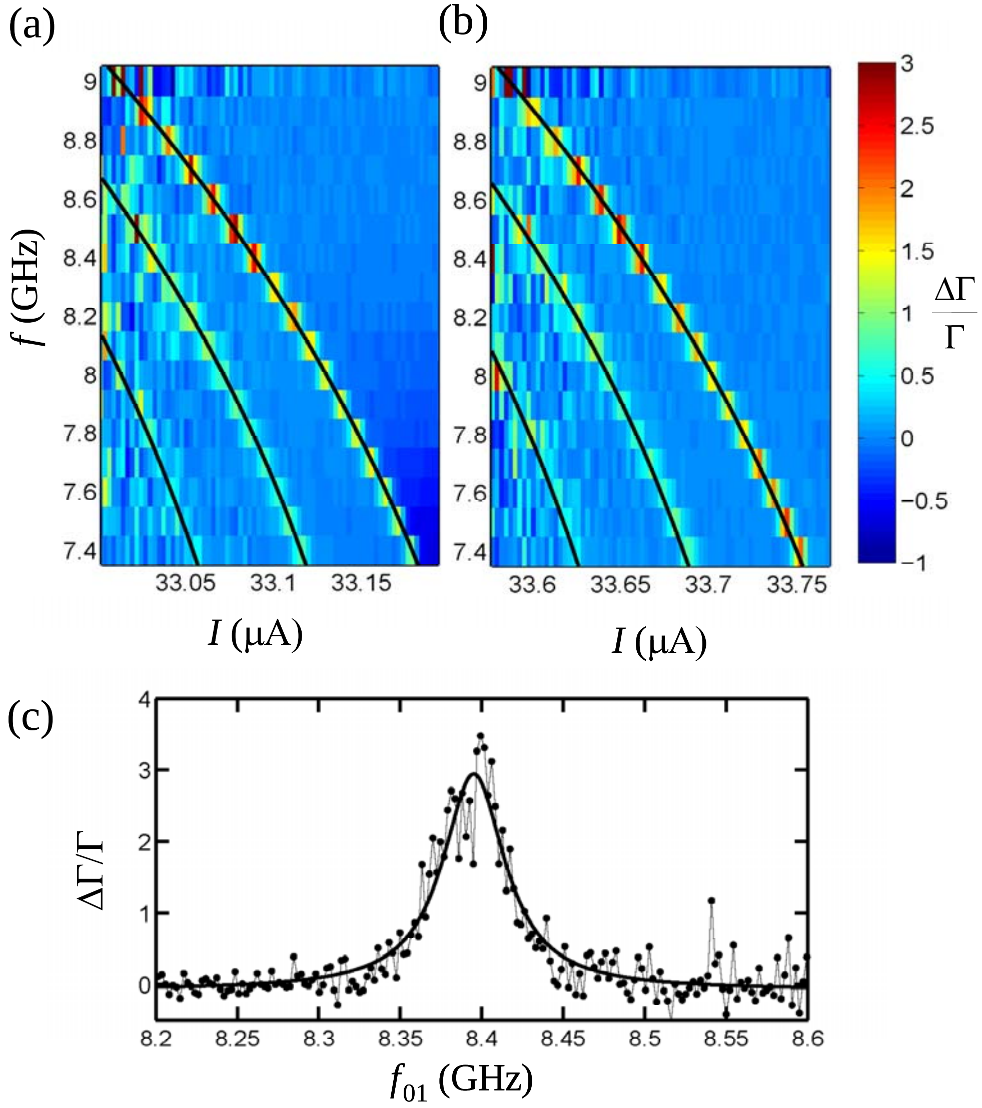

Figure 8.1: (a-b) Spectrum and fits for two flux states of dc SQUID phase qubit DS_1 and (c) a slice of the spectrum measured at 100 mK [37]. The color scale represents the enhancement $(\Gamma_m - \Gamma)/\Gamma = \Delta\Gamma/\Gamma$ in the escape rate, where Γ_m is the escape rate when continuous microwaves were applied and Γ is the background escape rate. The solid curves show a fit to the transitions using a single Josephson junction model. (c) Plot of $\Delta\Gamma/\Gamma$ vs. f_{01} for the $0 \rightarrow 1$ transition with 8.4 GHz microwaves applied. Solid curve is a fit to a Lorentzian to determine the spectroscopic width.

group [36, 37] and I present it here for completeness. For this measurement, the bias current and flux current were ramped as described in Chapter 6; the device was run effectively as a single current biased Josephson junction. Continuous low power microwaves were applied, such that power broadening was not significant (low power limit). When the energy level spacing was resonant with the microwave frequency an enhancement in the escape rate was observed. The ramp was repeated approximately 10^5 times for each microwave frequency to obtain adequate statistics. The enhancement in the escape rate $\Delta\Gamma/\Gamma = \left(\Gamma_m - \Gamma\right)/\Gamma$ is plotted in Fig. 8.1, where Γ_m is the escape rate with microwaves and Γ is without. In practice what is measured is the time at which the junction switches to the voltage state, I converted the switching time to qubit junction current I in the plot by separately measuring I vs. time t (see Chapter 5).

Figure 8.1(a) shows the spectrum of DS_1 for the flux state $n_f = -1$ and Fig. 8.1(b) shows the next flux state $n_f = 0$ at 100 mK. The solid curves are fits using a single junction model, numerically solved, with a capacitance of $C = 4.468 pF$ and a critical current of $I_0 = 33.4 \mu A$ in Fig. 8.1(a) and $I_0 = 33.97 \mu A$ for Fig. 8.1(b). The difference in the critical currents in the two fits corresponds to the expected difference in trapped circulating current in the two flux states $\Phi_0 / L \cong 0.59 \mu A$. The two fits demonstrate that regardless of the flux state the single Josephson junction model fits the spectrum quite well.

Along with the first excited state, higher-level transitions are also visible in the spectra, which provide an additional check on the model. For example in Fig. 8.1(a) at $I = 33.05 \mu A$, the $n = 0 \rightarrow n = 1$ resonant frequency is $f_{01} = 8.7 GHz$, $f_{12} = 8.2 GHz$

and $f_{23} = 7.4\,GHz$. I note that these transitions are visible due to a small population in higher levels; this population occurs even without applying microwaves at 100 mK due to thermal excitation. The escape rate readout technique is extremely sensitive to population in the higher levels, making a measurement of higher-level transitions like f_{12} relatively easy. By applying microwaves at approximately 13-14 GHz, I was also able to map out the $n = 0$ to $n = 2$ transition, as will be shown in section 8.2.3.

The spectrum also allows me to find the spectroscopic coherence time T_2^*. Provided I use a low enough power so as to not induce significant power broadening [see Eq. (3.26)], I can use

$$\rho_{11}^{eq} = \frac{\Omega_{01}^2 T_1 T_2 / 2}{1 + (\omega_d - \omega_{01})^2 T_2^2} \quad . \tag{8.1}$$

Figure 8.1(c) shows a slice of the DS$_1$ spectrum when the resonance was at 8.4 GHz. In this plot, I converted the x-axis from current I to f_{01} using the single junction fit shown in Fig. 8.1(a). I should emphasize that for these plot I used a relatively slow current ramp with $dI/dt < 20\mu A/ms$. The solid curve in Fig. 8.1(c) is a lorentzian fit with a full-width-at-half-maximum $\Delta f = 47\,MHz$. Using Eq. (3.19), I find $T_2^* = \pi / \Delta f = 6.8\,ns$. I note that the spectroscopic coherence time is determined by T_1, T_ϕ and T^+, *i.e.* relaxation, dephasing, and inhomogeneous broadening, as well as tunneling. If low frequency noise (inhomogeneous broadening) is present the width will depend on $\left| df_{01} / dI \right|$, which is a function of bias current [38, 57, 107]. Thus T_2^* depends on the current, through both the tunneling rate Γ_1 and $\left| df_{01} / dI \right|$. Spectroscopic coherence times in this device ranged from $T_2^* = 1ns$ to approximately $7\,ns$; in general longer times were found at lower currents where df_{01}/dI is smaller, as expected.

8.1.2 SQUID DS$_1$ Rabi Oscillations and Relaxation

The relaxation time of SQUID DS$_1$ was measured using a variety of techniques before I joined the group. A list of the measured characteristic times in this device and the techniques used to obtain them are given in Ref. [108]. Here I quote these results, as given by S. K. Dutta [34]. A relaxation time of approximately 14 ns was found using a temperature dependent escape rate fit technique [109]. Measurements of the escape rate after preparing an initial population in the excited states yielded several exponential decay times, an initial one of $T_{1a} \approx 2\,ns$ for $t < 2\,ns$, then $T_{1b} \approx 6\,ns$ for $2\,ns < t < 20\,ns$, and a final one of $T_{1c} \approx 60\,ns$. The initial decay was found to arise from tunneling of population in the second excited state, while the final two time constants appear to be related to the population in $n = 1$ [110]. Unfortunately, with the escape rate measurement technique it is difficult to distinguish contributions from the different energy levels. Finally, Rabi oscillation measurements on this device showed an exponential decay constant of $T' = 6$ to 15 ns, depending on the bias point.

8.2 SQUIDs DS$_{2A}$ and DS$_{2B}$

8.2.1 SQUIDs DS$_{2A}$ and DS$_{2B}$ Spectrum

The behavior of SQUID phase qubits DS$_{2A}$ and DS$_{2B}$ were very similar to that of DS$_1$. It is worth noting that device DS$_1$ had a magnetic field applied to reduce the critical

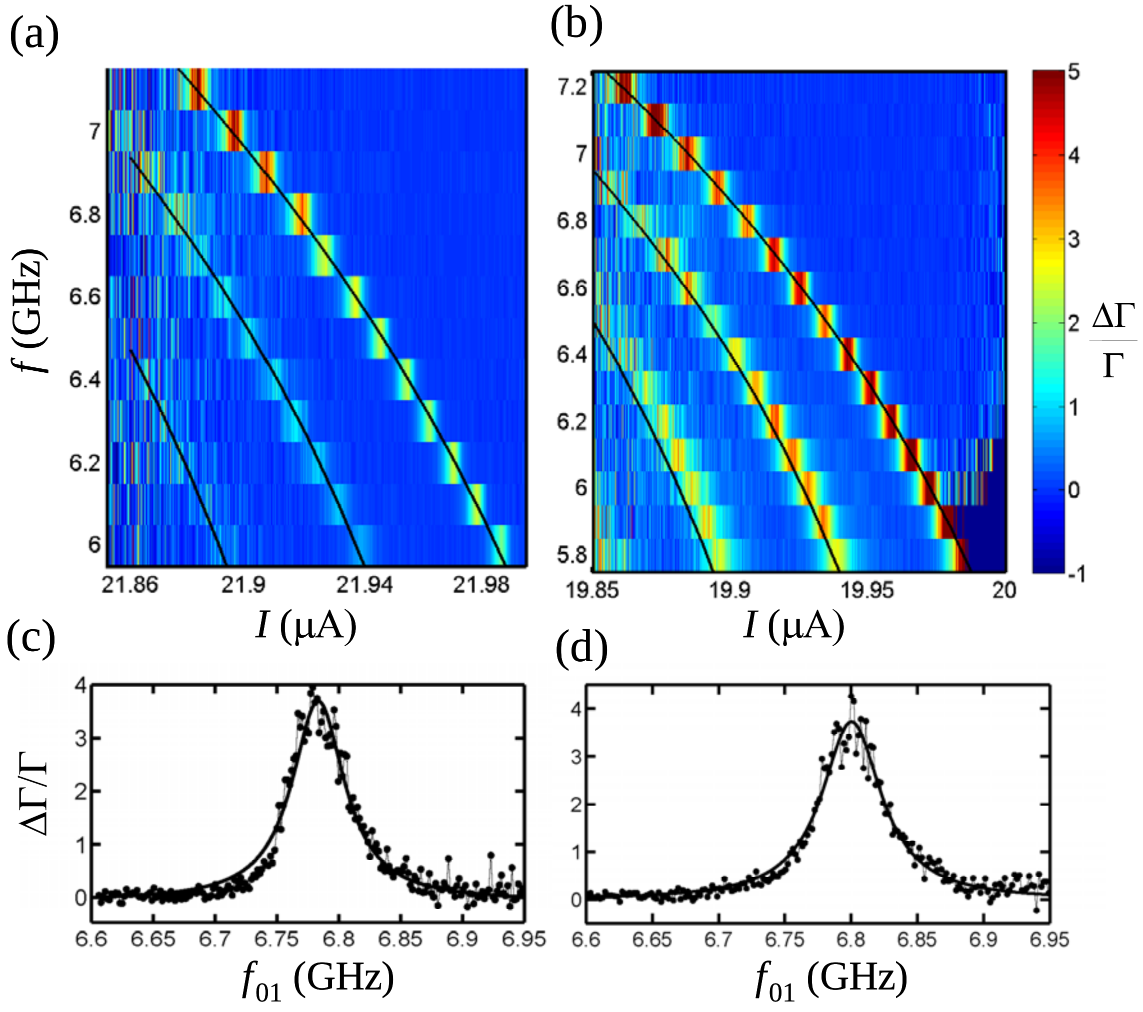

Figure 8.2: Spectrum and spectroscopic widths of devices DS$_{2A}$ and DS$_{2B}$ measured at 25 mK. False color plot of the enhancement $\Delta\Gamma/\Gamma$ versus applied microwave frequency f and current I in the escape rate maps out the spectrum of (a) SQUID DS$_{2A}$ and (b) SQUID DS$_{2B}$. The $0 \to 1$ transitions were fit using a single Josephson junction model (solid line). Plots also show higher-level transitions $1 \to 2$ and $2 \to 3$. The $\Delta\Gamma/\Gamma$ spectrum of $0 \to 1$ transition taken with 6.8 GHz applied microwaves for (c) DS$_{2A}$ and (d) DS$_{2B}$. Solid curves are fits to a lorentzian to determine the spectroscopic coherence time at 6.8 GHz.

current, while DS_{2A} and DS_{2B} did not. Spectra for DS_{2A} and DS_{2B}, obtained using the same procedure as described above, are shown in Figs. 8.2(a) and 8.2(b), respectively. The solid lines are fits using the single junction model with $C = 4.842\,pF$ and $I_0 = 22.153\,\mu A$ in Fig. 8.2(a) and $C = 4.557\,pF$ and $I_0 = 20.1364\,\mu A$ in Fig. 8.2(b). In taking the spectrum of DS_{2B} the background escape rate drifted (possibly due to simple drift in the flux). I removed the drift in Fig. 8.2 by lining up the escape rates without applied microwaves and applying the same shift to the data with microwaves.

Figures 8.2(a) and 8.2(b) also show signs of initial population in higher levels, even though the dilution refrigerator was at base temperature. This was later minimized by minimizing the time the device spent in the voltage state after it switched; the device was retrapped in the zero voltage state within a few μs after switching. This prevented the self-heating that lead to higher level population evident in Fig. 8.2(a) and (b).

As shown in Fig. 8.2(c), I measured $\Delta f = 52 MHz$ when 6.8 GHz microwaves were applied to DS_{2A} or a spectroscopic coherence time $T_2^* = \pi / \Delta f = 6\,ns$. Figure 8.2(d) shows the results for device DS_{2B}; I measured $\Delta f = 55\,MHz$ at 6.8 GHz, which gives a spectroscopic coherence time $T_2^* = \pi / \Delta f = 5.7\,ns$. These times were similar to those found in DS_1.

I also measured the spectroscopic coherence time in DS_{2B} using the pulse readout measurement technique. The bias was held constant, at a negligible tunneling rate and I applied continuous microwaves before performing the readout pulse. The microwaves were then stepped in 3 MHz intervals at this bias point. These measurements do not require a current versus time calibration since each frequency is a separate data set and results in only one population value. This technique allowed me to operate the qubit substantially deeper in the potential well, reducing the effects of inhomogeneous broadening and removing any effects of a continuously ramped current. At $f_{01} = 8.67\, GHz$, I found $\Delta f = 40\, MHz$ or a spectroscopic coherence time $T_2^* = \pi / \Delta f = 7.9\, ns$. A detailed study of the spectroscopic coherence time with respect to bias current for this device is given in Ref. [107].

8.2.2 SQUID DS_{2A} and DS_{2B} Rabi Oscillations and Relaxation

Figure 8.3(a-b) show six different Rabi oscillations (from –10 to –25 dBm in microwave power at the source) in DS_{2A} measured using escape rate readout with 6.8 GHz microwaves applied starting at $t = 0$. The microwaves were turned on at resonance, here $f_{01} = 6.8\, GHz$. The six curves in the top two plots clearly demonstrate the effects of higher levels in the device; higher power Rabi oscillations saturate at long times to higher escape rates as expected if the higher power microwaves produce more off-resonant transitions from $n = 1$ to $n = 2$.

Figure 8.3(c) shows a fit of the of the –16 dBm curve to a modified version of Eq. (3.30),

$$\Gamma = \Gamma_{1a}^{eq} - \Gamma_{1b}^{eq} \exp(-t / T') \left[\cos\left(\overline{\Omega}_{01} t\right) + \sin\left(\overline{\Omega}_{01} t\right) / T' \overline{\Omega}_{01} \right], \qquad (8.2)$$

using the fit parameters $\Gamma_a^{eq} = 7 / \mu s$, $\Gamma_b^{eq} = 5 / \mu s$, decay time $T' = 10.3\ ns$ and Rabi frequency $\overline{\Omega}_{01} = 2\pi / 3.8\, ns$. The initial discrepancy between the data and Eq. (8.2) is due to the several nanosecond rise time of the microwave source, which resulted in a poor fit at the start of the waveform [37].

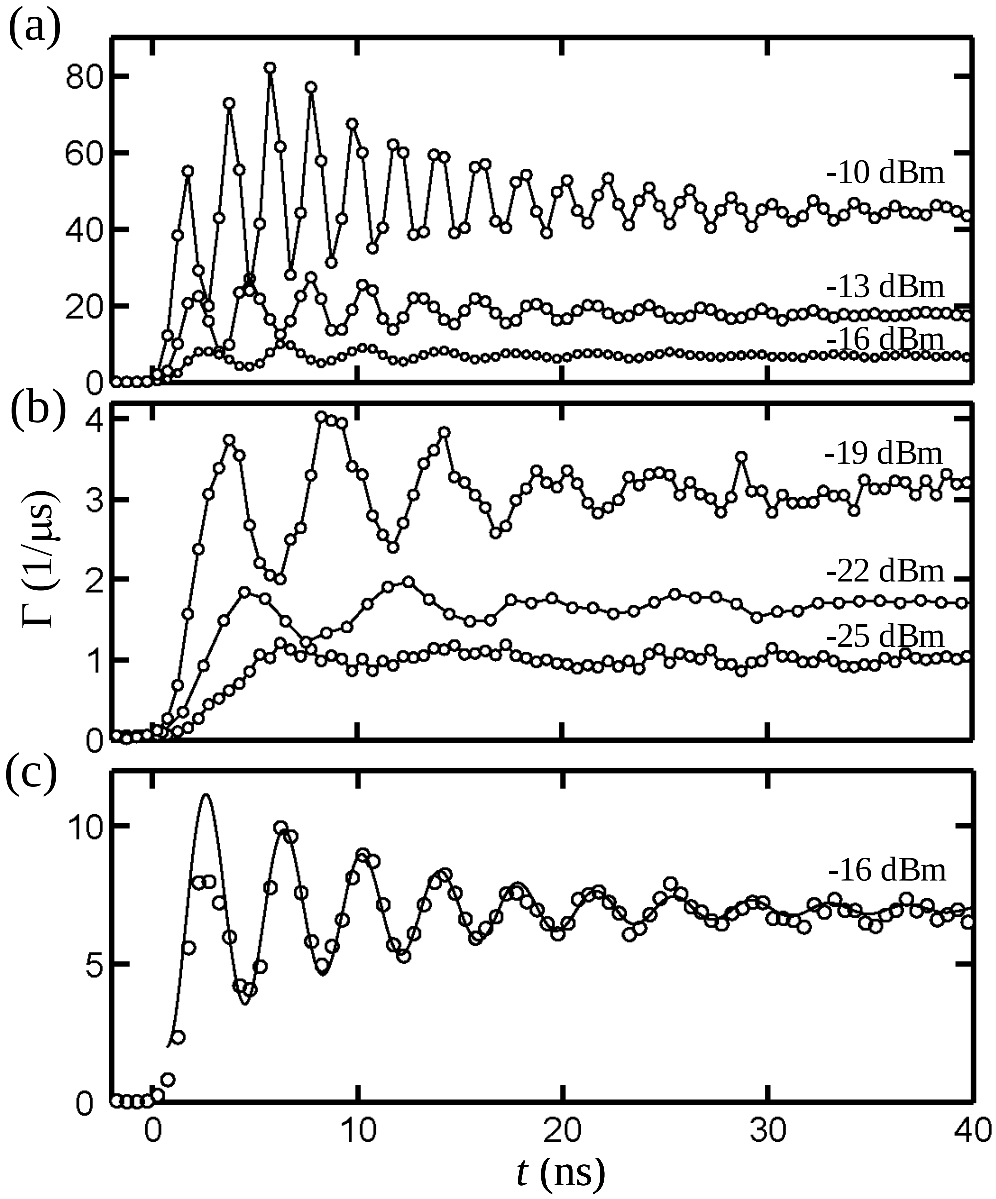

Figure 8.3: Rabi oscillations in the escape rate for dc SQUID phase qubit DS_{2A} (a) and (b) are Rabi oscillations driven using 6.8 GHz applied microwaves for a variety of microwave powers. The powers listed are those at the microwave source. The Rabi frequency increased as expected for increased microwave powers. (c) Fit (solid line) to the –16 dBm data using an exponential decay to determine the Rabi oscillation decay time constant $T^{'} = 10.3\ ns$.

Figure 8.4(a-b) show similar measurements of Rabi oscillation in the escape rate in SQUID DS_{2B}, with 6.6 GHz microwaves applied. Here the solid curve in Fig. 8.4(c) is a fit to Eq. (8.2) with $\Gamma_a^{eq} = 20/\mu s$, $\Gamma_b^{eq} = 16/\mu s$, $T' = 15\ ns$ and Rabi frequency $\overline{\Omega}_{01} = 2\pi/3.15\ ns$. I note the decay times in these devices did depend somewhat on the bias current, with some data containing decay times as short as 5 ns. However, none of these Nb devices (DS_1, DS_{2A}, DS_{2B}) had Rabi decay times T' exceeding 10 to 15 ns and none showed clear oscillations after about 40 ns.

While it was relatively easy to see Rabi oscillations in the escape rate, this measurement technique has several shortcomings. Under typical conditions, what is actually measured is mostly determined by the population in states with $n > 1$. Based on multi-level density matrix simulations [65], it appears that the population in the higher levels is typically proportion to p_1, since population in higher levels in mainly created by pumping from $n = 1$. However, even if no leakage to $n = 2$ existed, the escape rate method still requires precise knowledge of Γ_1 to determine p_1, which is subject to error. This measurement technique is also inefficient and somewhat susceptible to drift, since the entire oscillation is determined through repeated measurements of random tunneling events, many of which correspond to switching events at times, when the oscillations have died away.

For comparison, Figure 8.5 shows Rabi oscillations in the probability p_1 in device DS_{2B} [98] measured using the pulse technique. For these measurements, I found p_1 using pulse measurements with different pulse sizes (see Chapter 7) and fitting to the entire switching curve. I applied microwaves on-resonance at 6.2 GHz to induce Rabi

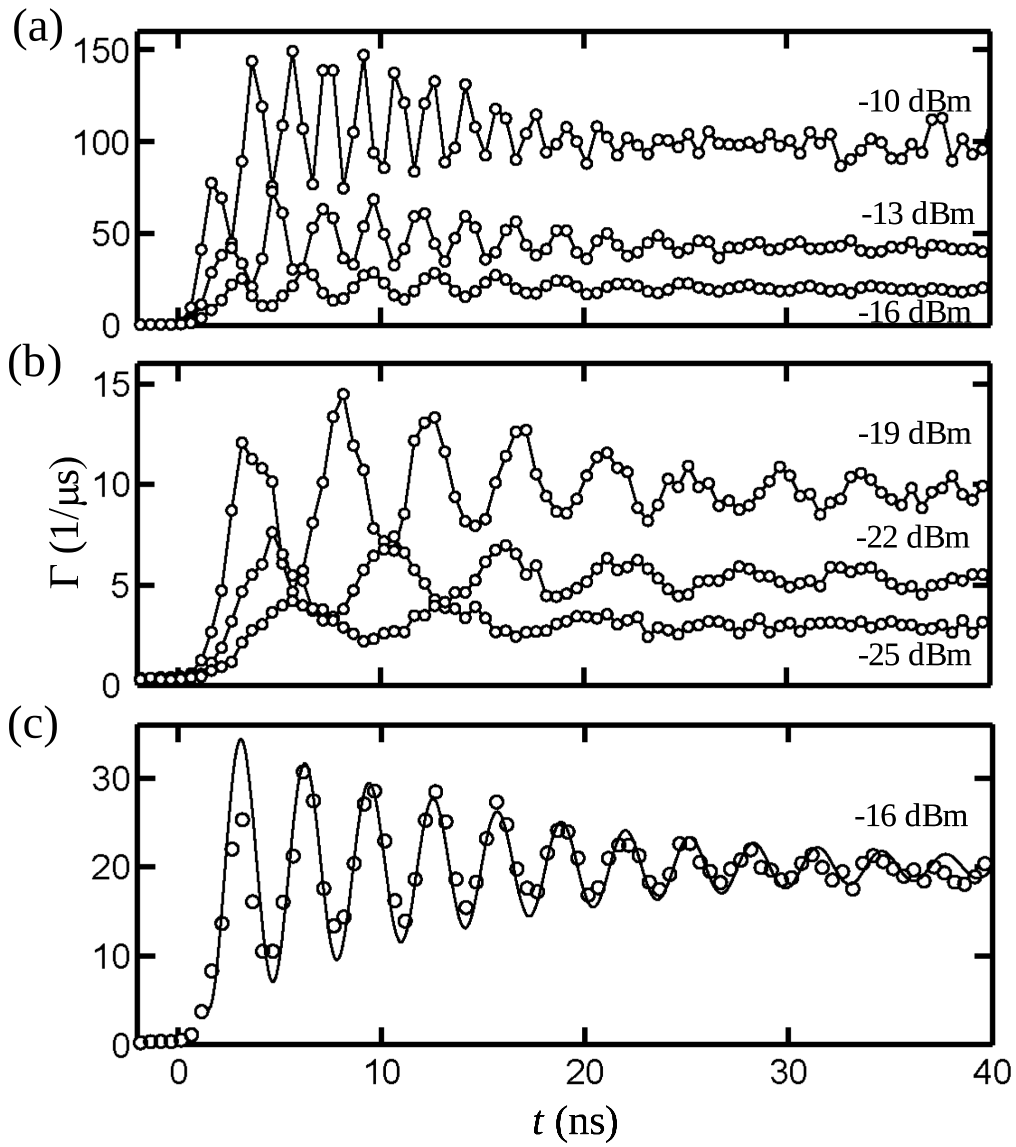

Figure 8.4: Rabi oscillation in the escape rate for device DS_{2B}. (a) and (b) show Rabi oscillations measured in the escape rate when 6.6 GHz microwaves were applied for a variety of microwave powers (referred to the microwave source). (c) Solid curve is a fit to the –16 dBm data using Eq. 8.1 to determine the Rabi oscillation decay $T' = 15\,ns$.

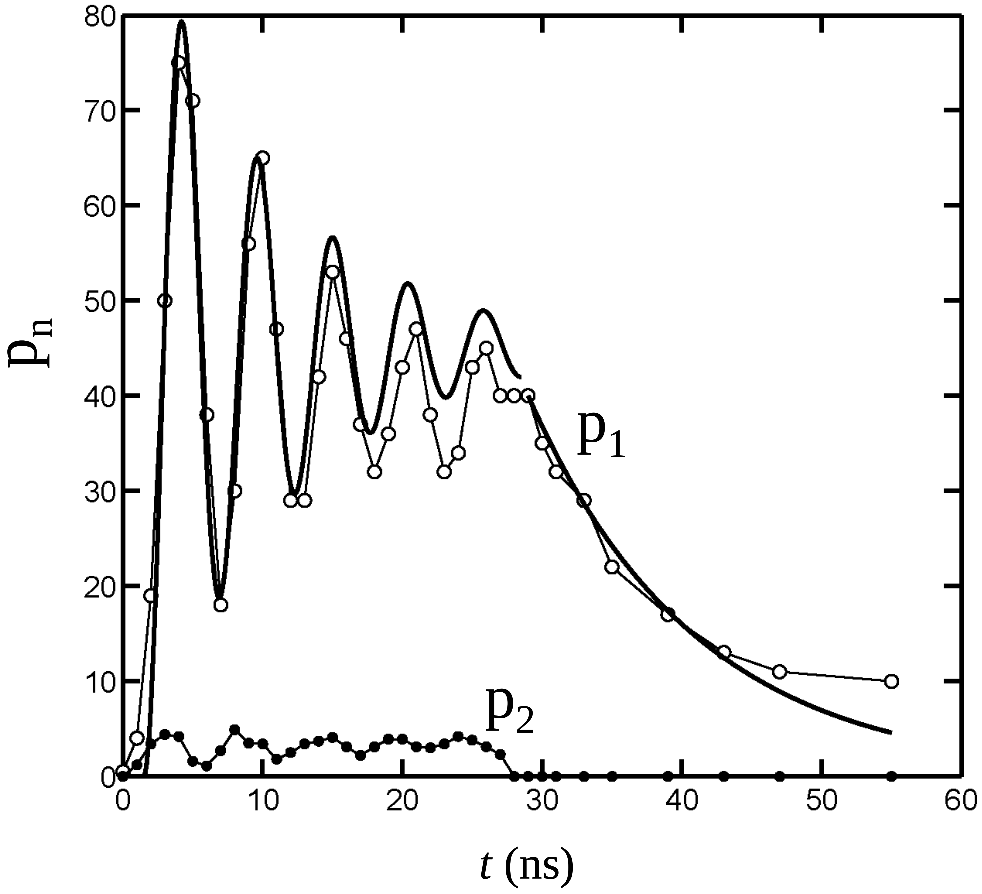

Figure 8.5: Rabi oscillation in the probability p_1 of occupying $n=1$ in device DS$_{2B}$ using the pulsed readout technique. On-resonance 6.2 GHz microwaves were applied to induce Rabi oscillations between $t=0$ and $t=28\,ns$. The microwaves were then shut off to measure the relaxation time. By fitting the entire switching curve (not shown) the population p_2 in $n=2$ was also determined. The dark curve is a fit to the Rabi oscillation and the subsequent decay in p_1. A single exponential relaxation time $T_1=12\ ns$ does a poor job of describing the entire decay.

oscillations from $t = 0\ ns$ to $t = 30\ ns$. I then switched off the microwaves and followed the subsequent decay. The open circles in Fig. 8.5 correspond to the probability p_1 of being in $n = 1$. At each time I took 15,000 points at 15 different pulse amplitudes. By fitting the entire switching curve, I also found p_2, the population in $n = 2$, which are plotted as solid circles. The dark solid curve is a fit of p_1 vs. t to the Rabi oscillation and the subsequent exponential decay. The Rabi oscillations from $t = 0\ ns$ to $t = 30\ ns$ was a fit to Eq. (3.30), with $\rho_{11}^{eq} = 0.45$, $T' = 10\,ns$ and $\overline{\Omega}_{01} = 2\pi / 5.3\,ns$. Ordinarily one would expect $\rho_{11}^{eq} = 0.50$, where here it is a factor of 0.9 smaller. This factor could account for Landau-Zener transitions causing loss of measurement fidelity or relaxation that might occur during the measurement pulse. Moreover p_2 was not included in Eq. (3.30) so it should not fit perfectly. Nevertheless, Fig. 8.5 shows reasonable agreement for the first three oscillations. However, the final two oscillations lie below the fit; this is quite peculiar and the cause is not known.

After the microwaves are shut off at $t = 29\ ns$ the subsequent relaxation appears to have two time constants, similar to what was seen in DS$_1$. Starting from when the microwaves were shut off, just before $t = 29\ ns$, the fit has an exponential decay of about 12 ns. This fits the data up to about $43\ ns$, but for $t > 43\ ns$ the data clearly has a much longer time constant.

The Rabi oscillations and subsequent decay as measured by the pulse technique can be directly compared to those found using the escape rate technique. Figure 8.6(a) shows the background escape rate that was used to find Γ_0. I also show in Fig. 8.6(a) the Rabi oscillation data as measured using the escape rate readout (visible as a spike near

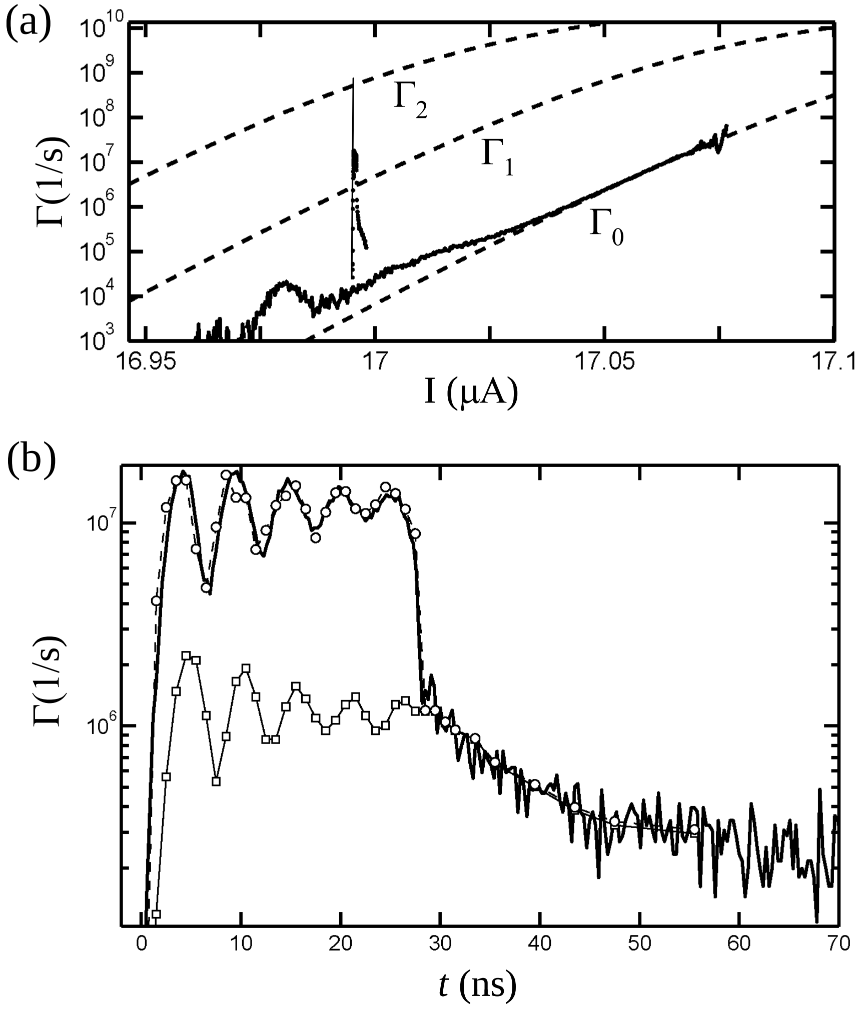

Figure 8.6: Comparison of escape rate and pulsed measurements of Rabi oscillations and subsequent relaxation. (a) Escape rate vs. current (solid curve) with no applied microwaves is fit to Γ_0 to determine Γ_n (dashed curves) during the Rabi oscillations and decay. (b) The dark solid curve is the escape rate of a Rabi oscillation and decay in DS$_{2B}$ (same experiment as in Fig. 8.5). The solid curve with open squares is the predicted escape rate only considering $n = 1$ using the pulsed measurements of p_1 from Fig. 8.5 and Γ_1 from the fit of Fig. 8.6(a). The dashed line with circles includes the lowest three levels.

$I = 16.99\,\mu A$. From the fit to Γ_0, I estimated that during the measurement $\Gamma_0 \approx 3x10^3 / s$, $\Gamma_1 \approx 3x10^6 / s$, and $\Gamma_2 \approx 6x10^8 / s$. The dark solid curve in Fig. 8.6(b) shows the Rabi oscillations measured using the escape rate. The semi-log plot is the same data shown in Fig. 8.6(a) as a spike, except here the time scale has been expanded to make the oscillations visible. This data was taken at the same bias current and microwave power as I used for taking the data in Fig. 8.5. The open squares highlighted with a solid curve show the escape rate contribution from the first excited state $\Gamma_1 p_1 = 3x10^6 * p_1$, with p_1 being the values plotted in Fig. 8.5, which were obtained from pulsed measurements. The open circles highlighted with the dashed line include $n = 0$, 1 and 2 with $\Gamma_2 = 4x10^8 / s$; this value for Γ_2 is about 30% smaller than I estimated based on Γ_0, perhaps because of uncertainty deducing Γ_2 from the fit to Γ_0.

After the Rabi oscillation ends at about 30 ns, p_1 and Γ_1 describe the subsequent decay of the escape rate very well. The two decay constants are also obvious in this semi-log plot, just as seen in the pulse data, with the second $T_1 > 50\,ns$. Also evident in Fig. 8.6 is the rapid decay of p_2 after the oscillation. A large fraction of the extremely rapid decay in p_2 can be attributed to the large escape rate $\Gamma_2 \cong 4x10^8 / s$.

8.2.3 Coupled Qubits DS_{2A} and DS_{2B}

Devices DS_{2A} and DS_{2B} were coupled to each other via an on-chip coupling capacitor [C_c in Fig. 4.2(b)]. This coupling allowed me to prepare entangled states of the system [45]. The coupling between the two qubits is most easily visualized in its

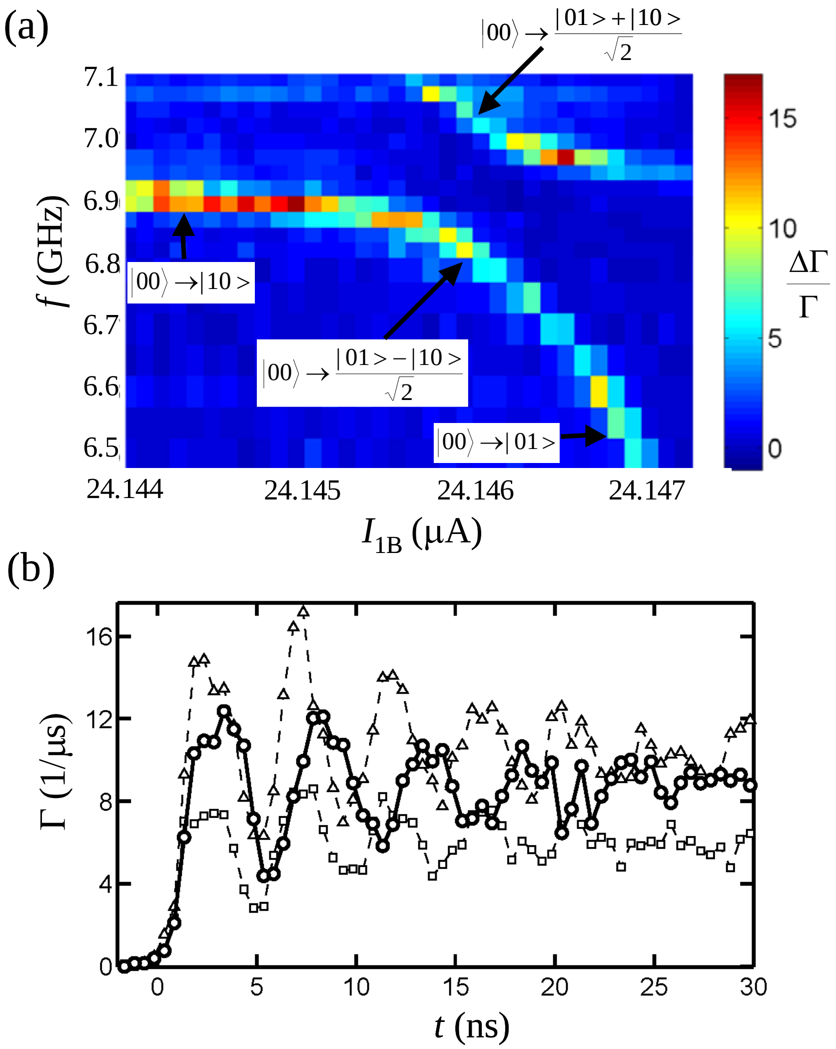

Figure 8.7: Coupled qubits DS$_{2A}$ and DS$_{2B}$. (a) A clear avoided level crossing is visible in the spectrum of the coupled qubits. False color map shows the microwave enhancement in the escape rate with microwaves. The current through qubit DS$_{2B}$ is ramped in time, while qubit DS$_{2A}$ is held fixed. A few of the transitions from $|00\rangle$ are labeled. (b) Bold curve shows Rabi oscillations when strong microwaves were applied at the upper avoided level crossing (7.037 GHz). The increased frequency for the detuned oscillations (dashed curves) is consistent with the qubit being driven to the entangled state during the oscillations.

spectrum. To obtain the spectrum shown in Fig. 8.7, I held qubit DS_{2A} at a fixed frequency f_{01}, while the current through qubit DS_{2B} I_{1B} was ramped. Unfortunately with the escape rate measurement technique it was problematic to measure qubit DS_{2B} at frequencies higher than 7.1 GHz or to couple the two devices together at frequencies lower than 6.9 GHz. The problem was that the escape rate of the device that is held at fixed bias needs to be small, but still experimentally measurable. I applied continuous microwaves and monitored the voltage line of qubit DS_{2A} to detect switches while the current through DS_{2B} was swept. In these experiments, DS_{2A}'s microwave line was used, but the microwaves strongly coupled to DS_{2B} as well. DS_{2A} was biased such that a switch in DS_{2B} would very quickly cause DS_{2A} to also switch to the voltage state.

Figure 8.7 shows a clear avoided level crossing for transitions from $|00>$ to $|01>$ and $|00>$ to $|10>$. Here the first index indicates the state of DS_{2A} and the second the state of DS_{2B}. The minimum splitting is about 250 MHz. Plugging the design values for C and C_c into Eq. (2.24), I find the expected coupling constant $\xi = 0.04$. The experimental value from Fig. 8.7 is $\xi = 250MHz/6900MHz = 0.036$, which matches the design value reasonably well.

When the two qubits are biased at different 0 to 1 transitions frequencies, they are dynamically decoupled [45]. In this case, applying resonant microwaves to either qubit produces Rabi oscillations as shown previously. On the other hand, if the qubits are biased to the same f_{01}, one gets maximal dynamical coupling and an avoided crossing. The solid curve and open circles in Fig. 8.7(b) shows a Rabi oscillations for this situation. I find clear Rabi oscillations consistent with the system cycling between $|00>$ and the entangled state. The open circles in Fig. 8.7(b) show an on-resonance Rabi oscillations for applied microwaves of 7.037 GHz (-14 dBm). These oscillations are consistent with $|00> \leftrightarrow \frac{|01>+|10>}{\sqrt{2}}$ transitions. The square and triangles show a Rabi oscillation at the same bias point, but with microwaves applied at 7.012 GHz and 7.062 GHz respectively, *i.e.* detuned by ±25 MHz. The off-resonance microwaves produced a faster Rabi-flopping frequency as expected [19, 37, 58] and therefore demonstrate that the oscillation when driving at 7.037 GHz is consistent with pumping to the entangled state $\Psi = \frac{|01>+|10>}{\sqrt{2}}$. In other words, if the microwaves were interacting with uncoupled qubits, the smallest flopping-frequency would be at 6.9 GHz. The same procedure was done at the anti-symmetric avoided crossing and oscillations were seen with microwaves applied at 6.76 GHz,.

Unfortunately the escape rate technique and the short coherence times of these qubits made it difficult to perform rigorous analysis of the dynamics of the entangled system. The Rabi decay time appears to be $T' \approx 15 ns$ for both coupled qubit frequencies, however it was difficult to see any oscillations after 20 ns so $T' \approx 15 ns$ is either an overestimate, or something more complicated is happening in the coupled system. This T' is roughly the same as the decay times of the individual qubits. In hindsight using the pulse technique would have allowed for a more detailed analysis of the coupled states and potentially seperate readout of the individual qubits [111].

It is also possible to observe higher energy level transitions. Figure 8.8 shows transitions from $|00>$ to $|20>$, $|02>$ and $|11>$. For this data, I again fixed $f_{01} = 6.95 GHz$ in qubit DS$_{2A}$, while qubit DS$_{2B}$'s frequency was ramped. At $I_{1B} \approx 24.146 \mu A$, qubit B had $f_{01} \approx 6.45 GHz$, based on my measurements of the f_{01}

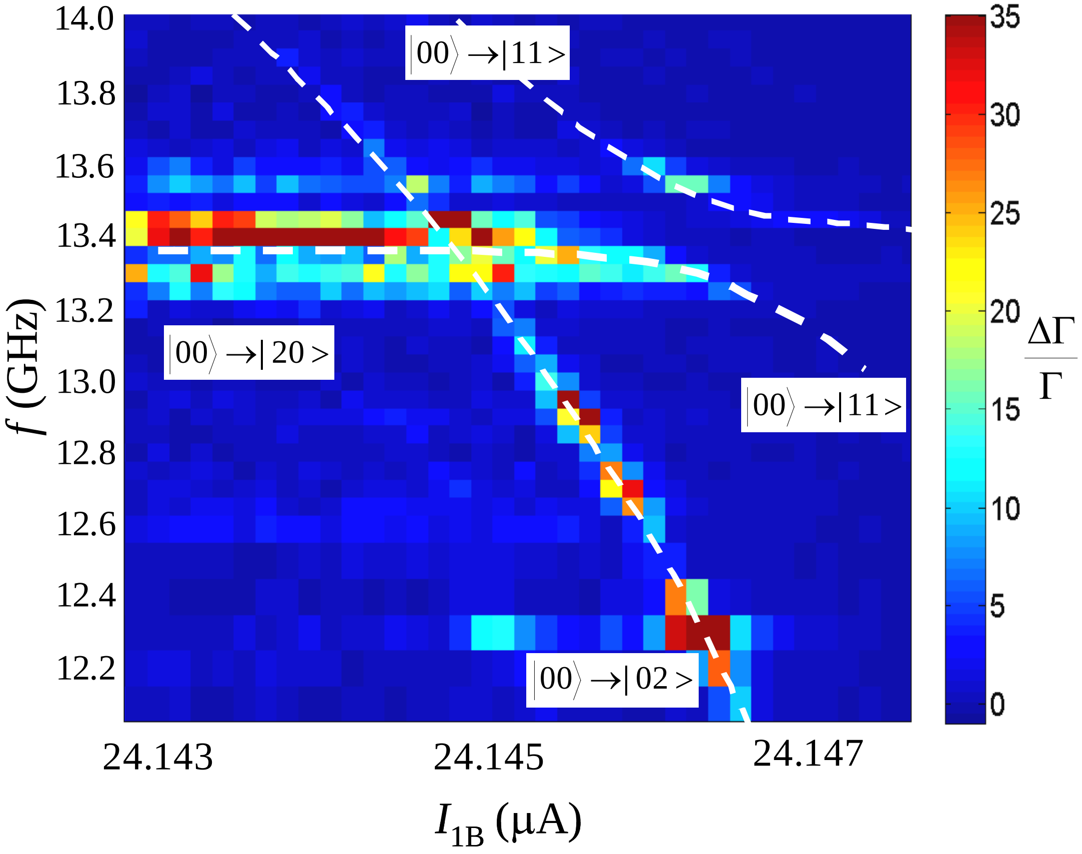

Figure 8.8: Higher level transition spectrum of coupled qubits DS_{2A} and DS_{2B}. The coupled qubits were driven with continuous microwaves from $|00\rangle$ to the labeled transitions. The false color map represents the enhancement in the escape rate when microwaves were applied. The $|11\rangle$ state transition is very weak but especially important since it is part of our computational basis. The location of the transition $|00\rangle \rightarrow |11\rangle$ matches fairly well with predictions from the lower spectrum in this data set, not shown here. The white dashed curves are guides to the eye.

transition spectrum (not shown); therefore one would expect the $|00> \rightarrow |11>$ transition at approximately 13.4 GHz. This is relatively close to the measured value of 13.5 GHz. Due to the larger microwave powers required to drive these transitions and the smaller coherence times of higher states, I found it difficult to finely resolve the spectrum.

In the coupled experiments described above, I used a single microwave line that coupled to both qubits. This line (A) was originally intended to only strongly couple to qubit DS_{2A}. I also had a microwave line for qubit B. By adding attenuators and an adjustable phase shifter, I could effectively send microwaves to each device separately by arranging that the combined signals from both lines cancelled at one qubit and not at the other. For example, Figure 8.9(a) shows a spectrum of the coupled qubits when the microwaves were “in-phase” (*i.e.* both devices received in-phase microwave currents). Figure 8.9(b) shows the situation when the microwaves were “out-of-phase” (*i.e.* when one device receives microwave currents that were 180° out of phase with respect to the other). As before, the resonant frequency of qubit DS_{2B} was ramped while qubit DS_{2A}‘s frequency was held fixed. To apply the different phases I used a splitter after the microwave source and placed a 3 dB attenuator on the input to microwave line A and a phase shifter in microwaves line B.

The phase shift required to produce the out-of-phase condition was calibrated by separately viewing the enhancement and Rabi oscillations in the individual qubits. For example at 6.8 GHz, when the phase shifter was set to 6.5° (which produced the minimum enhancement in each device and so was probably out of phase), -6 dBm at the source produced 5ns period Rabi oscillations in each qubit. Similarly at 33° (which produced the maximum enhancement in each device and so was probably in phase) a

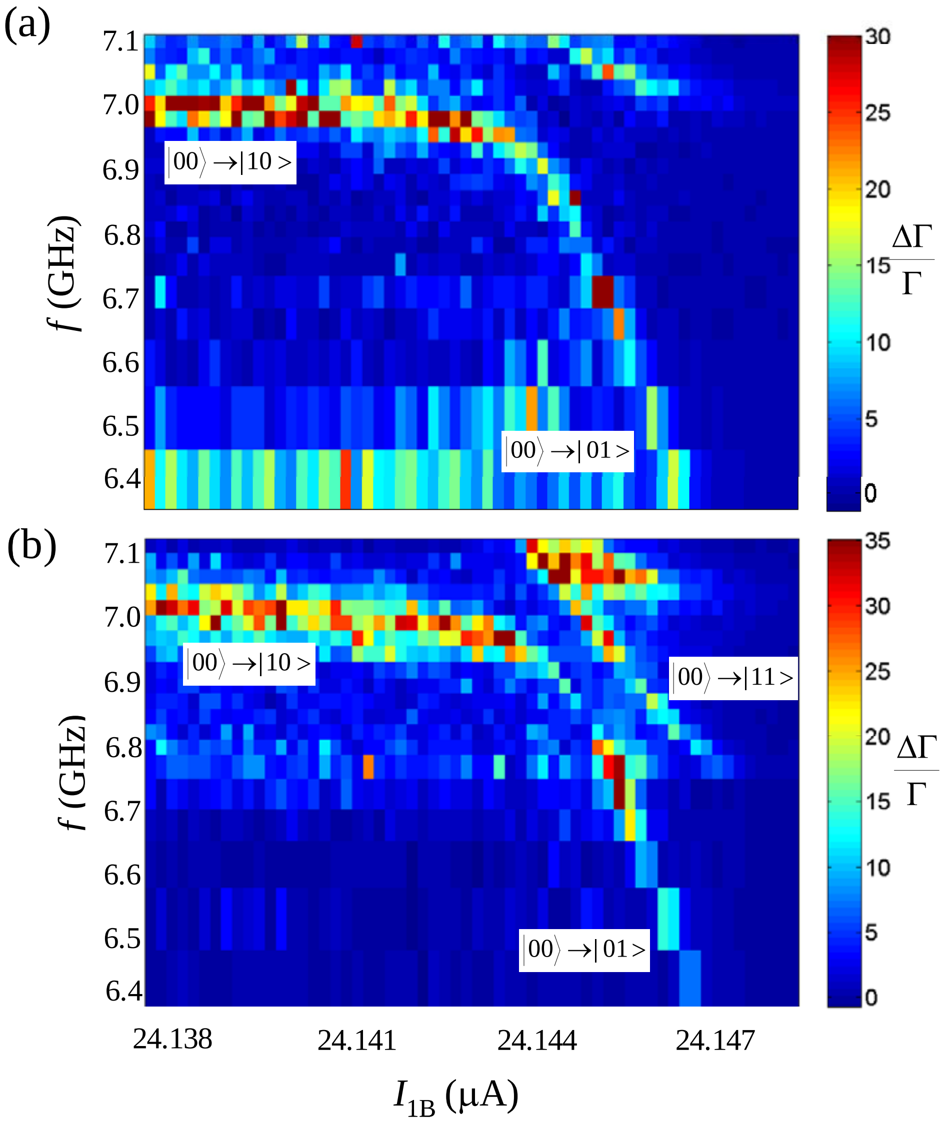

Figure 8.9: Phase dependent spectrum near the avoided crossing. The spectrum of two coupled qubits DS_{2A} and DS_{2B} was taken when the applied microwaves to each qubit was adjusted to be (a) in-phase at the qubits and (b) out-of phase relative to each other. The phases were calibrated by looking at the qubits individually. Notice that the $|00\rangle \rightarrow |11\rangle$ branch is much more prominent in the out of phase data. The color map is the enhancement in the escape rate when microwaves were applied. See Table 8.1 for powers used at each frequency.

Table 8.1: Microwave power at the source for the in-phase and out-of-phase spectrum of Fig 8.9(a) (33º) and 8.9(b) (6.5º). The source was then split to a 3 dB attenuator in microwave line A and a phase shifter in line B.

Freq (GHz)	**6.4**	**6.5**	**6.6**	**6.65**	**6.7**	**6.75**	**6.775**	**6.8**	**6.825**	**6.85**
Power (-dBm) in-phase	36	8	38	38	39	39	39	39	39	39
Power (-dBm) out-of-phase	35	32	32	28	25	20	20	20	20	20
Freq (GHz)	**6.875**	**6.9**	**6.925**	**6.95**	**6.975**	**7**	**7.025**	**7.05**	**7.075**	**7.1**
Power (-dBm) in-phase	40	40	40	39	37	35	34	32	30	27
Power (-dBm) out-of-phase	21	22	21	22	23	24	23	22	21	21

power at the source of only –16 dBm was required to produce 5 ns period Rabi oscillations. Table 8.1 shows the microwave power I used at different frequencies to produce Fig. 8.9(a) and Fig. 8.9(b).

Figure 8.9 requires some additional discussion. While the states $|10>$ at $I_{1B} = 24.138\,\mu A$ and $|01>$ at $I_{1B} = 24.146\,\mu A$ appear to match, the spectrums in Fig. 8.9(a) and 8.9(b) look quite different elsewhere. The in-phase data in Fig. 8.9(a) looks similar to that obtained using a single microwave source as shown in Fig. 8.7(a). In the out-of-phase data in Fig. 8.9(b) another transition becomes visible that was not seen before, while the lower avoided crossing becomes less visible, even at high microwave powers. This new peak may be a two-photon transition to $|11>$. In particular, this transition depends on qubit B, yet is also at a higher frequency than qubit B’s f_{01}. This behavior may be consistent with in-phase and out-of-phase pumping of the coupled system, but further analysis is clearly needed to understand the significance of the relative microwave phases on coupled qubits. Moreover, what I was trying to test was whether I could select the $|00> \leftrightarrow \frac{|01> + |10>}{\sqrt{2}}$ and $|00> \leftrightarrow \frac{|01> - |10>}{\sqrt{2}}$ transitions based on the relative phase of the two microwave signals. The evidence from Fig. 8.9 is weak at best.

8.3 SQUID DS_{3A}

8.3.1 SQUID DS_{3A} Spectrum

Figure 8.10 shows the transition spectrum of device DS_{3A}, measured using the pulse readout technique using the current flux trajectory shown in Fig. 6.10. Here the bias current, flux current and frequency were fixed for each data point. This device was coupled to another qubit, but the second device was not operational due to an open line; no clear effects of coupling to the other device was seen. Examining Fig. 8.10, many avoided level crossings are clearly visible. I found that the crossing locations did not depend on the flux current, bias current or offset flux combination used to reach the desired qubit frequency, so it was unlikely they were due to the other qubit. These unintended avoided crossings will be discussed in detail in Chapters 9 and 10. A fit to the entire spectrum, including the avoided crossings, will be presented in Chapter 10.

As mentioned above, almost all measurements of device DS_{3A} were taken using the pulsed readout technique. This was done because the alternative approach of using the escape rate technique required operating the device under poor isolation conditions (see discussion in Section 6.3). For the pulse measurement, I used a single-shot mode to extract an approximate p_1; I did not fit an entire switching curve. This significantly sped up the data collection and analysis, but meant that I could only determine the population

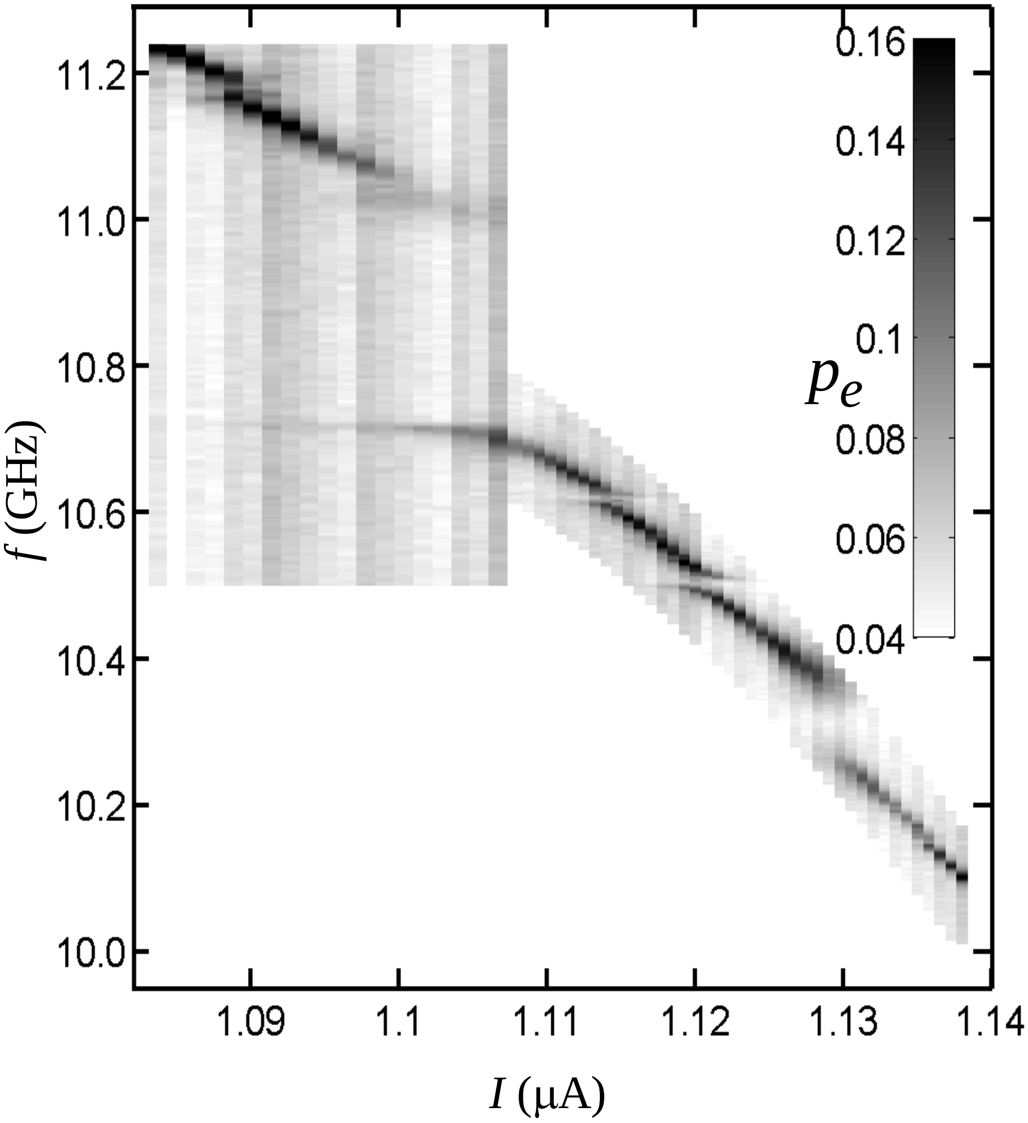

Figure 8.10: Transition spectrum of dc SQUID phase qubit DS_{3A} measured at 20 mK using the pulsed readout technique. The color map represents the fraction p_e that escaped after many repetitions of a single amplitude measurement pulse (each current bias point required a different amplitude). Pure white corresponds to where no data was taken. Several large unexpected avoided level crossings are clearly visible.

within a few percent and could not distinguish higher levels. Also, Landau-Zener tunneling due to the many avoided crossings in this device would be expected to degrade the readout fidelity [66].

8.3.2 SQUID DS_{3A} Rabi Oscillations and Relaxation

Figure 8.11(a) shows seven line spectra measured in device DS_{3A} at different bias currents. Fig 8.11(b) shows the corresponding on-resonance Rabi oscillation (and decay after the microwaves were shut off). For clarity, each curve in (a) and (b) is shifted by an offset; the offset is 0.2 for each successive curve in (a) and 0.5 for each successive curve in (b). In this range of bias currents, as the current through the qubit is decreased (resonance moves towards higher frequency), the system moves towards a small avoided-level crossing at 10.185 GHz and the spectroscopic width increases significantly. The Rabi oscillations and relaxation time also vary quite noticeably, and the spectrum looks less and less Lorentzian as I approach the avoided crossing. This figure explicitly demonstrates that the device behavior depends strongly on the bias point. This is quite unlike our earlier devices. In general, I took data away from any clearly observable splittings, unless otherwise noted, although very small crossing may have existed that affected the device performance.

Figure 8.12 shows the line spectrum and Rabi oscillations, away from any visible splittings. Figure 8.12(a) shows the escape probability spectrum versus microwave frequency when $f_{01} = 10.080\ GHz$ and the current bias is held fixed (circles). The solid line is a fit to a Lorentzian width with the FWHM $\Delta f = 15.0\,MHz$. This gives a good fit and corresponds to $T_2^* = 21.2\,ns$. Figures 8.12(b) and 8.12(c) show on-resonance (10.080

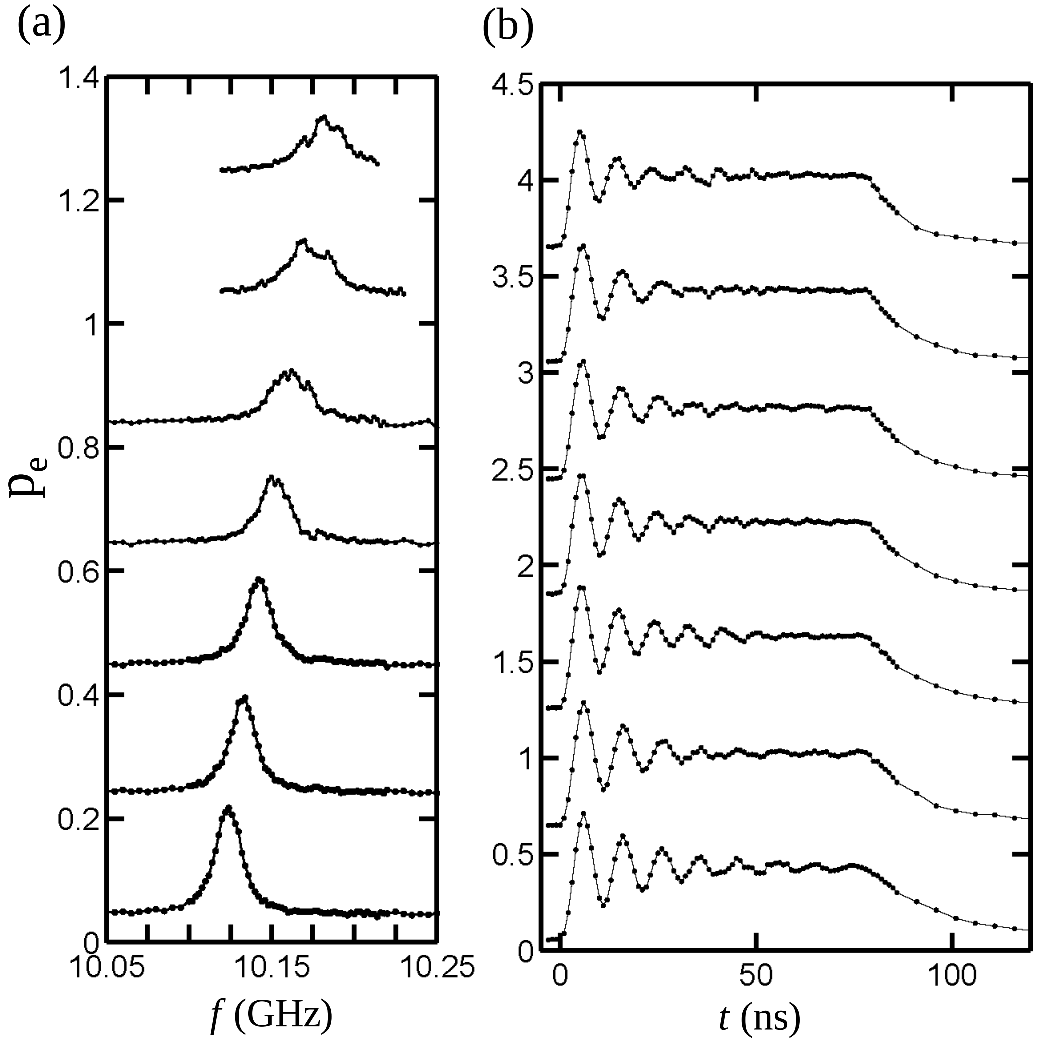

Figure 8.11: Bias dependence of transition linewidth and Rabi oscillation dc SQUID phase qubit DS_{3A}. As the qubit resonance approached a small avoided level crossings at 10.175 GHz, the performance of the device varied significantly. (a) The spectroscopic width varied significantly over a relatively small bias range. (b) The variation in performance with bias point is visible in the decay of Rabi oscillations (taken on resonance with the peaks) and the subsequent relaxation when microwaves were turned off.

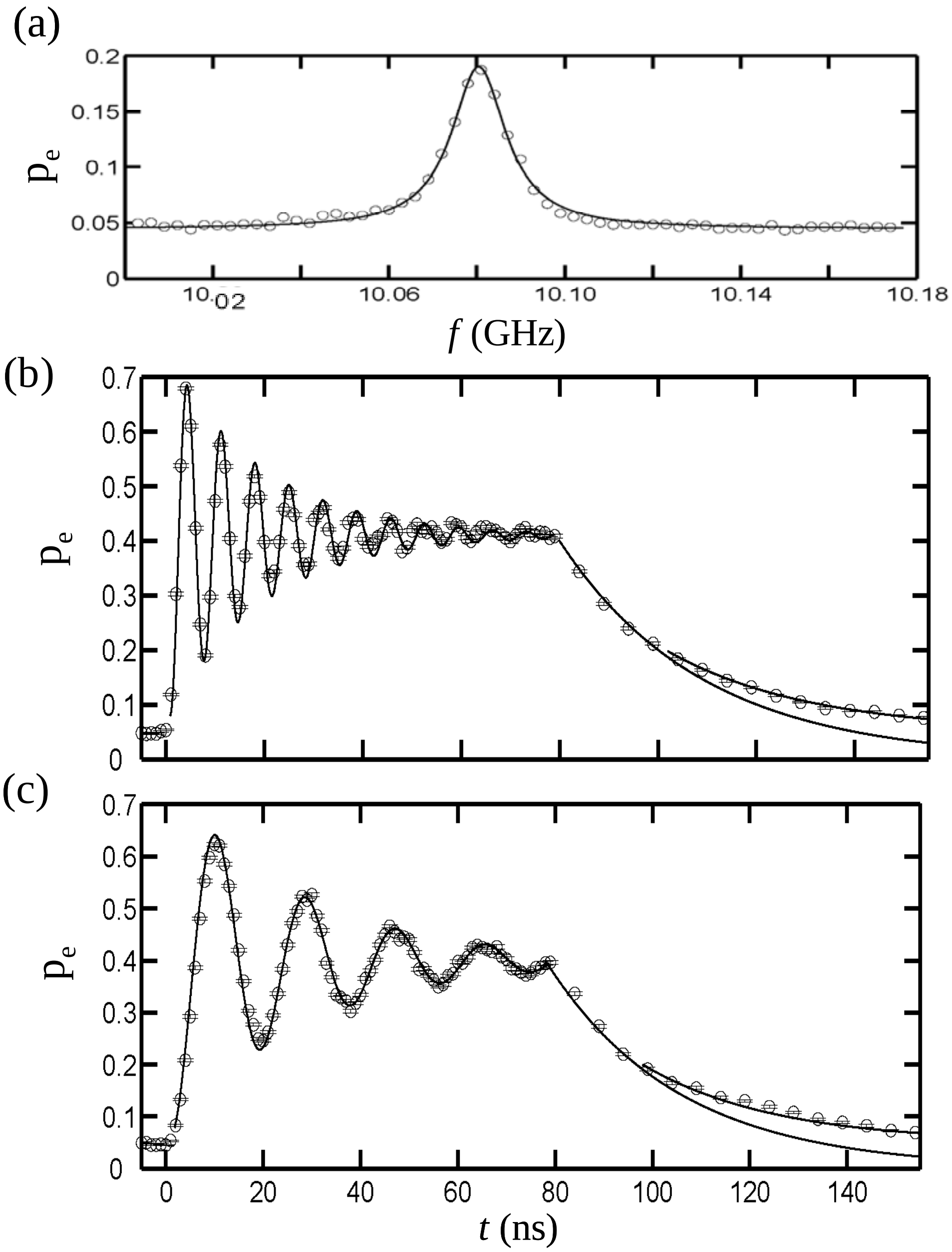

Figure 8.12: Spectroscopic width, Rabi oscillations and relaxation in SQUID DS$_3$. (a) The resonance at 10.080 GHz fits to a single lorentzian peak, with no indication of avoided level crossings. Rabi oscillations and decay (after $t = 80\,ns$) were fit to determine T' and T_1 for two microwave powers (b) –16 dBm and (c) –25 dBm (at the microwave source) at $f_{01} = 10.080\ GHz$.

GHz) Rabi oscillations at powers of –16 and –25 dBm, respectively, followed by relaxation in the devices after the microwaves were shut off at $t = 80\ ns$. The Rabi oscillations in Fig. 8.12(b) were fit using

$$p_e = \rho_{11a}^{eq} - \rho_{11b}^{eq} \exp(-t/T')\left(\cos(\overline{\Omega}_{01}t) + \sin(\overline{\Omega}_{01}t)/\overline{\Omega}_{01}T'\right) \tag{8.3}$$

with $T' = 19\,ns$, $\overline{\Omega}_{01} = 2\pi/7\,ns$, $\rho_{11a}^{eq} = 0.41$ and $\rho_{11b}^{eq} = 0.33$. The subsequent decay is fit with a decay time $T_1 = 29\,ns$. Since I am using a single shot pulse measurement, even with $p_0 = 1$, I still expect $p_e = 0.05$ due to P_{01}. To account for this I have added a second line for $t > 100\,ns$ that includes a 0.05 offset, *i.e*.

$$p_e = 0.05 + 0.4\exp\left(-(t - 80\,ns)/29\,ns\right). \tag{8.4}$$

For Fig 8.12(c), the –25 dBm data was fit using $T' = 27\,ns$, $\overline{\Omega}_{01} = 2\pi/18.5\,ns$, $\rho_{11a}^{eq} = 0.40$ and $\rho_{11b}^{eq} = 0.34$. The subsequent decay is fit with a decay time $T_1 = 27\,ns$. I find rather good agreement for these fits.

As expected the relaxation times were very similar (29 ns versus 27 ns), however the Rabi decay time of the two were quite noticeably different (19 ns at high power versus 27 ns at low power). This is somewhat surprising, but might be caused by current noise around 100 MHz (the qubit is most sensitive to noise at the Rabi frequency) [49]. Another possible explanation is that the qubit is crossing more two-level systems at high microwave power causing an increase in the loss.

The low measured saturation value of 0.40 may be due to Landau-Zener transitions during the measurement pulse. It would have been better to fit the entire switching curve, as this would have yielded a more accurate value for p_1. I note that from the discussion in Chapter 7, even a single ideal pulse with $p_1 = 0$ still produces $p_e > 0$ due to escapes from $\left|0\right\rangle$ and $p_1 = 1$ gives $p_e < 1$; this accounts for the 5% offset visible in Figs. 8.12 (b) and (c) at $t = 0$.

8.3.3 SQUID DS$_{3A}$ Ramsey Fringes and Discussion

The coherence times in device DS$_{3A}$ were long enough to perform a Ramsey Fringe experiment using the pulsed readout technique. Figure 8.13, shows a Ramsey experiment where I applied two detuned $\pi/2$-pulses separated by a time Δt and then performed a pulsed state measurement. The qubit was biased such that $f_{01} = 10.104 \pm 0.003 GHz$ and the microwaves were applied with power such that the on-resonance Rabi frequency was $\overline{\Omega}_{01} = 2\pi/24 ns$, thus $\pi/2$-pulses were 6 ns long. The open circles in Fig. 8.13(a) correspond to detuned microwaves at 10.139 GHz, Fig. 8.13(b) at 10.144 GHz and Fig. 8.13(c) at 10.149 GHz. The solid and dashed lines are fits to the data using a density matrix simulation that takes into account the finite length of the $\pi/2$-pulses (6 ns). The oscillation frequencies closely match the estimated detuning. The solid line is a fit with $T_1 = 28 ns$, $T_2 = 25 ns$ and with detuning $\Delta f = 38 MHz$, $\Delta f = 43 MHz$ and $\Delta f = 48 MHz$ in Figs. 8.1 (a), (b), and (c) respectively. To roughly take into account the reduced measurement fidelity, the fit in Fig. 8.13 used $p_e = .75 p_1 - .05(1 - p_1)$, where p_1 is found from the simulation.

The dashed curves in Fig. 8.13 correspond to the simulation with $T_2 = 20 ns$ instead of $T_2 = 25 ns$. From these results, I estimate $T_2^{ramsey} \approx 24 \pm 4 ns$. I note that this

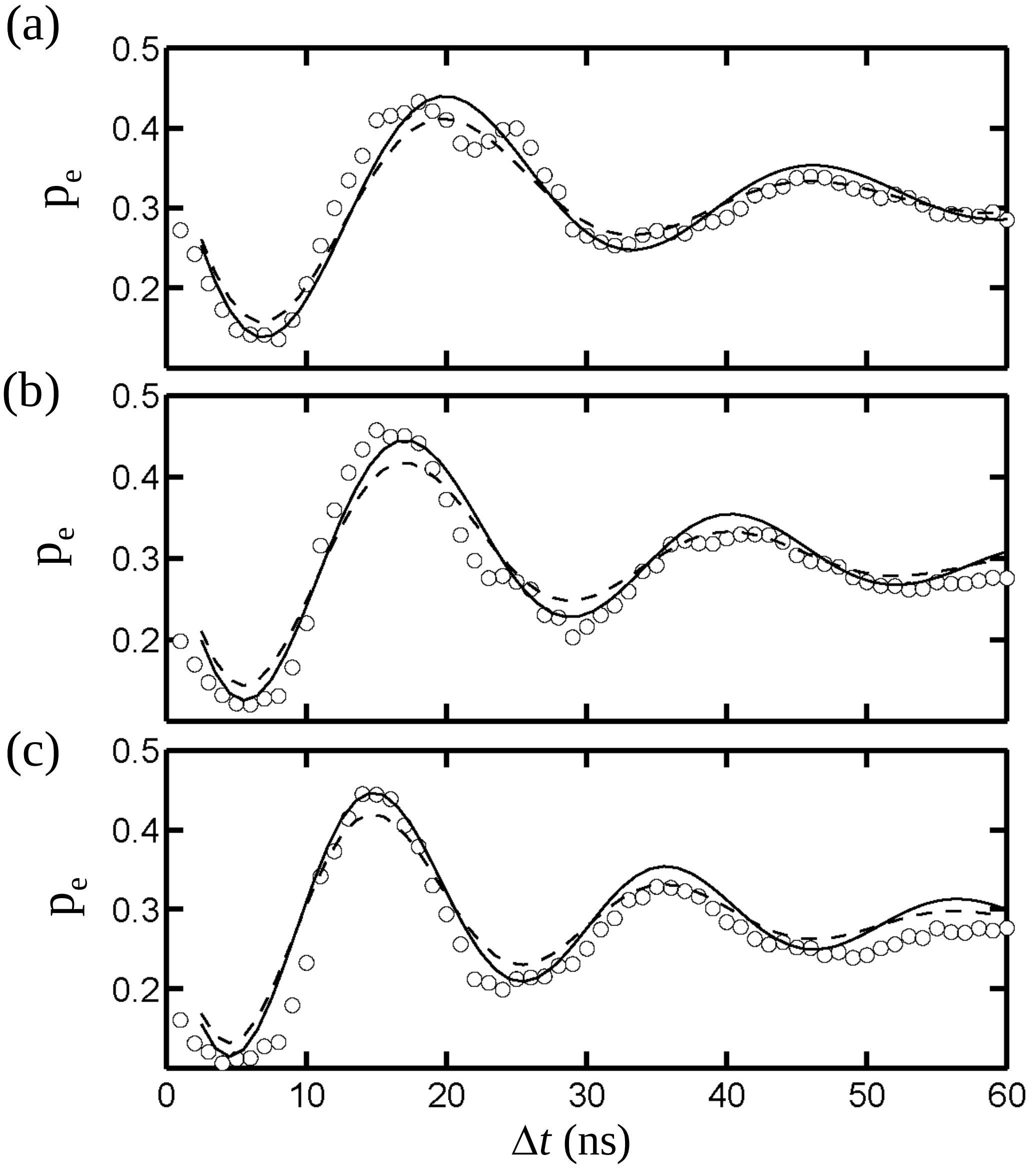

Figure 8.13: Ramsey fringes in dc SQUID phase qubit DS_{3A}. The probability of escape during a measurement pulse is plotted versus the time between two detuned π/2-pulses. The three curves (a-c) show three different microwave detunings (with $f_{01} = 10.104 \pm .003\,GHz$), $f = 10.139\,GHz$, $f = 10.144\,GHz$ and $f = 10.149\,GHz$, respectively. The solid line and dashed lines are fits using a density matrix simulation with $T_1 = 28\,ns$ and either $T_2 = 20\,ns$ (dashed) or $T_2 = 25\,ns$ (solid).

was the only device I measured Ramsey oscillations in; in part this was because the relaxation time was relatively long.

As expected, the Ramsey Fringe decay time matches fairly well with the spectroscopic coherence time, $T_2^{ramsey} \approx 24 \pm 4 ns$ and $T_2^* \approx 21 ns$. Both measurements are sensitive to low frequency noise and should measure the same thing. Unfortunately the short relaxation time of the device did not allow me to make spin-echo measurements and remove dephasing due to low frequency noise.

I also note that the true coherence time T_2 can be found from [59]

$$1/T_2 = 1/T_2^{ramsey} - 1/T_2^{+}, \tag{8.5}$$

where T_2^{+} is the inhomogeneous broadening time scale. If I assume $T_2^{+} = \infty$, so $T_2 = T_2^{ramsey} = 24\ ns$ and use the measured value of $T_1 = 28\ ns$, I find an expected Rabi oscillation decay $T' \approx 26 ns$ using Eq. (3.30). This predicted time is close to the measured low power value of $T' = 27 ns$. This suggests the system has little inhomogeneous broadening. If I also assume that only pure dephasing T_ϕ and dissipation T_1 affect my measurements of T_2, I can then estimate a dephasing $T_\phi = 42 ns$ using Eq. (3.14).

With separate estimates of the relaxation time T_1 and coherence time T_2, I can predict the affect of power broadening on the spectroscopic resonance peak [see Eq. (3.27)]. The solid line in Fig. 8.14 shows the expected spectroscopic width versus Rabi frequency based on Eq. (3.28) with $T_1 = 28 ns$ and $T_2 = 24 ns$. The open circles correspond to data taken at $f_{01} = 10.078 GHz$ with powers ranging from –52 to –25 dBm in 3 dBm intervals. The crosses indicate points at which the microwave power was

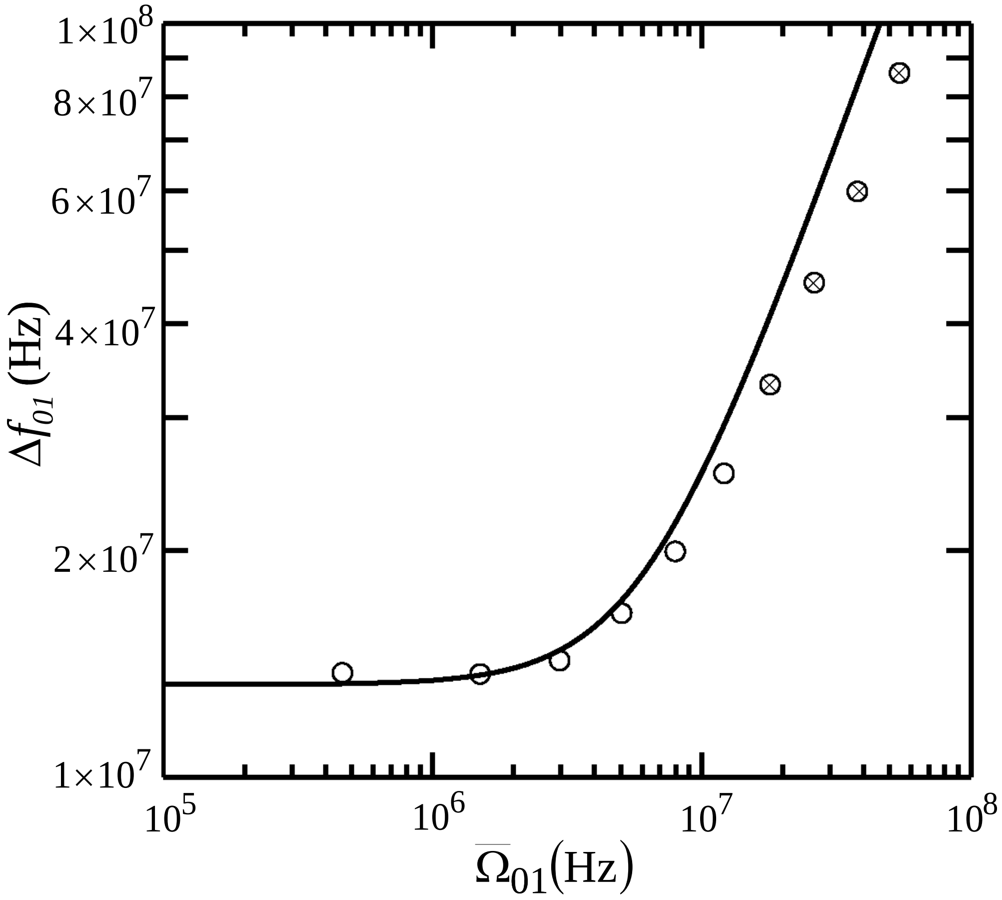

Figure 8.14: Power broadening observed by plotting FWHM of 0 → 1 resonance vs. Rabi frequency $\overline{\Omega}_{01}$ in SQUID DS_{3A}. The power broadening in the spectroscopic widths provides a check on the coherence times of the device. The solid line is a fit to Eq. (3.28) using the T_1 and T_2 times determined from other experiments on the device. Points with crosses indicate powers at which the Rabi frequency was calibrated.

calibrated against the Rabi frequency; the Rabi frequency could not be directly determined below about 70 MHz. I find fairly good agreement at low power (low Rabi frequency); at higher powers the spectral width decreases from the predicted values. Curiously the Rabi oscillations had shorter decay times as the microwave power increased, as shown in Fig. 8.12. This behavior is inconsistent with decoherence from $1/f$ noise, but suggests that additional crossings might be contributing at high powers.

8.3.4 SQUID DS$_{3A}$ Variable T$_1$

If the current bias leads limit the relaxation time in the qubit, varying the inductance of the isolation branch should produce a noticeable effect (see discussion in Section 4.1.1). If dissipation is solely due to the bias leads, Eqs. (4.2) and (4.4) predict a relaxation time of

$$T_1 \approx C_1 Z_0 \left(\frac{L_1 + L_2 + L_{J2}}{L_2 + L_{J2}} \right)^2 . \tag{8.6}$$

where,

$$L_{J2} = \frac{\Phi_0}{2\pi I_{02} \sqrt{1 - (I_2 / I_{02})^2}} . \tag{8.7}$$

Thus by varying the current I_2 through the isolation junction J2 I can produce a change in the expected relaxation time. Since there were many microstates in the spectra of device DS$_{3A}$, comparing the relaxation at different isolation factors requires a comparison at the exact same qubit frequency. Since I can separately control the current through the qubit junctions and isolation junction, different isolation factors are possible for the same qubit frequency. To reduce the isolation factor I simply increased the bias current, since the bias current passes almost entirely through the isolation junction this leaves the qubit bias almost unchanged while increasing L_{J2}.

Figure 8.15 shows the relaxation in the qubit for four different isolations for $f_{01} = 9993 \pm 8\, MHz$. Semi-log plots of p_e versus time are shown for four different isolations factors in Fig. 8.15(a). In each case I find a good exponential decay, implying no strong coupling to individual two-level systems. The open circles in Fig 8.15(b) show the relaxation time T_1 from fitting these decays, plotted versus the bias current I at which the data was taken. The relaxation time clearly decreases dramatically with bias current. The spectroscopic widths also varied [squares in Fig. 8.15(b)]. For $T_1 = 31 ns$, I found $T_2^* = 17 ns$, for $T_1 = 25 ns$, $T_2^* = 18 ns$ for $T_1 = 17 ns$, $T_2^* = 16 ns$ and for $T_1 = 12 ns$ I found $T_2^* = 11 ns$.

The solid line in Fig. 8.15(b) is a fit of the data to a simple model for relaxation due to the leads. There are two free parameters, the line impedance Z_0 and the inductance L_2 of the isolation arm of the SQUID (L_2 is too small to determine accurately from the I-Φ curves). Based on fits to the spectrum and I-Φ curves, I used $L_1 = 1.05 nH$, $C_J = 0.4 pF$, $I_{01} = 1.22 \mu A$, and $I_{02} = 8.63 \mu A$ in the model. Since $I_2 = I - I_1$, keeping $I_1 = 1.08 \mu A$ fixed and varying the bias allowed me to control L_{2J}. With $Z_0 = 285 \Omega$ and $L_2 = 25 pH$ I find good agreement, as shown in Fig. 8.15(b). A characteristic impedance of $Z_0 = 285 \Omega$ is high but not unreasonable if one considers the effect of the inductive impedance of the wire bonds. For a rigorous physical simulation, the precise length of the wire bonds must also be considered since they are not negligible compared to the wavelength of the qubit's frequency. Regardless of the

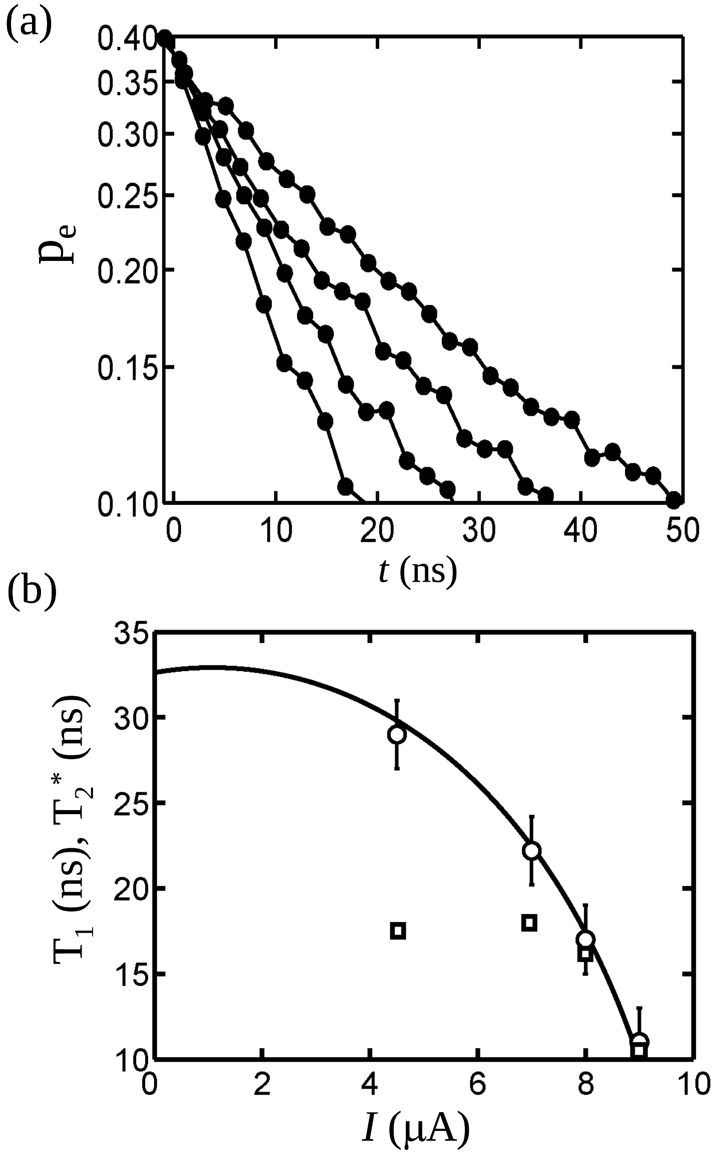

Figure 8.15: Variable isolation in DS_3. By varying the bias current to the SQUID the impedance that the qubit sees was varied. (a) Pulse measurement of escape probability versus time for four different isolations with $f_{01} = 9.993 \pm .008\,GHz$. (b) Fit relaxation plotted versus bias current (open circles) and the spectroscopic coherence times T_2^* (open squares). Solid curve is fit to T_1 assuming the sole source of dissipation is the current bias line with $Z_0 = 285\Omega$.

impedance used in the model, the fact that a large change was produced in T_1 is quite noteworthy. In particular, similar experiments on previous devices (DS_{2B} and AL1) showed no evidence of such a variation in the relaxation rate based on the line impedance [69]. This was a good indication that DS_{3A} was functioning with much lower intrinsic loss or two-level effects than our prior devices (at least at this operating point). Unlike the previous devices we tested, DS_{3A} was built on a sapphire substrate, with smaller junctions and no SiO_2 insulation layer.

8.4 SQUID DS_{4B}

The fact that device DS_{3A} showed a relaxation time that depended on the bias line isolation factor suggested trying to do even better by increasing the isolation by simply increasing L_1. Of course if extraneous factors such as the wire bond length strongly affected Z_0, this might not work. Device DS_{4B} had roughly identical critical currents to DS_3, but a loop inductance L_1 that was roughly 3 times larger, *i.e.* $L_1 = 3nH$. If T_1 was limited by the bias line isolation and everything else was the same, this should have produced a 9-fold increase in the relaxation time of the qubit compared to that in DS_{3A}.

In SQUID DS_{4B} the qubit was coupled to SQUID DS_{4A}. Both SQUIDs were wired to bias leads and fully operational. A rough spectrum for DS_{4B} is shown in Fig. 8.16; several large and small splittings are clearly visible. Figure 8.17 shows spectroscopic widths and the corresponding on-resonance Rabi oscillation and decay after microwaves were shut off at several different f_{01}. This bias range seemed to have the least number of large splittings. However, the device had many splittings and a splitting is clearly visible at 9.43 GHz that affected the qubit performance, shown in Fig. 8.17(b).

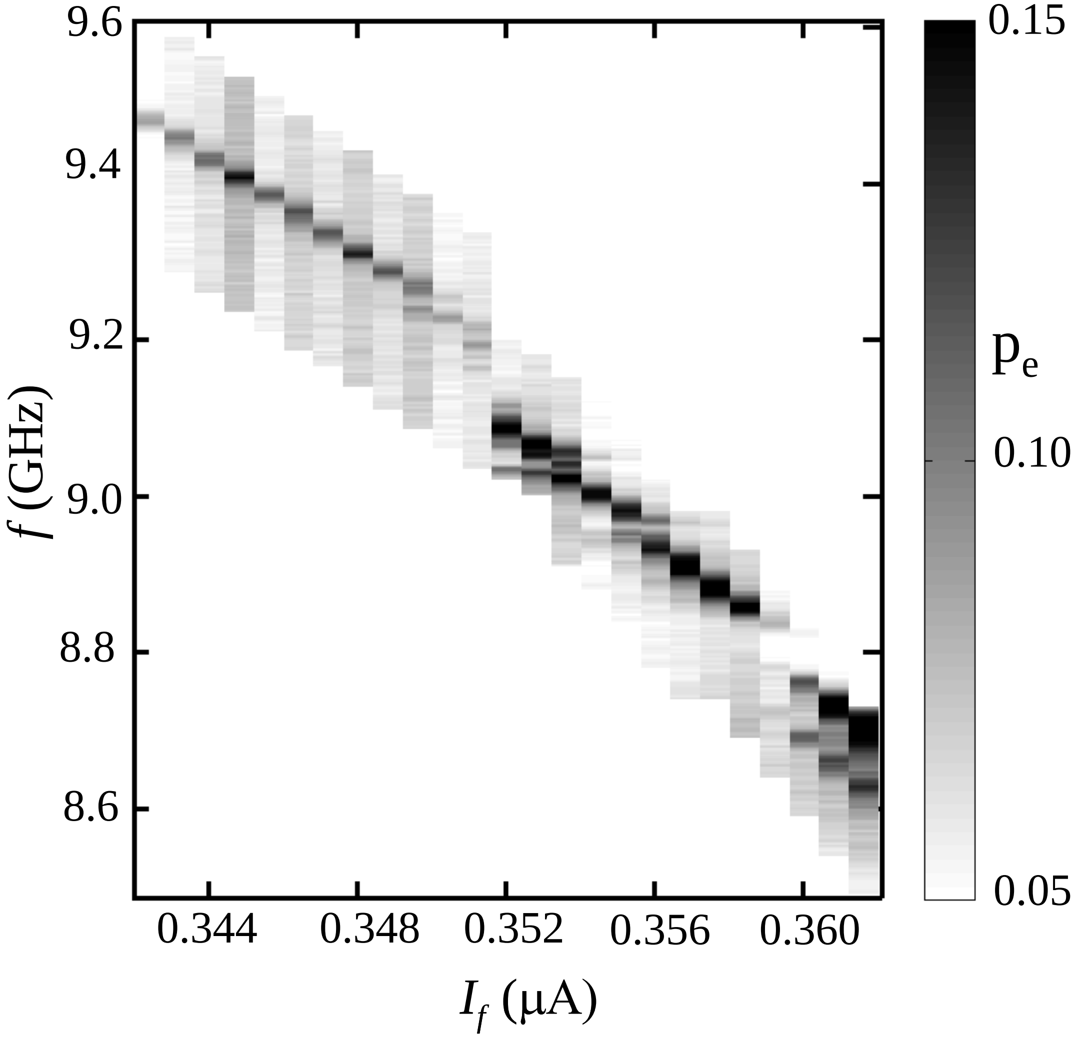

Figure 8.16: Transition spectrum of device DS_{4B} measured at 20 mK. Using the pulsed readout technique the spectrum of the device showed several clear avoided level crossings. The false color map shows the fraction that escaped with a single amplitude measurement pulse.

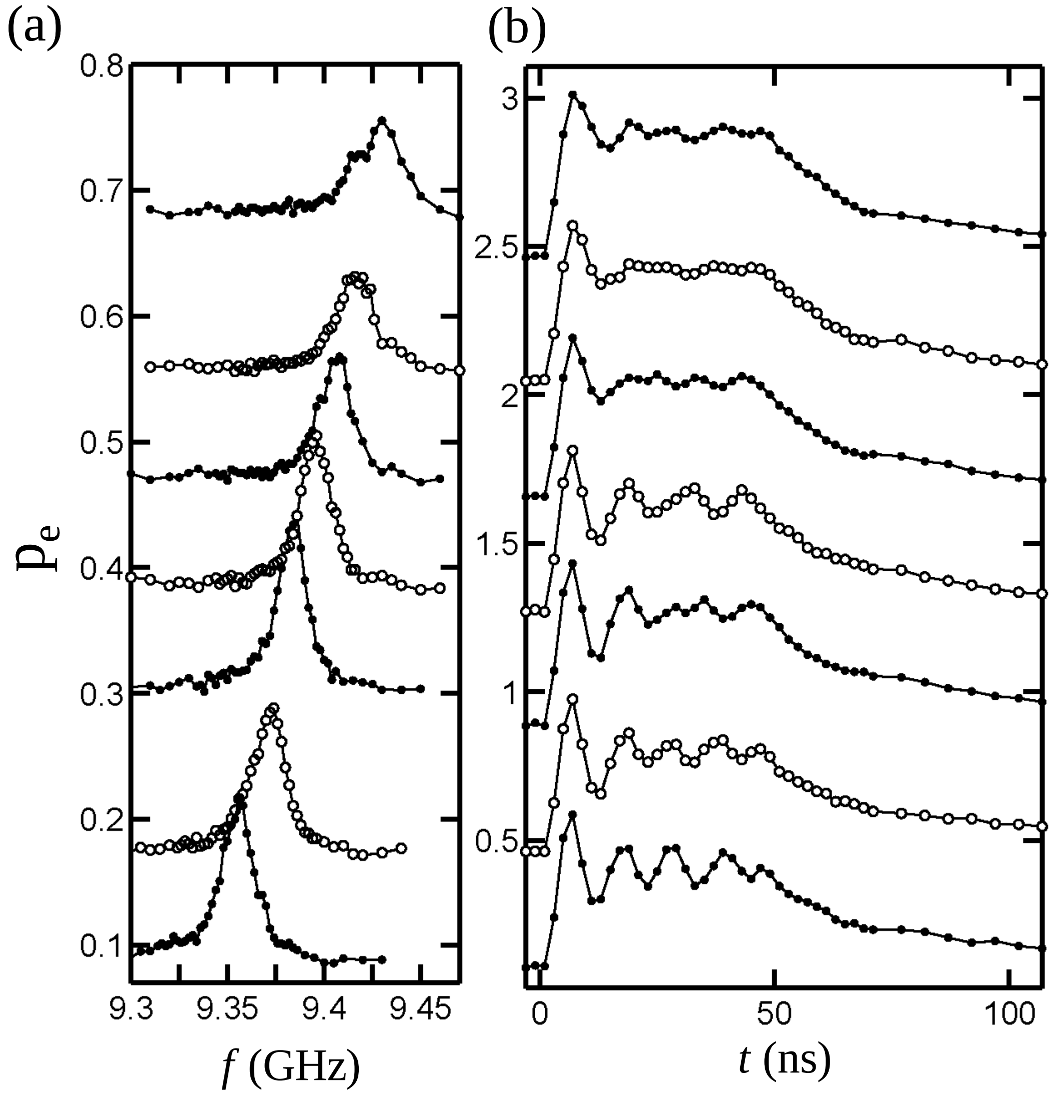

Figure 8.17: (a) Spectroscopic widths and (b) on-resonance Rabi oscillations in device DS_{4B} for different resonant frequencies f_{01}. The performance of the device away from large splittings appeared to be no better than device DS_{3A}.

From these results, I concluded that qubit DS_{4B} appeared to be no better than DS_3. From Figs. 8.16 and 8.17 one can immediately see that it certainly did not have a T_1 that was 9 times longer. There also seemed to be more microstates. Qubit DS_{4A} did not produce better results either. This suggests that the junction quality or some other factor in DS_{4B} was worse than DS_{3A} and this prevented the device from operating as well as expected.

8.5 Summary

In this chapter, I described a series of measurements I made to demonstrate coherent quantum control of several dc SQUID qubits. Some of the qubits showed substantial bias dependent variations in the performance. The best coherence times from the Al devices (DS_{3A} and DS_{4B}) were clearly superior to those of the Nb ones (DS_1, DS_{2A} and DS_{2B}). The relaxation times in the Nb devices were at least an order of magnitude shorter than expected if they were solely due to the impedance of the bias leads. In contrast, for the Al device DS_{3A}, T_1 did depend on the isolation from the leads.

In the Nb devices (DS_1, DS_{2A} and DS_{2B}), SiO_2 was used as an insulator between the metal layers (see Chapter 4). Other groups have reported substantial loss due to this insulator and saw dramatic improvements above removing it [81]. Our aluminum devices (DS_{3A} and DS_{4B}) have no SiO_2. On the other hand our devices have AlO_x between the two aluminum layers, and this may still be causing loss and microstates. Our aluminum devices also have extraneous loops and junctions that were created from the double-angle fabrication procedure (see Fig. 4.4). It is not known if these parasitic structures create additional dissipation or decoherence.

The tunnel barriers in our junctions appear to contain other parasitic quantum system that couple to the qubit and are visible as avoided level crossings in the spectra. If large splittings are clearly visible, perhaps many small ones exist that affect the qubit. Nb devices DS_{2A} and DS_{2B} showed what were apparently several very small avoided level crossings of less than 10 MHz in size [37]. By reducing the size of the junction, as was done in aluminum devices (DS_{3A} and DS_{4B}) I should have reduced the number of coupled parasitic systems and perhaps been able to operate the qubit away from them. These parasitic quantum systems will be discussed in detail in Chapters 9 and 10. I should also note that another aluminum device (AL1) on a Si substrate was tested in our lab. This device had a larger qubit junction with an area of 80 μm^2 [68]. It showed Rabi decay times $T_2^{'} = 18 ns$ to $28 ns$, but a much lower spectroscopic coherence time ($T_2^{*} = 4 ns$ to $10 ns$) [68], measured using an escape rate readout.

Finally, I note that other loss mechanisms may play a role, For example, another possible source of dissipation is radiation resistance. The relatively long inductance L_1 could be acting like an antenna that radiates electromagnetic energy from the qubit. Consider device DS_{4B} at $f = 10\ GHz$. At this frequency the isolation junction has an impedance ωL_{2J} of only a few ohms, much less than the impedance of free space. This suggest modeling the qubit as the driving source in a circular loop with a diameter of order 1 mm, which will act like an oscillating magnetic dipole [see Fig. 8.18(a)]. In the limit where the wavelength in the substrate (here $\lambda' \approx 16 mm$) is much longer than the loop diameter (here $d \approx 0.8\ mm$), I can estimate the radiation resistance as [112]

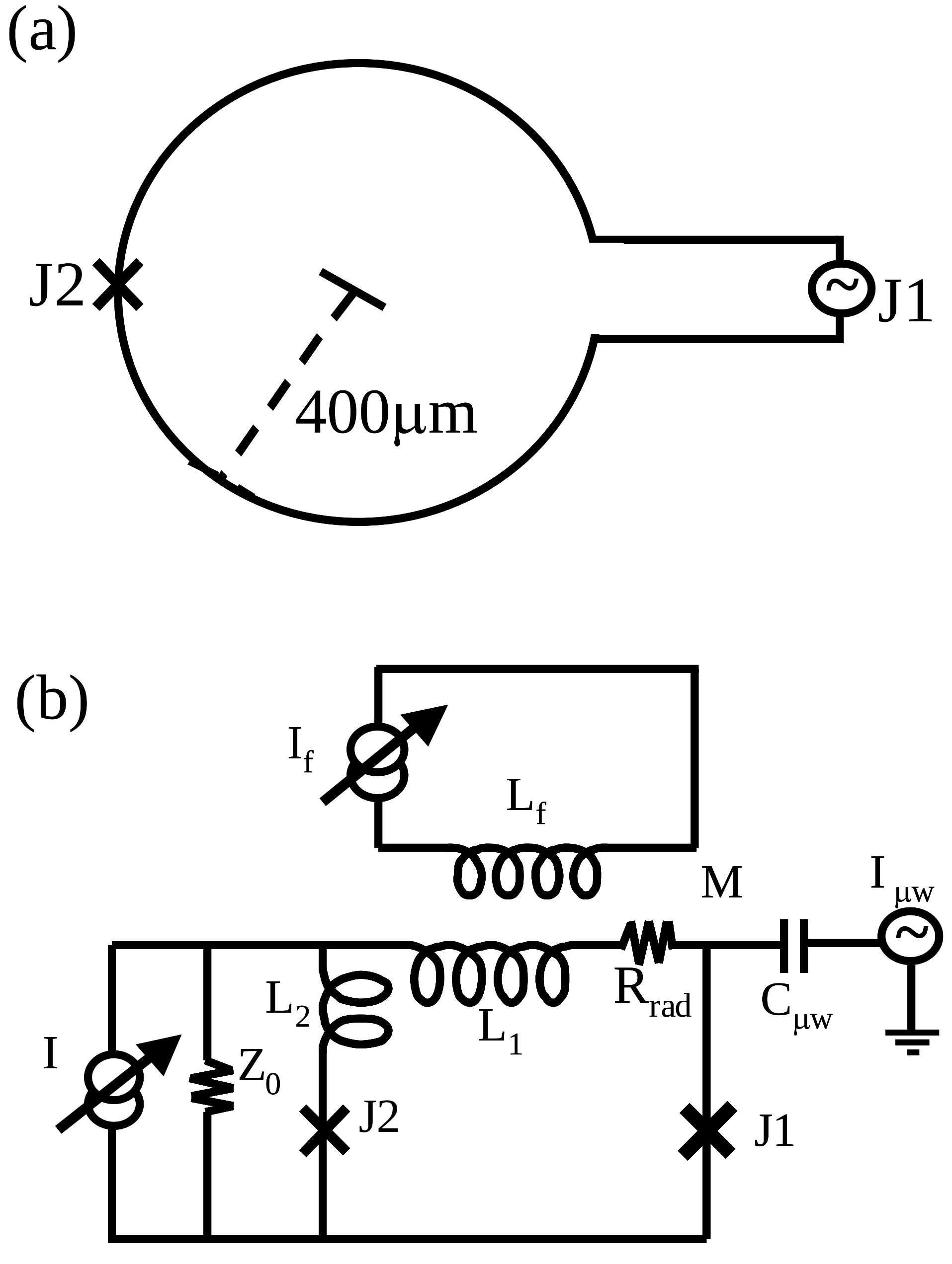

Figure 8.18: (a) SQUID loop of device DS_{4B} is modeled as a superconducting loop driven by the qubit junction J1. The loop radiates energy like an oscillating magnetic dipole. (b) Schematic of SQUID including radiation resistance R_{rad} used to calculate the effect on the relaxation time T_1.

$$R_{rad} \approx \frac{1}{2}\left(19{,}200\left(\frac{d}{\lambda}\right)^4\right) \approx 0.05\,\Omega \tag{8.8}$$

The factor of ½ in Eq. (8.8) is to account the substrate occupying only the space below the loop.

The radiation resistance can be modeled as a resistor that is in series with the loop inductance L_1. A schematic including this resistance is shown in Fig. 8.18(b). The new effective parallel resistance across the qubit junction for this model (not including losses intrinsic to the junctions, the flux line or microwave line) is

$$R_{eff} \approx Z_0 \frac{\omega^2 (L_1 + L_2 + L_{2J})^2}{\left(Z_0 R_{rad} + \omega^2 (L_2 + L_{2J})^2\right)} \tag{8.9}$$

Using $L_{2J} = 3nH$ $L_2 = 20\,pH$, $Z_0 = 300\,\Omega$, $L_2 = 20\,pH$, $L_{2J} = 40\,pH$, $C = 0.4\,pF$ and $f_{01} = 10\,GHz$, I find $R_{eff} = 380\,k\Omega$. This would give $T_1 \approx 150\,ns$. If $R_{rad} = 0.0\,\Omega$, I find $R_{eff} = 780\,k\Omega$ and $T_1 \approx 310\,ns$. Using this crude model I can conclude that the radiation resistance may not be negligible in our device and should be considered. If I had assumed the isolation junction acted as an open, the system would have been more accurately modeled as an electric dipole. This situation may in fact lead to a substantially larger radiation resistance [63]. Perhaps in SQUID DS$_{4B}$ this factor dominated any gain from the larger isolation factor from the bias leads.

Further work is needed to clarify the causes of relaxation in our devices.

Chapter 9

Coupling Between a Phase Qubit and a Two-Level System

In this chapter, I discuss a model of parasitic quantum systems coupled to a phase qubit. In particular, I consider the combined Hamiltonian $H = H_J + H_{tls} + H_c$, where H_J is the Hamiltonian of the qubit as given in Eq. (2.6), H_{tls} is the Hamiltonian of the two-level parasitic quantum system (TLS) and H_c is the Hamiltonian coupling the TLS to the junction. With two coupled quantum systems, states will now exist such as $\left|1e\right\rangle$, where the first index refers to the qubit state (here $n = 1$) and the second index refers to the state of the parasitic quantum system (here the first excited state $\left|e\right\rangle$). The interaction is most easily understood by considering the spectrum of the coupled system. When the energy level spacing of the qubit equals that of the two-level system, the coupling between the two systems lifts the degeneracy, producing an avoided crossing or "splitting" (see Fig. 9.1).

In amorphous solids, anomalous effects have been observed at very low temperatures and been attributed to the tunneling of unknown ions, atoms, or molecules between two potential wells [113]. Since the exact microscopic nature of the object that is tunneling is not known, I will simply call them "particles". In this model, the particle can occupy different positions of almost equal potential producing a two-level system. Presumably the particles also have a series of vibrational states separated by energies $\hbar\Omega$, which one might expect to be on the order of the Debye energy. However, since $k_B T << \hbar\Omega$ in my experiments, only the two lowest states are considered. I will

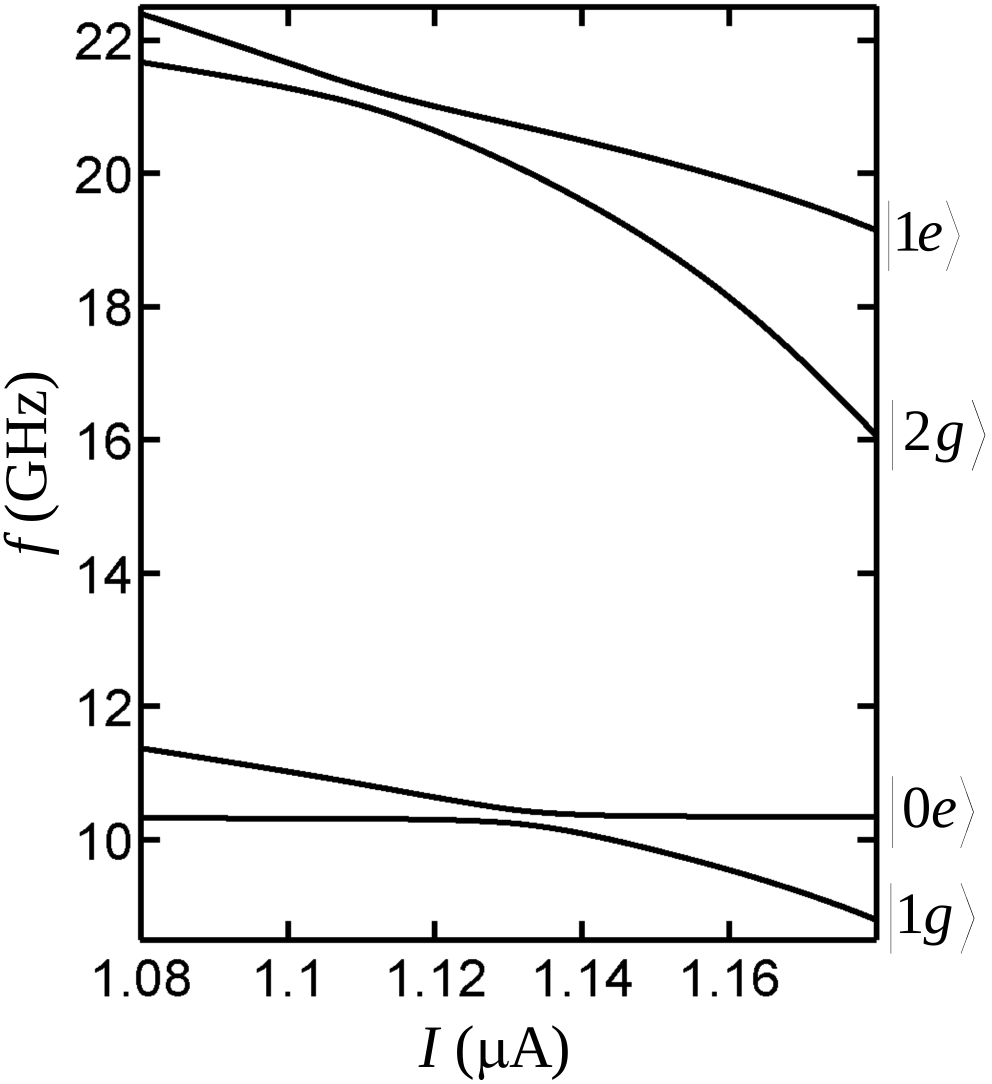

Figure 9.1: Simulation of avoided level crossing or "splitting" in a phase qubit. At $I \cong 1.13\,\mu A$, the degeneracy between the $|0e\rangle$ state and $|1g\rangle$ state is lifted. Here the parameters of device DS_{3A} ($C = 0.38\,pF$ and $I_0 = 1.26\,\mu A$) are used with a microstate with $f = 10.3\,GHz$ and $\Delta_f = 25\,MHz$. Coupling between states $|1e\rangle$ and $|2g\rangle$ is also shown; the splitting is expected to be roughly $\sqrt{2}$ larger than the $|0e\rangle - |1g\rangle$ splitting.

generally assume the particle is of microscopic origin, and will use the terms two-level system (TLS), parasitic quantum system, and microstate interchangeably.

Clear experimental evidence has been found that superconducting qubits can be coupled to microstates located or closely associated with the Josephson junctions [106]. The aluminum oxide used in tunnel barriers appears to have an amorphous component, which could contain ionic two-level system. To model the microstates here, I will assume that the particles can occupy two different positions of almost equal energy, are located in the tunnel barriers, and can possess a charge [see Fig 9.2(a)].

In the remainder of this chapter, I briefly outline the two-level system model. I then consider two different mechanisms for how the TLSs could couple to the qubit, through the critical current and through the charge. I then discuss an approach that could be used to determine the coupling mechanism experimentally. Since the microstates are likely caused by random disorder in the materials, I next consider the distribution of splittings based on a few simple assumptions. Finally, I conclude with a brief discussion of how microstates could cause relaxation in the junction. In Chapter 10, I compare these models with experimental results.

9.1 Two-level Systems

The Hamiltonian of a single isolated two-level system can be written in the form

$$H_{tls} = -\frac{1}{2}\left(U_a|L\rangle\langle L| + T_{LR}|L\rangle\langle R| + T_{LR}|R\rangle\langle L| - U_a|R\rangle\langle R|\right), \tag{9.1}$$

where U_a is the difference in energy between the left and right well (“asymmetry energy”), T_{LR} is the tunneling matrix element, and $|L\rangle$ or Ψ_L and $|R\rangle$ or Ψ_R represents

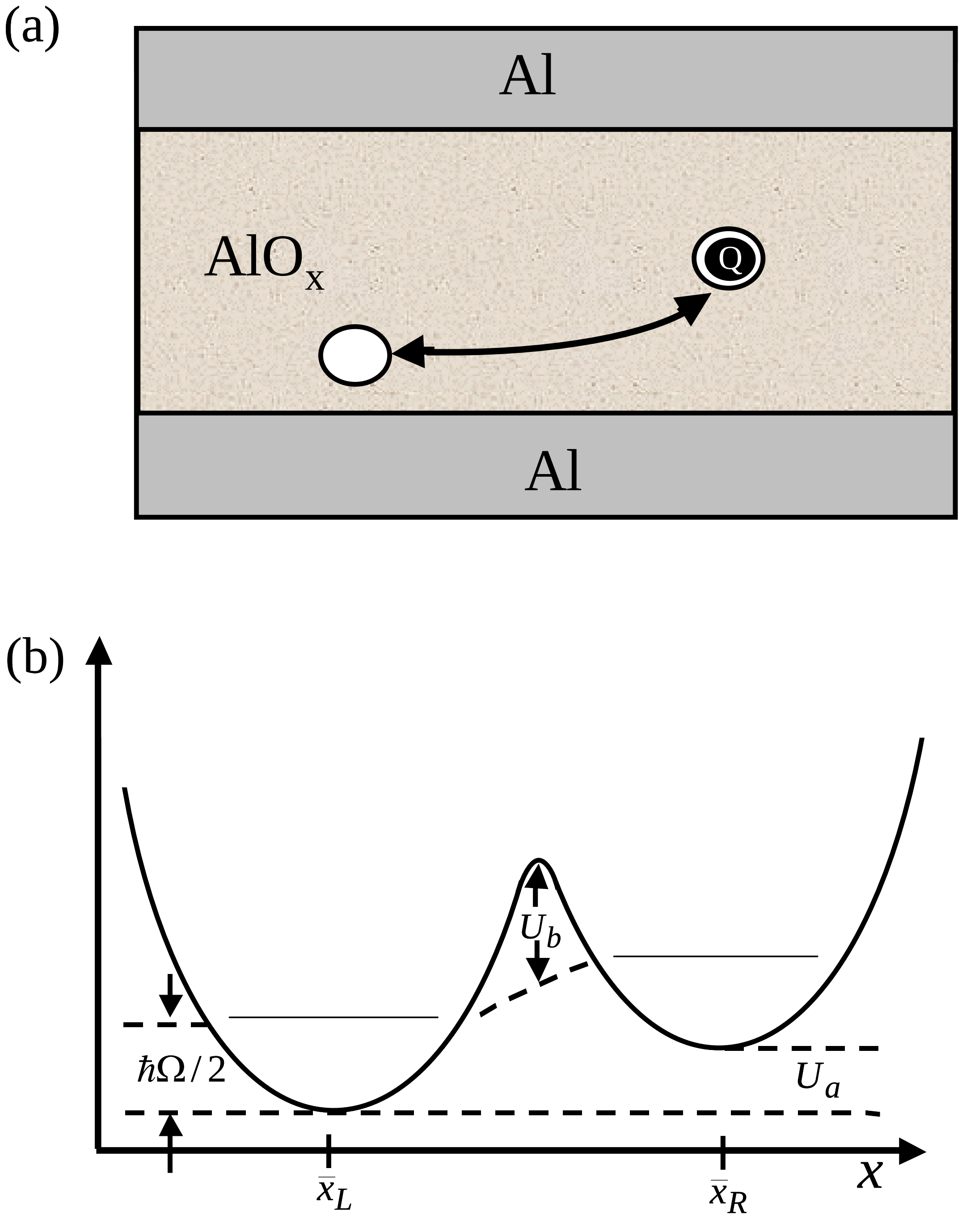

Figure 9.2: (a) Picture of two-level system in which a charge located in the Josephson junction tunnel barrier can tunnel between two locations. (b) Potential energy versus position for a two-level system model [113]. The tunneling between the two wells is a function of U_b and the distance between the two wells $\left|\bar{x}_L - \bar{x}_R\right|$.

the eigenstates in the absence of tunneling. This model is easily understood by considering Fig. 9.2(b). Here Ψ_L and Ψ_R are the states of the system in the left and right well, centered on $\bar{x}_L$ and $\bar{x}_R$, respectively and U_b the height of the barrier. For a square or flat barrier the tunneling element can be written as

$$T_{LR} = T_0 e^{-\lambda} \ , \tag{9.2}$$

where $\lambda = 2\alpha \left|(\bar{x}_R - \bar{x}_L)\right| \sqrt{U_b}$ (reflects the overlap of the wavefunctions) and α and $T_0 = \hbar\Omega$ are constants.

The eigenstates of the system are then given by

$$\left|g\right\rangle = \cos\frac{\theta}{2}\left|L\right\rangle + \sin\frac{\theta}{2}\left|R\right\rangle \text{ and} \tag{9.3a}$$

$$\left|e\right\rangle = -\sin\frac{\theta}{2}\left|L\right\rangle + \cos\frac{\theta}{2}\left|R\right\rangle , \tag{9.3b}$$

where $\theta \equiv \arctan\left(\dfrac{T_{LR}}{U_a}\right)$. Alternatively I can write

$$\left|L\right\rangle = \cos\frac{\theta}{2}\left|g\right\rangle - \sin\frac{\theta}{2}\left|e\right\rangle \text{ and} \tag{9.4a}$$

$$\left|R\right\rangle = \sin\frac{\theta}{2}\left|g\right\rangle + \cos\frac{\theta}{2}\left|e\right\rangle \tag{9.4b}$$

The energy of the eigenstates can be shown to be

$$E_- = E_g = -\frac{1}{2}\sqrt{U_a{}^2 + T_{LR}^2} = -\frac{E_{tls}}{2} , \tag{9.5a}$$

$$E_+ = E_e = +\frac{1}{2}\sqrt{U_a{}^2 + T_{LR}^2} = +\frac{E_{tls}}{2} . \tag{9.5b}$$

A few basic limits provide some intuition about the model:

(1) As $T_{LR} \to 0$, $\theta \to 0$ and the eigenstates are $\left|L\right\rangle$ and $\left|R\right\rangle$, with $E_\pm = \pm\frac{1}{2}U_a$.

(2) As $U_a \to 0$, $\theta \to \pi/2$ and the eigenstates are $|g\rangle = (|L\rangle + |R\rangle)/\sqrt{2}$ and $|e\rangle = (-|L\rangle + |R\rangle)/\sqrt{2}$, with $E_{\pm} = \pm\frac{1}{2}|T_{LR}|$.

9.2 Critical Current Coupling

One way that a TLS could couple to a phase qubit is if the critical current of the junction depends on the state of the TLS. Specifically, I mean that if the microstate is in state Ψ_L the junction has a critical current I_{0L} and if the microstate is in state Ψ_R it has a critical current I_{0R}. In principle, the tunneling particle could be an atom, ion, electron, or trapped flux quantum that has two possible locations in space. The particle's position could affect the local potential in the junction tunnel barrier and thus give different supercurrent tunneling matrix elements; this would produce a critical current that depends on the particles position. Similarly, a critical current variation could occur from a single-charge trap that blocks tunneling over a section of the junction due to the Coulomb repulsion [114].

In this case, I can now write the total Hamiltonian as [115]:

$$H = H_J + H_{tls}, \tag{9.6}$$

where

$$H_J = \frac{p^2}{2m} - \frac{\Phi_0 I}{2\pi}\gamma - \frac{\Phi_0 I_{0R}}{2\pi}\cos(\gamma) \otimes \left[|R\rangle\langle R|\right] - \frac{\Phi_0 I_{0L}}{2\pi}\cos(\gamma) \otimes \left[|L\rangle\langle L|\right] \tag{9.7}$$

and p_γ is the canonical momentum of the junction and H_{TLS} is the Hamiltonian of the two-level system. I now define the difference in the two critical currents

$\delta I_0 \equiv I_{0R} - I_{0L}$. Setting I_0 as the critical current when the microstates is in the ground state Ψ_g seems reasonable and using Eq. 9.3(a), one finds

$$I_0 = I_{0L}\cos^2(\theta/2) + I_{0R}\sin^2(\theta/2). \tag{9.8}$$

Using Eq. (9.4) and (9.8), the trigonometric identities $\cos^2(\theta/2) - \sin^2(\theta/2) = \cos\theta$ and $\cos(\theta/2)\sin(\theta/2) = (\sin\theta)/2$, I can simplify Eq. (9.7) to get

$$\begin{aligned} H &= \frac{p_\gamma{}^2}{2m} - \frac{\Phi_0 I}{2\pi}\gamma - \frac{\Phi_0}{2\pi}\cos(\gamma) I_0 + H_{tls} \\ &- \delta E_J \cos(\gamma) \otimes \left[\cos\theta |e\rangle\langle e| + \sin\theta(|g\rangle\langle e| + |e\rangle\langle g|)/2\right] \end{aligned}, \tag{9.9}$$

where $\delta E_J \equiv \Phi_0 \delta I_0 / 2\pi$. The coupling term is therefore

$$H_c = -\delta E_J \cos(\gamma) \otimes \left[\cos\theta |e\rangle\langle e| + \sin\theta(|g\rangle\langle e| + |e\rangle\langle g|)/2\right]. \tag{9.10}$$

As in Chapter 2, I can expand the $\cos(\gamma)$ term to order γ'^2 about the potential minimum γ_0, where $\gamma' = \gamma - \gamma_0$ now represents a small variation and is an operator. I can write

$$\cos(\gamma) = \cos(\gamma_0 + \gamma') = \cos(\gamma_0) - \sin(\gamma_0)\gamma' - \frac{\cos(\gamma_0)}{2}\gamma'^2. \tag{9.11}$$

Inserting Eq. (9.11) into Eq. (9.10), I can write the coupling term as

$$\begin{aligned} H_c &= -\delta E_J \left(\cos(\gamma_0) - \sin(\gamma_0)\gamma' - \frac{\cos(\gamma_0)}{2}\gamma'^2\right) \\ &\otimes \left[\cos\theta |e\rangle\langle e| + \frac{\sin\theta}{2}(|g\rangle\langle e| + |e\rangle\langle g|)\right] \end{aligned}. \tag{9.12}$$

Using the harmonic oscillator approximation for the first three energy levels of the phase qubit, I find the following matrix elements:

$$\langle n'|\gamma|n\rangle = \sqrt{\frac{2e^2}{C\hbar\omega_{01}}}\left[1\left(\delta_{n'=0,n=1}+\delta_{n'=1,n=0}\right)+\sqrt{2}\left(\delta_{n=2,n'=1}+\delta_{n=1,n'=2}\right)\right] \quad (9.13a)$$

$$\langle n'|\gamma^2|n\rangle = \frac{2e^2}{C\hbar\omega_{01}}\begin{bmatrix}\sqrt{2}\left(\delta_{n'=2,n=0}+\delta_{n'=0,n=2}\right) \\ +\delta_{n=0,n'=0}+3\delta_{n=1,n'=1}+5\delta_{n=2,n'=2}\end{bmatrix} \quad (9.13b)$$

The coupling terms between specific states can then be determined. For example:

$$\langle 0e|H_c|0e\rangle = -\delta E_J\cos\theta\left(\cos(\gamma_0)-\frac{\cos(\gamma_0)}{2}\frac{2e^2}{C\hbar\omega_{01}}\right), \quad (9.14)$$

$$\langle 1e|H_c|1e\rangle = -\delta E_J\cos\theta\left(\cos(\gamma_0)-3\frac{\cos(\gamma_0)}{2}\frac{2e^2}{C\hbar\omega_{01}}\right), \quad (9.15)$$

$$\langle 0e|H_c|0g\rangle = \langle 0g|H_c|0e\rangle = -\delta E_J\frac{\sin\theta}{2}\left(\cos(\gamma_0)-\frac{\cos(\gamma_0)}{2}\frac{2e^2}{C\hbar\omega_{01}}\right), \quad (9.16)$$

$$\langle 0e|H_c|1g\rangle = \langle 1g|H_c|0e\rangle = \delta E_J\frac{\sin\theta}{2}\sin(\gamma_0)\sqrt{\frac{2e^2}{C\hbar\omega_{01}}}, \quad (9.17)$$

$$\langle 1e|H_c|2g\rangle = \langle 2g|H_c|1e\rangle = \sqrt{2}\delta E_J\frac{\sin\theta}{2}\sin(\gamma_0)\sqrt{\frac{2e^2}{C\hbar\omega_{01}}}, \quad (9.18)$$

$$\langle 0e|H_c|2g\rangle = \langle 2g|H_c|0e\rangle = \sqrt{2}\delta E_J\frac{\sin\theta}{2}\frac{\cos(\gamma_0)}{2}\frac{2e^2}{C\hbar\omega_{01}}. \quad (9.19)$$

I note that the coupling term $\langle 0e|H_c|1g\rangle$ depends on θ, γ_0 and δI_0. It is largest for $T_{LR} >> U_a$ $(\theta=\pi/2)$ and disappears when $T_{LR} << U_a$. The maximum value is found for $\gamma_0=1$; *i.e.* the junction is biased at its critical current,

$$\left|\langle 0e|H_c|1g\rangle\right|^{\max} = \frac{h\Delta_{f\,\max}}{2} = \frac{\delta I_0}{2}\sqrt{\frac{\hbar}{2\omega_{01}C}}. \quad (9.20)$$

The term $\langle 1e|H_c|1e\rangle$ also depends on θ, γ_0 and δI_0 but is a minimum for $T_{LR} >> U_a$ and decreases as the qubit is biased closer to its critical current $\gamma_0 \to \pi/2$. Interestingly, a term $\langle 0e|H_c|0e\rangle$ exists, meaning $\langle 0e|H|0e\rangle \neq \langle e|H_{tls}|e\rangle + \langle 0|H_J|0\rangle$. This term also decreases for $T_{LR} >> U_a$ and will diminish as the qubit is biased closer to its critical current $(\gamma_0 \to \pi/2)$. Finally, to first order, I find

$$\frac{\langle 1e|H_c|2g\rangle}{\langle 0e|H_c|1g\rangle} \approx \sqrt{2}\,. \tag{9.21}$$

I note that this is only an approximation since the splittings will be at different bias currents and thus γ_0 will differ at the $|0e\rangle - |1g\rangle$ and $|1e\rangle - |2g\rangle$ avoided crossings (see Fig. 9.1).

9.3 Charge Coupling

The second physical mechanism I consider for coupling involves an ion in the dielectric layer that couples electrostatically to the voltage across the junction. I want to emphasize here that the voltage is not the result of the junction tunneling out of the zero-voltage state, but the quantum operator. The two ion states correspond to real space locations inside the junction barrier with position expectation values equal to $\bar{x}_L$ and $\bar{x}_R$, where I will assume $\langle L|x|R\rangle << \langle L|x|L\rangle$. The individual Hamiltonians H_J and H_{TLS} are given by Eq. (2.6) and Eq. (9.1), respectively, and the coupling to the qubit can be written as

$$H_c = -Q\overline{E} \cdot (\bar{x} - \bar{x}_0), \tag{9.22}$$

where Q is the charge of the ion, $\overline{E}$ is the electric field produced by the junction in the junction dielectric, and $(\bar{x}-\bar{x}_0)$ is the distance of the ion from the ground plate capacitor.

If I now assume a parallel plate capacitor, the coupling term can be written as

$$H_c = QVz_a / d\,, \tag{9.23}$$

where V is the voltage across the junction, z_a is the perpendicular distance of the ion from the ground plate and d is the distance between the two plates, generally 1-2 nm. The voltage can be expressed in terms of the canonical momentum as defined in Chapter 2, $p_\gamma = C(\Phi_0/2\pi)^2 d\gamma/dt = C(\Phi_0/2\pi)V$. The coupling Hamiltonian can then be written with p_γ and z_a as operators,

$$H_c = \frac{2\pi Q}{Cd\Phi_0} p_\gamma z_a\,. \tag{9.24}$$

For comparison, if I had assumed the object was a dipole with charge Q with a displacement distance x_a between the charges, the coupling term would be $H_c = \frac{2\pi Q}{Cd\Phi_0} p_\gamma x_a \cos\eta$, where η is the relative angle of the dipole moment with respect to the field [81]. Here I follow the model of a charge, as in Ref. [63].

The canonical momentum operator p_γ will act only on the qubit, whereas the distance operator z_a acts on the ion. From Eq. (9.3) and Eq. (9.24) and the harmonic oscillator approximation, I find the following coupling matrix elements:

$$\langle 0e|H_c|1g\rangle = \frac{2\pi Q}{Cd\Phi_0}\langle 0|p_\gamma|1\rangle\langle e|z_a|g\rangle = -i\frac{Q}{d}\sqrt{\frac{\hbar\omega_{01}}{2C}}(z_R - z_L)\frac{\sin\theta}{2}\,, \tag{9.25}$$

$$\langle 1e|H_c|2g\rangle = \frac{2\pi Q}{Cd\Phi_0}\langle 1|p_\gamma|2\rangle\langle e|z_a|g\rangle = -i\sqrt{2}\frac{Q}{d}\sqrt{\frac{\hbar\omega_{01}}{2C}}(z_R - z_L)\frac{\sin\theta}{2}, \quad (9.26)$$

$$\langle 0e|H_c|0e\rangle = \langle 1e|H_c|1e\rangle = \langle 2g|H_c|0e\rangle = 0\,. \quad (9.27)$$

It is worth making a few comments about these coupling terms. The $|\langle 0e|H_c|1g\rangle|$ term is bias current dependent (since ω_{01} depends on I) and increases as T/U_a increases. The maximum coupling occurs when the two ion positions are on opposite sides of the junction dielectric, i.e. $z_R - z_L = d$, and $U_a = 0$. In this case,

$$\frac{h\Delta_{f\,\max}}{2} = |\langle 0e|H_c|1g\rangle|^{\max} = \frac{1}{2}\sqrt{\frac{Q^2\hbar\omega_{01}}{2C}}\,. \quad (9.28)$$

Note also that $\langle 1e|H_c|2g\rangle/\langle 0e|H_c|1g\rangle = \sqrt{2}$ for the same microstate. Finally, if I use the cubic approximation to the junction states, I find

$$\langle 0e|H_c|2g\rangle = \langle 0e|H_c|1g\rangle/\sqrt{54N_s}\,. \quad (9.29)$$

This relation implies that when the $n = 2$ level of the junction crosses the excited state of the ion, it will produce about an order of magnitude smaller splitting than that when the same microstate crosses the $n = 1$ level, for typical junction parameters (*i.e.* $1 \le N_s \le 5$).

9.4 Magnetic Field Effects

By applying a magnetic field to the qubit junction it may be possible to determine whether charge or critical current coupling dominates. For a magnetic field $\overline{H} = H_y\hat{y}$ pointing in the plane of a Josephson junction (the junction in the x-y plane) the critical current density $J(x)$ is position dependent [116] and varies with the applied field. The total current through the junction I can be found by integrating $J(x)$ over the area of the junction. To calculate the effect of a magnetic field on the coupling between the qubit and a microstate, I need to first calculate the Josephson coupling energy for a junction in an applied magnetic field. I will set the junction center at $L_x / 2$, $L_y / 2$, so x varies from 0 to L_x and y varies from 0 to L_y.

Considering the junction without any microstate, current conservation gives

$$\begin{gathered} I = C\frac{dV}{dt} + \int_0^{L_x}\int_0^{L_y} J_1 \sin(\gamma + kx)dydx = \\ C\left(\frac{\Phi_0}{2\pi}\right)\frac{d^2\gamma}{dt^2} + \int_0^{L_x} J_1 L_y \sin(\gamma + kx)dx \end{gathered}, \tag{9.30}$$

where $k = 2\pi d H_y / \Phi_0$, $d = 2\lambda + h_0$, h_0 is the thickness of the junction oxide, which is negligible compared to the penetration depth λ, and J_1 is the unsuppressed critical current density. I can rearrange Eq. (9.30) to give

$$C\left(\frac{\Phi_0}{2\pi}\right)^2 \frac{d^2\gamma}{dt^2} = -\frac{\Phi_0}{2\pi}\frac{d}{d\gamma}\left[-I\gamma - \int_0^{L_x} J_1 L_y \cos(\gamma + kx)dx \right]. \tag{9.31}$$

The effective potential U can then be written as

$$U = -\frac{\Phi_0}{2\pi} I\gamma - \frac{E_{J1}}{\varphi_1 / 2}\sin(\varphi_1 / 2)\cos\left(\gamma + \frac{\varphi_1}{2}\right), \tag{9.32}$$

where $E_{j1} = \frac{\Phi_0}{2\pi} J_1 L_x L_y$ and $\varphi_1 = kL_x$.

For a critical current coupling mechanism, I now need to find the change δU_L or δU_R in the potential U of the junction due to the microstate blocking tunneling over some effective area of the junction based on its position in the left or right well, respectively. I will assume that the microstate blocks an effective tunneling area A_R in the right well and A_L in the left potential well, where $A_L << L_x L_y$ and $A_R << L_x L_y$. When the microstate is in the left well I find

$$\begin{aligned} \delta U_L &= -\frac{\Phi_0 J_1}{2\pi}\left[A_L \int_0^{L_y}\int_0^{L_x} \cos(\gamma + kx)\delta(x - x_L)\delta(y - y_L)dxdy \right] \\ &= -\frac{E_{j1}A_L}{L_x L_y}\cos(\gamma + kx_L) \end{aligned} \tag{9.33}$$

If the microstate is in the right well, I similarly find

$$\delta U_R = -\frac{E_{j1}A_R}{L_x L_y}\cos(\gamma + kx_R) \tag{9.34}$$

If the microstate is in the right well, the potential is $U - \delta U_R$ and if it is in the left well $U - \delta U_L$. The Hamiltonian is therefore

$$H = \frac{p_\gamma^2}{2m} + H_{TLS} - (U - \delta U_R) \otimes |R\rangle\langle R| - (U - \delta U_L) \otimes |L\rangle\langle L| \ . \tag{9.35}$$

I will set

$$U_0 = (U - \delta U_L)\cos^2(\theta/2) + (U - \delta U_R)\sin^2(\theta/2), \tag{9.36}$$

since this is the potential when the microstate is in the ground state.

Using the same procedure as in Section 9.2, I can simplify this to find

$$\begin{aligned} H = \frac{p_\gamma^2}{2m} + H_{TLS} - U_0 - (\delta U_R - \delta U_L) \\ \otimes \left[\cos\theta |e\rangle\langle e| + \frac{\sin\theta}{2}(|e\rangle\langle g| + |g\rangle\langle e|) \right] \end{aligned} . \tag{9.37}$$

To reduce this expression further I will assume that the separation between the L and R wells is very small compared to the dimensions of the junction, *i.e.* $\cos(\gamma + kx_R) \cong \cos(\gamma + kx_L)$. I can then write

$$\delta U_R - \delta U_L \approx -\frac{E_{j1}(A_R - A_L)}{L_x L_y}\cos(\gamma + kx_L)\ . \tag{9.38}$$

After expanding $\cos(\gamma + kx_L)$ about the potential minimum γ_0, I find a coupling term,

$$\left|\langle 1g|H_c|0e\rangle\right| = E_{j1}\left(\frac{A_R - A_L}{L_x L_y}\right)\frac{\sin\theta}{2}\sqrt{\frac{2e^2}{C\hbar\omega_{01}}}\sin\left(\varphi_1\left(\frac{x_L}{L_x} + \frac{\gamma_0}{\varphi_1}\right)\right). \tag{9.39}$$

This coupling term has the same magnetic field dependence as found by Tian *et. al.* [117] if I set $\gamma_0 = -\varphi_1/2$. It also reduces to Eq. (9.17) in the limit of zero-field.

In principle, the change in the coupling term when a magnetic field is applied could be used to determine if a microstate couples to the qubit through the critical current. In particular the $|0e\rangle - |1g\rangle$ avoided level crossing would change in size as the magnetic field through the junction is varied because $\varphi_1 = 2\pi d H_y L_x / \Phi_0$ depends on the applied field H_y. If I divide the coupling term in a field $\left|\langle 0e|H_c|1g\rangle\right|$ [Eq. (9.39)], to the zero field coupling [Eq. (9.17)] and set $\delta I_0 = J_1(A_R - A_L)$, I find

$$\frac{\left|\langle 0e|H_c|1g\rangle\right|^{field}}{\left|\langle 0e|H_c|1g\rangle\right|^{B=0}} = \frac{\sin(\varphi_1(x_L/L_x + \gamma_{0m}/\varphi_1))}{\sin(\gamma_{0n})}, \tag{9.40}$$

where I have written γ_0 with additional subscripts γ_{0m} (with field) and γ_{0n} (without field) to highlight they will not be equal at the same qubit frequency. This of course, assumes that the qubit can be biased to give the same frequency with the new critical current density. If the microstate couples to the qubit through a term other than the critical current, applying a magnetic field will produce a different effect. In the case of charge coupling the coupling term $\langle 1g|H_c|0e\rangle$ should remain constant.

9.5 Distribution of Splittings

Here I discuss the distribution of splitting sizes and frequencies in a charge-coupling model. The volume density of defects D per frequency interval df and per splitting frequency interval $d\Delta_f$ can be written as

$$D(f,\Delta_f) = \frac{1}{Ad}\frac{d^2N}{dfd\Delta_f}, \tag{9.41}$$

where

$$\Delta_f \equiv 2\left|\langle 0e|H_c|1g\rangle\right|/h \tag{9.42}$$

and $N(f,\Delta_f)$ is the number of defects with splitting size smaller than Δ_f and frequency less than f. I first derive the form of this distribution using the Tunneling Model, developed to describe amorphous solids [113]. After this result, I will quote results from a model that is perhaps more realistic as written in Ref. [63]. The Tunneling Model makes a major simplification by combining the barrier height and distance between the two wells into a constant distribution $P(\lambda)$, while the splitting size is dependent on the z component of the tunneling distance.

The Tunneling Model assumes that the tunneling rate λ (*i.e.* $T_{LR} = T_0 e^{-\lambda}$ Eq. (9.2)) and the well asymmetry energy U_a (see Eq. (9.1)) are independent of each other and have constant distributions, $P(\lambda) = 1/\lambda_{a\max}$ and $P(U_a) = 1/U_{a\max}$, where $\lambda = 2\alpha\left|(\bar{x}_R - \bar{x}_L)\right|\sqrt{U_b}$ (see Fig. 9.2). I now define a new variable $u \equiv T_{LR}/E = \sin\theta$. The distribution for the total energy E and the variable u for the two-level system is then [113]

$$P(E,u) \propto 1/u\left(1-u^2\right)^{1/2} \propto 1/\cos\theta\sin\theta\,. \tag{9.43}$$

I note that this function is energy independent, by assumption.

Assuming that the location of the two wells are uniformly distributed in the junction and taking into consideration that I need to only consider the distance $z = |z_R - z_L|$ between them parallel to the field, the distribution of z can be shown to be given by $P(z) = 2(d - z)/d^2$.

It is worth noting a few expressions that will prove valuable later. The splitting size as given by Eq. (9.25) and (9.42) can be written as

$$\Delta_f = \frac{Qz}{hd\sqrt{2C}}\frac{T_{LR}}{\sqrt{E}} = \Delta_{f\,\max}\frac{T_{LR}z}{Ed}\ , \tag{9.44}$$

with $\Delta_{f\,\max} = \sqrt{\dfrac{fQ^2}{2Ch}}$.

For a given splitting size Δ_f, I can use Eq. 9.44 to write $z \geq \dfrac{\Delta_f}{\Delta_{f\,\max}}d$ since $T_{LR}/E \leq 1$. This lends itself to define a minimum distance $z_{\min}(\Delta_f) = \Delta_f d/\Delta_{f\,\max}$. From Eq. (9.44) and (9.5), I can also write the asymmetry energy in terms of variables Δ_f, f and z,

$$U_a = \frac{hf}{z}\sqrt{z^2 - \Delta_f^2 d^2/\Delta_{f\,\max}^2}\,. \tag{9.45}$$

The total number of splittings can be expressed as

$$\begin{aligned} N &= \int\!\!\int \frac{d^2N}{d\Delta_f df}d\Delta_f df = \int\!\!\int\!\!\int \frac{d^3N}{d\Delta_f dfdz}dzdfd\Delta_f \\ &= \int\!\!\int\!\!\int NP(\lambda)P(U_a)P(z)\left|\frac{\partial(U_a,\lambda)}{\partial(\Delta_f, f)}\right|dzdfd\Delta_f \end{aligned}\ . \tag{9.46}$$

Comparing the different expressions for N, I can write the distribution as

$$\frac{d^2N}{d\Delta_f\, df} = \int_{z_{\min}}^{d} NP(\lambda)P(U_a)P(z)\left|\frac{\partial(U_a,\lambda)}{\partial(\Delta_f, f)}\right| dz, \tag{9.47}$$

where the Jacobian $\left|\frac{\partial(U_a,\lambda)}{\partial(\Delta_f, f)}\right| = \frac{h^2 f}{U_a \Delta_f}$. The distribution can then be determined by integrating Eq. (9.47),

$$\frac{d^2N}{d\Delta_f\, df} = \frac{Nh}{\lambda_{\max} U_{a\max} \Delta_f}\frac{2}{d}\int_{z_{\min}}^{d} \frac{z - z^2/d}{\left(z^2 - \Delta_f^2 d^2/\Delta_{f\max}^2\right)^{1/2}} dz\ . \tag{9.48}$$

Finally I find

$$\begin{aligned}\frac{d^2N}{d\Delta_f\, df} &= \frac{Nh}{\lambda_{\max} U_{a\max}} \frac{\sqrt{1-\left(\Delta_f/\Delta_{f\max}\right)^2}}{\Delta_f} \\ &\quad - \frac{Nh}{\lambda_{\max} U_{a\max}} \frac{\Delta_f}{\Delta_{f\max}^2} \ln\left(\frac{\Delta_{f\max}}{\Delta_f} + \sqrt{\frac{\Delta_{f\max}^2}{\Delta_f^2} - 1}\right)\end{aligned}\ . \tag{9.49}$$

The distribution can be derived for a more realistic model [63] by replacing the Tunneling Model with one that assumes:

(1) The ion positions (wells) are uniformly distributed in the dielectric volume.

(2) The tunnel barrier energy U_b has a uniform distribution, $P(U_b) = 1/U_{b\max}$.

(3) λ is dependent on the total distance between the wells and the barrier height.

(4) The asymmetry energy U_a is uniformly distributed, $P(U_a) = 1/U_{a\max}$.

Using the above assumptions in a junction with area LxL, Wellstood found [63]

$$
\begin{aligned}
D(f,\Delta_f) \approx{}& \frac{4h\eta\pi\ln(L/d)}{\alpha^2 L^2 U_{a\max} U_{b\max}} \ln\left(\frac{T_0}{hf}\right) \frac{\sqrt{1-\left(\Delta_f/\Delta_{f\max}\right)^2}}{\Delta_f} \\
&- \frac{4h\eta\pi\ln(L/d)}{\alpha^2 L^2 U_{a\max} U_{b\max}} \frac{\Delta_f}{\Delta_{f\max}^2} \ln\left(\frac{T_0}{hf}\right) \ln\left(\frac{\Delta_{f\max}}{\Delta_f} + \sqrt{\frac{\Delta_{f\max}^2}{\Delta_f^2} - 1}\right)
\end{aligned}, \qquad (9.50)
$$

where $\eta = N/Ad$. A few general observations can be made about Eq. (9.49) and Eq. (9.50). Both have the same dependence on Δ_f and are separable in terms of Δ_f and f. For splittings sizes $\Delta_f < \Delta_{f\max}/2$ the distributions are very close to being equal to $\Delta_{f\max}/\Delta_f$ (see Fig. 9.3). Also the first term in Eq. (9.49), which is proportional to $\sqrt{1-\left(\Delta_f/\Delta_{f\max}\right)^2}/\Delta_f$ matches that of Ref. [81]. Finally, the density of splittings depends only weakly on frequency in Eq. (9.50) and is constant in Eq. (9.49).

The distribution of frequencies and splitting sizes could also be estimated for the case of critical current coupling. The distribution for the uncoupled TLS would be the same as above if I used the Tunneling Model. The splitting size for a critical current coupling model is a function of δI_0, which we would expect to depend on the critical current density as well as details of how the particle influences the Josephson tunnel barrier. Therefore, a spatial approximation of the potential in the barrier and how the particle affects it would need to be considered to proceed further with the analysis.

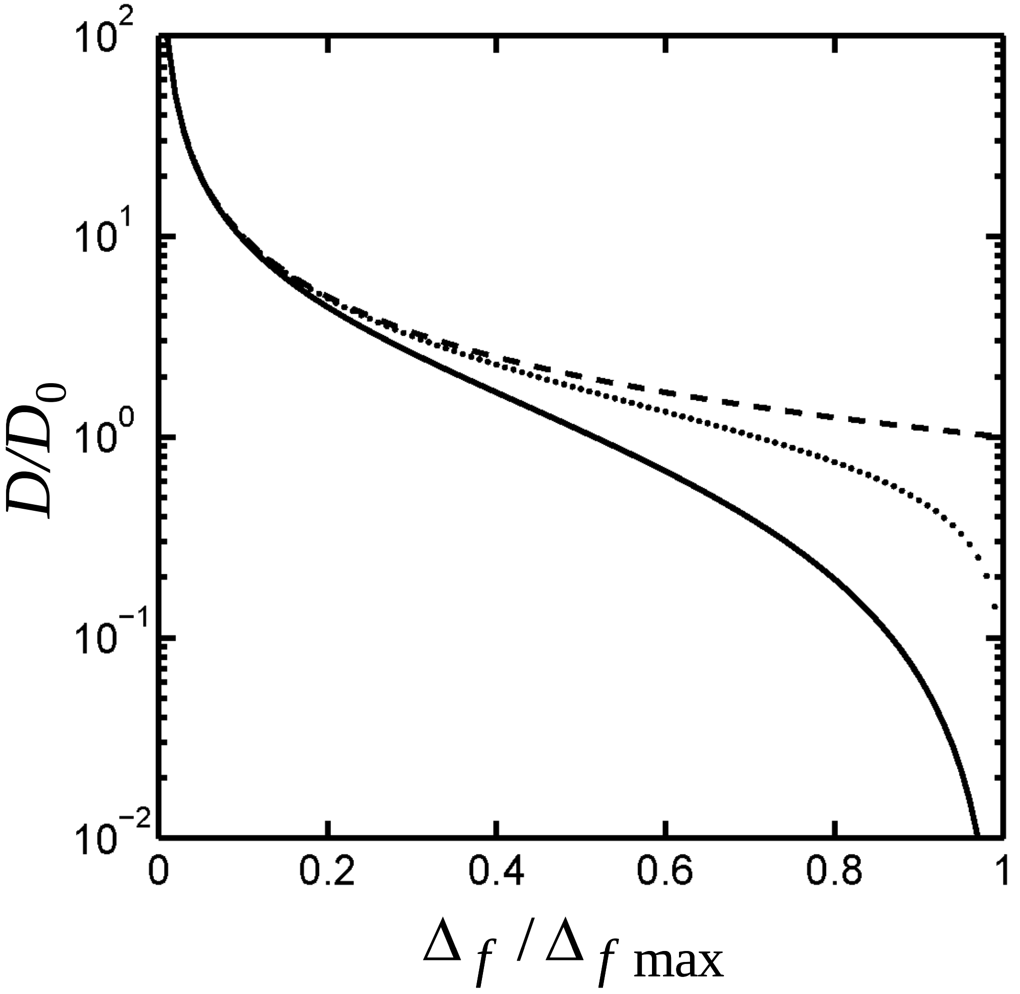

Figure 9.3: Distribution of splitting size versus $\Delta_f / \Delta_{f\,\max}$. The solid curve shows the dependence on $\Delta_f / \Delta_{f\,\max}$ as determined from the distribution of Eq. (9.49) or (9.50). The dotted curve is the first part of the distribution of Eq. (9.49), which matches that of Ref. [81]. The dashed curve is the distribution $\Delta_{f\,\max} / \Delta_f$ for comparison.

9.6 TLS Induced Relaxation

In Chapter 3, I modeled the admittance across the junction as an infinite set of harmonic oscillators. In some sense this admittance models the situation where many two-level systems are coupled to the junction. Fermi's golden rule can be used to calculate the relaxation of the qubit due to a density of coupled microstates using [81]

$$1/T_1 = \pi^2 \int \left(\left| \Delta_f \right|^2 \frac{d^2 N}{df d\Delta_f} \bigg|_{f_{01}} \right) d\Delta_f \ . \tag{9.51}$$

The resulting loss tangent is $\tan(\delta) = 1/2\pi f_{01} T_1$.

The same equation can be found by considering Landau-Zener transitions, in the limit of a negligible frequency sweep range. The probability of losing energy when sweeping through a series of splittings, $i = 1$ to N in the low loss limit is [63]

$$P_{1 \to 0} = \sum_{i=1}^{N} \left(1 - \exp(-\pi^2 \left| \Delta_{fi} \right|^2 / \dot{f}) \right) = \sum_{i=1}^{N} \pi^2 \left| \Delta_{fi} \right|^2 / \dot{f} \ , \tag{9.52}$$

where $\dot{f}$ is the rate at which the frequency is swept. Turning the summation into an integral gives $P_{1 \to 0} = \int\int \pi^2 \frac{d^2 N}{df d\Delta_f} \left| \Delta_f \right|^2 \frac{dt}{df} d\Delta_f df$. As $df \to 0$, I find Eq. (9.51), as expected.

9.7 Summary

In this chapter I discussed how parasitic two-level quantum systems in the tunnel barrier could interact with a phase qubit. I modeled these systems based on a two-level system model commonly used in amorphous solids and looked at two different coupling mechanisms between them and the qubit (charge and critical current coupling). The precise physical nature of the two-level systems remains an open question and I have avoided a detailed discussion of the “particles” themselves. I have also made no remarks on the potential relationship between the microstates described here and $1/f$ noise [70]. The random filling and emptying of charge traps is sufficient to explain $1/f$ charge noise, and critical-current noise in junctions [74]. In the model of Ref. [74] an attempt is made to explain anomalous low temperature flux noise in terms of a magnetic moment associated with the trapped particle, which I made no mention of here. In this chapter, I also examined the distribution of the splittings and the effect of a magnetic field on splittings in the charge and critical current coupling models. Finally I discussed how splittings produce an additional relaxation mechanism, which can impact device performance. In the next chapter, I show experimental results of dc phase qubits coupled to parasitic quantum systems and test some of these predictions.

Chapter 10

Measurements of Microstates in a Phase Qubit

In this chapter, I discuss my measurements of microstates coupled to phase qubits. The fact that phase qubits are sensitive to charge microstates is perhaps discouraging from the point of view of quantum computation. However, we could also view this as an opportunity to apply sensitive detectors (the junction) to study these poorly understood systems. In particular, the spectrum of a phase qubit provides an easily accessible window into the coupling strengths and transition frequencies of the microstates. By applying microwaves resonant with the qubits transition frequency f_{01}. I can map out the energy levels of the qubit. If the qubit junction is coupled to a two-level system through $\langle 1g | H_c | 0e \rangle$, an avoided crossing will be produced in the spectrum when the qubit's frequency f_{01} equals that of an individual two-level system. Unintended splittings in phase qubits were first reported by Simmonds *et. al.*, [106] at NIST to some skepticism [118]. Subsequently the NIST group was able to show that the coherence times of their devices improved substantially after they reduced the number of unintended splittings when they used a smaller area junction and removed much of the insulating SiO_2 [81]. The implication was that there were defects in the junction and the deposited or grown SiO_2 layers had a loss tangent that could produce significant relaxation.

Device DS_{3A} was designed with the NIST results in mind; it was made on a sapphire substrate, with a smaller junction area than any of our previous devices and no SiO_2. I found clear unintended splittings in this device as I discussed in Chapter 8. Here, I first discuss the splittings characteristics and then show coherent dynamics of the coupled system. These measurements highlight the quantum mechanical nature of the microstates. To provide a check on the coupling model, I also examined higher-level interactions. This provides a fairly powerful test because no new free parameters should be necessary to fit upper levels once the lower level states have been found. Higher-level interactions are also important if the second excited state $n = 2$ of the qubit is to serve a role in the readout, in the gating operation of the qubit, or if the state $|1e\rangle$ is considered [119]. In this chapter, I also discuss some of my preliminary results on applying a magnetic field to the qubit to determine the coupling mechanism. I briefly discuss a proposal to use the microstates themselves as qubits [120] and conclude with a comparison of the experimental results with the predictions of Chapter 9.

10.1 Unintended Avoided Level Crossings

Although, our group had made many spectroscopic measurements on phase qubits, it was several years before splittings were clearly observed. S. K. Dutta first observed what appeared to be very small avoided-level crossings in device DS_2 [37]. He found approximately 10 avoided crossings with splitting sizes $\Delta_f < 10\,MHz$ over a range of $f_{01} = 5.5\,GHz$ to $6.25\,GHz$. These spectroscopic measurements were made by ramping the current through the junction at a fixed microwave frequency. Unfortunately, analyzing the splittings in detail proved to be difficult due to the remarkably small size of all the splittings; the spectroscopic widths of the qubit was large compared to the splitting sizes. Another difficultly was with the technique; the spectrum was made up of slices at a given frequency, which can hide splittings that are smaller than the slice-to-slice frequency change. Given the very small size of the splittings S. K. Dutta observed, it was not surprising that they went undetected in our qubits until a specific search was made.

In contrast, Device DS_{3A} and the technique I used were far more conducive to observing avoided level crossings. For this device, the current was held fixed, a single frequency was applied, and the state was then measured using a pulsed readout technique. The resulting spectrum is a collection of individual points, as opposed to fixed frequency slices. Figure 10.1 shows a gray scale plot of a measured spectrum when I drove the qubit near the $n = 0$ to $n = 1$ transition. The qubit was biased at approximately 60 different currents, continuous microwaves were applied in 5 MHz or 3 MHz steps and the population in $n = 1$ was measured by applying single-amplitude measurement pulses at each bias point. Examination of Fig. 10.1 reveals that several avoided crossings are clearly visible with sizes ranging several MHz to about 250 MHz. Splittings less than a few MHz are also probably present, but would not be clearly resolvable.

To quantify the splittings, at each current bias the probability of escape p_e versus f was χ^2-fit to a sum of Lorentzian peaks, one Lorentzian for each distinguishable peak. Figure 10.2(a-d) shows four sample fits (see Table 10.1 for fit parameters). The offset of about 4% is due to population in $|0\rangle$ tunneling during the single amplitude readout pulse. I note that when the qubit is coupled to a TLS simply adding two lorentzians may not be rigorously correct. However, I found it gave a rather accurate fit for the spectroscopic width and peak location, as shown. Away from any splittings, the peaks fit well to a single Lorentzian, as shown in Fig. 8.12(a).

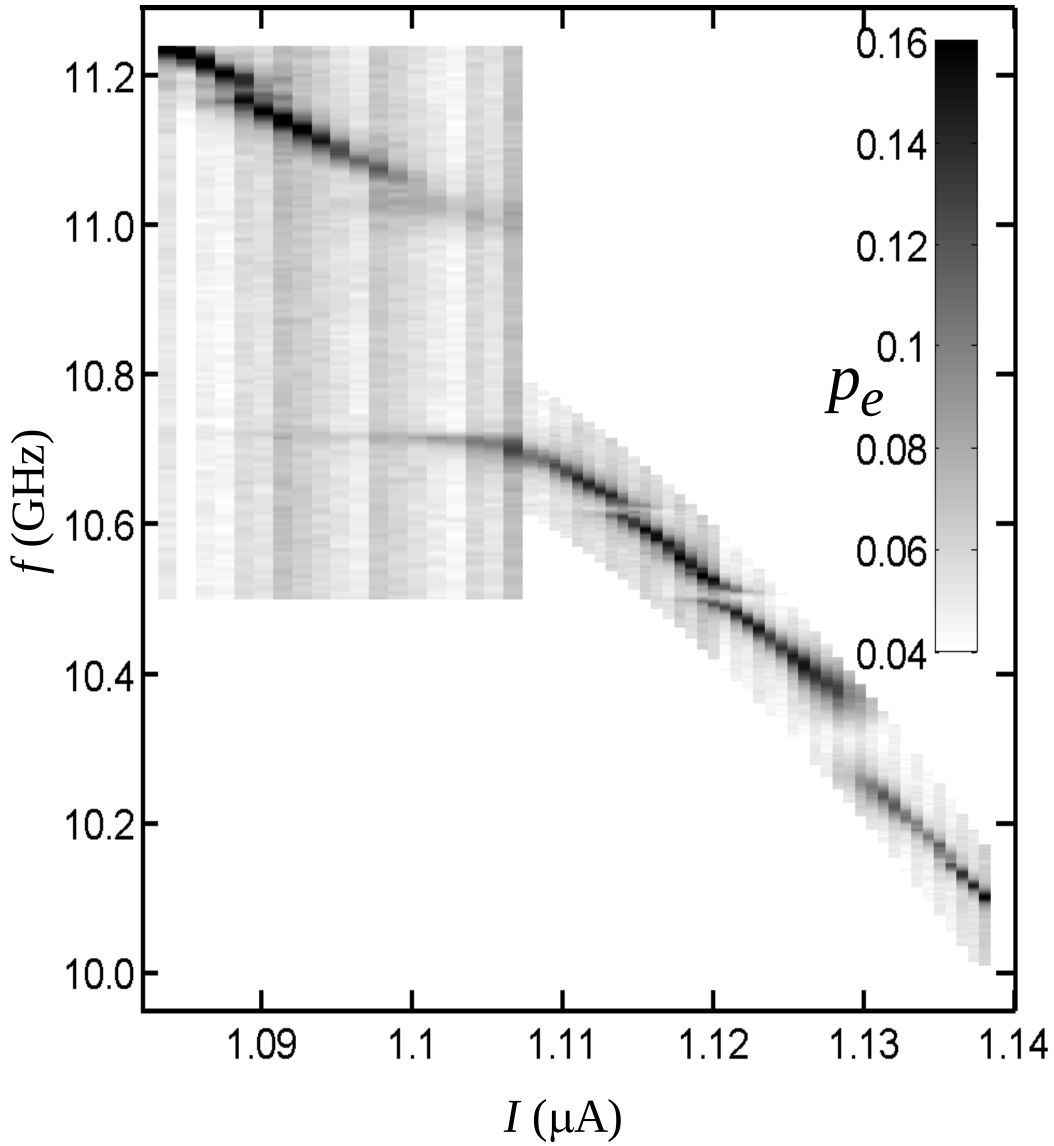

Figure 10.1: Transition spectrum of SQUID DS_{3A}. The false color map represents probability of escape during a pulse. Several prominent splittings are clearly visible.

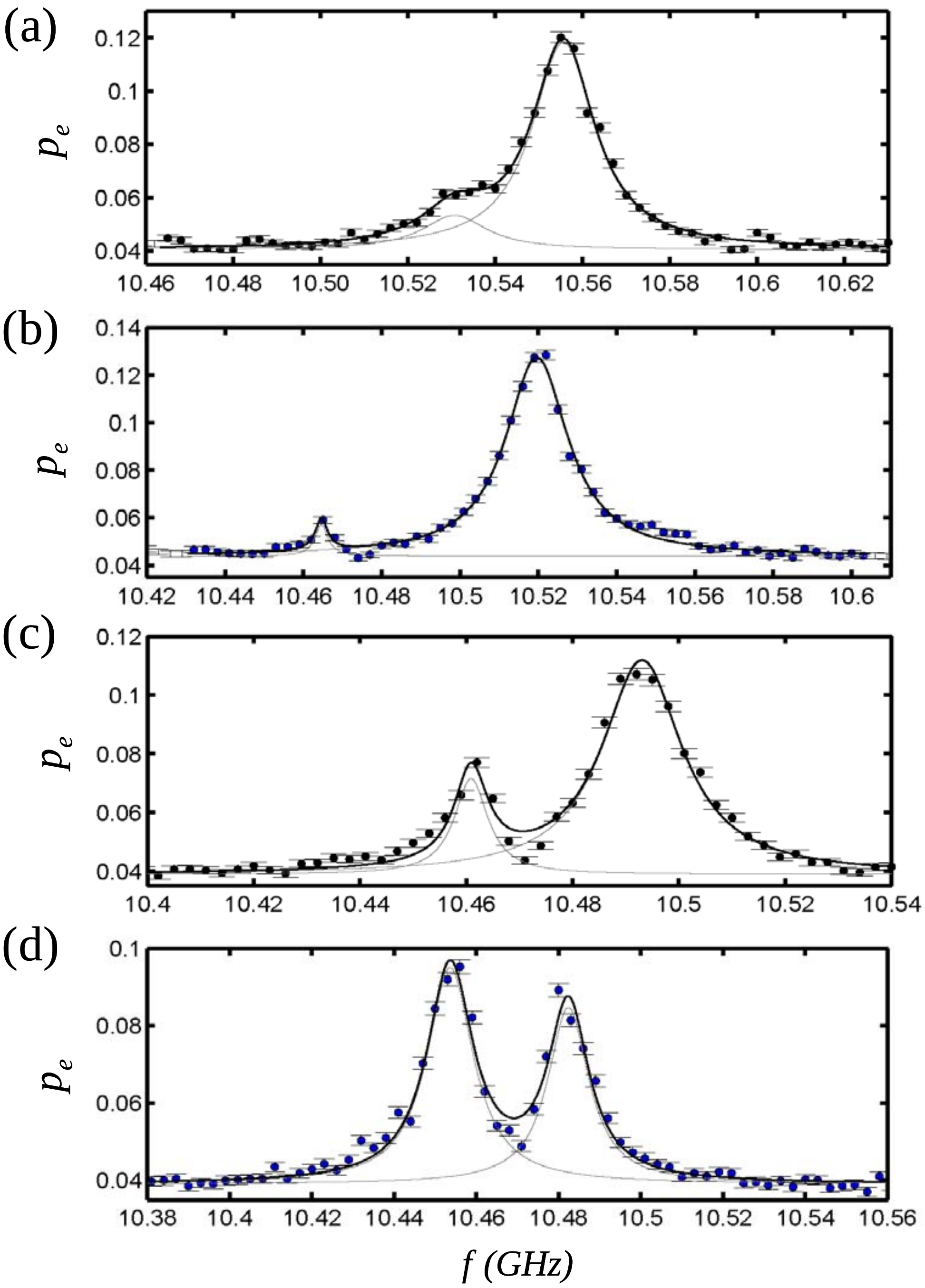

Figure 10.2: Lorentzian fits to resonant peaks in spectrum of SQUID DS$_{3A}$. At each bias current, p_e was χ^2 fit with an appropriate number of Lorentzians. From these fits (see Table 10.1) the location and full-width-half-max Δf for each peak was determined.

Table 10.1: Parameters from Lorentzian fits shown in Fig. 10.2.

plot	Peak (GHz)	Δf (MHz)	Amplitude	Offset
a	10.531	17.8	0.0128	0.0406
a	10.556	17.2	0.0778	0.0406
b	10.465	3.9	0.0132	0.0438
b	10.520	19.3	0.0837	0.0438
c	10.461	7.7	0.0325	0.0387
c	10.493	18.2	0.0726	0.0387
d	10.454	13.9	0.056	0.0386
d	10.482	12.0	0.0457	0.0386

Figure 10.3 summarizes the result of the analysis. The circles in Fig. 10.3 correspond to the location of the resonance peaks and the vertical lines the FWHM, found using the fitting procedure at each current. The open circles at 10.714 GHz correspond to “peaks” that were not Lorentzian. The enhancement for these points immediately drops to zero above 10.714 GHz, regardless of the bias current and the enhancement at frequencies less than 10.714 GHz. This suggests that microwaves were not able to reach the qubit here. I have therefore ignored these points in my fit.

Figure 10.4(a) is an enlarged section of Fig. 10.3 where I have also added labels to several of the states; microstates subscripts not shown are in their ground state, i.e. $\left|0e_4\right\rangle = \left|0g_1g_2g_3e_4g_5g_6g_7g_8\right\rangle$. In Figure 10.4(a), I have represented some branches with triangles for clarity. The solid lines in Figs. 10.3 and 10.4(a) are a fit to the energy levels of the qubit coupled to eight microstates. The uncoupled junction spectrum is found from solving Schrodinger’s equation for a single Josephson junction, which depends on only the critical current, here $I_0 = 1.263\,\mu A$ and capacitance of the junction qubit $C = 0.377\,pF$. In the fit to the full spectrum, I assume that each TLS has a first excited state energy that is independent of I and does not directly couple to other

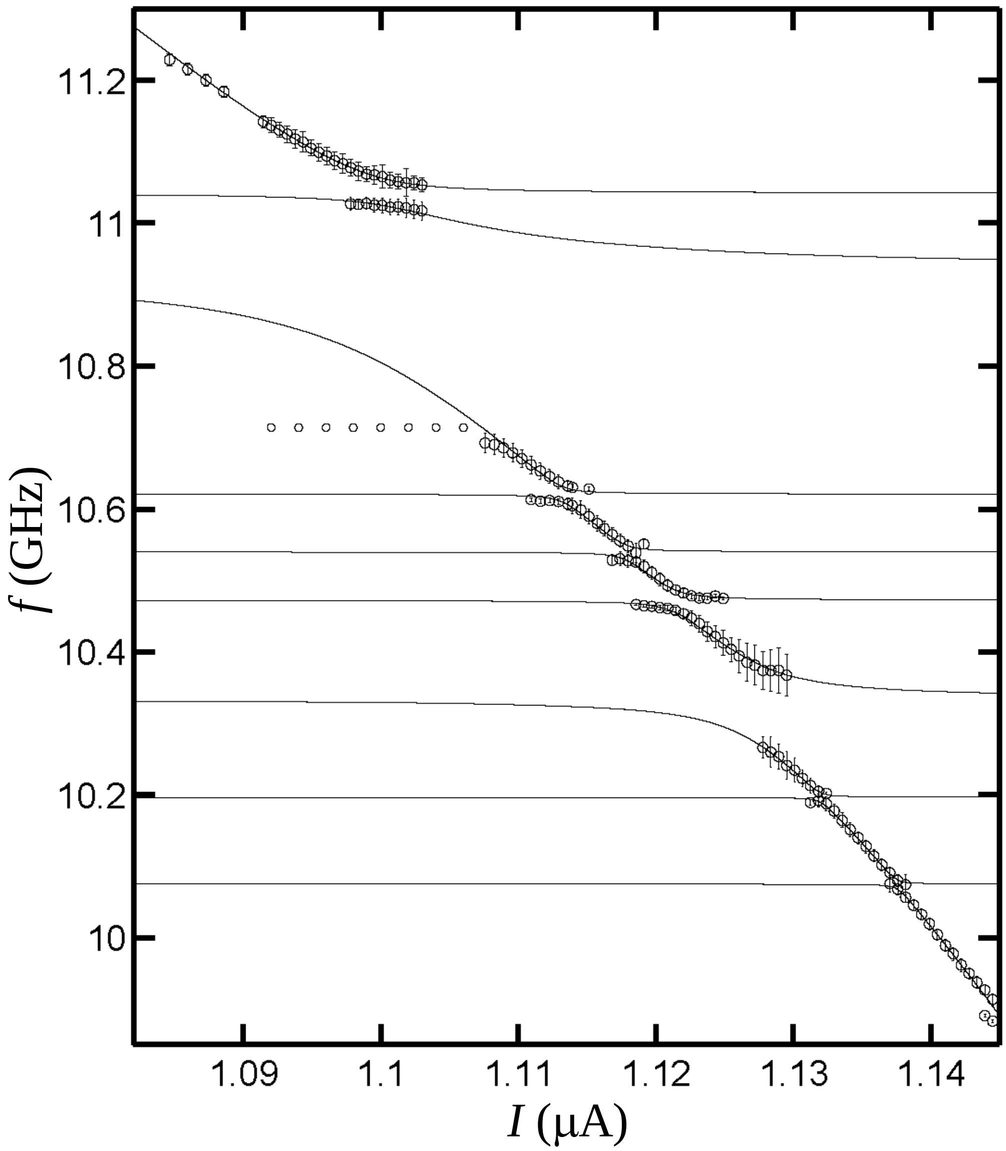

Figure 10.3: Transition spectrum for DS_{3A} showing the peak location (circles) and FWHM (vertical lines) from fitting each bias point. The solid line is a fit to the data using a single junction model, and 8 microstates. The frequency and coupling strength for each microstate was varied to give the best χ^2 fit. The microstates are assumed to only couple to the junction and not directly to each other. Table 10.2 shows the best-fit values used here for the fit.

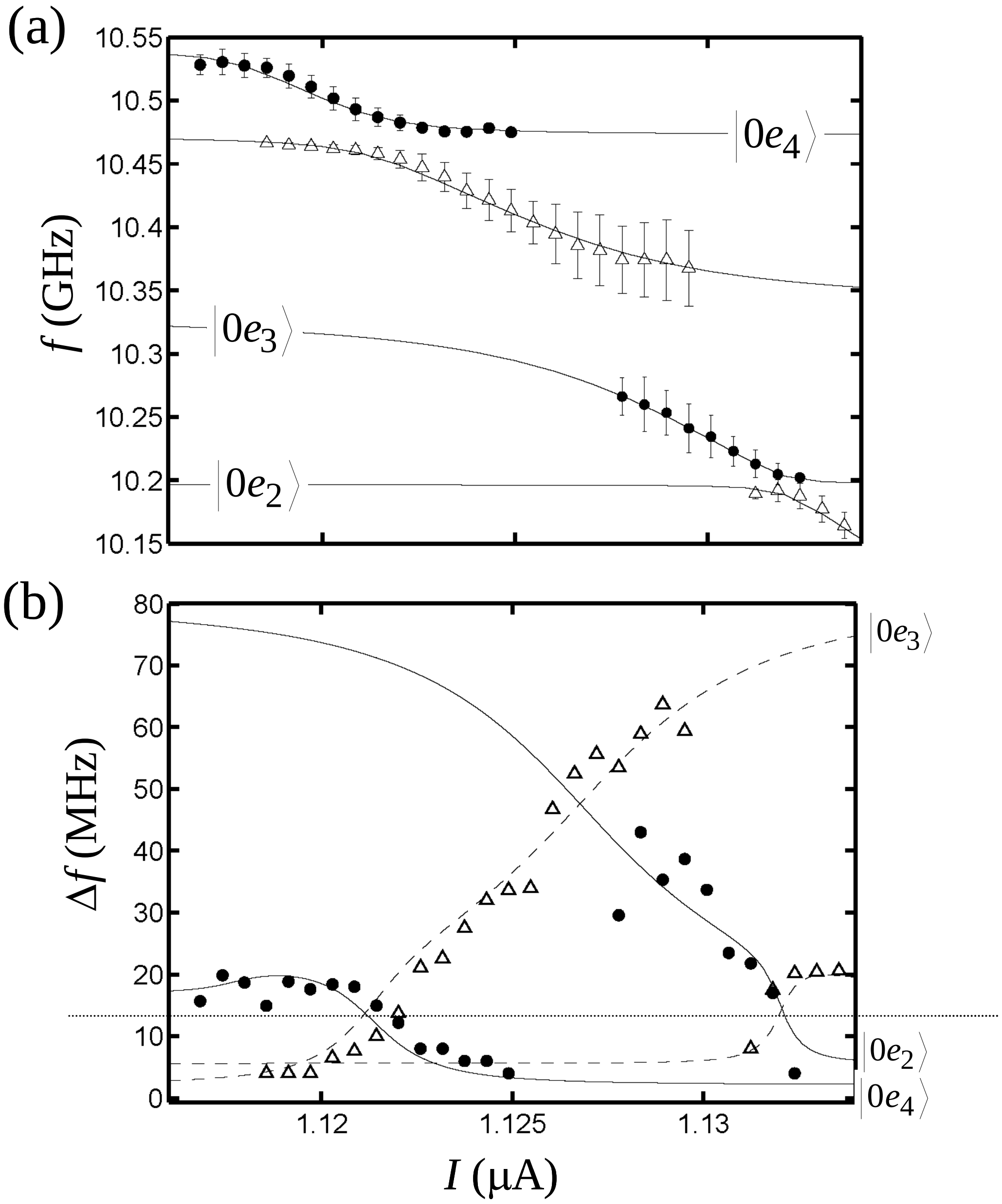

Figure 10.4: Enlarged sections of Fig. 10.3 and 10.5. (a) An enlarged section of spectrum in Fig. 10.3 with several states labeled. Circles and triangles are used to clarify the different branches. (b) Corresponding section of FWHM from Fig. 10.5 with the same states labeled. The dashed curve is the fit to the triangle points and the solid curves fit the circles. The FWHM of the junction as determined from the entire fit is plotted as a horizontal dashed line at $\Delta f = 12\,MHz$.

microstates. Here, I will add a subscript to clarify the different microstates, for example Δ_{fi} and f_i are the splitting size and frequency of the ith microstate, respectively.

For the fit curves in Fig. 10.3 and 10.4, each f_i and Δ_{fi} and the qubit parameters I_0 and C were varied to determine the best fit to the peak locations for the entire spectrum simultaneously. The resulting best fit values are given in Table 10.2. For example, in a two microstate system coupled to the qubit the eigenvalues of the following Hamiltonian would have been determined:

$$\begin{bmatrix} \langle 0eg|H|0eg\rangle & \langle 0eg|H|0ge\rangle & \langle 0eg|H|1gg\rangle \\ \langle 0ge|H|0eg\rangle & \langle 0ge|H|0ge\rangle & \langle 0ge|H|1gg\rangle \\ \langle 1gg|H|0eg\rangle & \langle 1gg|H|0ge\rangle & \langle 1gg|H|1gg\rangle \end{bmatrix} = \begin{bmatrix} f_1 & 0 & \Delta_{f1}/2 \\ 0 & f_2 & \Delta_{f2}/2 \\ \Delta_{f1}/2 & \Delta_{f2}/2 & f_{01}(I) \end{bmatrix}. \qquad (10.1)$$

With eight microstates, the actual Hamiltonian, I used was a 9x9 matrix (see Appendix A).

The data in Fig. 10.3 was taken several months after that shown in Fig. 10.1, yet most of the splittings remained relatively fixed. A few observations can be made from the spectrum of Figs. 10.1 and 10.3. All the splittings here are much larger than any seen in DS$_2$, the implications of this fact are discussed in Section 10.5. Examination of Fig. 10.3 shows that I obtained excellent agreement between the data and the fit, especially considering the simplicity of the model. While I assume the microstates do not couple to each other, they affect the fit of each other through the qubit. Unfortunately, the fit in itself does not reveal much about the microscopic nature of the TLSs.

Figure 10.5 shows the full-width-at-half-maximum ($FWHM$ or Δf) of the resonant peaks as a function of current. The circles and triangles represent the $FWHM$ values as determined by the Lorentzian fits described above; two different symbols are

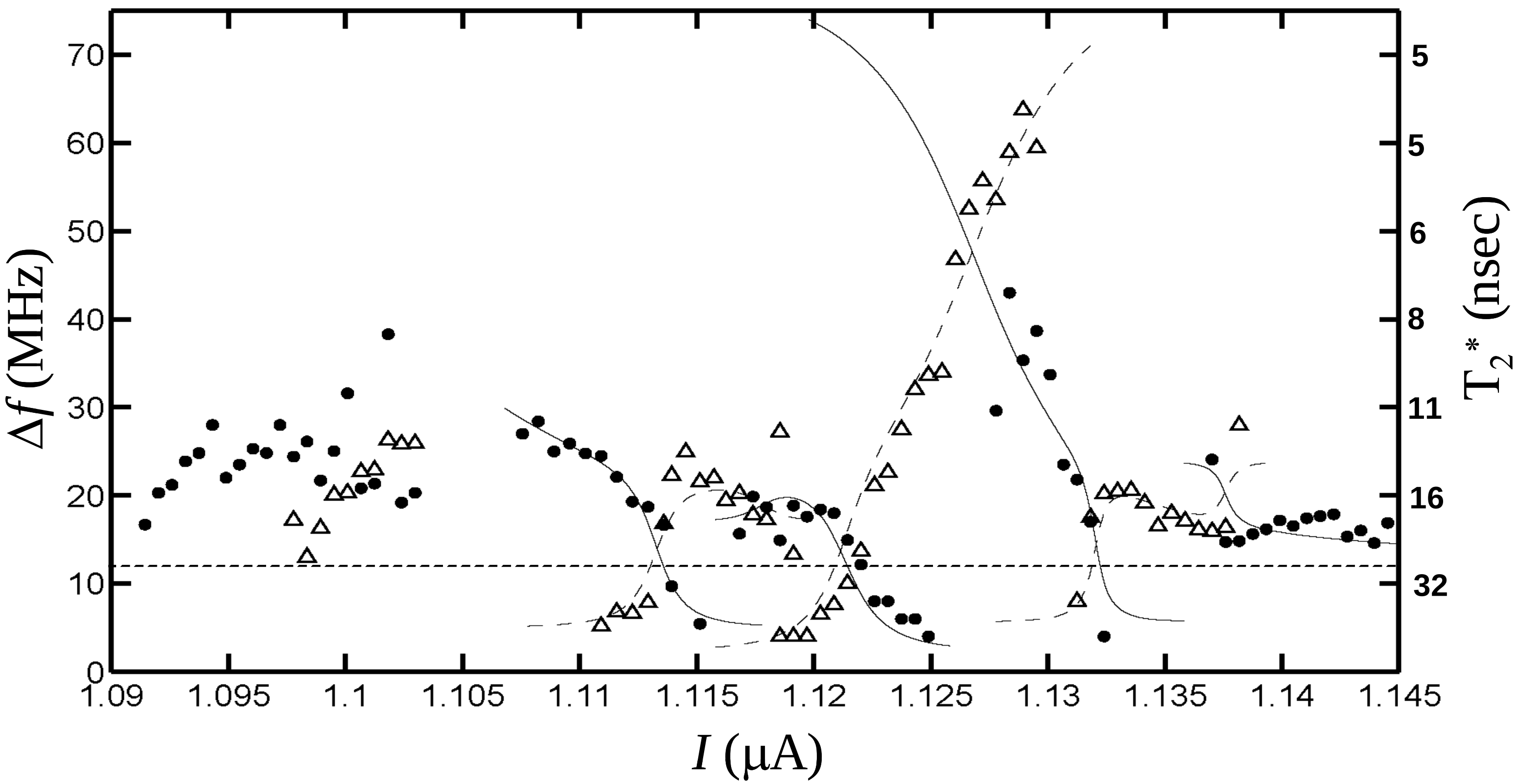

Figure 10.5: FWHM and spectroscopic coherence times T_2^* of the microstates and qubit DS_{3A}. The circles and triangles represent the measured FWHMs found from Lorentzian fits. With the microstates energies and coupling fixed from the fit in Fig. 10.3, the microstate and junction spectroscopic coherence times vs. current were then χ^2 fit (solid and dashed curves). When the microstates frequency is significantly far away from the qubit's the fit curves are removed for clarity in the plot.

Table 10.2: Best fit microstate parameters for DS_{3A} spectrum as shown in Fig. 10.3.

Microstate	$f(GHz)$	$\Delta_{fi}(MHz)$	$\Delta f\ (MHz)$	$T_2^*\ (ns)$
1	10.075	14	23	14
2	10.197	16	6	53
3	10.335	114	80	4
4	10.472	36	2	159
5	10.540	24	17	19
6	10.621	24	5	64
7	10.935	240	~ 80 [121]	4
8	11.042	60	< 20 [122]	>15
Qubit	$f_{01}(I_0, C, I)$		12	27

used to clarify distinct branches in the spectrum. As the qubit comes in and out of resonance with the microstates, the $FWHM$ of the eigenstates reflects this. The $FWHM$ can also be written as a spectroscopic coherence time T_2^*, where $T_2^* = 1/\pi\Delta f$ (see right hand axis in Fig. 10.5). Figure 10.4(b) shows an enlarged view of the fit in the same region as Fig. 10.4(a) to help clarify the relationship between the two curves and the fitting procedure.

The solid lines in Fig. 10.5 and 10.4(b) are fits to the widths of the coupled systems. Imaginary energy terms representing T_2 were added to the microstates and qubit energies in the Hamiltonian of Eq. (10.1); then the eigenvalues of the system at each bias point were again determined. The real component of the resulting eigenvalue is the frequency f and the imaginary component is $\Delta f/2$. The coupling strengths and real part of the energies were completely determined from fitting the peak Lorentzian locations, only the coherence times were varied to fit the widths (see Table 10.2 for fit parameters used). The best fit produced a qubit $\Delta f = 12\ MHz$ or $T_2^* = 27\ ns$. For clarity in Fig. 10.5, the values for Δf are only shown near the avoided crossing, since otherwise they appear as constant horizontal lines. I generally observe good qualitative agreement, with the $FWHM$ reflecting its composition from the different systems. However, some discrepancies are clearly visible. For example, in Fig. 10.4(b) at $I \approx 1.122\,\mu A$, the crossing in the $FWHM$ points does not quite match the predicted crossing. As expected, eigenstates that are predominantly an individual TLS have a fixed $FWHM$ that changes as the crossing is approached. Finally, I found that at $I \approx 1.108\,\mu A$, the peaks are very poorly fit by Lorentzians and at $I \approx 1.10\,\mu A$ the data is very scattered, and thus no fits are shown for $I < 1.108\,\mu A$.

I note that several of the microstates I found had $\Delta f < 5\ MHz$ or $T_2^* > 64\ ns$. For example, fine scale measurements with 1 MHz steps in a region where the 4th microstate (at 10.472 GHz) was only very weakly coupled showed $\Delta f = 4\,MHz$ or $T_2^* = 80\,ns$ (see Fig. 10.6). The star in Fig. 10.6(a) represents the peak location and Fig. 10.6(b) shows the spectrum that determined the peak. Interestingly, the 3rd microstate has a much larger $FWHM$ ($\Delta f = 80\,MHz$ or $T_2^* = 4\ ns$) along with a much larger splitting size $\Delta_{f3} = 114\,MHz$. Perhaps this splitting has a different physical origin than the others.

Away from resolvable splittings, the coherence time of the qubit also appears to vary somewhat, potentially due to smaller unresolved splittings. The best $FWHM$ measured for the qubit was $\Delta f = 15\ MHz$ or $T_2^* = 21\ ns$ at $f_{01} = 10.080\ GHz$ as shown in Chapter 8. This was close to the 12 MHz value used in the fit shown in Fig. 10.3. I note that as the current through the junction is decreased, $\partial f_{01} / \partial I$ decreases, suggesting a smaller spectroscopic width should be expected at higher frequencies if the device is limited by low-frequency current noise (a similar argument can be made for flux noise or

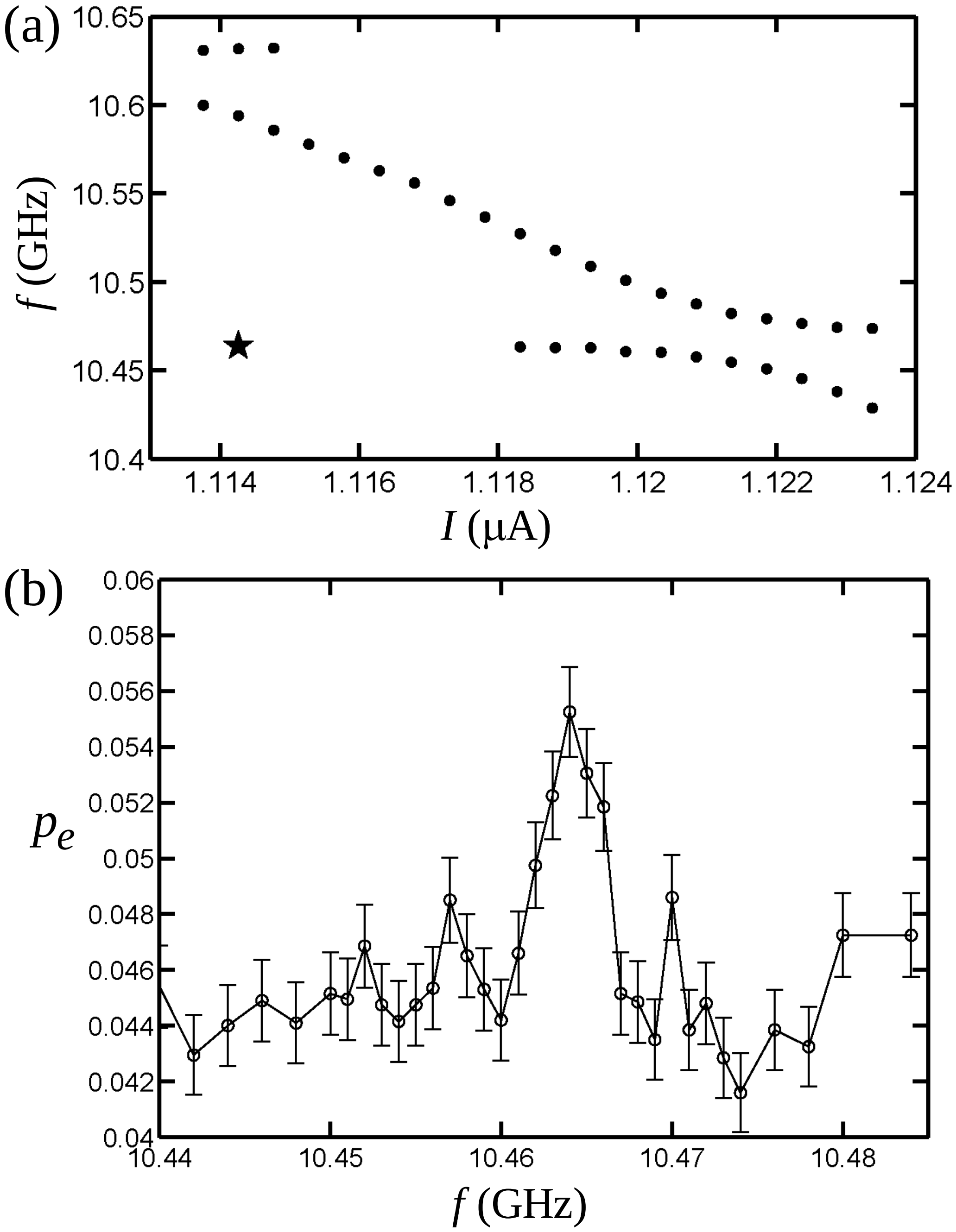

Figure 10.6: Fine scale measurement of the spectrum with 1 MHz steps. (a) The splitting centered at $I = 1.121\mu A$ (microstate 4) was followed down to $I \sim 1.114\mu A$, far from the avoided crossing. The peak frequency location as determined from (b) is plotted with a star in (a). The FWHM is approximately 4 MHz.

critical current noise). This effect does not appear in my data, although the lowest frequency in this data set is fairly deep (less sensitive) compared to our previous measurements.

Similar splittings were also seen in DS_{4B} (see Fig. 8.16). In this device I did not analyze the spectrum in detail, but it is clear from the rough spectrum that a wide range of splitting sizes are visible. For example, at 9.25 GHz and 8.95 GHz splittings with $\Delta_f \approx 30\,MHz$ are visible as well as a much larger ones at 8.8 GHz and 9.1 GHz.

10.2 Coherent Dynamics

While splittings are indicative of the qubit coupling to other quantum systems, seeing real time dynamics associated with it provides an additional window into the interaction. To look for coherent dynamics associated with the TLS, the qubit was biased at $I \approx 1.122\,\mu A$, where the qubit was maximally entangled with the 4th microstate. In this experiment, taken several months before the fit data in Table 10.2, at the maximally entangled current the splitting was $25 \pm 3\,MHz$ (compared with 36 MHz shown in Table 10.2). In Fig. 10.7(a) the circles represent the eigenstates for this splitting. A short microwave π-pulse (~5 ns) at 10.469 GHz was applied, [represented by the 3rd star in Fig. 10.7(a)]. This frequency is midway between the transition frequencies at the avoided crossing. This was chosen with the idea that the microwaves would only pump the junction, leaving it in the state $\left|1g\right\rangle$, which is not an eigenstate of the system. In an idealized system without decoherence or relaxation after the pulse the state of the system would then evolve as

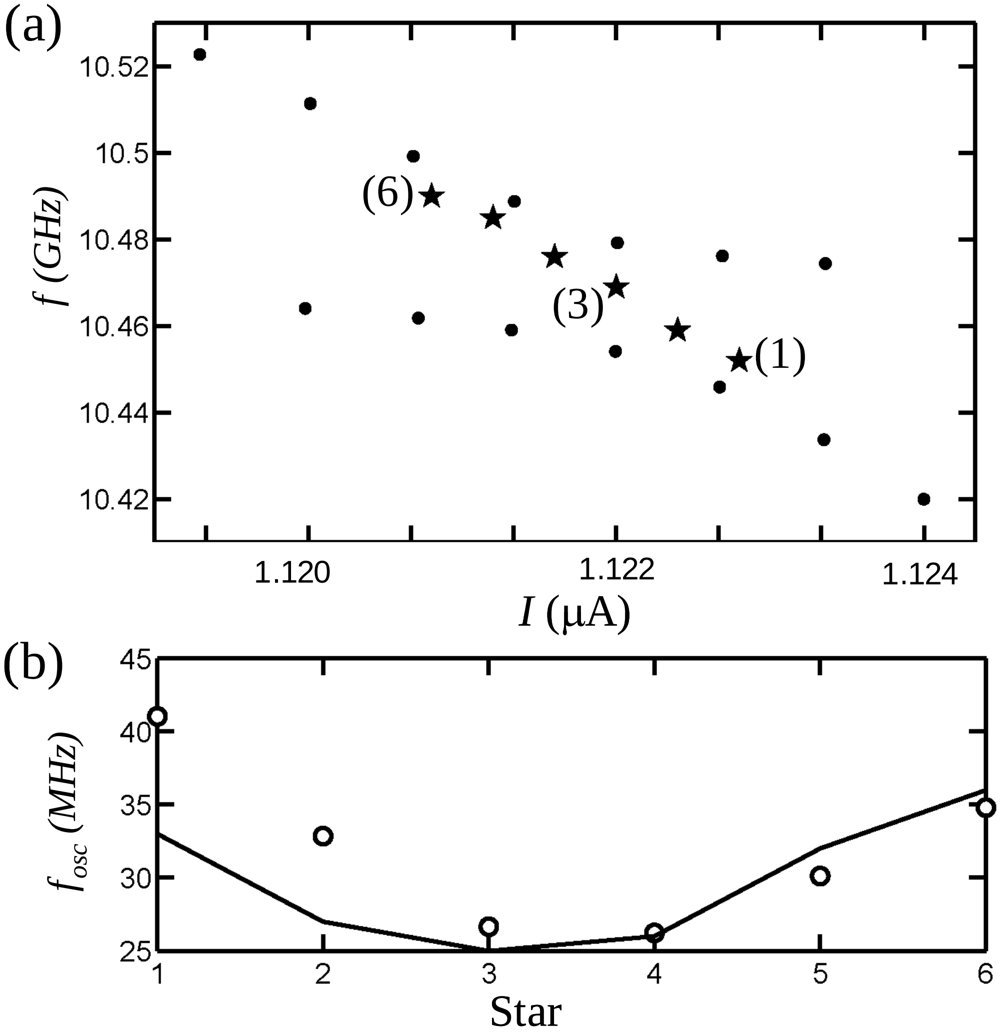

Figure 10.7: Spectrum and coherent dynamics near the 4th microstate. (a) The circles represent the eigenstates of the coupled system near the 4th microstate. The stars show the current I and microwave frequency applied to excite the system into a non-eigenstate. (b) Points show oscillation frequency as roughly determined from Fig. 10.8(c) for the six locations in Fig. 10.7(a). Solid curve shows splittings size as determined from the spectrum.

$$\psi(t) = \exp(-i\omega_{01}t)\left(\cos(\pi\Delta_f t)|1g\rangle + i\sin(\pi\Delta_f t)|0e\rangle\right) . \qquad (10.2)$$

A measurement of the probability of finding the qubit in its excited state would give

$$\left|\langle 1g\|\psi(t)\rangle\right|^2 = \left[\cos(\pi\Delta_f t)\right]^2 = \frac{1}{2} + \frac{1}{2}\cos(2\pi\Delta_f t). \qquad (10.3)$$

The filled circles in Fig. 10.8(a) shows the probability in $n = 1$ versus time as measured using the pulse readout technique. After the 5 ns π-pulse, the subsequent decay oscillates weakly with a period close to 40 ns, which would be expected based on the splitting. Figure 10.8(b) shows p_1 versus time if the microwaves are not shut off after 5 ns. Figure 10.8(c) shows the results of a π-pulse and subsequent decay if the qubit is biased at different locations near the splitting; the locations are represented as stars in Fig. 10.7(a). For clarity, the successive curves in Fig. 10.8(c) are offset in p_e for each larger qubit bias current. For comparison, the curve in Fig. 10.8(a) is again plotted in Fig. 10.8(c) with a solid line (3rd from the top). As the eigenstates become further separated, the frequency of the oscillation in the free evolution decay increases, as expected. This change in the oscillation frequency, as roughly estimated from Fig. 10.8(c) is shown for the 6 bias locations in Fig. 10.7(b). The solid curve shows the splitting size as determined from the spectrum. The frequencies from the two measurements follow the same trend.

The coupled system can be modeled using the density matrix to include effects of relaxation and decoherence. For this simulation, I assumed that the microwaves only couple to the qubit junction and chose the qubit and TLS relaxation and dephasing times to achieve a good it. The population from the simulation was multiplied by 0.78 and given an additional 0.07 to roughly account for the measurement fidelity of the single-shot pulse measurement. The solid lines in Fig. 10.8(a) and (b) show the results of these

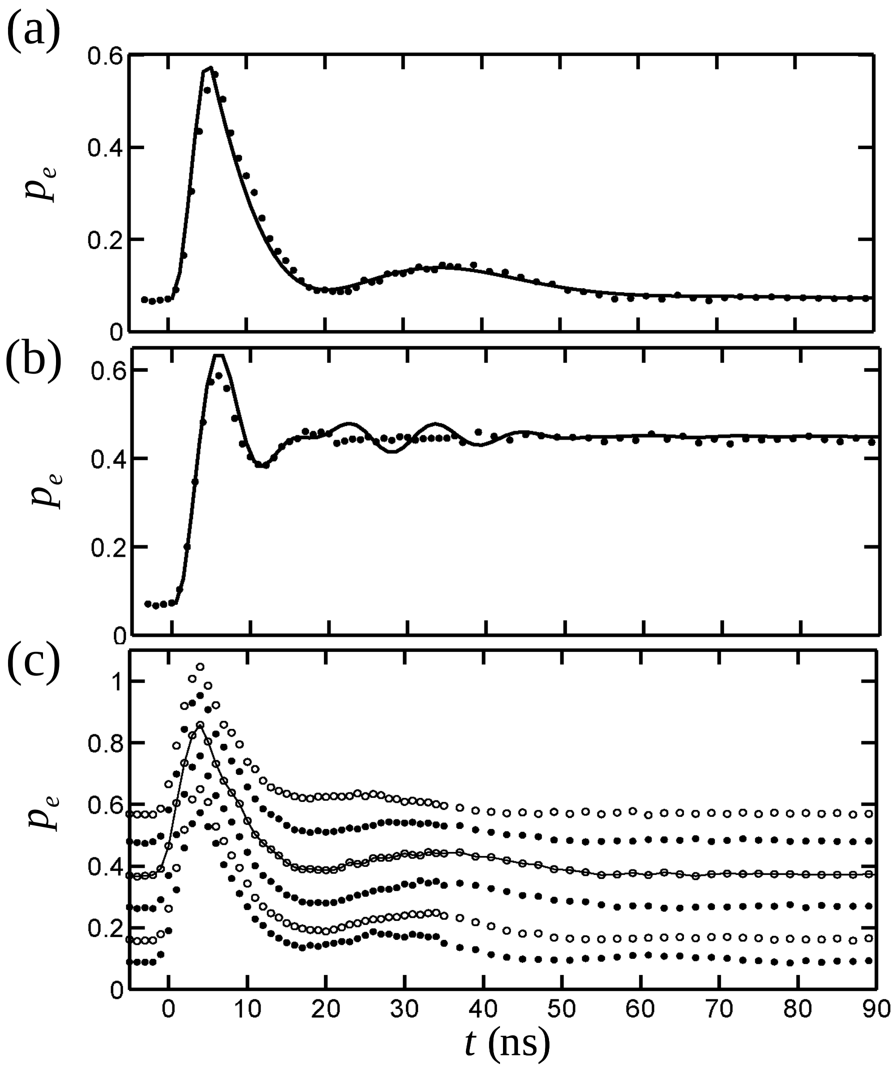

Figure 10.8: Coherent dynamics of microstate #4 coupled to device DS_{3A}. (a) The system was prepared in a non-eigenstate by applying a 10.469 GHz, 5ns, π-pulse. After the microwaves were shut off at $t = 5ns$ the system decayed with a weak oscillation. (b) Measured switching probability when the microwaves were left on. The solid line in (a) and (b) is a density matrix fit to the data with $T_1 = 9ns$ and $T_\phi = 30ns$ for the qubit and $T_1 = 100ns$ and $T_\phi = 400ns$ for the TLS. The simulation is in rough agreement, but predicts some features not seen in the data in (b). (c) The same experiment as (a) for the bias locations shown in Fig. 10.7(a) as stars. Solid curve is same as in (a).

simulations with $T_1 = 9\ ns$ and $T_\phi = 30\ ns$ in the qubit, $T_1 = 100\ ns$ and $T_\phi = 400\ ns$ in the two-level system, $\Delta_f = 25\ MHz$ and $f = 10.469\,GHz$. Using these parameters I was able to model the free evolution data rather well [see Fig. 10.8(a)]. In fitting the data, the key parameters were $T_1 = 9\,ns$ in the qubit and $\Delta_f = 25\ MHz$; the fit was not very sensitive to T_1 and T_ϕ of the TLS, provided they were much longer than the corresponding times for the qubit. Using these same parameters I fit the case where microwaves were left on, as shown in Fig. 10.8(b).

The simulation in Fig. 10.8(b), however, showed some interesting behavior from $t = 20\ ns$ to $40\ ns$ that was not seen in the data. In the simulation, the coherent population in the TLS seems to have leaked back to the qubit to produce the effects around $t = 20 - 40\,ns$. This effect wasn't seen in the experimental data, perhaps due to the other microstates near by in frequency. If I assume $T_1 = 30\,ns$ in the qubit, I was unable to fit the data, regardless of the splitting size. Since the known microstate is accounted for, it is curious that the data seemed to require a qubit relaxation time $T_1 \sim 9\,ns$ that is much shorter than that found elsewhere in the device away from splittings $T_1 \sim 30\,ns$. Perhaps this is due to other microstates near by. I note that in both the free evolution and spectroscopic fits, TLS #4 appears to have a substantially longer T_2^* than the qubit. The relatively long T_2^*, and the presence of coherent oscillations in the free evolution decay, suggests the microstates may be good qubits themselves, as suggest by Zagoskin *et. al*. [120].

10.3 Higher Level Spectroscopy

The interaction of a microstate with the second excited state of the qubit $n = 2$ can provide a check on our understanding of the coupled system. In particular, if $\left|0e\right\rangle$ and $\left|1g\right\rangle$ have the same energy, then at this same bias current $\left|1e\right\rangle$ should have about the same energy as $\left|2g\right\rangle$. Based on the analysis of Chapter 9, I would expect $\left|1e\right\rangle$ to strongly couple with $\left|2g\right\rangle$, while $\left|2g\right\rangle$ should only very weakly couple to $\left|0e\right\rangle$.

To check the higher-level spectrum, I applied microwaves to excite $n = 0 \to n = 2$ qubit transitions in the 20-21 GHz range. Figure 10.9 shows the corresponding gray scale plot of the spectrum. Unlike the $n = 0 \to n = 1$ spectrum, two "tilted" avoided crossings are visible, while no "horizontal" splittings are evident. For other data sets as well, I found no signs of horizontal splittings from 21.4 GHz down to 20.0 GHz. I note that at 19.93 GHz and 21.420 GHz peaks did emerge and their frequency did not appear to depend on the qubit junction. Presumably they were due to a resonance in the system of unknown origin.

As was done for the lower frequency spectrum, this spectrum was fit with a series of Lorentzians at each bias point. For the higher-level spectrum data, a Lorentzian peak was included for every clear distinguishable peak; often more than two were required. Several sample slices are shown in Fig. 10.10(a-d). The dashed curves represent the individual Lorentzian peaks used to fit the measured points (circles) and the dark curve is the result of the combined Lorentzians. A list of the parameters used in these fits is given in Table 10.3. While the resolution is worse than the lower spectrum due to the larger widths and greater number of peaks involved, the spectra are fairly well represented by

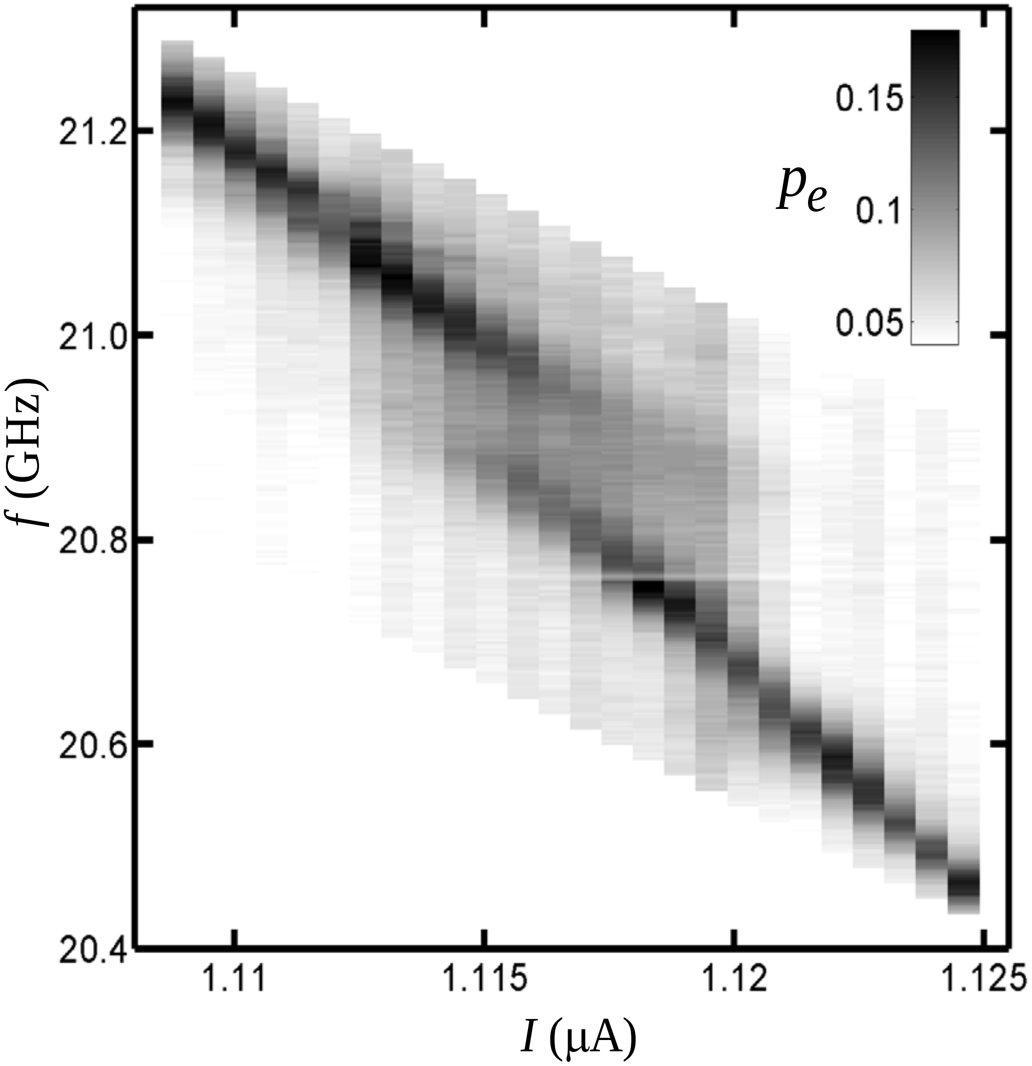

Figure 10.9: Transition spectrum of the qubit and microstates from 20.4 to 21.3 GHz. The false color map represents the fraction that escaped with a measurement pulse. Two "tilted" splittings are visible, one near 20.9 GHz and one near 21.1 GHz. No horizontal splittings are visible; the light horizontal band near 20.78 GHz is likely due to an anti-resonance in the microwave line, since no bending of the spectrum occurs as the frequency is approached.

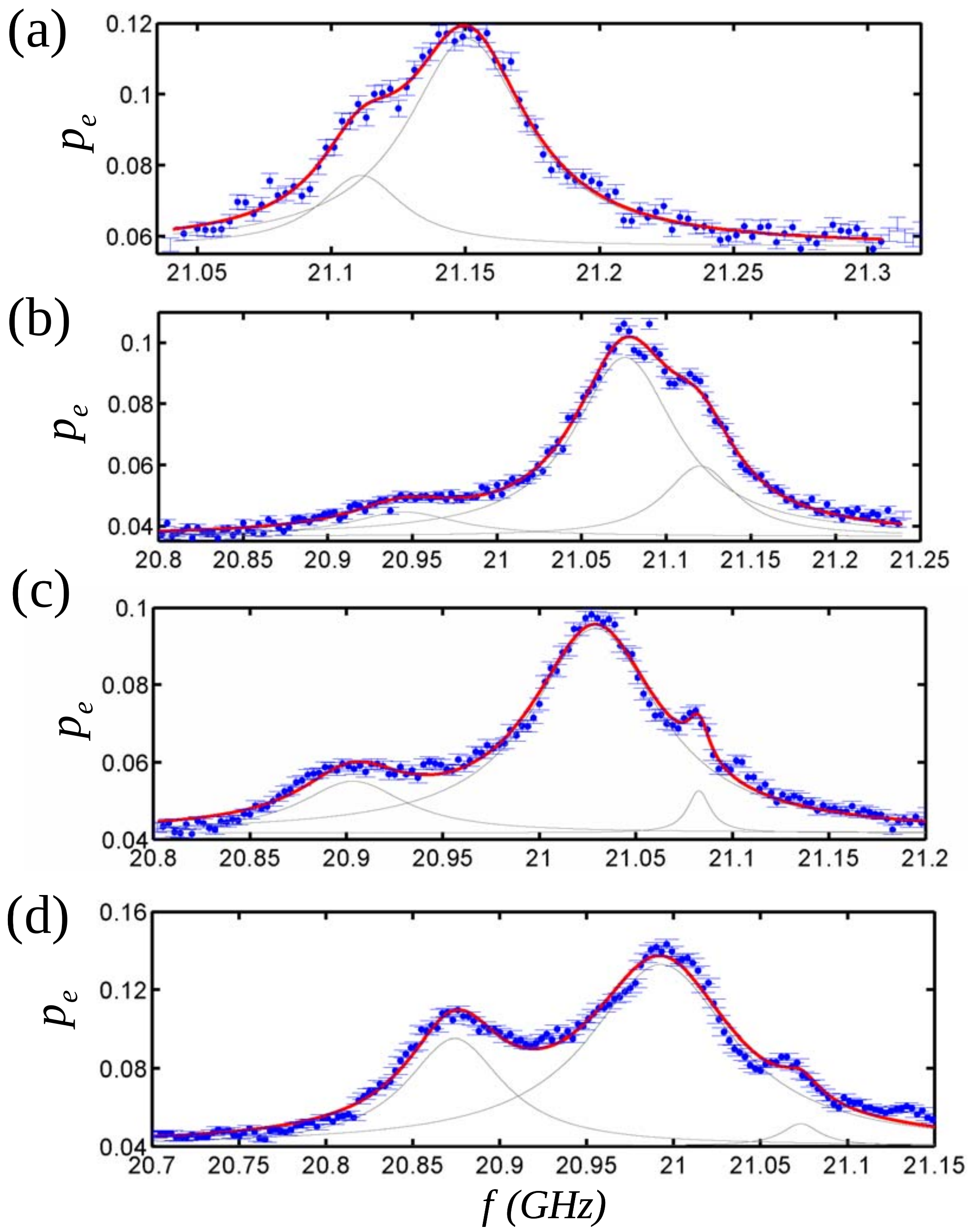

Figure 10.10: Sample fits to the higher frequency spectrum. (a-d) Sample slices at fixed current show how several Lorentzians were used to fit the data. The parameters used for the fits are given in Table 10.3.

Table 10.3: Fit parameters for resonant peaks shown in Fig. 10.10.

plot	Peak (GHz)	Δf (MHz)	Amplitude	Offset
a	21.111	37.5	0.02	0.057
a	21.150	54	0.058	0.057
b	20.945	78.4	0.0079	0.0366
b	21.076	73	0.058	0.0366
b	21.120	52.1	0.023	0.0366
c	20.903	66	0.0133	0.0417
c	21.029	80.6	0.0528	0.0417
c	21.0826	14	0.0109	0.0417
d	20.874	68	0.0548	0.04
d	20.993	0.101	0.0925	0.04
d	21.073	0.027	0.0112	0.04

the fit. Figures 10.10 and 10.11, taken two months after Fig. 10.5, show the corresponding higher-level transitions associated with Fig. 10.3. The two spectra shown in Fig. 10.3 and 10.11 were taken within a week of each other to enable a direct comparison and to minimize bias calibration drift and possible changes in the splittings sizes and locations. In Fig. 10.11 and 10.12, the circles and "error bars" again show the peak location and FWHM at each bias current.

Examination of Fig. 10.11 reveals clear slanted avoided level crossings. This qualitative behavior is exactly what one expects for $\left|2g\right\rangle$ states coupling to $\left|1e\right\rangle$ states. The solid curves in Fig. 10.11 are uncoupled predictions of the $\left|0g\right\rangle \rightarrow \left|1e\right\rangle$ transition versus bias, determined solely from the fits in Fig 10.3. The predictions ignore coupling and come from simply adding the single junction transition frequency $f_{01}(I)$ and microstate transition frequency f_i determined previously (*i.e.* $f = f_{01}(I) + f_i$) with no free parameters. The three curves represent the three largest splittings found in the lower frequency spectrum that would be expected in this higher frequency spectrum. I note that

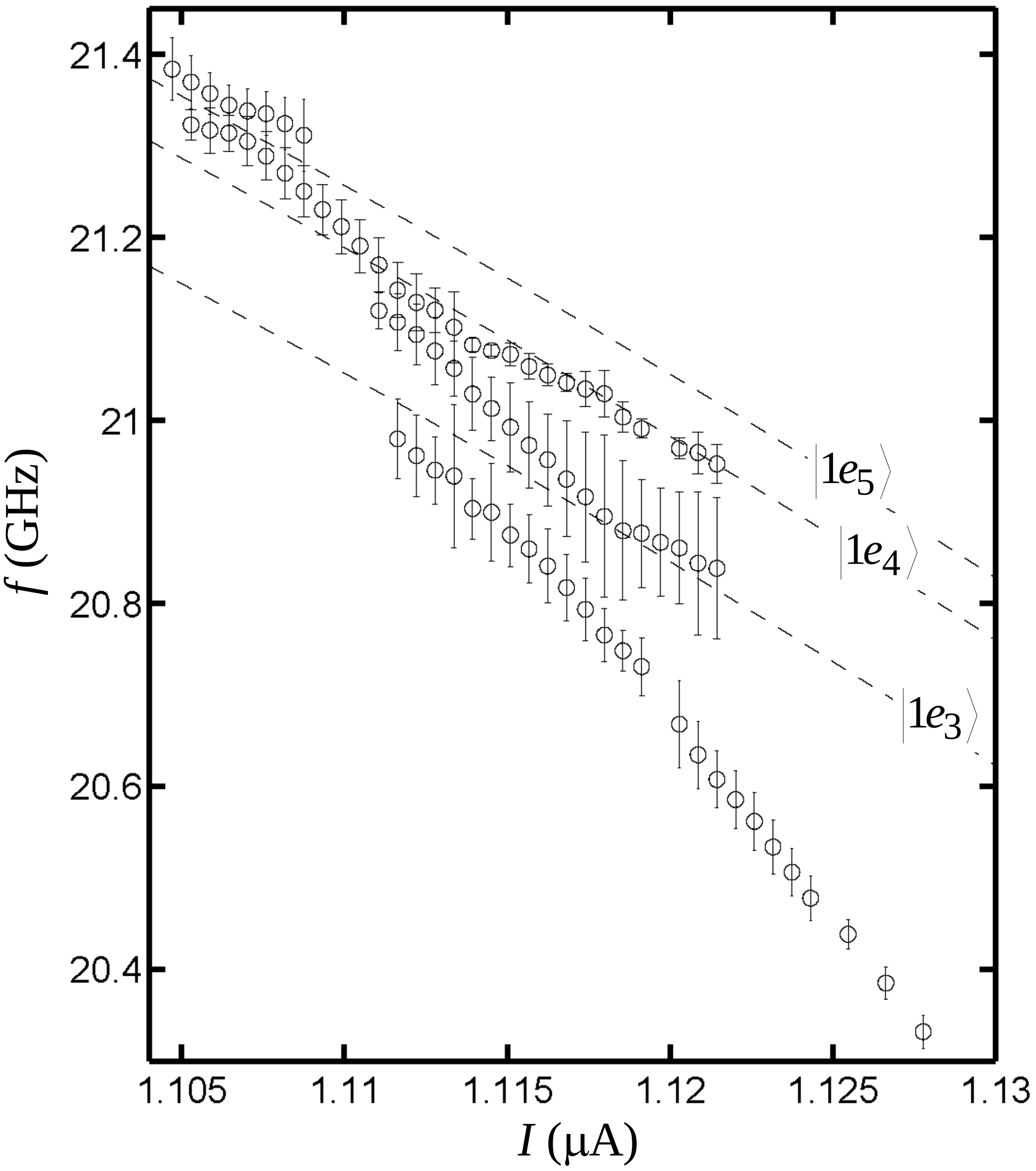

Figure 10.11: Higher frequency transition spectrum in DS_{3A}. The circles correspond to the fit peaks and the "error bars" the FWHM at each bias point. The dashed curves represent the transition frequency found by adding the qubit f_{01} and the different microstate transitions as determined from Table 10.2, with no new fit parameters. Three "tilted" avoided crossings are clearly visible.

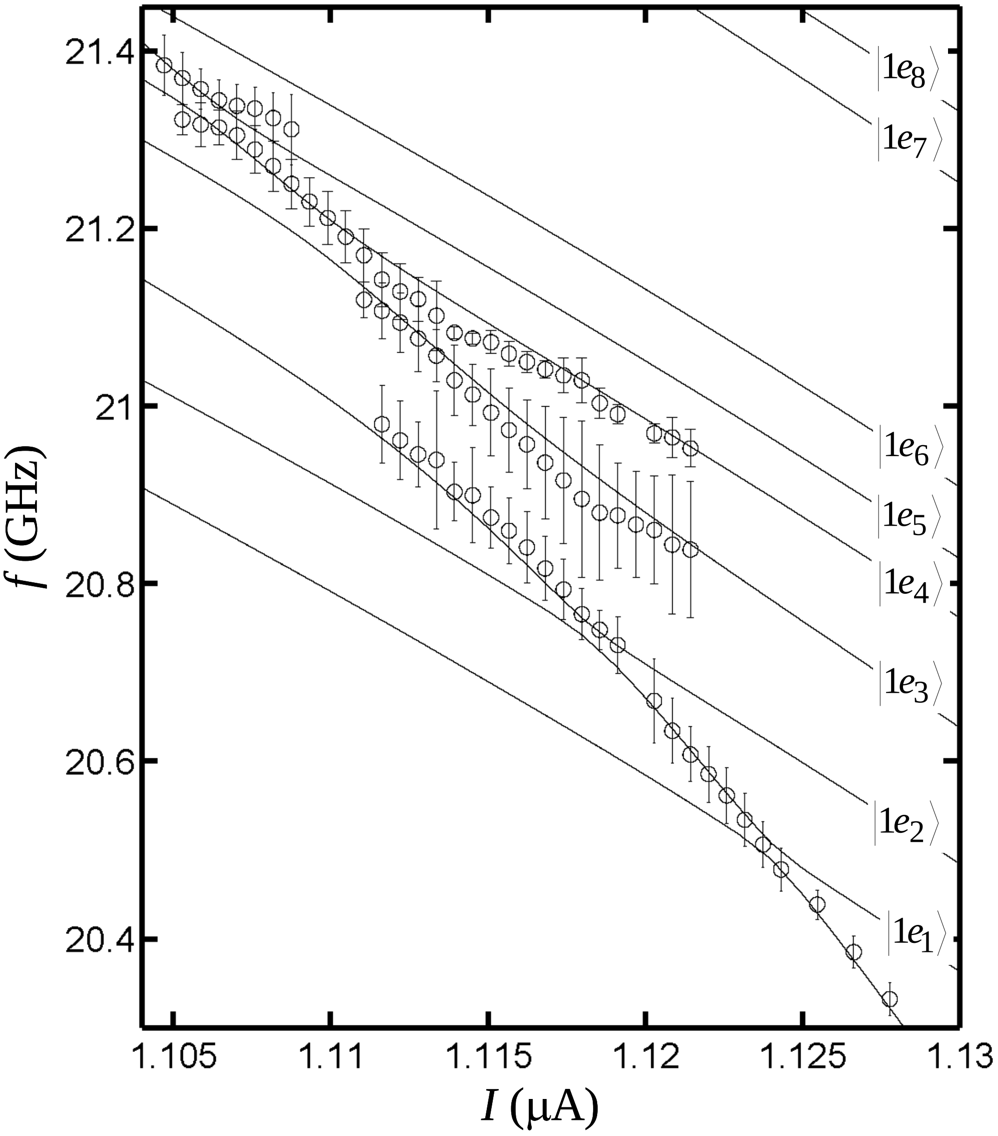

Figure 10.12: Fit to the higher frequency spectrum in DS_{3A}. The circles correspond to the fit peaks and the "error bars" are FWHM at each bias point. The solid curves show fits to the second excited state energy of eight TLSs and a junction model with $\frac{\langle 2g|H_c|1e\rangle}{\langle 1g|H_c|0e\rangle}=\sqrt{2}$. The microstate frequencies and coupling strengths are fixed from the lower spectrum (see Table 10.2).

the three curves predict the tilted experimental crossings seen in the data fairly well.

Figure 10.12 takes this model a step further by fitting the slanted avoided crossings using the second excited state of a junction and including coupling between the junction and microstate. With the $|1e\rangle$ energy determined from the lower spectrum, the coupling between $|2g\rangle$ and $|1e\rangle$ for each microstate was fixed at $\sqrt{2}\Delta_{fi}$, which is what one would expect for harmonic states in the junction (see Section 9.2). This assumption comes directly from both coupling models of Chapter 9. For the fits in Fig. 10.12, the Hamiltonian shown in Eq. (10.1) must be expanded to include higher states, with terms including $|1e\rangle$ and $|2g\rangle$. Unfortunately, the single junction model with the same parameters as before was unable to fit the $n=0 \rightarrow n=2$ transition even away from splittings. This may be because the qubit is not actually a single current bias Josephson junction, but part of a dc SQUID [42] or because the current had changed slightly over two weeks. To obtain the fit shown, a single junction model with a critical current of $I_0 = 1.266\,\mu A$ and $C = 0.374\,pF$ was used for $n=2$, slightly different than what I used for the $n=1$ transition ($I_0 = 1.263\,\mu A$ and $C = 0.377\,pF$). The resulting curves are in good agreement with the data, although some discrepancies are obvious. I note that if the coupling of the three slanted avoided crossing is adjusted for the χ^2 best fits, I find the best fits for coupling are 1, 1.5 and 2 times the lower coupling (*i.e*. coupling size of 64 MHz for the 3rd microstate, 23 MHz for the 4th microstate and 25 MHz for the 5th microstate).

In theory another type of avoided level crossing should be present in the higher-level spectrum. If one can resolve the spectrum sufficiently, a splitting may appear where a $\left|1eg\right\rangle$ state couples to $\left|0ee\right\rangle$. Here the second and third indices refer to separate TLSs. This would be a horizontal crossing. There is possibly evidence of such a crossing at 21.093 GHz, which is $f_4 + f_6$. As Figs. 10.13(a) and (b) show, there appear to be very small additional peaks near this frequency. The arrows highlight the additional peaks that could be this interaction, which I ignored during earlier fits. Unfortunately the resolution precludes making a definitive experimental statement about this interaction.

It is also worth emphasizing that I see no clear horizontal splittings in the $n = 0 \to n = 2$ spectrum in Fig. 10.9, Fig. 10.11 or any other data I took. This range includes frequencies where $n = 2$ level would be if the TLS was actually a simple harmonic oscillator.

10.4 Magnetic Field

In principle, applying a magnetic field in the plane of the junction to suppress the critical current can be used to distinguish critical current coupling from charge coupling, as I discussed in Chapter 9. For a critical current fluctuator the coupling is dependent on δI_0, which should be a function of the applied field. In particular by applying a field, I can reduce the current density difference between the two defect locations, thus changing the coupling. For a charge fluctuator the coupling to first order would not change with field. One complication is that applying a magnetic field through the junction does not uniformly change the critical current density. Therefore the change in coupling would also be sensitive to the position of the critical current fluctuator. TLSs located in certain areas of the junction could change their coupling to the qubit drastically, while others

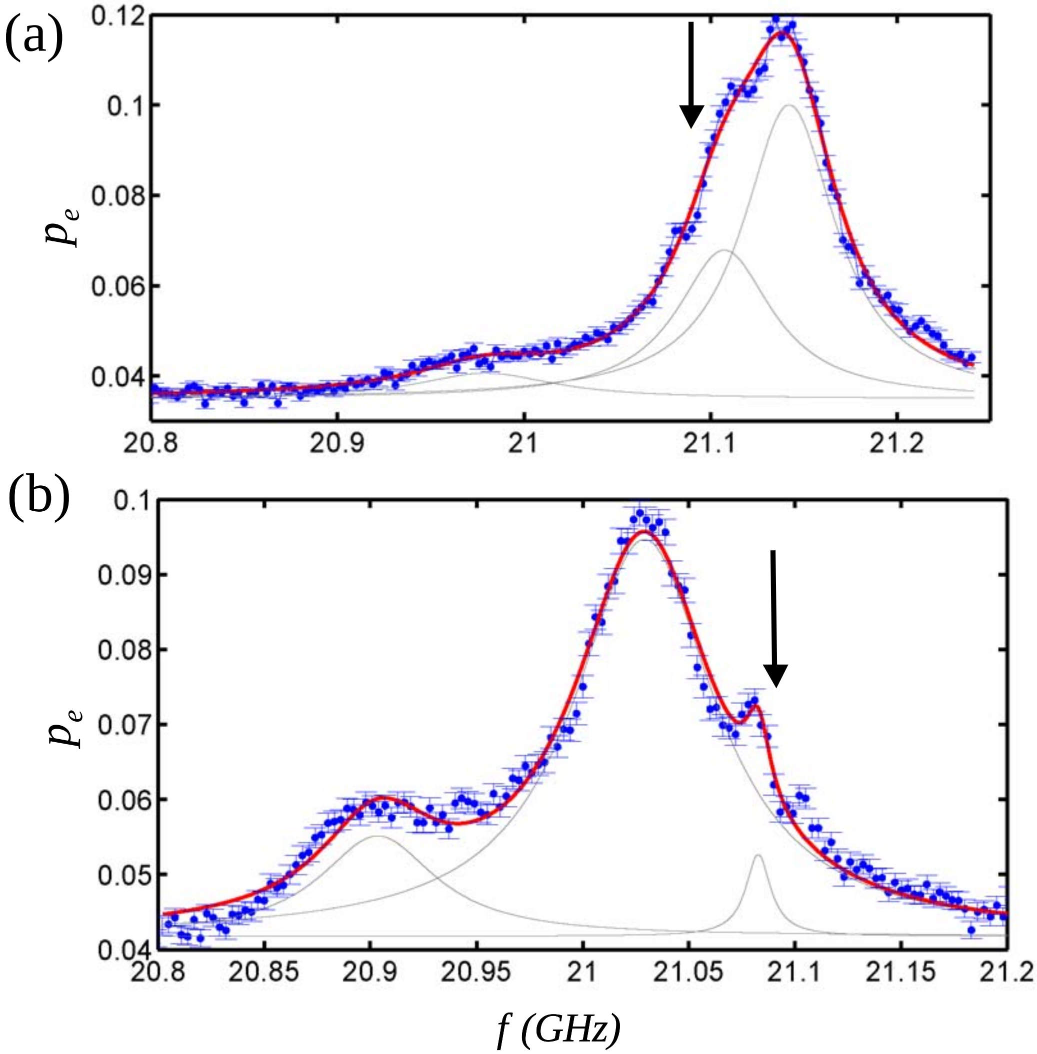

Figure 10.13: Possible $\left|1eg\right\rangle$ - $\left|0ee\right\rangle$ interactions. The 4th microstate and 6th microstate have a combined frequency of 21.093 GHz, which matches reasonably well with the small features (potentially an avoided crossing) highlighted by the arrows. This feature is seen in both (a) and (b), which were taken at different currents I_1 where the qubit is less strongly coupled to the $\left|1e_4\right\rangle$ state. The lack of resolution precludes making a definite statement and similar interactions were not seen at other locations where it would have been expected. Previously, I limited myself to a maximum of three Lorentzians at any single bias current.

may not change their coupling at all. As discussed in Chapter 9, the current density in the junction is given by

$$J(x) = J_1 \sin(\gamma + kx) \quad , \tag{10.4}$$

where $k = 2\pi d H_y / \Phi_0$ and $d \approx 100\,nm$.

I made some preliminary tests to check for effects upon the application of a magnetic field. For these tests, I heated the mixing chamber to slightly over 1 K, such that magnetic field could easily penetrate the aluminum sample box, applied the magnetic field in the plane of the junction and then cooled the device back down to base temperature. I then took an I-Φ curve to determine the new critical currents. This process was repeated several times until I found roughly the maximum change in the critical currents where the device could be operated in the 9-10 GHz frequency range.

The maximum field I applied (nominally 32 G) changed the critical current of the qubit junction to $I_0 \approx 1.04\,\mu A$ or about 83% of its non-field value. I determined an effective H_y by setting the integral of Eq. 10.4 over the junction area ($4\,\mu m\, x\, 4\,\mu m$) equal to the critical current found experimentally. Surprisingly, the effective magnetic field was approximately $H_y = 16\ G$. A similar deviation was seen previously by S. K. Dutta in a Nb device [37]. Figure 10.14 shows the calculated current density through the junction when it is biased so $f_{01} \approx 10.5\ GHz$ with an effective magnetic field of $H_y = 16\,G$ applied to an ideal junction. Also shown is the current density with no field applied and with $H_y = -16\ G$ applied. For no applied field $I_0 = 1.22\mu A$ and thus $I = 1.07\mu A$ gave $f_{01} \approx 10.5 GHz$. Using Eq. (10.4) this implies $\gamma = 1.075$. With

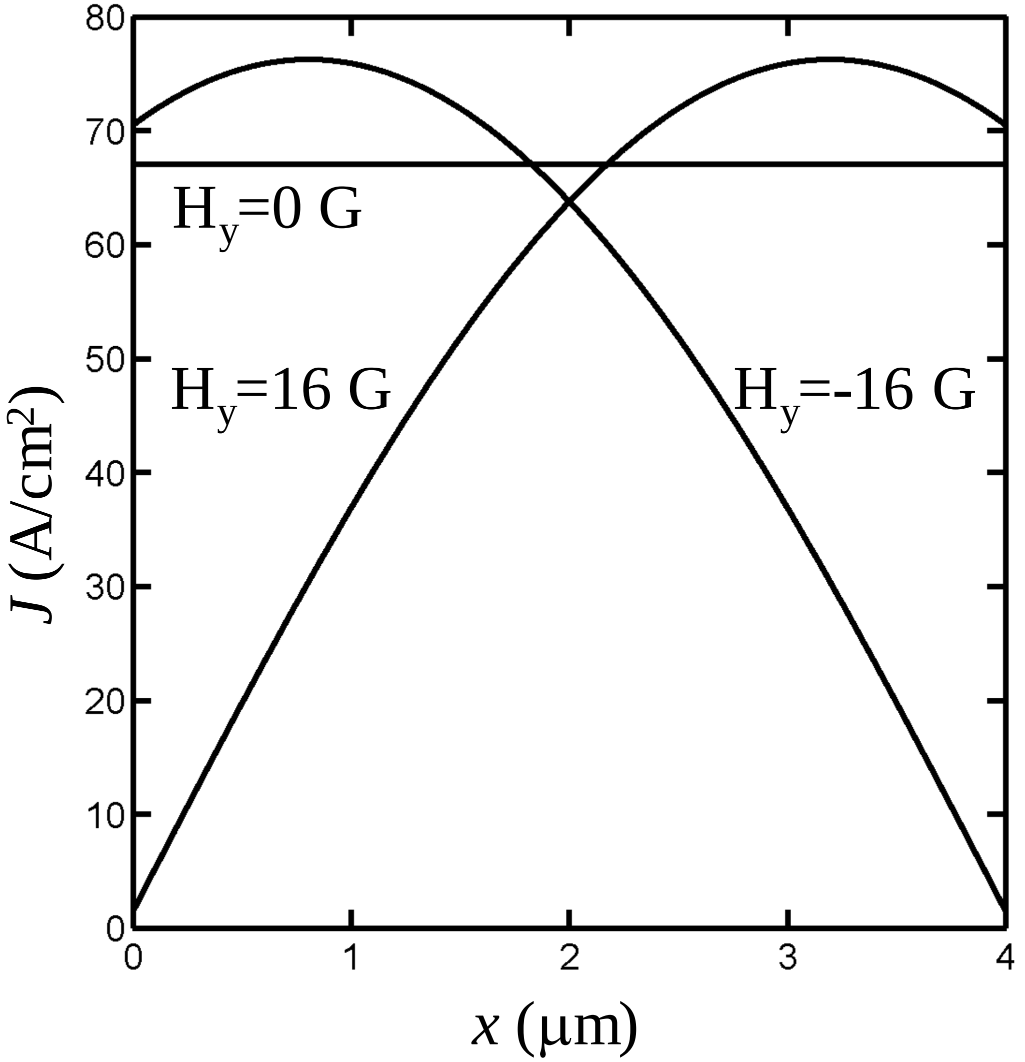

Figure 10.14: Current density J through the qubit junction versus location x in device DS$_{3A}$ for three different applied fields H_y. The total current for each field is set such that $f_{01} \approx 10.5 GHz$. By reversing the applied magnetic field the current could be modified over a larger area of the junction.

$H_y = 16\ G$, $I_0 = 1.04\mu A$ and $I = 0.867\mu A$ was required to get $f_{01} \approx 10.5 GHz$, implying $\gamma = 0.019$.

I found that applying this magnetic field experimentally produced no measurable change in the location or splitting size for the microstates with energies of $f_4 = 10.472 GHz$ and $f_5 = 10.540 GHz$ (microstates #4 and 5 in Table 10.2). The resolution in determining the splitting size would have allowed me to detect a change as small as about 10% in the splittings (*i.e.* several MHz). One possibility is that these microstates fluctuators could have been located in the roughly 40 percent of the junction area where the current density was not modified enough to generate a detectable change in the coupling (as seen from Fig. 10.14). Of course, another possibility is that the coupling was not dependent on critical current.

On the other hand, the TLS at $f_3 = 10.335 GHz$ (TLS #3 in Table 10.1) did change its coupling strength to the qubit. The coupling increased from roughly $\Delta_{f3} = 114\, MHz$ to $\Delta_{f3} = 160\, MHz$ upon application of the field. Needless to say, one would naively have expected the critical current to decrease upon application of a field. Examination of Fig. 10.14 shows that the current density actually does increase in some parts of the junction, although not by much, so this result is not entirely consistent. Interestingly this microstate also had a spectroscopic coherence time much shorter than the other splittings ($T_2^* = 4\, ns$). Perhaps this microstate has some current density component to its coupling.

Finally, I note that by applying a magnetic field in the opposite direction ($i.e.\, H_y = -16\ G$) I should have been able to significantly modify the critical current density over a different region in the junction (see Fig. 10.14). Unfortunately, this was not attempted.

10.5 Comparison with Theory

My experimental results can be used to test some of the predictions of Chapter 9. In particular, I was able to simulate the coupled spectrum, coupled spectroscopic coherence times and coherent dynamics using the models of Chapter 9. Although the fits contained a large number of free parameters there were many more data points than fitting parameters and the general form of the data matched the fits.

For device DS_{3A} the maximum splitting size in a charge-coupling model, with $Q = e$ would be approximately 750 MHz at 11 GHz (see Eq. 9.28). The largest experimental splitting I found was 240 MHz, at 10.935 GHz corresponding to a single electron charge hopping about 1/3 of the dielectric thickness or about 3 Å if the barrier thickness is 1 nm.

The light lines in Fig. 10.15 are the experimental cumulative number N of splittings with sizes larger than 10 MHz and less than Δ'_f in device DS_{3A} (dashed curve) and the average of the distributions from DS_{3A} and DS_{4A} (medium solid curve). For device DS_{4A} I estimated five splittings (16, 17, 27, 94, 115 MHz) over the 800 MHz range measured. The darker curves are fits using the distribution of Eq. (9.50), multiplied by a constant to match the total number of splittings. The dark dashed curve is with $\Delta_{f\,\max} = 700\,MHz$ and the dark solid curve is for $\Delta_{f\,\max} = 250\,MHz$. Qualitatively the

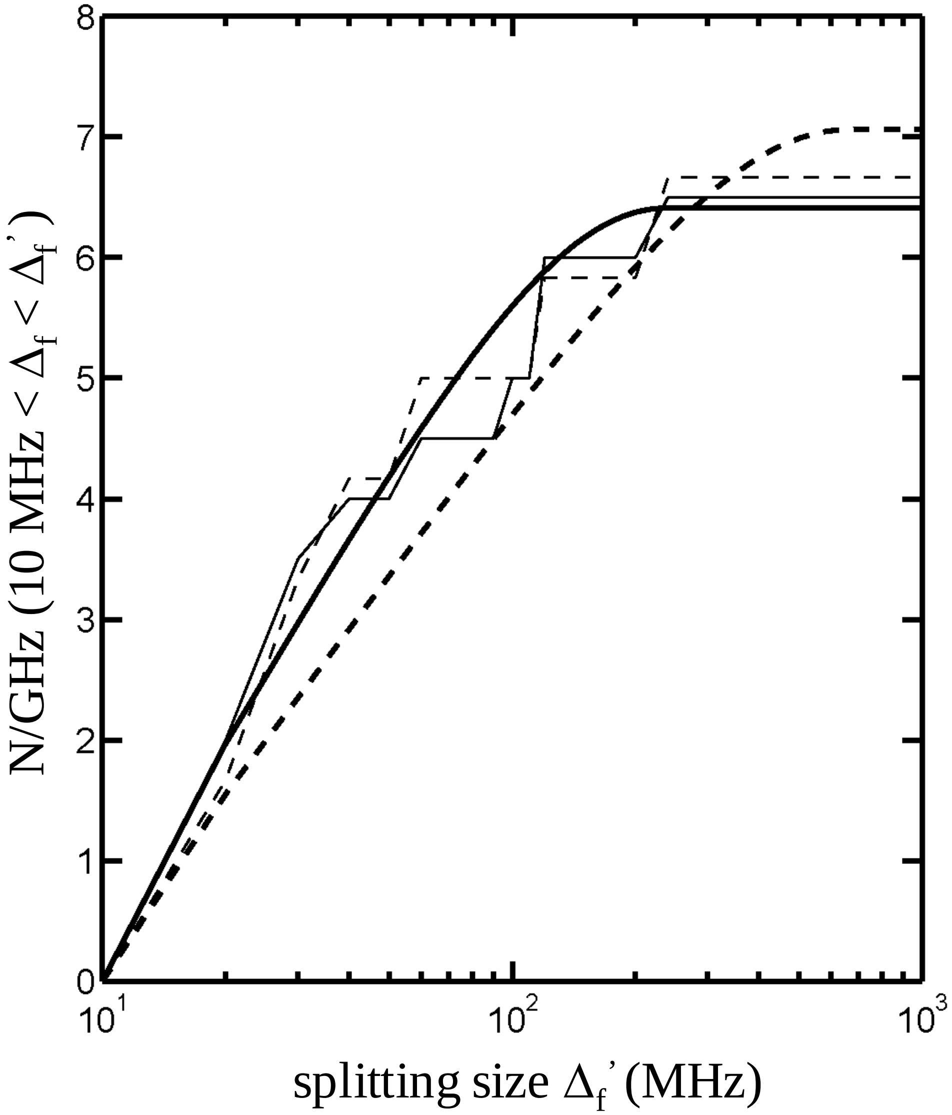

Figure 10.15: Number of splittings per GHz with splitting size smaller than Δ'_f and larger than 10 MHz versus splitting size Δ'_f. The lighter dashed curve corresponds to the splitting distribution for device DS_{3A} and the lighter solid line shows very rough estimates including DS_{4B} also. The dark solid curve uses the distribution given by Eq. (9.49) with $\Delta_{f\,\max} = 250\,MHz$ and the dark dashed curve is with $\Delta_{f\,\max} = 700\,MHz$.

distribution seems consistent with the data, however such a small sample set prevents a quantitative comparison.

In comparison, the lack of any large splittings in DS_{2A} or DS_{1A} and “similar” Nb devices is striking. The capacitance of the devices were roughly an order of magnitude higher, so naively one might expect splitting sizes only about 3 times smaller from Eq. (9.28). If I scale the maximum splittings of 240 MHz seen in the Aluminum devices DS_{3A} this should have produced a splitting of about 80 MHz, which would have been easily seen. Many more splittings should have existed as well due to the much larger area of dielectric. Perhaps many more very small splittings did exist that were not resolvable and those were the dominant relaxation source in the qubit, as modeled in Section 9.6. Devices DS_{2A} and DS_{2B} were of course fabricated using a completely different process, and no doubt this affected the distribution of defects. Never the less, the lack of large splittings in Nb devices is suggestive of significant differences in the respective defect density and coupling.

I note that my measurements of the higher-level interactions were not able to determine the coupling mechanism since both charge and critical current coupling models predict $\frac{\langle 2g|H_c|1e\rangle}{\langle 1g|H_c|0e\rangle} \approx \sqrt{2}$, and this was roughly supported by the data. The effect of $\langle 1e|H_c|1e\rangle$ on the energy of the $|1e\rangle$ state in a critical current coupling model (see Section 9.2) is also smaller than the experimental resolution. Conditions in the model that predict a large splitting size, lead to a small $\langle 1e|H_c|1e\rangle$ term, as seen from Eq. 9.15 and 9.17. The higher-level interactions do, however, provide another test of the two-coupled systems. Not seeing the tilted avoided level crossing would have been surprising and given reason to reconsider the basic models of the TLSs, as would the existence of harmonic TLS levels.

I also note that one would reasonably expect some microstates to have first excited states in the 20 GHz range. In a charge-coupling model the maximum splitting is actually expected to scale as $\Delta_{f\,\max} \propto \sqrt{f}$, [see Eq. (9.25)] and the distribution only weakly depends on the frequency (see Eq. (9.50)). The lack of $|0e\rangle$ and $|2g\rangle$ splittings is consistent with $|0e\rangle$ coupling weakly with $|2g\rangle$, as expected in the coupling models.

A promising approach to study the coupling mechanism is to measure changes in the splitting upon application of a magnetic field. I found that the two smaller splittings (microstates #4 and #5 in Table 10.1) remained fixed with an applied magnetic field, while one of the larger splittings (microstate #3) actually increased. A slight increase in splitting size is possible, if the qubit is not biased at the critical current and is coupled via critical current to the qubit. The increase would occur if the microstate position had an increased current density when a field was applied. If I had decreased the critical current of the qubit further or applied an opposite field, perhaps some concrete conclusions could have been reached using this technique.

10.6 Summary

I have measured multi-level spectra of two-level systems that are coupled to Josephson junction phase qubits. Splittings were clearly visible in the qubit's $n=0 \rightarrow n=1$ transition. Using a simple model I was able to accurately model the interactions of the two-level systems and the first excited state of the qubit. The effects are consistent with charged ions coupling to the qubit, including the maximum splitting size. By fitting the lower spectrum, *i.e.* $0g \rightarrow 1g$ and $0g \rightarrow 0e$ I was able to predict interactions between higher level states. As expected, the much smaller qubit junction area dramatically increased the size of the splittings and allowed for a more complete study of these two-level systems.

Chapter 11

Conclusion

In this thesis, I reported research on a dc SQUID phase qubit. A variety of techniques were developed and studied with the ultimate goal of satisfying some elements of the DiVincenzo criteria for quantum compuation. In particular, I focused on control of the dc SQUID, a pulse readout technique and the coupling of microstates to the qubit.

Designing a dc SQUID phase qubit that is well isolated from the bias source tends to produce a device with many stable flux states. To operate the SQUID as a qubit, the system must be initialized to the same potential well with near perfect accuracy. By applying a "flux shaking" technique, I was able to satisfy this requirement. By using different flux versus bias current trajectories I was also able to operate dc SQUID phase qubits with substantially different critical currents and inductance ratios. This made designs with a much smaller qubit junction possible.

By employing a pulsed current readout technique, I was able to significantly improve the measurement resolution compared to an escape rate readout technique. Direct measurements of the relaxation time T_1 became possible. I showed that very small levels of leakage to higher levels $n = 2$ were also directly measurable using this technique. The very short pulse time (a few ns) makes single-shot measurements possible.

Our qubits showed avoided level crossings in the transition spectrum resulting from microstates coupling to the qubit. I analyzed two possible models for this coupling, through the critical current and the charge. Unfortunately, both models can produce very similar results and I was not able to experimentally verify which coupling was dominant in our qubits. By applying a magnetic field, one might be able to distinguish these coupling mechanisms. I did obtain some preliminary results using this technique, but the parameters of the device (DS_{3A}) prevented a complete verification. I was able to test some theoretical predictions of the coupling models, specifically: variations in the spectroscopic coherence time as the two quantum systems interact, higher level interactions of the systems and the distribution of avoided level crossings. In general, I found relatively good agreement.

The relaxation and coherence times in our dc SQUID phase qubits were generally lower than expected if the current lines were the dominant source of dissipation. In device DS_{3A}, I found a best-case relaxation time $T_1 \approx 30\,ns$, Rabi decay time $T' \approx 30\,ns$, spectroscopic coherence time $T_2^* \approx 20\,ns$ and a coherence time $T_2 \approx 20\,ns$. These times were twice as large as the best experimental values I obtained in device DS_{2A}, DS_{2B} and DS_1, even though DS_{2A}, DS_{2B} and DS_1 were much better isolated from the current lines. While the bias current admittance could be made to affect the relaxation rate in DS_{3A}; DS_{4B}, which was better isolated from the bias leads, performed no better.

Several other possible sources of dissipation have not been ruled out in our qubits. Defects in the materials, possibly related to the splittings, could still be limiting the performance of our qubits, even if no splittings are visible in the spectrum. Our AlO_x tunnel barriers could simply be lossy. Other groups have invested substantial effort into investigating the materials used [81]. Another source that should be considered in the future is radiation resistance. Most of the superconducting qubits that have relatively long coherence times, of order μs, have tended to be very small compared to my devices [53, 123].

Even very modest gains in the coherence times of our devices would open up new experiments. The simplest would be spin-echo measurements, which would further quantify the coherence times in the qubits. Another interesting experiment would be the coupled qubit gates developed by Strauch *et. al*. [96] for phase qubits. As the qubit's coherence times improve, less microwave power would be needed to observe coherent dynamics. Experiments with less microwave power have less leakage to higher level, which would enable more precise gates. If the state $n = 1$ has a long lifetime, a drive at f_{12} could selectively pump the state to $n = 2$ for readout. This would enable a larger single shot measurement fidelity based on the much higher tunneling rate, $\Gamma_2 >> \Gamma_1$`.

Finally, while much work remains, phase qubits have advanced remarkably over the last few years. The long-term prospects of implementing some preliminary algorithms using superconducting qubits look very positive.

.

Appendix A

MATLAB Code

The following programs calculate the eigenfunctions, energy levels, and tunneling rates for a single current-biased Josephson junction and a qubit coupled to TLSs. The algorithms were written by S. K. Dutta [37] and Huizhong Xu [36].

A.1 Solutions of the Junction Hamiltonian

```
function [stuff,wavefn] = …
      jjspectrum(Io, Cj, Iri, Irf, dIr, levelmaxIr, E0, psi0)

% [stuff, wavefn] =
%     jjspectrum(Io, Cj, Iri, Irf, dIr, levelmaxIr, E0, psi0)
% This calculates all the energies and wavefunctions for a single
% junction with critical current 'Io' (Amps), junction capacitance
% 'Cj' (Farads), from reduced bias current 'Iri' to 'Irf', in 'dIr'
% steps. 'levelmaxIr' sets the number of levels to calculate; it's
% defined in 'keeplevels'. 'E0' and 'psi0' are optional -- they
% specify the initial guesses for all the levels. Everything sent
% back in a big structure.
% calls: hbar, keeplevels, jjeigentbc, wp, plotlevels, xaxis

more off
diary on
global hbar;

stuff.params.Io = Io;
stuff.params.Cj = Cj;
stuff.params.Iri = Iri;
stuff.params.Ifr = Irf;
stuff.params.dIr = dIr;
stuff.params.levelmaxIr = levelmaxIr;
stuff.params.start = clock;

NIr = floor( (Irf - Iri) / dIr ) + 1;

for Ircount = 1 : NIr
      Ir = Iri + (Ircount-1) * dIr;
      stuff.Ir(Ircount) = Ir;
      disp(['Reduced current ' num2str(Ir)]);

% After the first current, use the previous wavefunction as the
% initial guess. Use the same n, which (at a higher current) will
% give a lower initial guess for the energy.
```

```
for levelcount = keeplevels(levelmaxIr, Ir)
      disp(['Level ' num2str(levelcount)]);

      if Ircount == 1
      if nargin == 8
            % User supplied energy and wavefunction
            solution = jjeigentbc(Ir*Io, Io, C length(levelmaxIr)-1,...
            E0(levelcount+1)/hbar/wp(Ir*Io, Io, Cj) - 0.5, ...
            psi0(levelcount+1,:));

      elseif nargin == 7
            % User supplied energy -- use a random initial wavefunction
      solution = jjeigentbc(Ir*Io, Io, Cj, length(levelmaxIr)-1,...
      E0(levelcount+1)/hbar/wp(Ir*Io, Io, Cj) - 0.5);

      else
      % User didn't give you anything. Guess the energy and use a
      % random psi.
      corr = 0.15 - 5 * (1 - Ir - 0.005);
      solution = jjeigentbc(Ir*Io, Io, Cj, length(levelmaxIr)-1,...
      levelcount*(1-corr));
      end

      stuff.params.xleft = solution.x(1);
      stuff.params.dx = solution.dx;
      stuff.params.Ngrid = length(solution.x);

      else
      solution = jjeigentbc(Ir*Io, Io, Cj, length(levelmaxIr)-1, ...
            n0(levelcount+1), psi(levelcount+1,:));
      end

      energy = real(solution.E);
      gamma = -imag(solution.E) / (hbar/2);

      psi(levelcount+1,:) = solution.wavefn;
      n0(levelcount+1) = energy / hbar / wp(Ir*Io, Io, Cj) - 0.5;

      levstr = num2str(levelcount);
      Irstr = num2str(Ircount);
      eval(['stuff.energy' levstr '(' Irstr ') = energy;']);
      eval(['stuff.gamma' levstr '(' Irstr ') = gamma;']);
      eval(['wavefn.level' levstr '(' Irstr ',:) = solution.wavefn;']);
end

if Ircount == 1
      Eplot = figure;
end

      figure(Eplot);
      plotlevels(stuff);
      xaxis([stuff.Ir(1) 1]);
      shg;
end

stuff.params.stop = clock;
more on
```

```
diary off
```

This is the primary routine that calculates the solutions for a single value of the bias current, using transmission boundary conditions.

```
function solution = jjeigentbc(Ib, Io, Cj, nmax, n0, psi0)

% solution = jjeigentbc(Ib, Io, Cj, nmax, n0, psi0)
% Calculates the energy, potential, and wavefunction (on a grid x,
% with steps dx) for bias current 'Ib', critical current 'Io',
% capacitance 'Cj', maximum number of levels 'nmax', and current
% level 'n0' (or the best guess of what it is). 'psi0' is the
% (optional) inital guess for the wavefunction. Uses transmission
% boundary conditions. Results sent back in a structure.
% calls: mj, wp, hbar, jjeigengrid

% Some constants
global hbar;

% Set up a grid to solve Schrodinger's eq.
[xleft, dx, Ngrid] = jjeigengrid(0.97, 0.999, Io, Cj, nmax);

disp(['xleft = ' num2str(xleft) ' dx = ' num2str(dx) ' ...
Ngrid = ' num2str(Ngrid)]);

% This constant is in front of d2(psi)/dx2. Multiply it over to
% V and E and call them Vp and Ep (p for prime)

m = mj(Cj);
a = 2 * m * (dx / hbar)^2;

Umin = twb(Ib, Io, asin(Ib/Io));

for i = 1 : Ngrid
      x(i) = xleft + dx * (i-1);
      Utwb(i) = twb(Ib, Io, x(i)) - Umin;
end

Uleft = Utwb(1);
Uright = Utwb(Ngrid);

% The matrix is N-2 x N-2, because the boundary conditions are
% evaluated in the 2 and N-1 equations. Set up H*psi = E*psi.

A(1 : Ngrid-2) = -1;
C(1 : Ngrid-2) = -1;

for i = 1 : Ngrid-2
B(i) = 2 + Utwb(i+1) * a;
end
```

```
% Here's the first guess at the eigenvalue. Start with a random
% wavefunction (if one isn't provided) and use inverse iteration
% (Numerical Recipes 11.7) to improve it.

Ep = (n0 + 0.5) * hbar * wp(Ib, Io, Cj) * a;

if nargin == 6
      newpsi = psi0(2:end-1);
else
% This is the MATLAB R12 command
% newpsi = random('unif', 0, 1, 1, Ngrid-2);

% This is the MATLAB R14 command
newpsi = rand(1, Ngrid-2);
end
newpsi = newpsi / sqrt(sum(newpsi.^2));

% Boundary conditions for first go round.
Btbc = B;
Kleft = sqrt(2 * m * (Uleft - Ep/a)) / hbar;
Btbc(1) = B(1) - exp(-1 * Kleft * dx);
Kright = sqrt(2 * m * (Ep/a - Uright)) / hbar;
Btbc(Ngrid-2) = B(Ngrid-2) - exp(sqrt(-1) * Kright * dx);

% First iterate a couple times, without updating the eigenvalue.
diff = 2; err = 0;
count1 = 0;
while (diff > 1e-6) & (err == 0)
oldpsi = newpsi;
[temppsi, err] = tridiag(A, Btbc - Ep, C, oldpsi);
newpsi = temppsi / sqrt( sum(abs(temppsi).^2) );
diff = max(abs( (abs(newpsi)./abs(oldpsi)).^2 - 1 ));
count1 = count1 + 1;
end

% Now update the energy too
oldEp = Ep;
newEp = oldEp + sum( conj(temppsi) .* oldpsi ) ...
/ sum(abs(temppsi).^2);
diff = 1;
count2 = 0;
while((diff > 1e-7) ...
      | max(abs( imag(newEp)/imag(oldEp) - 1 )) > 1e-7) & err==0
      oldpsi = newpsi;
      oldEp = newEp;
      Kleft = sqrt(2 * m * (Uleft - oldEp/a)) / hbar;
      Btbc(1) = B(1) - exp(-1 * Kleft * dx);
      Kright = sqrt(2 * m * (oldEp/a - Uright)) / hbar;
      Btbc(Ngrid-2) = B(Ngrid-2) - exp(sqrt(-1) * Kright * dx);
      [temppsi, err] = tridiag(A, Btbc - oldEp, C, oldpsi);
      newpsi = temppsi / sqrt( sum(abs(temppsi).^2) );
      diff = max(abs( (abs(newpsi)./abs(oldpsi)).^2 - 1 ));
      newEp = oldEp + sum( conj(temppsi) .* oldpsi ) ...
      / sum(abs(temppsi).^2);
      count2 = count2 + 1;
end
```

```
% So far, have been normalizing the vector psi. But to make it
% a 'continuous' function on x, do a Riemann sum.

newpsi = -sqrt(-1) * newpsi / sqrt(dx);
wavefn = [newpsi(1)*exp(-1 * Kleft * dx) newpsi ...
newpsi(Ngrid-2)*exp(sqrt(-1) * Kright * dx)];
wavefn = wavefn / sqrt( sum(abs(wavefn).^2) ) / sqrt(dx);
solution.E = newEp/a;
solution.x = x;
solution.Utwb = Utwb;
solution.wavefn = wavefn;
solution.dx = dx;
disp([num2str(count1) ' iterations of first loop; ' ...
num2str(count2) ' iterations of second']);
```

This sets up the grid on which the solution is calculated.

```
function [xleft, dx, Ngrid] = jjeigengrid(Irmin, Irmax, Io, Cj, nmax)
% [xleft, dx, Ngrid] = jjeigengrid(Irmin, Irmax, Io, Cj, nmax)
% This calculates a grid for jjeigentbc. It should select the
% smallest grid compatible for currents between 'Irmin' and 'Irmax',
% critical current 'Io', capacitance 'Cj', and maximum quantum level
% 'nmax'. If everything is done on the same grid, then you can take
% inner products and stuff with the wavefunctions later.
% calls: mj, wp, hbar, twb
% Some constants

global hbar;
m = mj(Cj);

% Ideally, you would use the smallest range for a given Irmin/max and
% Cj. However, this is complicated.
% First, you need to find the values of the phase, where the
% washboard hits (again) the local max (to the left) and min (to the
% right) of the first well. The widest range of phase occurs for the
% smallest bias current. Just pick a fixed [0.8, 2.3], which should
% cover down to Ir = 0.95.
% Then, you want enough phase outside of this to capture some
% oscillations (to the right of the well) and the decay (to the
% left). This is set by the constant alpha below. The longest
% spatial scale occurs at the highest current, opposite of the
% previous paragraph -- ignore this. Don't really know how many of
% these spatial constants to keep. This should be optimized.

wpmin = wp(Irmax*Io, Io, Cj);
alphamin = sqrt(m*wpmin/hbar);
wpmax = wp(Irmin*Io, Io, Cj);
alphamax = sqrt(m*wpmax/hbar);
xleft = 0.8 - 4/alphamin;
xright = 2.3 + 4/alphamin;

% Next get the step size, which is based on the oscillations of the
% highest energy you plan to calculate. These should be evaluated at
% the highest current, where the potential is steep and the energy
```

```
% differences are large.

xmin = asin(Irmax);
Umin = twb(Irmax*Io, Io, xmin);
Uleft = twb(Irmax*Io, Io, xleft) - Umin;
Uright = twb(Irmax*Io, Io, xright) - Umin;
Emax = (nmax + 0.5) * hbar * wpmax;
lambdal = sqrt(2*m * (Uleft - Emax)) / hbar;
lambdar = sqrt(2*m * (Emax - Uright)) / hbar;
dx = 1 / max([alphamax lambdal lambdar]) / 10;
Ngrid = floor((xright - xleft) / dx) + 1;
```

The main M-files above call several simple routines, given below. In addition, global variables called hbar and Phio (which are equal to ħ and Φ_0) should be defined in the workspace.

```
function levels = keeplevels(levelmaxIr, Ir)

% levels = keeplevels(levelmaxIr, Ir)
% This returns a vector of the levels to keep at a given reduced bias
% current, 'Ir'. 'levelmaxIr'(i) gives the reduced current where the
% (i-1)th state leaves the well (or least where you don't want it
% anymore). If you should keep it, i-1 is included in 'levels'.
% 0 is the ground state. The number of elements in 'levelmaxIr' sets
% the maximum number of levels to keep.

levels = [];
for i = 1 : length(levelmaxIr)
      if Ir <= levelmaxIr(i)
      levels = [levels i-1];
      end
end

function omegap = wp(Ib, Io, C);

% wp(Ib, Io, C) gives the plasma frequency of a junction

global Phio;
omegap = sqrt(2*pi*Io/C/Phio) .* (1-(Ib./Io).^2).^(1/4);
```

plotlevels plots the energy levels as the solutions are calculated. Running the program for a large number of bias currents can be time-taking, so this is a useful way of spotting trouble early.

```
function plotlevels(eigenstuff)

% plotlevels(eigenstuff)
% This assumes 'eigenstuff' has fields named Ir and energy0, energy1.

colors = 'bgrcmy';
plotcnt = 0;
fields = fieldnames(eigenstuff);
for i = 1 : length(fields)
      if strncmp(fields(i), 'energy', 6) == 1
            data = getfield(eigenstuff, char(fields(i)));
            plot(eigenstuff.Ir(1:length(data)), data, ...
            colors(mod(plotcnt, 6) + 1));
            hold on
            plotcnt = plotcnt + 1;
      end
end

function xaxis(xbounds)
% xaxis([xmin xmax])
% This replots the current graph, using new x bounds.

graphaxes = axis;
graphaxes(1) = xbounds(1);
graphaxes(2) = xbounds(2);
axis(graphaxes);

function mass = mj(Cj);

% mass = mj(Cj) returns the phase particle mass, given the junction
% capacitance.
% calls: Phio
global Phio;
mass = Cj * (Phio/2/pi)^2;

function U = twb(Ib, Io, gamma);

% U = twb(Ib, Io, gamma) returns the tilted washboard potential.
% calls: Phio

global Phio;
U = -Phio/2/pi * (Io * cos(gamma) + Ib * gamma);
```

This calculates the escape rate from the nth level.

```
function gamman = Gn(n, Ib, Io, Cj)

% gamman = Gn(n, Ib, Io, Cj)
% This calculates the escape rate from the nth level (where 0 is the
% ground state).  It ought to be good everywhere.  It needs the spline
```

```
% structure PPG<n> (which came form jjspectrum or whatever).  Be sure
% to load it from the .mat file.
% created 2/21/04    modified 2/21/04

eval(['global PPG' num2str(n) ';']);
eval(['PP = PPG' num2str(n) ';']);

x = ex(Ib, Io, Cj);
gamman = wp(Ib, Io, Cj)./2./pi .* exp(-7.2./x) .* (7.2./x).^(n+0.5);

% Assume a constant exponential above and below the spline range.
% This will depend on the spline used.
%x(x < 0.1205) = 0.1205;
x(x < 0.0725) = 0.0725;
x(x > 12.164) = 12.164;

polyn = ppval(PP, x);
gamman = gamman .* exp(polyn);
```

A.2 Coupled Qubit and TLS

```
function f = FfvsIbTLS(Ib, params, n)

%f = FfvsIbTLS(Ib, params, n)
%This calculates the energy levels of a junction that interacts with a
%series of two-level systems (whose energy levels are independent of
%the current bias, 'Ib' (in Amps)).  This gives f as a function of Ib,
%so the function is multi-valued.
%
%params is [Io Cj fwhmJJ f1 d1 fwhm1 f2 d2 fwhm2 ...]
%Io (Amps) and Cj (Farads) are the critical current and capacitance
%of the junction.  'f1' (Hertz) and 'd1' (Hertz) are the location and
%interaction energy of the first TLS.  'fwhmJJ' and 'fwhm<#>' are the
%full width at half max of the junction and TLSs in Hertz, which will $
%be incorporated in the Hamiltonian as imaginary energies.  Set any to
%0 for infinite lifetimes.  The length of 'params' sets the number of %
%TLSs. 'f' (Hertz) is a matrix of complex frequencies, where each row %
%corresponds to a value of 'Ib'.  'n' is an optional argument that
%%specifies that only the nth (1-based) eigenvalue (in increasing
%order) %should be returned. 'n' may either be a single number which
%will apply % to all 'Ib' or a vector as long as 'Ib', so that
%different   eigenvalues can be chosen --
%this second option is useful for fitting to multiple branches of a
%spectrum.
%
% calls: wnm, ensurerow, ensurecolumn
% created 4/19/07    modified 4/21/07

for j = 1 : length(Ib)
  Ham(1, 1) = wnm(0, Ib(j), params(1), params(2)) / 2 / pi;

  for k = 1 : (length(params)-3)/3
    in = 4 + 3 * (k-1);
    Ham(k+1, k+1) = params(in);
```

```
    Ham(k+1, 1) = params(in+1);
    Ham(1, k+1) = params(in+1);
  end

  for k = 1 : length(params)/3
    in = 3 * k;
    Ham(k, k) = Ham(k, k) - i * params(in) / 2;
  end

% Order the eigenvalues by the real energies

  evs = ensurerow(eig(Ham));
  [e, in] = sort(real(evs));
  f(j, :) = evs(in);
end

if nargin == 3
  if length(n) == 1
    f = f(:, n);

  elseif length(n) == length(Ib)
    temp = f;
    clear f;

    for j = 1 : length(Ib)
      f(j) = temp(j, n(j));
    end

    f = ensurecolumn(f);

  else
    disp('n is the wrong size');
    clear f;
    return;
  end
end
```

A.3 Coupled Qubit and TLS Including Higher Levels

```
function f = FfvsIbTLS2(Ib, params, n)
%I've added some more params 06/15/07
% f = FfvsIbTLS2(Ib, params, n)
% This calculates the energy levels of a junction that interacts with a
% series of two-level systems (whose energy levels are independent of
% the current bias, 'Ib' (in Amps)).  This gives f as a function of Ib,
% so the function is multi-valued.
%
% This is similar to FfvsIbTLS.m, except that the second excited state
% of the junction is kept, as are the |11> states of all of the TLSs
% (which assumes the TLSs interact with |10> and |11> interacts with
% |20>).
%
% params is [dIb Io Cj fwhmJJa fwhmJJb f1 d1a fwhm1a d1b fwhm1b
%            f2 d2a fwhm2a d2b fwhm2b ...]
```

```
% 'dIb' is a current offset (Amps); it is added to 'Ib' before
% calculatingthe energy levels.  'Io' (Amps) and 'Cj' (Farads) are the
% critical current and capacitance of the junction.  'fwhmJJa' and
% 'fwhmJJb' (Hertz) are the idths of the junction levels |10> and |20>;
% they are incorporated in the Hamiltonian as imaginary energies.  'f1'
% (Hertz) is the frequency of the
% first TLS.  'd1a' (Hertz) is the interaction energy of it with the
% first excited state of the junction and 'fwhm1a' (Hertz) is its
% width.  'd1b' is the interaction energy of this |11> with the |20>;
% 'fwhm1b' is the width of the |11>.  Any of the widths can be set to 0
% for infinite lifetimes.  The length of 'params' sets the number of
% TLSs.
%
% 'f' (Hertz) is a matrix of complex frequencies, where each row
% corresponds to a value of 'Ib'.  'n' is an optional argument that
% specifies that only the nth (1-based) eigenvalue (in increasing
% order) should be returned.'n' may either be a single number which
% will apply to all 'Ib' or a vector as long as 'Ib', so that different
% eigenvalues can be chosen --this second option is useful for fitting
% to multiple branches of a spectrum.
%
% calls: wnl, ensurerow, ensurecolumn
% created 4/19/07    modified 4/21/07

% Calculate the 0 -> 1 and 0 -> 2 transitions separately; this is
faster
% (maybe...) and hopefully is still accurate.

for j = 1 : length(Ib)
  JJ1 = wnl(0, 1, Ib(j), params(1), params(3)) / 2 / pi;
  JJb= wnl(0, 1, Ib(j), params(5), params(6)) / 2 / pi;
  JJ2 = wnl(0, 2, Ib(j), params(2), params(4)) / 2 / pi;

  Ham1(1, 1) = JJ1 - i * params(7) / 2;
  Ham2(1, 1) = JJ2 - i * params(8) / 2;

  for k = 1 : (length(params)-8)/5
    in = 8 + 5 * (k-1) + 1;

    Ham1(k+1, k+1) = params(in) - i * params(in+2) / 2;
    Ham1(k+1, 1) = params(in+1);
    Ham1(1, k+1) = params(in+1);

    Ham2(k+1, k+1) = JJb + params(in) - i * params(in+4) / 2;
    Ham2(k+1, 1) = params(in+3);
    Ham2(1, k+1) = params(in+3);
  end

% Order the eigenvalues by the real energies

  evs = [ensurerow(eig(Ham1)) ensurerow(eig(Ham2))];
  [e, in] = sort(real(evs));
  f(j, :) = evs(in);
end

if nargin == 3
  if length(n) == 1
```

```
    f = f(:, n);

  elseif length(n) == length(Ib)
    temp = f;
    clear f;

    for j = 1 : length(Ib)
      f(j) = temp(j, n(j));
    end

    f = ensurecolumn(f);

  else
    disp('n is the wrong size');
    clear f;
    return;
  end
end
```

Appendix B

Dilution Refrigerator

The following gives detailed instructions on operating the dilution refrigerator that I used, as of 2007. The instructions were originally recorded by S. K. Dutta.

B.1 Cooling the Dilution Refrigerator

I. Preliminary stuff
  A. Clean the mix – can start several days before cool down if you're worried
    1. Presumably, all the valves are closed and the mix is behind the Rotary and in the closed dumps.
    2. Fill the trap with nitrogen or your favorite soda.
    3. Open #8A a crack to let some gas into the trap and cool the charcoal. The liquid might bubble.
    4. Open up the circulation path: right dump valves, #7A, (pump), 8A, (trap), 1A, 13, left dump valves.
    5. Throttle #5 to give, say, 2 mbar on P2. Keep an eye on P2, G4 (for blocks), and the nitrogen level.
    6. To get the mix back, close #8A, 5, and the left dump valves. Open #2 to clean the panel / trap and #9 to return mix. Close everything when you're done.
  B. If you want, take out the IVC charcoal and bake it.
  C. Pump out the vacuum space of the dewar.
  D. Sample stuff
    1. With yourself grounded and the junction lines shorted at the fridge top, put the sample box on the mixing chamber.
    2. Put on the other filter boxes and stuff and silver paint the joints.
    3. When everything is ready (and any extra grounding wire bonds have been removed), you can test the junctions by measuring resistance at the grounding boxes on the 40 kΩ scale (to limit current).

II. Prepare to cool down
  A. Raise the can
    1. Raise the still shield and make sure there are no thermal shorts. Tape over any light leaks.
    2. Clean both sealing surfaces for the o-ring seal. Prepare a new (possibly greased) indium o-ring.
    3. Make sure the push-out screws are out.
    4. Raise the IVC, connecting the can charcoal heater on the way. Might want to secure the leads so they don't cause any shorts.
    5. Do the bolt tightening jig.
  B. Pump on the can.
    1. Open the can valve on the fridge top – it's the honkin' big Speedivalve on the "right" side
    2. Turn on Rotary A, open #35 and 29, and monitor pressure on P3; should go down to 10^{-1} mbar.
    3. Throttle #25A to rough out everything, until P3 is vertical or so (0.12 mbar). It'll take a while.
    4. Close #25A and 29.
    5. Turn on two diffusion pump switches and open #30 to back it.
    6. Wait for oil to heat and turn on Penning gauge. It should get below 10^{-5} mbar (perhaps 10^{-6}).
    7. Open #27 and throttle #25A, keeping the Penning gauge below 10^{-4} mbar. Let it go overnight – it should get below 10^{-5}. The next day, retighten the IVC bolts.
  C. Fire up the leak detector.

   1. Hook it up to the gas panel and wait until it's ready to go.
   2. Close #25A to protect the LD.
   3. Close #35 (and maybe turn off Rotary A) and open #36 so the LD is backing the diffusion pump.
   4. Slowly open #25A, watching the Penning and the LD leak / pressure.
   5. To make sure everything is working, heat the IVC charcoal a bit.

D. Leak test the pot.
   1. Close both needle valves.
   2. Turn on the pot pump and perhaps let it warm up a bit. Open #24 and 22 to pump out. Close #24.
   3. Fill it with Helium through Vent 3, by throttling #21A. Try not to slam G6. Monitor LD.
   4. When you're done, close #22 and #21A.

E. At some point, check the needle valves, by opening each of them in turn, while putting a beaker of acetone (volatile) under the siphon. Should see bubbles at about ¾ turn.

F. Leak test the DR.
   1. Clean mix if you want
   2. Close all gas panel valves. Open the right dump valves.
   3. Open condenser valve on fridge top and open #3 to monitor G3.
   4. Open #7. Slowly open #5, watching G2 and the LD. G1 should go from 650 to 350 mbar or so when it's at equilibrium.

G. Check impedance.
   1. If you want, close #7 and 5. Turn on ^{3}He Rotary and open #7A, 2, and 3 to empty condenser. Close #2.
   2. Watch G3 – ought to increase by about 10 mbar in 5 minutes.

H. Empty DR.
   1. Close everything and make sure ^{3}He Rotary is on. Open #9 and make sure the right dump valves are open.
   2. Open #3, 2, and throttle 7A (keeping P2 below 1 mbar) to empty panel and condenser.
   3. Empty Still by throttling #12. Can keep pumping on condenser.
   4. When P2 bottoms out (maybe $7\text{x}10^{-2}$ mbar) and G1 is back to normal, close #3, 2, 7A, 12, and 9. Close the dumps too.

I. Leak test can and the fridge top connectors. Do this one last if the microwave ports are still leaky.

J. Set-up the magnet.
   1. Solder the current leads together and connect the voltage tap and switch heater.
   2. Check resistances at the panel on the outside of the screen room: current = 7.8 Ω, voltage = 8.7 Ω, heater = 40.7 Ω.

K. Check heaters and thermometers.
   1. Using the bridge at 1 mV: #0 (Allen-Bradley on 4 K flange) = 69 Ω, #1 (Ge on MXC) = 5.2 Ω, #2 (RuO_2 on MXC) = 1010 Ω, #3 (Carbon on MXC) = 430 Ω, #4 (Carbon on 1 K pot) = 900 Ω – varies a lot, #5 (Carbon on Still) = 3200 Ω – varies a lot, #6 (used to be RuO_2 on MXC) = Ahhh!!, #7 (RuO_2 on MXC) = 1009 Ω.
   2. Off box, inside screen room: pot = 214 Ω, still = 504 Ω, MXC = 730 Ω.
   3. IVC charcoal (screwed up connectors on fridge top): 107.1 Ω.

L. Transfer siphon.
   1. Screw on the siphon extension and tape it into place.
   2. Insert the L-tube (the one for Nitrogen) and bring it close to seating (will it freeze?).

III. Cool down to 77 K

A. Raise dewar (may take up to 40% on motor controller), making sure that it is level, and μ-metal (anytime before sample goes super).

B. Last leak check (if L-tube is out or you can plug it)
   1. Close #32.
   2. Make sure #24 is closed and turn on the ^{4}He Rotary.
   3. Throttle #31 and watch G5 – ought to get to 20 mbar with big leak.
   4. Close #31. Fill the bath with He through Vent 3, by opening #21A and 21. Watch the LD.
   5. Close #21 and 21A. Leave the He. Open #32.

C. Flush pot a couple times and leave pressurized over 1 atm. Leave the bottle hooked up to the gas panel, so you can keep the pot pressure high, during the transfer (without worrying about adding small volumes of air).
D. Start lN_2 transfer with L-tube seated. Monitor T0 and T1 with Fridge9.vi.
E. Stop pumping on the can.
   1. Close #27.
   2. Start Rotary A.
   3. Close #36 and stop the leak detector.
   4. Open #35 to continue to back diffusion pump.
   5. Turn off two diffusion pump switches and Penning gauge. After 30 minutes, close #30 and 35 and turn off Rotary A. Unplug heater and fan.

D. Add exchange gas to can.
   1. Hook up H_2 bottle to Vent 1 with metal bellows.
   2. Turn on Rotary B.
   3. With reg closed (but main bottle valve open), open #11 and 10. Open #34 slowly, watching P4, to flush out bellows.
   4. Close #10 (for example) and open regulator to maybe 5 psi. Wait a few seconds and close regulator.
   5. Open #10 to flush. Repeat.
   6. Close #34, turn off Rotary B if you want, and make sure the can's not being pumped on.
   7. Close #10, set the reg to a couple psi, then close #11. Open #10, 26, and 25A to dose this volume in.
   8. Keep the H_2 hooked-up, to maintain the H_2 at about P4 = 1 mbar during the transfer.

E. Keep on transferrin'.
   1. Keep the pot above an atmosphere and the exchange above 1 mbar, either by periodic doses, or by adjusting the regulators for continuous flow.
   2. Probably want to start out with transfer siphon seated in the extension, but it really restricts the throughput. At some point, unseat it.
   3. Wait until thermometer 0 bottoms out (about 83 Ω) and keep going for at least 30 minutes. The whole deal will take 3 to 8 hours, depending on stuff.

F. Stop transfer.
   1. Depressurize dewar and slide around in the rain.
   2. Make sure the pot and IVC are pressurized where you want and close the bottles. Close #10, 11, 21A, and 22.
   3. Hopefully, the fridge will cool overnight. If not, transfer some more and quickly move on.
   4. At some point, check the junction resistances with a DMM on the 40 kΩ scale.

IV. Preparing to go to Helium

A. Get rid of exchange gas.
   1. Close #26 and #25A.
   2. Start Rotary A.
   3. Open #35, 29, and throttle 25A.
   4. When P3 hits base pressure, close #25A and 29.
   5. Turn on two diffusion pump switches and open #30 to back it.
   6. When it's ready, open #27 and throttle #25A, keeping the Penning gauge below 10^{-4} mbar. Pump down to base (should be real low when it's cold).

B. While this is going on, siphon out Nitrogen.
   1. Seat the Nitrogen L-tube in the transfer siphon extension and get an empty dewar to catch the fun.
   2. Hook up a Nitrogen gas bottle at Vent 3 or He gas.
   3. Close #32. Pressurize the bath, by opening #21A and 21, making sure #22, 23A, and 23B are closed. Adjust the regulator so that G5 is at 100 (past atmosphere). At this value, liquid should really be pissin' outta there.
   4. Keep going until no liquid it coming out. The Nitrogen regulator will probably let a lot more gas through when this happens (you can hear it).

5. Close the gas bottle, #21 and #21A. Open #32 a little. Maybe it's worth having a little nitrogen gas flowing from this point on, so ice won't condense on the DR?
6. Let the lines defrost. Remove the L-tube and plug up the port.

C. Leak check the DR

1. Fire up the leak detector and close #25A.
2. Close #35 and open #36 so the LD is backing the diffusion pump.
3. Slowly open #25A, watching the Penning and the LD leak / pressure.
4. With the right dump valves open, open #7. Slowly open #5, watching G2 and the LD.
5. As long as you're here, check the impedance: open #3 and watch G3 – it should increase by 20 mbar in about 100 s.
6. Empty DR, using the same method as RT.

D. Leak check bath (do this after DR, because leaky microwave ports could contaminate everything).

1. Close #32. Make sure #24 is closed and turn on the ^{4}He Rotary.
2. Throttle #31 and watch G5 – it should get below 50 mbar, but it's painfully slow. (100 mbar means Nitrogen is still there)
3. Close #31. Fill the bath with He through Vent 3, by opening #21A and 21. Watch the LD.
4. Close #36 and open #35. Shut off the leak detector.

V. Cool down to 4 K

A. Start He bath transfer with L-tube seated and other end of siphon just barely in liquid or even out of it. You need very little pressure and have recovery open. It'll take at least 5 hours.

B. Keep transferrin'

1. As it cools, ideally want to keep siphon in liquid and T0 between 150 and 200 Ω, by periodically releasing the pressure in the storage dewar (don't need to pressurize it externally). Keep an eye on the temperature and pressure – doesn't take long for liquid to accumulate.
2. Watch T0 (which you want to keep under 160 Ω, which is about 20 K) and T1. The idea is get T1 to 19 Ω and then stop. If you go too fast, you'll freeze out the Hydrogen.
3. Keep the IVC pressurized to 1 mbar (same as during nitrogen transfer). It might take a lot, so open #11 and #26 and throttle #10 to maintain the desired pressure.
4. If you think the can is too cold (e.g. the charcoal is sucking down lots of Hydrogen), heat the IVC charcoal with about 10 V (1 W) and the pot heater with something. [Maybe have the IVC charcoal at 27V / 0.265A] The IVC pressure should increase and the MXC cooling rate should increase. By the way, this is a gosh darn good idea.

C. Get rid of exchange gas when T1 is near 20 Ω. The can and bath have to be cold enough to get the fridge cold, but not so cold that the pump out is slow. The timing is important.

1. If you added a lot of hydrogen, start pumping some of it out before T1 hits 20.
2. When it's ready, close #27 and 30 and "quickly throttle" 29. The diff pump will be ok for a while.
3. Heat the IVC charcoal with maybe 16 V if you weren't before.
4. Let it go for about 15 minutes – P3 should be about 0.2 mbar. T1 will probably go down some, but that's ok.
5. Close #29 and 25A. Open #27 and 30. Throttle #25A, keeping the Penning below 10^{-4} mbar, hopefully opening it all the way. Go for 10 or 20 minutes. Probably won't hit base pressure.
6. During this time, make sure the transfer is going real slow.
7. Empty the panel of hydrogen.

D. If you used helium instead of hydrogen for exchange gas

1. Probably still want to stop cooling at 20 K (the heat capacity of the metal is mostly gone by then).
2. Making sure that it's not still cooling, pump out the can with the IVC charcoal heater going. Eventually want the leak detector backing the diffusion pump and LR < 10^{-6}.
3. If the leak rate doesn't come down, turn on the pot and still heaters.
4. After an hour or so, finish the bath transfer. However, if the LR > 10^{-6}, don't start the pot or fridge. Pump overnight, if needed.

E. Finish helium transfer.

1. Turn off all heaters. Can keep pumping – Penning gauge will bottom out.
2. Fill up the dewar. Unseat the siphon once there is level on the meter.

VI. Start the fridge
  - A. Start the water chiller for the ^{3}He pump, if it's not already on.
  - B. Last leak check.
    1. Fire up leak detector and close #25A.
    2. Close #35 and open #36. Open #27 and throttle #25A. Pressure and leak ought to be real low. Can also check DR here.
    3. Close #25A and #27. Close #36 and stop leak detector. Open #35 and turn off diff pump heater.
    4. Wait 30 minutes, unplug diff pump power, close #35, and stop Rotary A. Maybe keep pumping????
  - C. Start pot.
    1. Make sure #22 is closed and try to throttle #24.
    2. Monitor pot level (may be easier to empty it and watch it fill), pressure on G6, and T4.
  - D. Prep the mix.
    1. If you haven't already, pump out the nitrogen trap with Rotary B and fill the trap.
    2. Clean mix, as above, if you haven't.
    3. Make sure #8A is open, to cool charcoal.
  - E. Start condensing mix.
    1. Want pot cold before adding any mix, around 1800 ohms
    2. Open 9, 8A, 1A,2,7 right dump.
    3. Use 1A to control flow and keep G3 between 50 and 100 mbar, less than 200 mbar for sure
    4. When G1<100 mbar open 1A all the way
    5. When G3<100 mbar close 2 and 7 and open 3
    6. Slowly open 12 assuming pump is running and keep P2 < 2 mbar for sure
    7. Eventually open 12 all the way
    8. Close 9 and suck out the rest of the dumps by opening 5 and 7A or 7 but keep P2 reasonable
  - F. Turn off all electronics inside the screen room, turn off the circuit breaker, and shut the door.
  - G. Finish condensing.
    1. If you've been pumping on the can all this time, turn it off and close the can valve on the fridge top.
    2. When R7 is above 5 or 10 kΩ or so (may take overnight), close #12, and turn on the Mag Valve and Roots.
    3. Once you're sure everything is super, check the junction resistances with a DMM on 40 kΩ. There will be a thermal voltage, so flip the leads.

In little fridge, 1Kpot if it's too full the temp will oscillated since He is overflowing and making a thermal leak.

B.2 Dilution Refrigerator Procedures

I. Cleaning the cold traps
  - A. Stop circulation.
    1. If Roots is going, turn it off, wait for it to slow down, close the Mag Valve.
    2. If it's not, close #12.
    3. Close condenser valve on fridge top (it's after the trap).
    4. Start Rotary B, so it can warm up a bit.
  - B. Save gas panel mix.
    1. Close #8A to isolate the bottom section of the gas panel.
    2. Close #5 to keep dumps isolated.
    3. Close #1A, 3. Now everything's closed.
    4. Open #7A slowly. Open #2 to pump out panel to maybe 10^{-1} mbar on P2.
  - C. Save Nitrogen trap mix.
    1. Open #1A to empty Nitrogen trap. Pump for about 5 minutes or until P2 goes down to base pressure. G4 might go up a bit.

    2. Close #1A, 2, 7A. Everything's closed again.
  - D. Save Helium trap mix.
    1. Make sure #1A is closed.
    2. Open #7A, 2, 3. P2 will rise. Wait 5 minutes for it to come back down.
    3. Close #7A, 2, and 3.
  - E. Clean Nitrogen trap.
    1. Turn on Rotary B.
    2. Open #34 and switch to measuring P4.
    3. Take out trap.
    4. Making sure #2 and 3 are closed, open #1A to monitor pressure on G3.
    5. Open #4A. P4 will go up.
    6. Heat gun it until it's warm to the touch. After 10 or 20 minutes, P4 will drop below 10^{-1} mbar or so.
  - F. Finish Nitrogen trap.
    1. When P4 is low enough, close #4A and #1A.
    2. Open #8A momentarily for heat exchange to charcoal. Wait for it to cool off and put it back in the dewar. After a while, open it all the way.
  - G. Clean Helium trap.
    1. With #1A and 2 closed, open #3 to monitor pressure.
    2. Pull out trap all the way to ceiling – watch the bellows. G3 could increase by several hundred mbar.
    3. After it's warm, open #10, 6, 2. G2 should be zero (before opening #6) and P4 shouldn't rise until #2 is opened. P4 will go off-scale and come back fast.
    4. When P4 is below 10^{-1} mbar, close #3, 2, 6, 10.
    5. Close #34, shut off pump, and switch back to P3 (if you were measuring it to begin with).
  - H. Finish up.
    1. Put the Helium trap back slowly, watching the bath boil-off.
    2. Once Nitrogen trap has stopped bubbling, open #1A and then #3 slowly to cool Helium trap.
    3. Wait a minute and then open condenser valve on fridge top.
    4. Open #12 slowly enough to keep P2 less than 8×10^{-1} mbar or so.
    5. Open #5 eventually.
    6. When P1 is well on scale and the MXC is getting cold, close #12. Open the Mag Valve and then turn on the Roots.

- II. Pulling the mix
  - A. Stop the circulation
    1. If it's on, turn off the Roots and then the Mag Valve.
    2. Monitoring P2, slowly open #12 all the way.
    3. Make sure right dump valves are open. Close #5 and 8A. Open #9 so mix can go to dumps.
  - B. Heat fridge
    1. Turn on MXC heater – can eventually ramp it up to 2 mW.
    2. Turn on Still heater to max (slowly).
    3. May want to keep the pot going, so that ^{4}He boil off isn't too violent. Otherwise, close #24 to stop it. Probably want to eventually stop it.
    4. Probably want to keep P2 below 2 mbar. Some mixture will want to come out when R7 hits about 2.2 kΩ (phase separation?), so don't get there too fast. Will have to increase MXC heat over time to keep it there. At about 300 mbar or so, even 20 mW on MXC won't do much. Wait as long as you want – maybe a couple hours and then move on.
  - C. Pump on the can if you want to (definitely if this is during a warm-up) if bath is nearly empty
    1. Turn on Rotary A, open #35, and monitor pressure on P3; should go down to 10^{-1} mbar.
    2. Rough out room temperature lines by opening #29 and 25A.
    3. When pressure comes back down, close #29 and 25A.
    4. Make sure diffusion pump heater / fan is plugged in. Fan should be on. Turn on two pump heater switches and open #30 to back it.
    5. Wait for oil to heat and turn on the Penning gauge (it may take a while for it to warm up). It should get below 10^{-5} mbar.

    6. Open #27 and throttle #25A to pump down room temperature lines. Close #25A.
    7. Open can valve on fridge top – it's the honkin' big Speedivalve on the "right" side. Throttle #25A.
  D. Heat the mixing chamber some more to remove mix
    1. Monitor the Germanium thermometer (T1). 20.23 Ω = 20 K, which is a safe goal.
    2. With the MXC heater at 20 mW, #1 probably won't get any lower than 35 Ω.
    3. Then hook up the MXC charcoal heater. Use the V+ and V- leads of #2 on the auxiliary box – may have to pull some tricks to get two BNC's to one. Send it outside the screen room to a power supply. The resistance should be 650 Ω.
    4. Start with perhaps a few volts to get the last of the mix out. When you finally heat to 20K, don't want any violent boiling in the mixing chamber.
    5. Heat with up to 20 V, keeping P2 under a couple mbar. It should take 15 – 20 minutes and it'll speed waaaay up at the end! If the Penning gauge goes up, make a run for it.
  E. If you really want every little bit…
    1. Wait for P2 to bottom out and G1 to hit 650 mbar (or whatever it should be).
    2. Close #1A and open #7A , 2, and 3 to pump out the condenser. Wait for P2 to come down.
    3. Close #3 (and perhaps #12) and open #1A to clean out Nitrogen trap. When it's done, close #1A to clean out panel. Finally close #2 and 7A. Might want to re-open #12.
    4. If you want to protect the mix, close #9 and the right dump valves. If the ^{3}He Rotary is still on, make sure the exhaust won't blow up.
  F. Whenever you're done what you're doing, stop pumping on the can
    1. Close the can valve on the fridge top.
    2. Close #25A and 27.
    3. Turn off two diffusion pump switches and Penning gauge. After 30 minutes, close #30 and 35 and turn off Rotary A. Unplug the heater and fan.

III. Cycling the sample to 20 K
  A. Follow the instructions for pulling the mix.
    1. Only have to get most of it out. Want to warm up relatively quickly (so the whole fridge isn't warm), but not so fast that any mix boils too quickly.
    2. Keep the ^{3}He Rotary going and #12, 1A, and #3 open.
    3. Shut all heaters off immediately when the Germanium thermometer (T1) is at 20 Ω. Don't worry – it'll stay warm without any more help.
  B. Check junctions
    1. If you're really bored, look at the IV curve to see when it stops switching. Remember to make the bias resistor small enough to be able to measure large critical currents.
    2. Measure the junction resistance directly. Use an Ohmmeter on the 100 kΩ scale (where the sourced current is small). It ought to be 1.1 kΩ (or whatever).
  C. Cool down
    1. Turn off all electronics by the time the junction goes super, to avoid stray fields. Turn off the screen room power.
    2. Wiggle the field if you think it'll do any good.
    3. Open #24 (slowly, if you can) to start the pot.
    4. Throttle #8A to reintroduce mix, keeping G3 at about 200 mbar.
    5. It'll take a long time. Might try closing #9 and just circulate what's inside. Wait for some cooling before adding more mix. When you're done, make sure #5 is open and #9 is closed.
    6. At some point, close the fridge can valve, #25A, and 27. Turn off the diffusion pump heater (but keep the fan on) and the Penning gauge. It should cool in about 30 minutes. Close #30 and #35, turn off Rotary A, and turn off the fan.

IV. Warming up
  A. Discharge the magnet.
  B. Follow the instructions for pulling the mix.
    1. Make sure to pump on the can if it has been a long run.

  2. When the mix is out, return to pumping on the still just in case. When you're sure it's out, close #12 and turn off the pump.
  3. Close #9 and the right dump valves to protect the mix.

- C. Stop the pot
  1. While the mix is coming out, can stop the pot once the can is being pumped on.
  2. Can try closing the needle valves and pumping the pot out, but they leak, so it probably won't work.
  3. Close #24 and turn off pump.
  4. Heat pot heater (outside screen room) with up to 10V / 60 mA. The relief valve will hiss if the pressure is too high and open valve to release pressure to bath.
  5. Monitor T4 and G6. Check the pot level meter.
- D. When the mix is out, blow out the bath with helium gas (few psi) down the transfer line and pump on can.
- E. If you want, heat the IVC charcoal (screwy connectors on fridge top) with a few volts.
- F. Once the mix is out of the Nitrogen trap, close #8A and #1A. Clean it with Rotary B and leave it out.
- G. Heat the fridge overnight, at least
  1. Turn up all the heaters: Still and MXC to max. Pot, MXC charcoal, and IVC charcoal to 20 V. Monitor T0.
  2. May not want to pump on the can the whole time though. Not sure.
- H. Drop the shield and dewar if there is nothing in bath or ice may form and get the dewar stuck

  Make sure you are sure the bath is empty
  1. Open the trap door and move the "lock" out of the way. Clear space below.
  2. Drop the mu-metal shield. Will take 25-30% power.
  3. Switch the lines over to the dewar and hope that their lengths haven't changed. Also make sure the lines are wound on the drum nicely. Tighten them way up and check that both have the same tension.
  4. Start pumping on can again, if you stopped.
  5. Undo both sets of bolts (5 small and 6 big) and drop the dewar – 20% power. Try not to screw this part up.
  6. Maybe pause half way down and check P3.
  7. May want to switch to just Rotary A if you're worried about a lot of stuff coming out.
- I. Let the fridge warm up
  1. At some point (perhaps when the fridge is about 77 K), may want to stop Rotary A, so that you don't oil the fridge.
  2. Hook up a nitrogen gas bottle to Vent 3. Open #21A and throttle 23A to add some exchange gas. Can monitor with P3, P4, or the dial gauge. Close everything when done.
- J. Drop can when the fridge is above freezing
  1. Untape stuff. Unsolder the magnet leads and unplug the voltage and heater leads. Take off the siphon extension.
  2. Vent the can to atmosphere (or Nitrogen) through #23A and #21A.
  3. Unbolt the can, leaving two bolts.
  4. Loosen those two, while tightening the push-out screws. When the indium gives, the two bolts should hold the can up.
  5. Drop the can, unplugging the charcoal heater on the way. Drop the still shield.

V. Changing the field

- A. Set-up
  1. Monitor the magnet voltage with a DMM.
  2. Hook up a power supply to the persistent current switch heater.
  3. Send the positive lead of the magnet power supply to the series resistor (maybe 4 W) and then to a magnet terminal. The return should go back to the supply.
  4. Monitor the voltage across the resistor. If the positive power supply went to the red banana magnet terminal, this voltage is positive.
- B. Turn on the magnet power supply
  1. Hit "Output On/Off".

2. Hit "Current" and set it to about an Amp, so you're guaranteed to be in constant voltage mode.
3. If there's current in the magnet, set the voltage to match the current.

C. Drive the switch normal. Need at least 55 mA; use about 70 (about 2.5 V). The magnet voltage shouldn't go nuts.

D. Adjust the magnet current, making sure the magnet voltage stays well below 3 V. Note the final value.

E. Turn off the switch heater and wait a bit.

F. Turn down the magnet supply voltage, making sure the magnet voltage doesn't change. Go home.

VI. Breaking vacuum on the ^{3}He pump

A. The fridge has got to be cold for this method to work

B. Get the pump ready

1. Stop Roots and turn the Mag Valve off. Close #12.
2. Close #3 to the condenser and #5 to the dumps.
3. When P2 is at base pressure, turn off Rotary and let it cool down (maybe 30 minutes). To minimize the time that the fridge is warm, don't proceed until you're ready to yank the pump (i.e. it's cold). Transferring at some point might help keep everything cold.

C. Shove the mix in the panel into the fridge

1. Open #2 and slowly open #7 to the Still. Wait until G2, G3, and G4 are zero. Could take several minutes and G4 may never get there.
2. Close #8A and 1A to isolate trap.
2. Close #2 and #7.

D. Prep the lines

1. Turn on Rotary B and monitor P4.
2. If CT 2 is being used, hook up a section of bellows at CT 1.
3. Hook up Helium to Vent 1.
4. Open #10 and 4. Slowly open #11 to fill the whole deal with He.
5. Wait a second, close #11 and throttle #34 to flush. Close #34. Repeat a couple times.
6. Open #7A; use G2 to monitor front of pump. Open #8 and 4; use G4 to monitor the back of pump.
7. Open #11 and throttle #6 and 10. Fill both sides equally and slowly, up to 950 mbar. You want a layer of Helium on the bellows when you open up.
8. Close #11 and then all the valves.

E. Disconnect the lines to the pump and cap the bellows. Get up and do what needs to be done. Put the lines back.

F. Pump out the lines (in case there is any air and so as not to throw off the mix) – here's one way

1. Open #34.
2. Open #7A and 6; monitor the front of the pump with G2 and P2. Open #8; monitor the back of the pump with G4.
3. Throttle #10 and 4 to slowly bring down both sides of the pump. Probably pump out everything.
4. Close everything.
5. Clean any other parts of the panel that you used.
6. Close #34 and turn off pump.

G. Get the pump and panel ready

1. Turn on the ^{3}He Rotary and make sure P2 gets down to base pressure. See if garbage shows up at G4.
2. If you changed the oil, wait about 30 minutes for it to stop bubbling like crazy.
3. Open #8A, 1A, 2, and 7A to clean whatever's still around. Wait a while.

H. Finish up

1. At this point, R7 might be 6k, but the mix ought to be fine.
2. Close #2, wait, and then 7A.
3. Throttle #12, keeping P2 below 1 mbar. Might try one-shotting to get things going. Otherwise, open #3 and let it go.
4. When P2 is low enough, close #12, open the Mag Valve and start the Roots. Open #5.

VII. Recovering from power failure

A. Turn off Roots, Mag Valve, ^{3}He Rotary, ^{4}He Rotary. Close #12 and 24.
B. If it's been off a while, check temperatures and pressures (especially the dumps). Check the pump room for flames.
C. Hit "Fault Reset" if any of the indicator lights are on. May need to cycle the power of the gas panel and the main panel in the pump room if that doesn't work.
D. Start Pot Pump and let it warm up for a minute. "Slowly" open #24.
E. Start ^{3}He Rotary. Wait a while for it to warm up and the pot to cool.
F. Slowly open #12. Eventually turn on Roots if you want.

VIII. Pump explosion
A. If a pump fails, close relevant valves and turn off the gas panel power. Turn off the main power downstairs and check the main fuses.
B. If you think the pump isn't seized, replace the fuses and try again. To test the pump momentarily, push the little blank button on the relay for the pump (after turning all the power back on).
C. If a fail light is still on, try "Fault Reset" and/or cycling the power again.
D. If that doesn't work, try hitting the red breakers on the bottom of the contactors in the main power box. The contactor also has a test button.
E. If that doesn't fix it, it might be the 3 phase monitor at the top of the main box. There should be a green and yellow light if it's working ok.

IX. Trouble Shooting
A. Fridge won't cool
1. Symptoms: Still pressure low, even with a little heating. Nothing else unusual.
Problem: ^{3}He caught somewhere funny
Solution: Close #3 to stop circulation. Open #2, 5, and right Dump valves. Make sure there's enough still heat to give a decent still pressure once the circulation stops. Pull maybe 20 mbar into Dumps through cold trap; close #2. Open #3 again and go grab a sandwich. Open #7 (slowly) to cryopump mix into Still and perhaps heat a bit. Close #7 after Dumps are empty – could be a while.
B. Condenser pressure increases
1. Symptom: Cold traps are clean
Problem: Pot might be empty
Solution: Check pot level; fiddle with needle valve

X. Changing the He3 pump oil. -Tauno(summer2006) * Hasn't been double checked in practice
A. Preliminary stuff
1. Everything closed and all mix should be between He3 Rotary, 5, 8, and 8a;
2. Have He3 rotary on
3. Make sure you have enough new pump oil, 6 liters of Alcatel 111; Alcatel 111 has a low vapor pressure
B. Pump out everything,
1. Turn on Rotary B, turn on P4, and open #34 and #10
2. P4 should get below 0.1mBarr
3. Attach cryopump to vent #1
4. Open #11 and then open black knob on cryopump, pressure should again fall below 0.1mBarr
5.Close everything, (except black knob on cryopump)
C. Save Mix
1.Put the cryopump in the liquid Helium dewar
2. Open #9, #5, #6, #11 and watch the dump pressure fall, should get to be <20mBarr
3. To get even more saved…close #9 and #5 (#6 and #11 only things open)
4. Open right dump valve, dump pressure should go to 650ish,
5. Pull cryopump out of dewar watching the still pressure, when it gets above 650 open #5 to put more in the dumps.
6. When the dump pressure and still pressure become equal with #5 open, close everything (except black knob)

7. Put the cryopump back in the dewar and open #9, #5, #6, #11; Dump pressure should be at 0 now
8. Close every last thing now, and turn off the He3 rotary

D. Change oil
   1. There is a lot of oil in this pump so prepare for more than one load, and get paper towels
   2. Release pressure by opening both sides of pump and cover them up so nothing gets in
   3. Open release plug and watch it flow, catching oil, open pour valve for a better flow,
   4. Open secondary plug to get more oil.
   5. Check all o-rings for cracks while you're at it
   6. Put in clean Alcatel 111 oil until both windows are filled to the middle, about 6 liters after plugs returned
   7. Close up the oil pumps and openings
   8. Reattach the pump lines

E. Pumping out lines (with pumping on I'd guess?)
   1. Pump out line B, open #34 and then open #4 and #8 to pump out section behind pump, should take a while to get to base pressure
   2. After a day or two of pumping
   3. Flush the mix through the nitrogen traps before putting it in the fridge again.

Bibliography

[1] D. Loss and D. P. DiVencenzo, “Quantum computation with quantum dots,” Phys. Rev. A. **57**(1), 120 (1998).

[2] I. H. Deutsch, G. K. Brennen, and P.S. Jessen, “Quantum computing with neutral atoms in an optical lattice,” Fortschritte der Physik **48**, 925 (2000).

[3] J. Q. You and F. Nori, “Superconducting Circuits and Quantum Information,” Physics Today **58**(11), 42 (2005).

[4] R. P. Feynman, “Simulating Physics with Computers,” Int. J. Theor. Phys. **21**, 467 (1982).

[5] D. Deutsch, Proceedings of the Royal Society of London: Series A – Mathematical and Physical Sciences **A400,** 97 (1985).

[6] D. Deutsch and R. Jozsa, Proceedings of the Royal Society of London: Series A – Mathematical and Physical Sciences **A439**, 553 (1992).

[7] L. K. Grover, “Quantum mechanics helps in searching for a needle in a haystack,” Phys. Rev. Lett. **79**, 325 (1997).

[8] P. Shor, Proceddings, 35th Annual Symposium on Foundations of Computer Science IEEE Press, Los Alamitos, CA, (1994).

[9] J. S. Bell, “On the Einstein Podolsky Rosen Paradox”, Physics **1**, 195 (1964).

[10] S. J. Freedman and J. F. Clauser, “Experimental test of local hidden-variable theories,” Phys. Rev. Lett. **28**(14), 938 (1972).

[11] M. A. Rowe, D. Kielpinski, V. Meyer, C. A. Sackett, W. M. Itano, C. Monroe, and D. J. Wineland, “Experimental violation of a Bell’s inequality with efficient detection,” Nature **409**, 791 (2001).

[12] D. L. Moehring, M. J. Madsen, B.B. Blinov, and C. Monroe, “Bell inequality violation with two remote atomic qubits,” Phys. Rev. Lett. **93**, 9 (2004).

[13] M. A. Nielsen and I. L. Chuange, *Quantum Computation and Quantum Information* (Cambridge Univ. Press, Cambridge, 2001).

[14] D. P. DiVincenzo, Topics in Quantum Computers (16-Dec-96) *http://arxiv.org/PS_cache/cond-mat/pdf/9612/9612126v2.pdf*.

[15] E. Knill, "Scalable quantum computing in the presence of large detected-error rates," Phys. Rev. A **71**(4), 042322 (2005).

[16] J. I. Cirac and P. Zoller, "Quantum Computations with Cold Trapped Ions," Phys. Rev. Lett. **74**(20), 4091 (1995).

[17] B. E. Kane, "A silicon-based nuclear spin quantum computer," Nature **393**(6681), 133 (1998).

[18] Y. Nakamura, Y. A. Pashkin, and J.S. Tsai, "Coherent control of macroscopic quantum states in a single-Cooper-pair box," Nature **398**(6730), 786 (1999).

[19] A. Abragam, *The Principles of Nuclear Magnetism* (Oxford, London, 1961).

[20] B. D. Joesphson, "Possible new effects in superconductive tunneling," Phys. Lett. **1**(7), 251 (1962).

[21] M. Tinkham, *Introduction to Superconductivity*, 2nd ed. (Dover Publications, Mineola, New York , 1996)

[22] W. C. Steward, "Current-Voltage Characteristics of Josephson Junctions," Appl. Phys. Lett. **12**(8), 277 (1968).

[23] D. E. McCumber, " Effect of ac Impedance on dc Voltage-Current Characteristics of Superconductor Weak-Link Junctions," J. Appl. Phys. **39**(7), 3113 (1968).

[24] M. A. Gubrud, M. Ejrnaes, A. J. Berkley, R. C. Ramos, I. Jin, J. R. Anderson, C. J. Lobb, and F. C. Wellstood, "Sub-Gap Leakage in Nb/AlO$_x$/Nb and Al/AlO$_x$/Al Josephson Junctions," IEEE Trans, Appl. Supercond. **11**(1), 10002 (2001).

[25] Michel H. Devoret, John M. Martinis, and John Clarke, "Measurement of Macroscopic Quantum Tunneling out of the Zero-Voltage Sate of a Current-Biased Josephson Junction," Phys. Rev. Lett. **55**(18), 1908 (1985).

[26] F. W. Strauch, *Theory of Superconducting Phase Qubits*, Ph. D. thesis, University of Maryland, College Park (2004).

[27] A. J. Berkley, *A Josephson Junction Qubit*, Ph.D. thesis, University of Maryland, College Park (2003).

[28] T. A. Fulton and L. N. Dunkleberger, "Lifetime of the zero-voltage state in Joesphson tunnel junctions," Phys. Rev. B **9**(11), 4760 (1974).

[29] M. Bűttiker, E. P. Harris, and R. Landauer, "Thermal activation in extrememly underdamped Josephson-junction circuits," Phys. Rev. B **28**(3), 1268 (1983).

[30] A. J. Leggett, "Macroscopic Quantum Systems and the Quantum Theory of Measurement," Prog. Theor. Phys. (Suppl.) **69**, 80 (1980).

[31] P.W. Anderson, *Lectures on The Many-Body Problem, Volume 2*, E. R. Caianiello, editor (Academic Press, New York, 1964).

[32] J. J. Sakurai and S. F. Tuan (Editor), *Modern Quantum Mechanics*, rev. ed. (Addison-Wesley, Reading, MA, 1994).

[33] R. C. Ramos, M. A. Gubrud, A. J. Berkley, J. R. Anderson, C. J. Lobb, and F. C. Wellstood, "Design for Effective Thermalization of Junctions for Quanutm Coherence," IEEE Trans. Appl. Supercond. **11**(1), 998 (2001).

[34] J. M. Martinis, M. H. Devoret, and J. Clarke, "Energy-Level Quantization in the Zero-Voltage State of a Current-Biased Josephson Junction," Phys. Rev. Lett. **55**(15), 1543 (1985).

[35] J. M. Martinis, *Macroscopic Quantum Tunneling and Energy-Level Quantization in the Zero Voltage State of the Current-Biased Josephson Junction*, Ph. D. thesis, University of California (1985).

[36] H. Xu, *Quantum Computing with Josephson Junction Circuits*, Ph.D. thesis, University of Maryland, College Park (2004).

[37] S. K. Dutta, *Characterization of Josephson Devices For Use In Quantum Computation*, Ph.D. thesis, University of Maryland (2006).

[38] A. J. Berkley, H. Xu, M. A. Gubrud, R. C. Ramos, J. R. Anderson, C. J. Lobb, and F. C. Wellstood, "Decoherence in a Josephson-junction qubit," Phys. Rev. B **68**(6), 060502(R) (2003).

[39] J. M. Martinis, S. Nam, J. Aumentado, and C. Urbina, "Rabi Oscillations in a Large Josephson-Junction Qubit," Phys. Rev. Lett. **89**(11), 117901 (2002).

[40] C. D. Tesche and J. Clarke, *Noise and Optimization of the dc SQUID*, Ph.D. Thesis, University of California (1978).

[41] T. A. Palomaki, S. K. Dutta, H. Paik, H. Xu, J. Matthews, R. M. Lewis, R. C. Ramos, K. Mitra, P. R. Johnson, F. W. Strauch, A. J. Dragt, C. J. Lobb, J. R. Anderson and F. C. Wellstood, "Initializing the flux state of multiwell inductively isolated Josephson junction qubits," Phys. Rev. B **73**(1), 014520 (2006).

[42] K. Mitra, F. W. Strauch, C. J. Lobb, J. R. Anderson, F. C. Wellstood, and Eite Tiesinga, "Quantum behavior of the dc SQUID phase qubit," (accepted PRB).

[43] C. D. Tesche and J. Clarke, “dc SQUID: Noise and Optimization,” J. Low Temp. Phys. **29**(3/4), 301 (1977).

[44] P. R. Johnson, F. W. Strauch, A. J. Dragt, R. C. Ramos, C. J. Lobb, J. R. Anderson and F. C. Wellstood, “Spectroscopy of capacitively coupled Josephson-junction qubits,” Phys. Rev. B **67**(2), 020509(R) (2003).

[45] A. J. Berkley, H. Xu, R. C. Ramos, M. A. Gubrud, F. W. Strauch, P. R. Johnson, J. R. Anderson, A. J. Dragt, C. J. Lobb, and F. C. Wellstood, “Entangled Macroscopic Quantum States in Two Superconducting Qubits,” Science **300**(5625), 1548 (2003), comment, **301**(5637), 1183 (2003).

[46] H. Xu, F. W. Strauch, S. K. Dutta, P. R. Johnson, R. C. Ramos, A. J. Berkley, H. Paik, J. R. Anderson, A. J. Dragt, C. J. Lobb and F. C. Wellstood, “Spectroscopy of Three-Particle Entanglement in a Macroscopic Superconducting Circuit,” Phys. Rev. Lett. **94**(2), 027003 (2005).

[47] I. I. Rabi, J. R. Zacharias, S. Millman, and P. Kusch, “A New Method of Measuring Nuclear Magnetic Moment,” Phys. Rev. **53**(4), 318 (1938).

[48] F. Reif, *Fundamentals of Statistical and Thermal Physics*, 1st ed. (McGraw-Hill Publications, Mineola, New York , 1965)

[49] John M. Martinis, S. Nam, J. Aumentado, C. Urbina, and K. M. Lang, “Decoherence of a superconducting qubit due to bias noise,” Phys. Rev. B **69** 094510 (2003).

[50] H. B Callen and T. A. Welton, “ Irreversibility and Generalized Noise,” Phys. Rev. **83**, 34 (1951).

[51] J. B. Johnson, “Thermal Agitation of Electricity in Conductors,” Phys. Rev. **32**, 97 (1928).

[52] H. Nyquist, “Thermal Agitation of Electric Charge in Conductors,” Phys. Rev. **32**, 110 (1928).

[53] F. Yoshihara, K. Harrabi, A. O. Niskanen, Y. Nakamura, and J. S. Tsai, “Decoherence of Flux Qubits due to 1/*f* Flux Noise," Phys. Rev. Lett. **97**(16), 167001 (2006).

[54] A. O. Caldeira and A. J. Leggett, “Quantum Tunneling in a Dissipative System” Ann. Phys. (NY) 149(1983) 374.

[55] M. H. Devoret, in Fluctuations Quantiques (Elsevier, Science, 1997).

[56] Roger H. Koch, D. J. Van Harlingen, and John Clarke, " Observation of Zero-Point Fluctuations in a Resistively Shunted Josephson Tunnel Junction," Phys. Rev. Lett. **47**(17) 1216 (1981).

[57] H. Xu, A. J. Berkley, R. C. Ramos, M. A. Gubrud, P. R. Johnson, F. W. Strauch, A. J. Dragt, J. R. Anderson, C. J. Lobb, and F. C. Wellstood, "Spectroscopic resonance broadening in a Josephson junction qubit due to current noise," Phys. Rev. B **71**(6), 064512 (2005).

[58] L. Allen and J. H. Eberly, Optical Resonance and Two-Level Atoms (Dover, New York, 1987)

[59] L. M. K. Vandersypen and I. L. Chuang, "NMR techniques for quantum control and computation," Rev. Mod. Phys. **76** (2004).

[60] H. Carr and E. Purcell, "Effects of Diffusion on Free Precession in Nuclear Magnetic Resonance Experiments," Phys. Rev. 943, **630**(3) (1954).

[61] R. Hanson, L. P. Kouwenhoven, J. R. Petta, S. Tarucha, L. M. K. Vandersypen, "Spins in few-electron quantum dots," Rev. Mod. Phys. **79** (2007).

[62] R. P. Feynman, *Statistical Mechanics: A Set of Lectures* (W. A. Benjamin, Reading, MA, 1972).

[63] F.C. Wellstood, (unpublished).

[64] H. C. Torrey, "Transient Nutation in Nuclear Magnetic Resonance," Phys. Rev. **76**(8), 1059 (1949),

[65] S. K. Dutta, Frederick W. Strauch, R. M. Lewis, K. Mitra, Hanhee Paik, T. A. Palomaki, E. Tiesinga, J. R. Anderson, Alex J. Dragt, C. J. Lobb, and F. C. Wellstood, "Multi-level analysis of Rabi oscillations of a dc SQUID phase qubit," submitted to PRB.

[66] K. B. Cooper, M. Steffen, R. McDermott, R. W. Simmonds, S. Oh, D. A. Hite, D. P. Pappas, and J. M. Martinis, "Observation of a Quantum Oscillations between a Josephson Phase Qubit and a Microscopic Resonator Using Fast Readout," Phys. Rev. Lett. **93**(18), 180401 (2004).

[67] J. Lisenfeld, A. Lukashenko, M. Ansmann, J. M. Martinis, and A. V. Ustinov, "Temperature Dependence of Coherent Oscillations in Josephson Phase Qubits," Phys. Rev. Lett. **99**(17), 170504 (2007).

[68] Hanhee Paik, *Coherence in dc SQUID Phase Qubits*, Ph.D. thesis, University of Maryland (2007).

[69] Hanhee Paik, S. K. Dutta, R. M. Lewis, T. A. Palomaki, B. K. Cooper, R. C. Ramos, H. Xu, A. J. Dragt, J. R. Anderson, C. J. Lobb, and F. C. Wellstood, "Decoherence in dc SQUID phase qubits," accepted Phys. Rev. B. (2008).

[70] F. C. Wellstood, *Excess Noise in the dc SQUID; 4.2 K to 20 mK,* Ph.D. thesis, University of California (1988).

[71] F. C. Wellstood, C. Urbina, and J. Clarke, "Low-frequency Noise in dc Superconducting Quantum Interference Devices Below 1-K," App. Phys. Lett. **50**(12), 772, (1987).

[72] R. M. Lewis, "Flux Noise in the dc SQUID Phase Qubit Measured by Microwave Reflectometry" manuscript under preparation.

[73] R. C. Bialczak, R. McDermott, M. Ansmann, H. Hofheinz, N. Katx, E. Lucero, M. Neeley, A. D. O'Connell, H. Wang, A. N. Cleland, and J. M. Martinis, "1/f Flux Noise in Josephson Phase Qubits," Phys. Rev. Lett. **99**(18), 187006 (2007).

[74] R. H. Koch, D. P. DiVincenzo and J. Clarke, "Model for 1/f Flux Noise in SQUIDs and qubits," Phys. Rev. Lett. **98**(26), 267003 (2007).

[75] Hypres, Inc. 175 Clearbrook Road, Elmsford, NY 10523. www.hypres.com.

[76] T. A. Fulton and G. J. Dolan, "Observation of Single-electron Charging Effects in Small Tunnel Junctions," Phys. Rev. Lett. **59**(1), 109 (1987).

[77] MicroChem Corp., 1254 Chestnut Stree, Newton, MA 02464. http://www.microchem.com

[78] Berkeley Microlab, University of California, CA. http://microlab.berkeley.edu.

[79] University Wafer, 66 N Street Unit #9 South Boston, MA 02127 USA, http://www.universitywafer.com/

[80] SUSS MicroTec, Schleiβheimer Str. 90, D 85748 Garching, Germany. http://www.suss.com/.

[81] J. M. Martinis, K. B. Cooper, R. McDermott, M. Steffen, M. Ansmann, K. D. Osborn, K. Cicak, S. Oh, D. Pappas, R. Simmonds, and C. C. Yu, "Decoherence in Josephson Qubits from Dielectric Loss," Phys. Rev. Lett. **95**(21), 210503 (2005).

[82] Oxford Model 200 TLE Complete Dilution Refrigerator Instruction Manual (1989)

[83] Picowatt, RV-Elektroniikka Oy Picowatt Veromiehentie 14, FI-01510 VANTAA, Finland, http://www.picowatt.fi/.

[84] Cryomagnetics 10060 Alvin Weinberg Drive, Oak Ridge, Tennessee 37830 USA http://cryomagnetics.com/.

[85] Universal Shielding Corporation, 20 W Jefryn Blvd Deer Park, NY 11729-5769 USA, http://www.universalshielding.com/.

[86] THERMOCOAX SAS, BP 26, 61438 FLERS CEDEX, France http://www.thermocoax.com/.

[87] A. B. Zorin, “The thermocoax cable as the microwave frequency filter for single electron circuits," Rev. Sci. Instrum. **66**(8), 4296 (1995).

[88] Coaxicom, 10 DaVinci Drive, Bohemia, NY 11716-2601 USA, http://www.coaxicom.com/home.html.

[89] J. M. Martinis, M. H. Devoret, and J. Clarke, “Experimental tests for the quantum behavior of a mascroscopic degree of freedom: The phase difference across a Josephson junction,” Phys. Rev. B **35**(10), 4682 (1987).

[90] K. Bladh, D. Gunnarsson, E. HÄurfeld, S. Devi, C. Kristoffersson, B. Smalander, S. Pehrson, T. Claeson, P. Delsing, and M. Taslakov, “Comparison of cryogenic filters for use in single electronics experiments," Rev. Sci. Instrum. **74**(3), 1323 (2003).

[91] LakeShore 575 McCorkle Blvd, Westerville OH, 43082 USA, http://www.lakeshore.com/

[92] Rupert Lewis, Private Communication.

[93] V. Lefevre-Seguin, E. Turlot, C. Urbina, D. Esteve, and M. Devoret, “Thermal activation of a hysteretic dc superconducting quantum interference device from its different zero-voltage states,” Phys. Rev. B **46**(9), 5507 (1992).

[94] A. O. Caldeira and A. J. Leffett, “Influence of Dissipation on Quantum Tunneling in Macroscopic Systems,” Phys. Rev. Lett. **46**(4), 211 (1981).

[95] S. K. Dutta, H. Xu, A. J. Berkley, R. C. Ramos, M. A. Gubrud, J. R. Anderson, C. J. Lobb, and F. C. Wellstood, “Determination of relaxation time of a Josephson junction qubit” Phys. Rev. B **70**(14), 140502(R) (2004).

[96] Frederick W. Strauch, Philip R. Johnson, Alex J. Dragt, C. J. Lobb, J. R. Anderson, and F. C. Wellstood, “Quantum Logic Gates for Coupled Superconducting Phase Qubits,” Phys. Rev. Lett. **91**, 167005 (2003).

[97] J. Claudon, F. Balestro, F. W. J. Hekking, and O. Buisson, “Coherent Oscillations in a Superconducting Multilevel Quantum System,” Phys. Rev. Lett. **93**(18), 187003 (2004).

[98] T. A. Palomaki, S. K. Dutta, R. M. Lewis, H. Paik, K. Mitra, B. K. Cooper, A. J. Przybysz, A. J. Dragt, J. R. Anderson, C. J. Lobb, and F. C. Wellstood, “ Pulse Current Measurements and Rabi Oscillations in a dc SQUID Phase Qubit,” IEEE Trans. Appl. Supercond. **17**(2), 162 (2007).

[99] P. Silvestrini, V. G. Palmieri, B. Ruggiero, and M. Russo, “Observation of Energy Levels Quantization in Underdamped Josephson Junctions Above the Classical-Quantum Regime Crossover Temperature,” Phys. Rev. Lett. **79**(16), 3046 (1997).

[100] Qin Zhang, Abraham G. Kofman, John M. Martinis, and Alexander N. Korotkov, “Analysis of measurement errors for a superconducting phase qubit,” Phys. Rev. B **74**(21) (2006).

[101] Andrew M. Steane, “Overhead and noise threshold of fault-tolerant quantum error correction,” Phys. Rev. A **68**(4), 042322 (2003).

[102] Krysta M. Svore, Barbara M. Terhal, and David P. DiVincenzo, “Local fault-tolerant quantum computation,” Phys. Rev. A **72**(2), 022317 (2005).

[103] E. Knill, “Quantum computing with realistically noisy devices,” Nature **434**(7029), 39 (2005).

[104] T. A. Palomaki, unpublished.

[105] C. Zener, “Non-adiabatic Crossing of Energy Levels,” Proc. R. Soc. London A **137**, 696 (1932).

[106] R. W. Simmonds, K. M. Lang, D. A. Hite, S. Nam, D. P. Pappas, J. M. Martinis, “Decoherence in Josephson Phase Qubits from Junction Resonators,” Phys. Rev. Lett. **93**(7), 077003 (2004).

[107] R. M. Lewis, S. K. Dutta, Hanhee Paik , T. A. Palomaki, B. K. Cooper A. J, Przybysz, A. J. Dragt, J. R. Anderson,C. J. Lobb, F. C.Wellstood, “Increasing spectroscopic coherence times of a DC SQUID phase qubit by operating deeper in the potential well,” IEEE Trans. Appl Supercond. **17**(2), 101 (2007).

[108] S. K. Dutta, *Characterization of Josephson Devices For Use In Quantum Computation*, Ph.D. thesis, University of Maryland (2006) pg. 370.

[109] S. K. Dutta, *Characterization of Josephson Devices For Use In Quantum Computation*, Ph.D. thesis, University of Maryland (2006) pg. 256.

[110] S. K. Dutta, *Characterization of Josephson Devices For Use In Quantum Computation*, Ph.D. thesis, University of Maryland (2006) pg. 324.

[111] R. McDermott, R. W. Simmonds, M. Steffen, K. B. Cooper, K. D. Osborn, S. Oh, D. P. Pappas, and J. M. Martinis, "Simultaneous State Measurement of Coupled Josephson Phase Qubits," Science **307**(5713), 1299 (2005).

[112] M. Heald and J. Marion, *Classical Electromagnetic Radiation*, 3rd ed. (Saunders College Publishing, Fort Worth, (1995).

[113] S. Hunklinger and A. K. Raychaudhuri, "Thermal and Elastic Anomalies in Glasses at Low Temperatures" in D. F. Brewer (ed.), Progress in Low Temperature Physics, Elsevier, New York (1986), p. 281.

[114] D. J. Van Harlingen, T. L. Robertson, B. L. T. Plourder, P. A. Reichardt, T. A. Crane, and John Clarke, "Decoherence in Josephson-junction qubits due to critical-current fluctuations," Phys. Rev. B. **70**(6), 064517 (2004).

[115] Li-Chung Ku and Clare C. Yu, "Decoherence of a Josephson qubit due to coupling to two-level systems," Phys. Rev. B **72**(2), 024526 (2005).

[116] A. Barone and G. Paterno, *Physics and Applications of the Josephson Effect* (Wiley, New York, 1982).

[117] L. Tian and R.W. Simmonds, "Josephson Junction Microscope for Low-Frequency Fluctuators," Phys. Rev. Lett. **99**(13), 137002 (2007).

[118] P. R. Johnson, W. T. Parsons, F. W. Strauch, J.R. Anderson, A. J. Dragt, C. J. Lobb, and F. C. Wellstood, "Macroscopic Tunnel Splittings in Superconducting Phase Qubits," Phys. Rev. Lett. **94**(18), 187004 (2005), erratum, **95**(4), 049901 (2005).

[119] S. Ashab, J. R. Johansson, and F. Nori, "Rabi oscillations in a qubit coupled to a quantum two-level system," New J. Phys. **8**, 103 (2006).

[120] A. M. Zagoskin, S. Ashab, J. R. Johansson, and F. Nori, "Quantum Two-Level Systems in Josephson Junctions as Naturally Formed Qubits," Phys. Rev. Lett. **97**(7), 077001 (2006).

[121] The peaks were not lorentzian near $f = 10.714\,GHz$. This estimate only includes the bias currents as shown in Fig. 10.3

[122] The data was too scattered to obtain a meaningful fit. This is a very rough estimate, considering the splitting #7 appears to dominate the behavior near $I = 1.1\,\mu A$.

[123] J. Koch, T. M. Yu, J. Gambetta, A. A. Houch, D. I. Schuster, J. Majer, A. Blais, M. H. Devoret, S. M. Girvin, R. J. Schoelkopf, “Charge-insensitive qubit design derived from the Cooper Pair box,” **76**(4) 042319 (2007).